
Confined Bose superfluids:
*a study of vorticity in a rotating bucket, and
phase transitions and sound in a trap from two
to three dimensions*



NICK KEEPFER

Thesis submitted for the degree of
Doctor of Philosophy

Under the joint supervision of
Prof. Nick Proukakis
Prof. Franco Dalfovo

November, 2022

Acknowledgements

Allow me to begin by thanking my two supervisors, Nick Proukakis and Franco Dalfovo for their immeasurable contributions and support throughout these last four years. Each of you have been wonderful, patient mentors and I am incredibly grateful to you both.

On the topic of great mentors, I wish to thank Jackie Seils, for igniting my interest in Mathematics that led me to this point, over a decade ago. Thank you to Nick Parker for steering me towards the pursuit of a PhD and for all his support and assistance throughout my time at Newcastle. Additionally, I extend a very large thank you to Gary Liu who has been a valuable friend, mentor and colleague to me throughout my PhD.

Being a cotutelle student, I have been lucky enough to meet twice the amount of people I would otherwise have had chance to during my PhD. Thank you to the lovely people I got to share an office with in Newcastle: Nicola Hewett, Ryan Doran, Holly Middleton-Spencer, Kieran Peel, James Murray and Cameron Williams. An additional thanks goes to Nicola and Ryan for always making sure I had a place to stay in Newcastle whilst working remotely in the final year. A number of other Newcastle people I would like to thank are Tom Bland, Thomas Flynn, Keaghan Krog, Stephen Mason, Luca Galantucci, Richard Tattersall, Andrew Groszek, George Stagg, Sri Badariprasad and Fabrizio Larcher.

In Trento, I am enormously grateful to have shared an office with Arko Roy, your kindness and hospitality throughout my time in Trento made me feel most welcome. I extend the same gratitude to Miki Ota, Philipp Uhrich, Soumik Bandyopadhyay and Albert Gallemi whose conversations and warmth made lunchtimes and coffee breaks some of the brightest parts of the day. I extend a general thank you to everyone at San Bartolomeo for all the memories made and meals shared together, especially to Azaz, Ryo and Chiara. I would also like to thank all the members of the Trento physics department for their kindness and conversations during my time there.

I would like to thank Jamie, for the sporadic phone calls that kept me focused throughout these years. I thank Pablo for all the memories had in Trento and eventual memories to come in Mexico. I am grateful to my friends at Red Goat, who have shared many victories and defeats in bouldering with me throughout this PhD. I am also grateful to Ludovic, Sam and the rest of the Julia community for their generous support and assistance.

Most importantly, this undertaking would have never been possible without the love and encouragement from my family. I would like to extend the largest thanks of all to my parents Adele and Rick for their unwavering support. I would also like to thank my sister Gabrielle and her fiancé Sam for supplying me with much-needed reminders of my nerd status within the family and occasional sweets. Lastly I thank you, Stanley, for all your tail wagging, excitement and company of which I have enjoyed greatly.

Abstract

Quantum fluids are a fascinating state of matter, permitting extraordinary insights into the behaviour of macroscopic quantum systems. Most strikingly, they possess the property of superfluidity, enabling inviscid flow. Whilst irrotational in nature, singularities in the fluid provide localised vorticity in the form of quantised vortex filaments. Interaction between these vortex structures provides rich dynamical behaviour which is interrogated within the first part of this thesis. Furthermore, one expects the equilibrium and dynamical properties of a trapped superfluid system to vary in response to changes in dimensionality. Whilst dimensionality crossovers have previously been considered both experimentally and theoretically, the nature of the dimensional crossover between the 2D and 3D phase transitions in a trapped Bose gas remains relatively unexplored and forms the secondary focus of this thesis.

Initially, we consider the effects of disordered potentials, protuberances and remnant vortices for a zero temperature weakly interacting Bose gas under rotation. Focusing particularly on a rough bucket potential we draw parallels with superfluid helium experiments, where such effects must be considered. Our findings elucidate important insights on the effects of vortex proliferation in the spin-up dynamics of a quiescent system towards the simple and well-reproduced vortex lattice structure.

We then go on to discuss the effects of dimensionality on the finite temperature weakly interacting Bose gas, this time concentrating on a hybridised optical trap that allows one to modify the trapping strength along a singular direction. Utilising the stochastic projected Gross-Pitaevskii equation (SPGPE) we validate our approach based on previous findings at the dimensional extremes before considering in greater detail, the precise nature of the crossover region. We introduce a novel mixed basis numerical scheme to solve the SPGPE in the hybridised geometry. Using this, we identify and numerically extract a phase transition temperature as a function of dimensionality using a collection of equilibrium statistics. Building on this work, we subsequently conduct a numerical investigation into the propagation of sound as a function of dimensionality in the trapped Bose gas. We discover new insights on the properties of the sound across the phase transition at the dimensional extremes. We then extend our work into the dimensionality crossover region, paying particular attention to the behaviour of the sound at the phase transition critical point.

Contents

Introduction	1
Bose-Einstein condensation	1
Experimental realisations of Bose-Einstein condensation	2
Thesis motivation	4
Thesis outline	5
List of publications	7
Collaborative work	7
I Zero Temperature	8
1 Weakly interacting Bose gases	9
1.1 The ideal uniform non-interacting Bose gas	9
1.1.1 The ideal Bose gas in a 3D box	9
1.1.2 The ideal Bose gas in a 2D box	11
1.1.3 The ideal Bose gas in a rectangular box with transverse confinement	12
1.2 The Gross-Pitaevskii equation	16
1.2.1 The role of interactions in a dilute Bose gas	16
1.3 The weakly interacting Bose gas in a rectangular box under transverse harmonic confinement	20
1.3.1 Interactions at low temperature	22
1.4 Quasi-condensation	23
1.5 Bogoliubov theory	23
1.6 Sound speed of the weakly interacting Bose gas	28
1.7 Chapter summary	29
2 Spin-up of a superfluid vortex lattice driven by rough boundaries	30
2.1 Introduction to superfluidity	30
2.2 Numerical recipe	34
2.2.1 Bucket set-up	35

2.2.2	Surface roughness	36
2.2.3	Typical spin-up dynamics	38
2.2.4	Role of angular velocity and roughness	42
2.3	Other effects	44
2.3.1	Effect of a strong protuberance	44
2.3.2	Effect of remanent vortices	45
2.3.3	2D case	47
2.4	Chapter conclusions	50
II	Finite Temperature	53
3	Finite temperature stochastic Gross-Pitaevskii methods	54
3.1	The stochastic projected Gross-Pitaevskii equation	54
3.1.1	Formulating the SPGPE	55
3.1.2	Simple growth stochastic projected Gross-Pitaevskii equation	58
3.1.3	Addressing the ultraviolet catastrophe	59
3.1.4	Hybrid trapping geometry	60
3.1.5	Numerical implementation of the simple growth SPGPE	62
3.1.6	Numerical implementation of the projector	63
3.2	Incoherent atomic density in the SPGPE	64
3.2.1	Density normalisation across dimensionality through tuning of the chemical Potential	74
3.3	Chapter conclusions	77
4	Equilibrium analysis of the dimensionally reduced Bose gas from two to three dimensions	78
4.1	The role of dimensionality in the characterisation of the critical transition point	78
4.2	Equilibration physics inside the hybrid trapping Geometry	79
4.3	Normalising atomic density and Bogoliubov sound speed across dimensionality and temperature	80
4.4	Limiting regimes	83
4.4.1	The BEC transition	84
4.4.2	The BKT transition	85
4.5	Dimensional crossover	88
4.5.1	Equilibrium statistics	89
4.5.2	Determination of the phase transition via equilibrium statistic thresholding	94

4.6	Phase transition temperature as a function of dimensionality	95
4.6.1	Localising the BKT transition	95
4.6.2	Localising the BEC transition	95
4.6.3	From 2D to 3D	97
4.7	Chapter conclusions	101
5	Characterisation of sound speed in the weakly interacting Bose gas through the 2D-3D dimensionality crossover	103
5.1	Propagation of sound in quantum fluids	103
5.2	Collisional regimes	104
5.3	Experimental works on the second sound as a function of temperature	104
5.3.1	Experiments in quasi-1D geometry	105
5.3.2	Experiments in quasi-2D geometry	106
5.4	Excitation protocol	108
5.5	Dynamical evolution	109
5.6	Effects of dimensionality on the second sound speed	113
5.7	Chapter conclusions	119
Thesis conclusions and further work	121	
Appendices	126	
Appendix A Density of states across geometries	127	
A.1	Particle in a square box in two-dimensions	128
A.2	Particle in a rectangular box in two-dimensions	128
A.3	Particle in a square box in three dimensions	129
A.4	Harmonic trap in three dimensions	130
A.5	Square box with transverse harmonic potential	130
A.6	Rectangular box with transverse harmonic potential	131
Appendix B Hybrid basis SPGPE	134	
B.1	System preparation	134
B.2	Hybrid basis	136
B.3	Utilisation of GPUs	139
B.4	Fourth order Runge-Kutta numerical integration	141

Introduction

In recent decades, atomic Bose gases have proven to be an invaluable tool in the understanding and investigation of many-body systems [1, 2]. The successful implementation of highly-controllable trapping geometries, the tuning of inter-atomic interactions and the advances of in-situ visualisation of Bose gases have allowed them to be used as a platform for the discovery of novel phenomena. One potential avenue that remains relatively unexplored is the effect of dimensionality on phase transitions of the Bose gas. Phase transitions are ubiquitous and omnipresent in the universe around us. However, it is not often the case that we have direct control over the topology of a system in order to explore such phase transitions as a function of dimensionality. Recent experimental developments allow us to confine Bose gases in homogeneous and semi-homogeneous trapping geometries [3–5], permitting the direct investigation of the aforementioned scenario. Let us begin, by briefly introducing the theory of Bose-Einstein condensation.

Bose-Einstein condensation

The theory of quantum mechanics is split between two constituent particles: fermions and bosons. In fact, particle distinguishability lies at the very core of quantum mechanics. The Heisenberg uncertainty principle stipulates that particles cannot be considered as discrete entities and instead have a wave associated with them, known as *wave-particle duality*. In the language of quantum physics, this wave has a statistical nature and is described by means of a *wavefunction*. When exchanging two particles, the sign of the wavefunction is of profound importance. If the wavefunction maintains its sign, it is known as *symmetric*, and if it changes then it is *antisymmetric*. In the former case, corresponding to bosons, particles are free to macroscopically occupy the same quantum state. In the latter case, corresponding to fermions, particles are instead subject to the Pauli-exclusion principle which precludes particles from occupying the same quantum state within a system.

The theory of Bose-Einstein condensation arose when Bose predicted that a photon gas could accumulate into and macroscopically occupy the lowest accessible energy state [6]. Einstein later generalised this theory to apply to bosons in general [7] and together, they proposed a new exotic state of matter: the Bose-Einstein condensate. The theory

predicts that under specific conditions of mass and density, a large proportion of bosonic particles will accumulate into the same lowest quantum energy state, resulting in a giant matter wave, known as the *condensate*. In the context of dilute cold atoms, the atomic densities necessary for Bose-Einstein condensation require temperatures on the nanokelvin scale¹.

For non-interacting dilute Bose gases at high temperatures, the collisions between atoms are largely absent. Typically, the comparison is drawn to a system of colliding billiard balls. In 3D, the average distance between two given particles can be defined $d = \sqrt[3]{V/N}$ where N is the number of atoms and V is the volume containing them. As the energy of the system is lowered, typically through a reduction in temperature, this distance decreases. Close to quantum-degeneracy, where the classical description of particles is replaced by the discrete nature of quantum mechanics, these particles behave more like wavepackets. At this point, the average inter-particle spacing becomes of the same order of the uncertainty on the position of individual particles, as determined by the de Broglie wavelength

$$\lambda_{\text{dB}} = \sqrt{\frac{2\pi\hbar^2}{mk_B T}}. \quad (1)$$

Here $\hbar = 1.055 \times 10^{-34} \text{ Js}$, $k_B = 1.38 \times 10^{-23} \text{ JK}^{-1}$ are the reduced Planck constant and Boltzmann constant respectively. We also introduce m and T to reflect the particle mass and temperature. In fact, once $d \leq \lambda_{\text{dB}}$, the overlapping nature of the quantum particles permits a collective behaviour allowing them to behave as a singular macroscopic quantum object, the Bose-Einstein condensate (BEC).

Experimental realisations of Bose-Einstein condensation

Many decades after the predictions of Bose and Einstein, one of the first observations of a pure Bose-Einstein condensate was eventually realised by Anderson *et al* [9], performed at the JILA² laboratory, where the supercooling of approximately 10^7 ^{87}Rb atoms produced a small almost-pure condensate of 10^3 atoms at 170nK. The thermal velocity profile from this study is shown in Fig. 1, where we observe a clear narrowing in the velocity distribution with decreasing temperature, signposting a clear onset of condensation. Almost simultaneously, the group of Ketterle [10] at MIT³ formed a pure condensate comprised of ^{23}Na , evidenced by a bimodality in the measured velocity distribution, containing up to 5×10^5 atoms. A Bose-Einstein condensate from spin-polarised Lithium was also achieved

¹Within ultra-dense neutron stars, the same phenomenon is thought to occur at temperatures of approximately 10^9 K [8].

²Joint Institute for Laboratory Astrophysics, National Institute of Standards and Technology and University of Colorado.

³Department of Physics and Research Laboratory of Electronics, Massachusetts Institute of Technology.

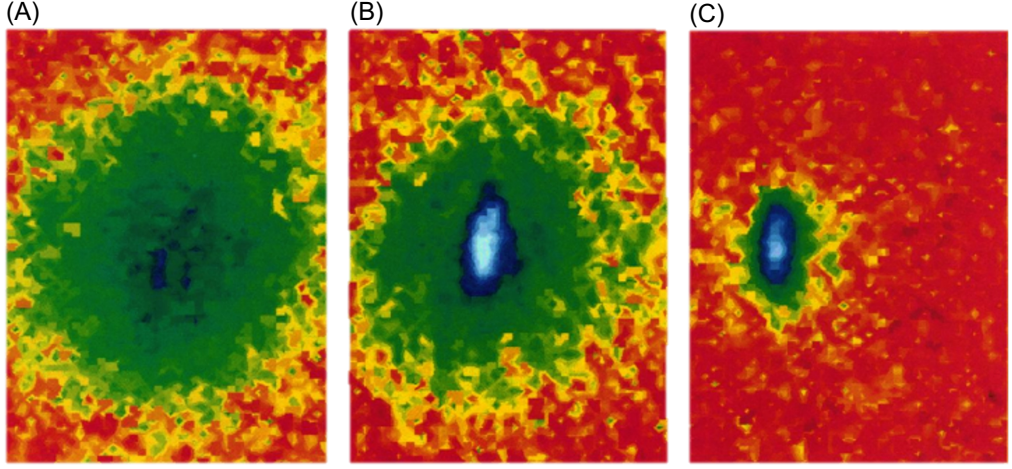


Figure 1: [From [9]. Reprinted with permission from AAAS]. False-colour thermal velocity distribution of a sample of expanded Rubidium atoms as they are cooled below the critical temperature of Bose-Einstein condensation. (A) Before a condensate emerges. (B) Mixed (thermal) condensate. (C) Nearly pure condensate.

that same year [11] from the group of Hulet at Rice University⁴. These breakthrough experiments were largely made possible by advancements in both laser [12–16] and evaporative [17–19] cooling techniques. The condensation of Alkali atoms is made possible by a combination of these techniques. Initially, atoms are laser-cooled by three pairs of counter-propagating laser beams whereby atom-light collisions scatter photons causing a “frictional force” which, on-average, blueshifts photons. As a result, the scattered light carries away more energy than has been absorbed by the atoms, resulting in a net cooling of the system. Once sufficiently cool temperatures have been reached, the lasers are switched off and replaced with a magnetic trapping confinement. Evaporative cooling is then performed through a progressive lowering of trapping depth, which permits the escape of high-energy atoms whilst the remainder rethermalise to increasingly cooler temperatures. Following the experimental breakthrough of BEC, interest in this quantum state of matter has intensified significantly. Whilst experiments initially utilised static harmonic traps [9–11], modern experimentalists have devised both magnetic and optical trapping apparatus that permit supreme control on the topology and the dynamics of a trapped gas. These allow the formation of BECs in novel and interesting geometries. One of the first deviations from static harmonic trapping was performed by Henderson *et al* [20] using a scanning tweezer beam. This study pioneered the generation of novel trapping geometries, and importantly was the first instance of a dynamic spatiotemporally variable trapping potential. Soon thereafter, other international groups were able to obtain quasi-uniform three-dimensional trapping [3] with spatial light modulators and

⁴Physics Department and Rice Quantum Institute, Rice University, Houston, Texas 77251-189.

recently the application of digital micromirror devices [4] allowing full arbitrary control over trapping potentials. Interactions for a dilute ultracold bosonic gas are dominated by *s*-wave collisions at the scattering length a_s which characterises the effective interaction lengthscale between two atoms. A negative scattering length implies that atoms are attracted to each other, leading to a system collapse without a sufficiently mitigating trapping potential. This collapse has been experimentally observed and coined the *Bose-nova* [21, 22]. Instead, a positive scattering length imparts repulsive inter-atomic interactions, decreasing the density of the gas. To ensure the gas remains sufficiently dilute, we require this scattering length to be smaller than the inter-particle distance d . The experimental tuning of the scattering length through Feshbach resonances [23] for a given atomic species is a largely solved problem and gives extraordinary control over BEC experiments. The combination of arbitrary trapping potentials and control over the atomic interactions for a given system constitute an experimental and theoretical armamentarium to thoroughly investigate the properties of BEC.

Thesis motivation

In this thesis we scrutinise the effects of confining geometries on the equilibrium characteristics and dynamics of a dilute Bose gas. We focus in particular on two main systems of interest: A rough-bucket geometry, designed to mimic experimental studies of liquid helium, and secondly a planar box trap under transverse confinement which can be arbitrarily varied.

Firstly, we investigate the effects of disorder and roughness on the nucleation and proliferation of vorticity in a zero temperature quantum fluid as it is spun up from a quiescent state into the rotational ground state solution. The resultant hexagonal vortex lattice structure that is generated encapsulates the paradigm of superfluidity, as the quantised vorticity structure portrayed is in stark contrast to the behaviour of classical fluids. So far, little research has been conducted on the mechanisms at play in the dynamical evolution towards this state. To this end, we utilise the Gross-Pitaevskii formalism to model a superfluid system in the presence of a hard-walled bucket potential whose topology has been altered to embody roughness under various rotational frequencies. We investigate the timescales of relaxation towards the expected vortex lattice structure of quantum vortices in the rotating frame. In addition, we track vortex filaments and their topological information as they diffuse inwardly from the turbulent boundary layer prior to aligning along the axial direction. We find evidence to support the proposition of a vortex-free region around the boundary and show the importance of interactions and reconnection events for vortex filaments as they form something as straightforward as the vortex lattice structure. We go on to modify the disorder of our system and investigate the effects

of protuberances and remnant vorticity, as an analogue to experimental uncertainty and unaccounted vorticity in bucket-like confining potentials for superfluid experiments.

The second avenue we explore is the characteristic and systematic response of a system to a varied dimensionality and temperature. More specifically, we probe the effects of dimensionality on the identification of the phase transition temperature, between the 2D and 3D dimensional extremes. In each dimensional limit there is already an established theory and experimental observations to describe the phase transition mechanism. Importantly, we note the transition between these archetypes remains relatively unexplored and provides a rich area of research for us to explore. To enable this study, we utilise the formalism provided by the stochastic projected Gross-Pitaevskii equation. Here, we perform numerical simulations to sample trajectories of a coherent field coupled directly to a thermal reservoir, assuming each to be in constant equilibrium with one another. Parameter control of the thermal reservoir therefore gives direct and immediate control over the full system. Averaging over multiple realisations, one may build a parameter-space picture on the effects of dimensionality and temperature on a particular system. This section emulates previous theoretical works in the 2D limit, before extending into the third dimension through a simple modification of the trapping potential. Our experimentally-viable trapping geometry is accessible to modern experimental groups and thus an experimental confirmation of our findings remains enticing. We find a monotonic increase in the phase transition temperature as a system becomes less dimensionally suppressed, continuously connecting the 2D and 3D phase transition mechanisms.

Lastly, we develop the results of our finite temperature analysis and use them to characterise the nature of the sound and its response to a change in dimensionality. Here, one would expect a discontinuity of the measured speed across the phase transition within the 3D limit. However, on the opposite side of the spectrum, recent experimental and theoretical research demonstrated that the sound persists across the transition supported by the existence of quasi-condensation. An interesting question emerges on the behaviour of the sound propagation through a dimensional crossover as the nature of the phase transition changes between the dimensional extremes.

Thesis outline

The aim of this thesis is to more deeply understand the effects of vorticity, dimensionality, phase transitions and critical temperature as it applies to the trapped Bose gas. It is comprised of two main parts and subdivided into 5 chapters as we will outline here.

I - Zero temperature

The first part of the thesis concerns the zero temperature fully condensed trapped Bose gas.

1 - Weakly interacting Bose gases

In this chapter we investigate the effects of dimensionality on the behaviour of the ideal Bose gas and discuss the implications of two-body interatomic interactions. We then introduce the Gross-Pitaevskii equation before introducing the specific trapping protocol we employ in the latter parts of this thesis to explore the 2D-3D dimensionality crossover. We discuss the role of interactions and energy in such a confined system and the definition of quasi-condensation. Lastly we introduce Bogoliubov theory to describe low-amplitude excitations on top of the ground state solution and use this to determine the sound speed of the weakly interacting Bose gas.

2 - Spin-up of a superfluid vortex lattice driven by rough boundaries

In this chapter we investigate the effects of a rough and disordered potential in the rotating frame, and how this affects the proliferation of vorticity as it enters from the boundary of an initially quiescent system.

II - Finite temperature

The second part of the thesis concerns the finite temperature trapped Bose gas.

3 - Finite temperature stochastic Gross-Pitaevskii methods

This chapter introduces the theoretical framework for investigating the finite temperature trapped Bose gas. We introduce the Stochastic Gross-Pitaevskii equation, and discuss the specific trapping geometry to study, at equilibrium, the dimensional crossover behaviour of the critical phase transition. We then elaborate on the numerical implementation of this formalism and the specific choice of the parameters and cutoff protocols we employ for this theory. Finally, we discuss a method to extract the total density of the system, including the above-cutoff atoms in our hybridised trapping geometry.

4 - Equilibrium analysis of the dimensionally reduced Bose gas from three to two dimensions

Within this chapter, we discuss in detail the effects of a dimensional crossover as applied to the finite temperature Bose gas. We pay specific attention to the monotonic shift in

numerically extracted phase transition temperature and how this changes between the 2D and 3D regimes.

5 - Characterisation of sound speed in the weakly interacting Bose gas across dimensionality

This chapter investigates the propagation of sound as a function of dimensionality and temperature. Here, we connect the understanding of the behaviour of sound at the dimensional extremes with that in the dimensional crossover. We pay particular attention to the behaviour of the sound at the phase transition temperature.

List of publications

- N. A. Keepfer, I.-K. Liu, F. Dalfovo and N. P. Proukakis, *Phase transition dimensionality crossover from two to three dimensions in a trapped ultracold atomic Bose gas*, accepted for publication in Phys. Rev. Research. Pre-print available at: arXiv:2204.10120 (2022), <https://arxiv.org/abs/2204.10120>
- N. A. Keepfer, G. W. Stagg, L. Galantucci, C. F. Barenghi and N. G. Parker, *Spin-up of a superfluid vortex lattice driven by rough boundaries* (2020), Phys. Rev. B <https://link.aps.org/doi/10.1103/PhysRevB.102.144520>
- N. A. Keepfer, I.-K. Liu, N. P. Proukakis and F. Dalfovo, **Writing-up in progress** *Second sound speed dimensionality crossover from two to three dimensions in the trapped Bose gas*

Collaborative work

The work in Part I of this thesis was partly covered in the publication “Spin-up of a superfluid vortex lattice driven by rough boundaries”, N. A. Keepfer, G. W. Stagg, L. Galantucci, C. F. Barenghi, and N. G. Parker, Phys. Rev. B 102, 144520(2020). A part of this project made use of a Fortran 3D vortex tracking code to track the length of vortex filaments. This was provided by L. Galantucci.

The work in Part II of this thesis was partly covered in “Phase transition dimensionality crossover from two to three dimensions in a trapped ultracold atomic Bose gas”, N. A. Keepfer, I.-K. Liu , F. Dalfovo, N. P. Proukakis. which has been accepted for publication in Phys. Rev. Research. In this work, a Matlab code for generating quadratures within a hybrid-basis was provided by I.-K. Liu.

Part I

Zero Temperature

Chapter 1

Weakly interacting Bose gases

We begin this chapter by introducing the ideal Bose gas and its response to various trapping potentials, before considering the effects of two-body interactions. We then introduce the Bogoliubov theory for describing perturbations to the ground state.

1.1 The ideal uniform non-interacting Bose gas

This section focuses on the effects of a number of experimentally-feasible trapping geometries as applied to the non-interacting Bose gas, which allows us to study the phenomenon of transverse-condensation currently accessible in dimensionally suppressed systems, as discussed in the latter parts of this thesis (see Part II).

1.1.1 The ideal Bose gas in a 3D box

Let us consider N non-interacting bosons of mass m in a cubic box of side length L . In this limit, the single-particle Hamiltonian is simply defined by the kinetic energy contribution, and written as

$$H^{(1)} = \frac{\mathbf{p}^2}{2m}. \quad (1.1)$$

Its eigenstates for periodic boundary conditions are plane waves with momentum \mathbf{p} , of the form

$$\psi_{\mathbf{p}}(\mathbf{r}) = e^{i\mathbf{p}\cdot\mathbf{r}/\hbar}, \quad (1.2)$$

with energy $\epsilon_{\mathbf{p}} = \mathbf{p}^2/2m$ and momentum $\mathbf{p} = 2\pi\hbar\mathbf{n}/L$ with $\mathbf{n} = (n_x, n_y, n_z) \in \mathbb{Z}^3$ and L corresponding to the box size. Assuming that eigenstates are distributed according to Bose-Einstein statistics, then the mean population of a state $\psi_{\mathbf{p}}$ in the grand canonical ensemble is

$$N_{\mathbf{p}} = \frac{1}{e^{(\epsilon_{\mathbf{p}} - \mu)/k_B T} - 1}, \quad (1.3)$$

where the thermodynamic variables μ and T are the chemical potential and temperature respectively. An important property here is that all $N_{\mathbf{p}} > 0$ which implies $\mu < E_0$, where E_0 is the energy of the lowest eigenstate. This eigenstate actually has zero energy, hence we always have $\mu < 0$. The total number of atoms is then simply the sum of these populations over all possible states, that is

$$N = \sum_{\mathbf{p}} N_{\mathbf{p}}. \quad (1.4)$$

With this in mind, we can now explicitly separate the lowest fundamental state $\mathbf{p} = 0$, from the excited states lying above, and write

$$N = N_0 + N_{\text{ex}}. \quad (1.5)$$

Focusing explicitly on these excited states, we can evaluate the sum over these states and replace our summation in Eq. (1.4) with an integral $\sum_{\mathbf{p}} \rightarrow (L/2\pi\hbar)^3 \int d\mathbf{p}$. This replacement is only valid if $k_B T \gg \hbar^2/2mL^2$. That is, if the energy spacing between single-particle levels is much less than the thermal energy. We now write the number of excited bosons as

$$N_{\text{ex}} = \sum_{\mathbf{p} \neq 0} \frac{1}{e^{(\epsilon_{\mathbf{p}} - \mu)/k_B T} - 1} = \left(\frac{L}{2\pi\hbar} \right)^3 \int \frac{d\mathbf{p}}{e^{(\epsilon_{\mathbf{p}} - \mu)/k_B T} - 1}. \quad (1.6)$$

For condensation to occur, we require a saturation of the excited states. In order to test for this, it follows to calculate the density of excited states $\rho_{\text{ex}}^{(3D)} = N_{\text{ex}}/L^3$, where the total density is given by

$$\rho^{(3D)} = \rho_0^{(3D)} + \rho_{\text{ex}}^{(3D)} \quad (1.7)$$

and $\rho_0^{(3D)}$ is the density of the lowest mode. In the thermodynamic limit, $N \rightarrow \infty$, $L \rightarrow \infty$ and so we expect $\rho_{\text{ex}}^{(3D)}$ to remain constant for saturation to hold. So we now calculate

$$\rho_{\text{ex}}^{(3D)} = \left(\frac{1}{2\pi\hbar} \right)^3 \int \frac{d\mathbf{p}}{e^{(\epsilon_{\mathbf{p}} - \mu)/k_B T} - 1} = \left(\frac{1}{2\pi\hbar} \right)^3 \int d\mathbf{p} \frac{z}{e^{\mathbf{p}^2/2mk_B T} - z}, \quad (1.8)$$

where we have introduced $z = e^{\mu/k_B T}$ as the fugacity, bounded between 0 and 1. Now we can Taylor-expand the z -terms, and invert the resultant integral and sum to get

$$\rho_{\text{ex}}^{(3D)} = \left(\frac{1}{2\pi\hbar} \right)^3 \sum_{n=1}^{\infty} z^n \int d\mathbf{p} e^{-n\mathbf{p}^2/2mk_B T}. \quad (1.9)$$

This can be analytically solved to give

$$\rho_{\text{ex}}^{(3D)} = \frac{1}{\lambda_{\text{dB}}^3} \text{Li}_{3/2}(z), \quad (1.10)$$

where we have introduced

$$\text{Li}_{3/2}(z) = \frac{2}{\sqrt{\pi}} \int_0^\infty dx \frac{x^{1/2}}{z^{-1}e^x - 1} \quad (1.11)$$

This is a specific case of the more general class of polylog or Bose functions of order p given by

$$\text{Li}_p(z) = \frac{1}{\Gamma(p)} \int_0^\infty dx \frac{x^{p-1}}{z^{-1}e^x - 1} = \sum_{l=1}^{\infty} \frac{z^l}{l^p}. \quad (1.12)$$

It is important to highlight here, that $\text{Li}_{3/2}$ saturates at a certain value when the fugacity goes to 1, specifically $\text{Li}_{3/2}(1) = 2.612$. As such, we can write

$$\rho^{(3D)} = \begin{cases} \lambda_{\text{dB}}^{-3} \text{Li}_{3/2}(z), & \text{if } \rho^{(3D)} < \sup(\rho_{\text{ex}}^{(3D)}) \\ \lambda_{\text{dB}}^{-3} (\rho_0^{(3D)} + \text{Li}_{3/2}(1)), & \text{if } \rho^{(3D)} > \sup(\rho_{\text{ex}}^{(3D)}) \end{cases}, \quad (1.13)$$

where we indeed have the saturation of the excited modes, allowing the onset of Bose-Einstein condensation in a 3D uniform system.

1.1.2 The ideal Bose gas in a 2D box

In 2D, Bose-Einstein condensation of a uniform Bose gas cannot occur. This stems from a special case of the Mermin-Hohenberg-Wagner theorem [24, 25], which prohibits the existence of off-diagonal long range order (ODLRO) by the breaking of continuous symmetry for dimension $d < 3$. We can observe this by proceeding in a similar manner to the 3D case presented in Section 1.1, with the substituting integral of the sum now becoming

$$\sum_p \rightarrow \left(\frac{L}{2\pi\hbar} \right) \int d^2\mathbf{p}, \quad (1.14)$$

which we can use to write a reformed version of Eq. (1.9) in the 2D case as

$$\rho_{\text{ex}}^{(2D)} = \left(\frac{1}{2\pi\hbar} \right)^2 \sum_{n=1}^{\infty} \int d^2\mathbf{p} e^{-\frac{n\mathbf{p}^2}{2mk_B T}}. \quad (1.15)$$

Again, we may utilise a Bose function to simplify this expression to

$$\rho_{\text{ex}}^{(2D)} = \frac{1}{\lambda_{\text{dB}}^2} \text{Li}_1(z). \quad (1.16)$$

On this occasion, the Bose function Li_1 is not bounded as the fugacity goes to 1. As such, there can be no saturation of the excited states and hence the ground state $\mathbf{p} = 0$ cannot become macroscopic. Because of this, we can approximate the density as simply $\rho^{(2D)} \approx \rho_{\text{ex}}^{(2D)}$ and write

$$\rho^{(2D)} = \frac{1}{\lambda_{\text{dB}}^2} \text{Li}_1(z). \quad (1.17)$$

Evidently, we see that Bose-Einstein condensation of the ideal uniform Bose gas cannot survive a reduction in dimensionality. This raises the pertinent question, at what point does dimensionality inhibit the condensation of the Bose gas? In other words, if we consider a box and proceed to suppress its dimensionality along a singular direction, at what point do we consider the Bose gas contained within it to be 2D and condensation precluded? This is one of the central questions we try to address in this thesis and is discussed at length in Chapter 4, where we perform a dimensional analysis across temperature to determine the critical transition behaviour across dimensionality.

1.1.3 The ideal Bose gas in a rectangular box with transverse confinement

In order to focus on the dimensional crossover of the Bose gas, we now consider the particular trapping of a rectangular box of size L_x, L_y with transverse harmonic potential of strength ω_z . This is precisely the setup utilised for a number of experiments and theoretical studies considering the quasi-2D Bose gas [5, 26–28]. For a particle in such confinement, the stationary solutions to the Schrödinger equation yield the energy spectrum as

$$E_{n_x, n_y, n_z} = \frac{\pi^2 \hbar^2}{2m} \left(\frac{n_x^2}{L_x^2} + \frac{n_y^2}{L_y^2} \right) + \left(n_z + \frac{1}{2} \right) \hbar \omega_z, \quad (1.18)$$

where n_x, n_y, n_z are positive integers denoting the energy level in that direction. Now consider an ideal gas of bosons in such confinement and suppose that the average number of particles occupying the state of energy E is given by the Bose-Einstein distribution of Eq. (1.3). We can arbitrarily shift the zero of the energy in such a way that the lowest state has zero energy (i.e., removing the zero-point energy, which would be the ground state energy for a single particle). Let us write

$$E = E_{\mathbf{n}} = \frac{\pi^2 \hbar^2}{2m} \left(\frac{n_x^2}{L_x^2} + \frac{n_y^2}{L_y^2} \right) + n_z \hbar \omega_z \quad (1.19)$$

and introduce the quantity $\zeta = L_x/L_y$. We can then write the quantity $E_{\mathbf{n}}/k_B T$ as it appears in the Bose-Einstein distribution as

$$\frac{E_{\mathbf{n}}}{k_B T} = \frac{\pi^2 \hbar^2}{2m k_B T L_x^2} (n_x^2 + \zeta^2 n_y^2) + n_z \frac{\hbar \omega_z}{k_B T}. \quad (1.20)$$

Utilising the thermal de Broglie wavelength λ_{dB} and the transverse harmonic oscillator length defined by

$$\ell_z = \sqrt{\frac{\hbar}{m \omega_z}}, \quad (1.21)$$

we can express Eq. (1.20) as

$$\frac{E_{\mathbf{n}}}{k_B T} = \frac{\pi}{4} \frac{\lambda_{\text{dB}}^2}{L_x^2} (n_x^2 + \zeta^2 n_y^2) + \frac{1}{2\pi} \frac{\lambda_{\text{dB}}^2}{\ell_z^2} n_z. \quad (1.22)$$

In currently accessible experimental geometries, the aspect ratio ζ is a number of order unity. This means that the thermodynamics of the gas is determined by the three length scales L_x , ℓ_z and λ_{dB} only through the two ratios λ_{dB}/L_x and $\lambda_{\text{dB}}/\ell_z$. We assume $\lambda_{\text{dB}}/L_x \ll 1$ in such a way that the states in the planar box can be considered as a continuum, and sums over n_x and n_y can be replaced by integrals. Instead, the ratio $\lambda_{\text{dB}}/\ell_z$ determines the dimensionality of the system. For values $\lambda_{\text{dB}}/\ell_z \ll 1$, the system is three-dimensional (the transverse modes also behave as a continuum), while if $\lambda_{\text{dB}}/\ell_z \gg 1$ the system is two-dimensional (the transverse profile is Gaussian and only planar modes with $n_z = 0$ contribute to thermodynamics). It is worth stressing that we are considering an ideal gas of noninteracting particles. In an interacting system, one should also include another length scale (or, equivalently, an energy scale) associated with interaction, which can change the way in which the system transitions from 2D to 3D. For N particles at a given temperature T , the chemical potential μ is fixed by the condition

$$N = \sum_{\mathbf{n}} \frac{1}{\exp[(E_{\mathbf{n}} - \mu)/k_B T] - 1}. \quad (1.23)$$

We can separate the sum in this way

$$N = \sum_{n_z=0}^{\infty} \sum_{n_x, n_y=1}^{\infty} \frac{1}{\exp[(E_{\mathbf{n}} - \mu)/k_B T] - 1} \quad (1.24)$$

and replace the second sum over the plane with an integral

$$N = \sum_{n_z=0}^{\infty} \int_0^{\infty} dE \frac{g(E)}{\exp[(E + n_z \hbar \omega_z - \mu)/k_B T] - 1}, \quad (1.25)$$

where E is the contribution to the energy due to planar states only and $g(E)$ is the corresponding density of states in the plane, as determined in Appendix A.6. We can then write

$$N = \frac{mL_x L_y}{2\pi\hbar^2} \sum_{n_z=0}^{\infty} \int_0^{\infty} dE \frac{1}{\exp[(E + n_z\hbar\omega_z - \mu)/k_B T] - 1}. \quad (1.26)$$

For compactness of notation let us introduce

$$t = \frac{E}{k_B T} \quad (1.27)$$

and

$$z(n_z) = e^{(\mu - n_z\hbar\omega_z)/k_B T}. \quad (1.28)$$

This allows us to express

$$N = \frac{mk_B T L_x^2}{2\pi\hbar^2 \zeta} \sum_{n_z=0}^{\infty} \int_0^{\infty} dt \frac{1}{\frac{e^t}{z(n_z)} - 1}, \quad (1.29)$$

or more simply

$$N = \frac{1}{\zeta} \frac{L_x^2}{\lambda_{dB}^2} \sum_{n_z=0}^{\infty} \int_0^{\infty} dt \frac{1}{\frac{e^t}{z(n_z)} - 1}. \quad (1.30)$$

This integral is a standard Bose-Einstein integral of order 1. We note the Bose-Einstein integral of order s is given by

$$\int_0^{\infty} dt \frac{t^{s-1}}{\frac{e^t}{z} - 1} = \Gamma(s) \text{Li}_s(z) \quad (1.31)$$

where Γ is the Gamma Euler function. For $s = 1$ one has

$$\text{Li}_1(z) = -\ln(1 - z) \quad (1.32)$$

and $\Gamma(1) = 1$, so that

$$N = -\frac{1}{\zeta} \frac{L_x^2}{\lambda_{dB}^2} \sum_{n_z=0}^{\infty} \ln \left(1 - e^{(\mu - n_z\hbar\omega_z)/k_B T} \right) \quad (1.33)$$

or instead

$$N = -\frac{1}{\zeta} \frac{L_x^2}{\lambda_{dB}^2} \sum_{n_z=0}^{\infty} \ln \left(1 - e^{\mu/k_B T} e^{-n_z\lambda_{dB}^2/2\pi\ell_z^2} \right). \quad (1.34)$$

We note that $L_x^2/\zeta = L_x L_y$ is the area of the planar box and $\zeta N/L_x^2$ is the number of atoms per unit area, i.e., the two-dimensional density n_{2D} . We can also define the phase-space

density $\mathcal{D} = \lambda_{\text{dB}}^2 n_{2\text{D}}$ and write this expression as

$$\mathcal{D} = - \sum_{n_z=0}^{\infty} \ln \left(1 - e^{\mu/k_B T} e^{-n_z \lambda_{\text{dB}}^2 / 2\pi \ell_z^2} \right). \quad (1.35)$$

This can be seen as the sum of two-dimensional phase-space densities, each one associated to a different value of n_z (i.e., to planar states with 0, 1, 2, ..., nodes in the transverse wave function). This result is the same as is reported in [29]. Assuming a fixed fugacity, we can interchange the sum with an integral and write

$$\mathcal{D} \simeq - \int_0^{\infty} \ln \left(1 - z e^{-n_z \lambda_{\text{dB}}^2 / 2\pi \ell_z^2} \right) dn_z = \frac{2\pi \ell_z^2}{\lambda_{\text{dB}}^2} \text{Li}_2(z). \quad (1.36)$$

Now, in the limit $z \rightarrow 1$, we converge to the critical phase space density

$$\mathcal{D}_c = \frac{\pi^3 \ell_z^2}{3 \lambda_{\text{dB}}^2}. \quad (1.37)$$

And so we can write the total phase space density as $\mathcal{D} = \mathcal{D}_0 + \mathcal{D}_{\text{ex}}$ where

$$\mathcal{D}_0 = \ln \left(1 - e^{\mu/k_B T} \right) \quad (1.38)$$

is the phase space density of lowest transverse occupation and

$$\mathcal{D}_{\text{ex}} = \sum_{n_z \geq 1} \ln \left(1 - e^{\mu/k_B T} e^{-n_z \lambda_{\text{dB}}^2 / 2\pi \ell_z^2} \right) \quad (1.39)$$

corresponds to the higher transverse modes. We can hence consider

$$\mathcal{D}_{\text{ex}} \simeq \begin{cases} \frac{2\pi \ell_z^2}{\lambda_{\text{dB}}^2} \text{Li}_2(z) \text{ and } \mathcal{D}_0 = 0 & \text{if } \mathcal{D} < \mathcal{D}_c, \\ \mathcal{D}_c \text{ and } z = 1 & \text{if } \mathcal{D} > \mathcal{D}_c. \end{cases} \quad (1.40)$$

Thus, we observe macroscopic occupation of the lowest transverse state when $\mathcal{D} > \mathcal{D}_c$, even if ℓ_z is considerably large. This phenomenon is known as transverse condensation [5, 30, 31] as was first predicted by van Druten and Ketterle and shows that even if the dynamics are not completely frozen across the transverse direction, macroscopic occupation is realised. This becomes crucial as we explore the dimensional crossover of the dilute Bose gas under this specific confinement, as we will in Chapter 4.

1.2 The Gross-Pitaevskii equation

1.2.1 The role of interactions in a dilute Bose gas

The theory of the dilute Bose gas was first developed by Landau in 1941 [32], in order to explain the extraordinary behaviour of helium-4. However, this theory is a closer match to dilute atomic BEC's, due to their comparably weaker interactions. More recently, the unique ability to tune the interaction strength in a Bose gas is an invaluable weapon in the physicists' arsenal. Using a Feshbach resonance, experimentalists are able to precisely tune the inter-atomic interaction strength between atoms giving unprecedented control. Up until now, we have considered the non-interacting Bose gas, we proceed now by considering the case of the weakly interacting Bose gas. That is to say, in the case where interactions are strictly limited to binary collisions between two atoms. For a dilute weakly interacting Bose gas, we can write the Hamiltonian for N interacting atoms as

$$\hat{H} = \sum_{k=1}^N \hat{h}_0(\mathbf{r}_k) + \frac{1}{2} \sum_{k,l=1}^N \hat{V}(\mathbf{r}_k, \mathbf{r}_l) \quad (1.41)$$

where

$$\hat{h}_0 = -\hbar^2 \nabla^2 / 2m + V_{\text{pot}}(\mathbf{r}) \quad (1.42)$$

is the operator on a free particle in some confining potential V_{pot} and the second term symmetrically considers the effect of binary inter-atomic collisions. It becomes convenient for what follows to move from ‘co-ordinate representation’ to ‘occupation number representation’, known as second quantisation [33]. In the formalism of second quantisation, we introduce the bosonic field operators

$$\begin{aligned} \hat{\Psi} &= \sum_i \hat{a}_i(t) \psi_i(\mathbf{r}, t), \\ \hat{\Psi}^\dagger &= \sum_i \hat{a}_i^\dagger(t) \psi_i^*(\mathbf{r}, t), \end{aligned} \quad (1.43)$$

which are summed over the complete orthonormal set of single-particle quantum numbers. Here, \hat{a}_i and \hat{a}^\dagger represent the standard single-particle annihilation and creation operators that destroy or create a particle in state i . Since the bosonic field operators are linear combinations of these operators, we can consider $\hat{\Psi}$ ($\hat{\Psi}^\dagger$) to represent the annihilation (creation) of a particle at position \mathbf{r} and time t . In the case of bosons, these field operators obey the following commutation relations

$$\begin{aligned} [\hat{\Psi}(\mathbf{r}, t), \hat{\Psi}^\dagger(\mathbf{r}', t)] &= \delta(\mathbf{r} - \mathbf{r}'), \\ [\hat{\Psi}^\dagger(\mathbf{r}, t), \hat{\Psi}^\dagger(\mathbf{r}', t)] &= [\hat{\Psi}(\mathbf{r}, t), \hat{\Psi}(\mathbf{r}', t)] = 0. \end{aligned} \quad (1.44)$$

Using these operators, we are able to transfer into the occupation number representation and write our system Hamiltonian as

$$\hat{\mathcal{H}} = \int d\mathbf{r} \hat{\Psi}^\dagger(\mathbf{r}, t) \hat{h}_0(\mathbf{r}) \hat{\Psi}(\mathbf{r}, t) + \frac{1}{2} \iint d\mathbf{r} d\mathbf{r}' \hat{\Psi}^\dagger(\mathbf{r}, t) \hat{\Psi}^\dagger(\mathbf{r}', t) V(\mathbf{r} - \mathbf{r}') \hat{\Psi}(\mathbf{r}, t) \hat{\Psi}(\mathbf{r}', t). \quad (1.45)$$

All current theoretical treatments of the dilute Bose gas effectively begin from this, or an equivalent expression. Such a Hamiltonian contains both thermal and quantum fluctuations. A detailed review of the many directions one could take can be found within [34].

From here on, it becomes important to consider the effect of collisions. The atoms within a low temperature dilute Bose gas are sufficiently spatially separated to be out of the typical range of the interatomic potential. As such, we can consider all interatomic interactions to be scattering processes, where at sufficiently low energies the scattering amplitude $f_{3D}(\mathbf{k})$ tends to a constant, and only so-called *s*-wave scattering is accessible. The standard approach [35] is to approximate the contact interaction via the expression

$$V(\mathbf{r} - \mathbf{r}') = g_{3D} \delta(\mathbf{r} - \mathbf{r}'), \quad (1.46)$$

where the strength of a scattering process is approximated by $g_{3D} = 4\pi\hbar^2 a_s/m$ with a_s defining the *s*-wave scattering length for the particular atomic species in question. Incidentally, this treatment doesn't hold in 2D systems, since the scattering amplitude retains a dependence on \mathbf{k} at small wave vectors. However, in the limit of a quasi-2D regime, the scattering amplitude can be approximated by a constant. This allows us to rewrite our system Hamiltonian as

$$\hat{\mathcal{H}} = \int d\mathbf{r} \hat{\Psi}^\dagger(\mathbf{r}, t) \hat{h}_0(\mathbf{r}) \hat{\Psi}(\mathbf{r}, t) + \frac{g}{2} \iint d\mathbf{r} d\mathbf{r}' \hat{\Psi}^\dagger(\mathbf{r}, t) \hat{\Psi}^\dagger(\mathbf{r}', t) \hat{\Psi}(\mathbf{r}, t) \hat{\Psi}(\mathbf{r}', t) \quad (1.47)$$

leading to, in the Heisenberg picture, the equation of motion

$$i\hbar \frac{\partial \hat{\Psi}(\mathbf{r}, t)}{\partial t} = \hat{h}_0 \hat{\Psi}(\mathbf{r}, t) + g \hat{\Psi}^\dagger(\mathbf{r}, t) \hat{\Psi}(\mathbf{r}, t) \hat{\Psi}(\mathbf{r}, t) \quad (1.48)$$

which contains essentially all the information we may need about the dynamics of our system. The phenomenon of Bose-Einstein condensation stipulates that we have macroscopic occupation of the same quantum state for the bosons in our system. Hence, it is convenient to separate our Bose field operator into an operator for the condensate part and one for the fluctuation part via

$$\hat{\Psi}(\mathbf{r}, t) = \hat{a}_0(t) \psi_0(\mathbf{r}, t) + \sum_{i \neq 0} \hat{a}_i(t) \psi_i(\mathbf{r}, t) \quad (1.49)$$

For notational brevity, we can simplify this expression to read

$$\hat{\Psi}(\mathbf{r}, t) = \hat{\phi}_0(\mathbf{r}, t) + \hat{\delta}(\mathbf{r}, t) \quad (1.50)$$

by introducing the terms $\hat{\psi}(\mathbf{r}, t)$ and $\hat{\delta}(\mathbf{r}, t)$ for the condensate and fluctuation operator respectively. This split is essentially equivalent to the one incurred in Eq. (1.5) where we separated the lowest momentum mode from any excited modes. The number of atoms in our condensate can be given by the operator $\hat{N}_0 = \hat{a}_0^\dagger \hat{a}_0$, where acting on our state with this operator returns the eigenvalue N_0 . Now, if we calculate

$$\frac{[\hat{a}_0 \hat{a}_0^\dagger, \hat{a}_0^\dagger \hat{a}_0]}{N_0} |N_0\rangle = \frac{1}{N_0} |N_0\rangle \quad (1.51)$$

in the limit of $N_0 \gg 1$, i.e. a macroscopically occupied state, then $1/N_0 \rightarrow 0$ and we can consider the single-particle operators to be commutative. This leads us to make what is known as the Bogoliubov approximation where we replace the condensate operator by the complex classical field

$$\psi(\mathbf{r}, t) = \sqrt{n_0(\mathbf{r}, t)} e^{iS(\mathbf{r}, t)}, \quad (1.52)$$

typically referred to as the condensate wavefunction. We note that the explicit definition of the phase for this order parameter is analogous to the spontaneous breaking of $U(1)$ symmetry [36, 37]. Hence, we can approximate our bosonic field operator with $\hat{\Psi}(\mathbf{r}, t) = \psi(\mathbf{r}, t) + \hat{\delta}(\mathbf{r}, t)$, thereby moving all operator dependence to the fluctuation term. To proceed, we can now substitute Eq. (1.50) into Eq. (1.47). In doing so, we acquire a result that has terms up to a quadratic in operators, which we separate into

$$\hat{H} = H_0 + \hat{H}_1 + \hat{H}_2 + \hat{H}_3 + \hat{H}_4 \quad (1.53)$$

with

$$\begin{aligned} \mathcal{H}_0 &= \int d\mathbf{r} \left[\psi^* \hat{h}_0 \psi + \frac{g}{2} |\psi|^4 \right], \\ \hat{H}_1 &= \int d\mathbf{r} \left[\hat{\delta}^\dagger (\hat{h}_0 + g|\psi|^2) \psi + \psi^* (\hat{h}_0 + g|\psi|^2 \hat{\delta}) \right], \\ \hat{H}_2 &= \int d\mathbf{r} \left[\hat{\delta}^\dagger (\hat{h}_0 + 2g|\psi|^2) \hat{\delta} + \frac{g}{2} ((\psi^*)^2 \hat{\delta} \hat{\delta} + \psi^2 \hat{\delta}^\dagger \hat{\delta}^\dagger) \right], \\ \hat{H}_3 &= g \int d\mathbf{r} \left[\psi \hat{\delta}^\dagger \hat{\delta}^\dagger \hat{\delta} + \psi^* \hat{\delta}^\dagger \hat{\delta} \hat{\delta} \right], \\ \hat{H}_4 &= \frac{g}{2} \int d\mathbf{r} \left[\hat{\delta}^\dagger \hat{\delta}^\dagger \hat{\delta} \hat{\delta} \right]. \end{aligned} \quad (1.54)$$

Ignoring quantum and thermal fluctuations entirely by dropping $\hat{\delta}$ terms, our Hamiltonian

becomes

$$H = \int d\mathbf{r} \left(-\frac{\hbar^2}{2m} |\nabla\psi(\mathbf{r}, t)|^2 + V_{\text{tr}}(\mathbf{r}, t) |\psi(\mathbf{r}, t)|^2 + \frac{g}{2} |\psi(\mathbf{r}, t)|^4 \right), \quad (1.55)$$

which in the Heisenberg picture, gives our equation of motion to be

$$i\hbar \frac{\partial\psi(\mathbf{r}, t)}{\partial t} = \left(-\frac{\hbar^2 \nabla^2}{2m} + V_{\text{pot}}(\mathbf{r}, t) + g|\psi|^2 \right) \psi, \quad (1.56)$$

the renowned time-dependent Gross-Pitaevskii equation (GPE) [38, 39]. We note here that our Energy functional described by Eq. (1.55) is time dependent, however, in the case of a static potential, time-independent solutions to this equation may exist. These take the form

$$\psi(\mathbf{r}, t) = \psi_0(\mathbf{r}) e^{-i\mu t/\hbar} \quad (1.57)$$

where μ is a constant known as the *chemical potential* and $\psi_0(\mathbf{r})$ minimises the expectation of Eq. (1.55), under the condition that

$$\int d\mathbf{r} |\psi(\mathbf{r})|^2 = N. \quad (1.58)$$

Thus, the chemical potential is commonly written as $\mu = \partial E / \partial N$. Using the substitution in Eq. (1.57) allows us to rephrase Eq. (1.56) as

$$\mu\psi_0 = \left(-\frac{\hbar^2 \nabla^2}{2m} + V_{\text{pot}}(\mathbf{r}) + g|\psi_0|^2 \right) \psi_0 \quad (1.59)$$

which is the time-independent GPE equation. Whilst this model describes a weakly interacting Bose gas, it is idealised when applied to superfluid helium. We can also find solutions in the moving frame in which the fluid moves at velocity \mathbf{v} . We can then rewrite Eq. (1.52) as

$$\psi'(\mathbf{r}, t) = \sqrt{n_0} e^{iS'(\mathbf{r}, t)} \quad (1.60)$$

with the modified phase [40]

$$S'(\mathbf{r}, t) = \frac{1}{\hbar} \left[m\mathbf{v}\mathbf{r} - \left(\frac{1}{2}mv^2 + \mu \right) t \right]. \quad (1.61)$$

This allows us to define the superfluid velocity of the fluid as

$$\mathbf{v}_s = \frac{\hbar}{m} \nabla S. \quad (1.62)$$

We may now go on to introduce the superfluid vorticity

$$\omega = \nabla \times \mathbf{v}_s = \frac{\hbar}{m} \nabla \times \nabla S = 0. \quad (1.63)$$

In this instance, we are taking the curl of a gradient which is exactly zero. Thus, in the uniform superfluid with a smoothly varying phase, we have an entirely irrotational flow. However, since superfluids may sustain topological defects characterised by 2π phase singularities, we instead have localised point-like contributions to the system vorticity. Let us consider a change in the phase along some closed contour C and write

$$\delta S = \oint_C \nabla S \cdot d\mathbf{l}, \quad (1.64)$$

where \mathbf{l} is the line element along C . The superfluid velocity can be written as the gradient of a scalar function and so doesn't depend upon the path around a closed curve. Therefore the wavefunction at the start and end of C must be single-valued and thus $\exp(i\delta S)$ corresponds to a full rotation around the Argand plane. Hence, $\delta S = 2\pi q$, for $q \in \mathbb{Z}$. We can also take the line integral around a closed contour C for the local superfluid velocity as given by Eq. (1.62) and write the circulation

$$\Gamma = \oint_C \mathbf{v}_s \cdot d\mathbf{l} = \frac{2\pi\hbar q}{m}. \quad (1.65)$$

We note here that the circulation takes integer values, quantised into units of $\kappa = 2\pi\hbar/m$, suggesting a quantised nature to the vorticity within superfluid systems.

1.3 The weakly interacting Bose gas in a rectangular box under transverse harmonic confinement

Now we refocus on the problem of the weakly interacting Bose gas in hybridised potential as introduced in Section 1.1.3. For clarity, we consider the gas to be confined by a potential of the form

$$V_{\text{tot}}^{(3D)}(\mathbf{r}, t) = V_{\text{box}}^{(2D)}(x, y, t) + V_{\text{harm}}^{(1D)}(z) \quad (1.66)$$

where the in-plane confinement is prescribed by, for example, a hard-walled box of extent $L_x \times L_y$. The harmonic confinement term then provides tight trapping along the transverse direction of strength ω_z , restricting dynamics to within the plane. The Hamiltonian of our system may then be specified by

$$H = \int d\mathbf{r} \left(-\frac{\hbar^2}{2m} |\nabla \psi(\mathbf{r}, t)|^2 + V_{\text{tot}}^{(3D)}(\mathbf{r}, t) |\psi(\mathbf{r}, t)|^2 + \frac{g}{2} |\psi(\mathbf{r}, t)|^4 \right). \quad (1.67)$$

In the limit of strong trapping we make the ansatz that dynamics are limited to the plane and frozen across the transverse dimension. This remains valid assuming that the thermal and interaction energies are small compared to the difference of energy between the ground state and the first excited transverse mode. As such we make the ansatz

$$\psi(\mathbf{r}, t) = \psi(x, y, t)\phi(z), \quad (1.68)$$

where $\phi(z)$ is the ground state solution for z known to be of the form

$$\phi(z) = \frac{e^{-\frac{z^2}{2\ell_z^2}}}{(\pi\ell_z^2)^{1/4}} \quad (1.69)$$

and ℓ_z is the transverse lengthscale as defined by Eq. (1.21). Following this, we can rewrite Eq. (1.67) as

$$H = \int d\mathbf{r} \left(-\frac{\hbar^2}{2m} |\nabla\psi(\mathbf{r}, t)|^2 + V_{\text{box}}^{(2D)}(x, y, t) |\psi(\mathbf{r}, t)|^2 + \frac{g_{2D}}{2} |\psi(\mathbf{r}, t)|^4 \right), \quad (1.70)$$

where we have omitted an additive constant that arises and have introduced

$$g_{2D} = g \int_{-\infty}^{\infty} |\phi(z)|^4 dz. \quad (1.71)$$

We now consider the effects of additional excited transverse modes. That is, what can be said about the interactions in the case of quasi-2D trapping. In fact, we need to consider the different regimes of 2D and quasi-2D and how interactions change as we follow the transition. To be rigorous concerning the boundaries between dimensionality, from hereon we consider:

- 2D to be the regime in which all dynamics in the transverse direction are effectively frozen. This is when $k_B T \ll \hbar\omega_z$. Of course, this is different from a purely 2D system, where the third coordinate is non-existent.
- Quasi-2D to be the regime corresponding to $k_B T \approx \hbar\omega_z$ in which there is significant occupation of atoms in the excited modes of the transverse dimension.

Whilst the reduced dimensionality interaction strength comes easily in the former case, more care is needed in the latter. In the second regime we can again approximate the contact interaction to be a scattering process as in Eq. (1.46) of the form

$$V(\mathbf{r} - \mathbf{r}') = g_{2D}\delta_{2D}(\mathbf{r} - \mathbf{r}') \quad (1.72)$$

with the interaction strength given by

$$g_{2D} = \frac{\sqrt{8\pi}\hbar^2}{m} \frac{1}{\ell_z/a_s - \ln(\pi q^2 \ell_z^2) / \sqrt{2\pi}}, \quad \text{where} \quad q^2 = \frac{2m\mu}{\hbar^2} \quad (1.73)$$

as derived by Petrov *et al* [41]. In fact, for most experimentally accessible parameters [42–45], ranging from a dimensionless coupling strength of 0.01 to 3, the logarithmic term becomes negligible and we are simply left with

$$g_{2D} = \frac{\sqrt{8\pi}\hbar^2}{m} \frac{1}{\ell_z/a_s} = \frac{\hbar^2 \sqrt{8\pi} a_s}{m \ell_z}. \quad (1.74)$$

This then yields the interaction energy

$$E_{\text{int}} = \frac{\hbar^2 \sqrt{8\pi} a_s}{2m \ell_z} \int \langle n^2(\mathbf{r}) \rangle d^2r. \quad (1.75)$$

1.3.1 Interactions at low temperature

Another way to attain the result of Eq. (1.75) is by defining the strongly interacting limit at which the interaction energy of N bosons, E_{int} , matches the kinetic energy E_{kin} of N non-interacting bosons equally distributed over the lowest N single-particle states. We do this for the case of in-planar box confinement in tandem with transverse harmonic trapping as specified by Eq. (1.66). Neglecting density fluctuations, we can assume $n(\mathbf{r}) \approx n$, and write the 3D interaction energy as

$$E_{\text{int}} = \frac{g_{3D}}{2} \int_{-\frac{L_x}{2}}^{\frac{L_x}{2}} \int_{-\frac{L_y}{2}}^{\frac{L_y}{2}} \int_{-\infty}^{\infty} n^2(x, y) \left(\frac{1}{(\pi \ell_z^2)^{\frac{1}{4}}} e^{-\frac{z^2}{2\ell_z^2}} \right)^2 dz dy dx = \frac{g_{3D} n^2 L_x L_y}{2} \quad (1.76)$$

where we have assumed the density profile in the transverse direction to take a Gaussian form, which is valid under the condition $a_s \ll \ell_z$. We now introduce the dimensionless interaction parameter as

$$\tilde{g}_{3D} = \frac{m}{\hbar^2} g_{3D}. \quad (1.77)$$

Using this, we can express the interaction energy as

$$E_{\text{int}} = \frac{\hbar^2 \tilde{g}_{3D} N n}{2m}. \quad (1.78)$$

Now, using the density of states as derived in Eq. (A.6), the energy of the N^{th} excited single-particle state is calculated as

$$E_N = \frac{n L_x L_y}{g(E)} \int_{-\infty}^{\infty} \frac{1}{\sqrt{\pi \ell_z^2}} e^{-\frac{z^2}{\ell_z^2}} dz = \frac{2n\pi\hbar^3\omega_z}{m E}. \quad (1.79)$$

Therefore, the kinetic energy follows as

$$E_{\text{kin}} = \frac{Nn\pi\hbar^3\omega_z}{mE}. \quad (1.80)$$

So, in the strongly interacting limit, we recover the relation

$$\tilde{g}_{3D} = \frac{2\pi\hbar\omega_z}{E}. \quad (1.81)$$

We see that the importance of interactions can be characterised by the energy scale $E/\hbar\omega_z$. Further, in the limit of pure 2D at which we consider the transverse and total energy to be comparable, we recover the result published in [46]. That is,

$$\lim_{\hbar\omega_z \rightarrow E} \tilde{g}_{3D} = 2\pi. \quad (1.82)$$

1.4 Quasi-condensation

Having derived the interaction energy, we can also consider the mean-field interaction energy per particle. At lower temperatures, this term dominates over the thermal energy and we can show

$$\frac{E_{\text{int}}}{Nk_B T} = \frac{\hbar^2 \tilde{g}_{3D} n}{2mk_B T} = \frac{\sqrt{8\pi} a_s / \ell_z}{4\pi} \mathcal{D} \gg 1. \quad (1.83)$$

Or conversely

$$\mathcal{D} \gg \frac{\sqrt{2\pi}\ell_z}{a_s}, \quad (1.84)$$

revealing that for sufficiently low temperatures, density fluctuations are suppressed. In fact, it is already known that density fluctuations are suppressed for $\mathcal{D} \gg 1$ [47–49] and is described here as the manifestation of a quasi-condensate. What is specifically meant by this term is that although density fluctuations are minimised, there is not an associated phase coherence as in the case of true condensation. The concept of quasi-condensation was first discussed by Popov [50] and later developed by Petrov *et al* [41].

1.5 Bogoliubov theory

By looking for time-dependent solutions of the GPE, we can recover information about collective excitations for our system. This is performed by considering some fluctuation $\delta\phi(\mathbf{r}, t)$ about the ground state of the system $\phi_0(\mathbf{r})$ via the expression

$$\phi(\mathbf{r}, t) = e^{-i\mu t/\hbar} [\phi_0(\mathbf{r}) + \delta\phi(\mathbf{r}, t)]. \quad (1.85)$$

Then, by substituting this into the time-dependent GPE and subtracting the time-independent GPE we recover a time-dependent equation governing the evolution of fluctuations about the ground state. Considering small amplitude fluctuations, we can linearise to first order in $\delta\phi(\mathbf{r}, t)$ to get

$$i\hbar \frac{\partial}{\partial t} \delta\phi(\mathbf{r}, t) = [\hat{h}_0 + 2g |\phi_0|^2 - \mu] \delta\phi(\mathbf{r}, t) + g\phi_0^2 \delta\phi^*(\mathbf{r}, t). \quad (1.86)$$

Now, it's possible to look for solutions in the plane-wave basis of the form

$$\delta\phi(\mathbf{r}, t) = \sum [u_i(\mathbf{r}) e^{-i\omega_i t} + v_i^*(\mathbf{r}) e^{i\omega_i t}], \quad (1.87)$$

where ω_i label the frequency of the i -th mode. Substituting Eq. (1.87) and its complex conjugate into Eq. (1.86), it is possible to recover the coupled Bogoliubov equations. When written in matrix form, these are expressed as

$$\begin{pmatrix} \hat{L}(\mathbf{r}) & \hat{M}(\mathbf{r}) \\ -\hat{M}^*(\mathbf{r}) & -\hat{L}^*(\mathbf{r}) \end{pmatrix} \begin{pmatrix} u_i(\mathbf{r}) \\ v_i(\mathbf{r}) \end{pmatrix} = \epsilon_i \begin{pmatrix} u_i(\mathbf{r}) \\ v_i(\mathbf{r}) \end{pmatrix}, \quad (1.88)$$

where the operators

$$\begin{aligned} \hat{L} &= \hat{h}_0 + 2g |\phi_0(\mathbf{r})|^2 - \mu \\ \hat{M}(\mathbf{r}) &= g [\phi_0(\mathbf{r})]^2 \end{aligned} \quad (1.89)$$

have been introduced. We have also defined ϵ_i as the dressed energy of mode i . Another way to derive the Bogoliubov equations is by diagonalising the Hamiltonian. Let us begin by truncating our full system Hamiltonian down to one that is quadratic ($\hat{H} \approx H_0 + \hat{H}_1 + \hat{H}_2$) in fluctuations. In the grand-canonical ensemble, where particles and energy are non-conserved we can replace \hat{H} by $\hat{K} = \hat{H} - \mu\hat{N}$ where $\hat{N} = \int d\mathbf{r} \hat{\Psi}^\dagger \hat{\Psi}$ is the number operator. Now, considering a time-dependent wavefunction as before and writing $\hat{\Psi}(\mathbf{r}, t) = \phi_0(\mathbf{r}) + \hat{\delta}(\mathbf{r}, t)$ we can write

$$\begin{aligned} \hat{K} &= \int d\mathbf{r} [(\phi_0^* + \hat{\delta}^\dagger) \hat{h}_0 (\phi_0 + \hat{\delta})] \\ &\quad + \frac{g}{2} \int d\mathbf{r} [(\phi_0^* + \hat{\delta}^\dagger)(\phi_0^* + \hat{\delta}^\dagger)(\phi_0 + \hat{\delta})(\phi_0 + \hat{\delta})] \\ &\quad - \mu \int d\mathbf{r} [(\phi_0^* + \hat{\delta}^\dagger)(\phi_0 + \hat{\delta})]. \end{aligned} \quad (1.90)$$

This can be separated by its order in terms of fluctuation operators into

$$\begin{aligned} K_0 &= \int d\mathbf{r} \left[\phi_0^*(\hat{h}_0 - \mu)\phi_0 + \frac{g}{2}|\psi_0|^4 \right] \\ \hat{K}_1 &= \int d\mathbf{r} \left[\hat{\delta}^\dagger(\hat{h}_0 + g|\phi_0|^2 - \mu)\phi_0 + \phi_0^*(\hat{h}_0 + g|\phi_0|^2 - \mu)\hat{\delta} \right] \\ \hat{K}_2 &= \int d\mathbf{r} \left[\hat{\delta}^\dagger(\hat{h}_0 + 2g|\phi_0|^2 - \mu)\hat{\delta} + \frac{g}{2} \left((\phi_0^*)^2 \hat{\delta} \hat{\delta} + \phi_0^2 \hat{\delta}^\dagger \hat{\delta}^\dagger \right) \right]. \end{aligned} \quad (1.91)$$

Considering each term separately we can in fact see that minimisation of K_0 for a constant chemical potential is entirely equivalent to the minimisation of the energy functional of Eq. (1.55) which leads to the derivation of the stationary GPE. Such a minimisation assumes that there exists a unique minimum where the condensate chooses a random coherent phase, consistent with our assumption of symmetry breaking. Now, substituting the GPE of Eq. (1.56) into the expression for \hat{K}_1 leads to the simple result $\hat{K}_1 = 0$. However, it is in fact possible to diagonalise the \hat{K}_2 term by utilising the Bogoliubov transformation relations

$$\hat{\delta}(\mathbf{r}, t) = \sum_i \left[u_i(\mathbf{r}) \hat{\beta}_i(t) + v_i^*(\mathbf{r}) \hat{\beta}_i^\dagger(t) \right], \quad \text{and} \quad \hat{\delta}^\dagger(\mathbf{r}, t) = \sum_i \left[u_i^*(\mathbf{r}) \hat{\beta}_i^\dagger(t) + v_i(\mathbf{r}) \hat{\beta}_i(t) \right]. \quad (1.92)$$

Here, we have introduced $\hat{\beta}^\dagger$ ($\hat{\beta}$) as the creation (annihilation) operators for quasiparticles which obey the Bose commutation relations

$$\begin{aligned} [\hat{\beta}_i, \hat{\beta}_j^\dagger] &= \delta_{ij} \\ [\hat{\beta}_i, \hat{\beta}_j] &= 0. \end{aligned} \quad (1.93)$$

Expressing the non-condensate operators in terms of quasiparticles via Eq. (1.92) is analogous to the expansion around the condensate mean field. From the commutation relations, one may also derive orthonormality relations for the non-condensate operators given by

$$\begin{aligned} \int d\mathbf{r} [u_i^*(\mathbf{r})u_j(\mathbf{r}) - v_i^*(\mathbf{r})v_j(\mathbf{r})] &= \delta_{ij} \\ \int d\mathbf{r} [u_i(\mathbf{r})v_j(\mathbf{r}) - v_i(\mathbf{r})u_j(\mathbf{r})] &= 0 \end{aligned} \quad (1.94)$$

To simplify the following steps we now split the second-order contribution \hat{K}_2 into two parts

$$\hat{K}_2^1 = \int d\mathbf{r} \left[\hat{\delta}^\dagger(\hat{h}_0 + 2g|\phi_0|^2 - \mu)\hat{\delta} \right] \quad (1.95)$$

and

$$\hat{K}_2^2 = \int d\mathbf{r} \left[\frac{g}{2} \left((\phi_0^*)^2 \hat{\delta} \hat{\delta} + \phi_0^2 \hat{\delta}^\dagger \hat{\delta}^\dagger \right) \right], \quad (1.96)$$

considering each separately. Substituting the Bogoliubov transformation relations Eq. (1.92) into Eq. (1.95) we get

$$\begin{aligned}\hat{K}_2^1 &= \int d\mathbf{r} \sum_i \left(u_i^* \hat{\beta}_i^\dagger + v_i \hat{\beta}_i \right) \left\{ \hat{h}_0 + 2g|\phi_0|^2 - \mu \right\} \sum_j \left(u_j \hat{\beta}_j + v_j^* \hat{\beta}_j^\dagger \right) \\ &= \int d\mathbf{r} \sum_i \left\{ u_i^* \hat{\beta}_i^\dagger \hat{h}_0 u_j \hat{\beta}_j + u_i^* \hat{\beta}_i^\dagger \hat{h}_0 v_j^* \hat{\beta}_j^\dagger + u_i^* \hat{\beta}_i^\dagger 2g|\phi_0|^2 u_j \hat{\beta}_j + u_i^* \hat{\beta}_i^\dagger 2g|\phi_0|^2 v_j^* \hat{\beta}_j^\dagger \right. \\ &\quad \left. - u_i^* \hat{\beta}_i^\dagger \mu u_j \hat{\beta}_j - u_i^* \hat{\beta}_i^\dagger \mu v_j^* \hat{\beta}_j^\dagger + v_i \hat{\beta}_i \hat{h}_0 u_j \hat{\beta}_j + v_i \hat{\beta}_i \hat{h}_0 v_j^* \hat{\beta}_j^\dagger \right. \\ &\quad \left. + v_i \hat{\beta}_i 2g|\phi_0|^2 u_j \hat{\beta}_j + v_i \hat{\beta}_i 2g|\phi_0|^2 v_j^* \hat{\beta}_j^\dagger - v_i \hat{\beta}_i \mu u_j \hat{\beta}_j - v_i \hat{\beta}_i \mu v_j^* \hat{\beta}_j^\dagger \right\} \end{aligned} \quad (1.97)$$

which simplifies to

$$\begin{aligned}\hat{K}_2^1 &= \int d\mathbf{r} \sum_{ij} \left\{ \left[u_i^* \hat{h}_0 u_j + u_i^* 2g|\phi_0|^2 u_j - u_i^* \mu u_j \right] \hat{\beta}_i^\dagger \hat{\beta}_j \right. \\ &\quad + \left[v_i \hat{h}_0 v_j^* + v_i 2g|\phi_0|^2 v_j^* - v_i \mu v_j^* \right] \hat{\beta}_i \hat{\beta}_j^\dagger \\ &\quad + \left[u_i^* \hat{h}_0 v_j^* + u_i^* 2g|\phi_0|^2 v_j^* - u_i^* \mu v_j^* \right] \hat{\beta}_i^\dagger \hat{\beta}_j^\dagger \\ &\quad \left. + \left[v_i \hat{h}_0 u_j + v_i 2g|\phi_0|^2 u_j - v_i \mu u_j \right] \hat{\beta}_i \hat{\beta}_j \right\}. \end{aligned} \quad (1.98)$$

Specifically considering the second contribution Eq. (1.96) we get

$$\begin{aligned}\hat{K}_2^2 &= \frac{g}{2} \int d\mathbf{r} \sum_{ij} \left\{ (\phi_0^*)^2 \sum_{ij} (u_i \hat{\beta}_i + v_i^* \hat{\beta}_i^\dagger) (u_j \hat{\beta}_j + v_j^* \hat{\beta}_j^\dagger) + (\phi_0)^2 \sum_{ij} (u_i^* \hat{\beta}_i^\dagger + v_i \hat{\beta}_i) (u_j^* \hat{\beta}_j^\dagger + v_j \hat{\beta}_j) \right\} \\ &= \frac{g}{2} \int d\mathbf{r} \sum_{ij} \left\{ (\phi_0^*)^2 u_i \hat{\beta}_i u_j \hat{\beta}_j + (\phi_0^*)^2 v_i^* \hat{\beta}_i^\dagger v_j^* \hat{\beta}_j^\dagger + (\phi_0^*)^2 u_i \hat{\beta}_i v_j^* \hat{\beta}_j^\dagger + (\phi_0^*)^2 v_i^* \hat{\beta}_i^\dagger u_j \hat{\beta}_j \right. \\ &\quad \left. + \phi_0^2 u_i^* \hat{\beta}_i^\dagger u_j^* \hat{\beta}_j^\dagger + \phi_0^2 v_i \hat{\beta}_i v_j \hat{\beta}_j + \phi_0^2 u_i^* \hat{\beta}_i^\dagger v_j \hat{\beta}_j + \phi_0^2 v_i \hat{\beta}_i u_j^* \hat{\beta}_j^\dagger \right\}, \end{aligned} \quad (1.99)$$

which is just

$$\begin{aligned}\hat{K}_2^2 &= \frac{g}{2} \int d\mathbf{r} \sum_{ij} \left\{ \left[(\phi_0^*)^2 u_i u_j + \phi_0^2 v_i v_j \right] \hat{\beta}_i \hat{\beta}_j \right. \\ &\quad + \left[(\phi_0^*)^2 v_i^* v_j^* + \phi_0^2 u_i^* u_j^* \right] \hat{\beta}_i^\dagger \hat{\beta}_j^\dagger \\ &\quad + \left[(\phi_0^*)^2 u_i v_j^* + \phi_0^2 v_i u_j^* \right] \hat{\beta}_i \hat{\beta}_j^\dagger \\ &\quad \left. + \left[(\phi_0^*)^2 v_i^* u_j + \phi_0^2 u_i^* v_j \right] \hat{\beta}_i^\dagger \hat{\beta}_j \right\}. \end{aligned} \quad (1.100)$$

To simplify and recombine our constituent expressions we introduce the operator $\hat{\mathcal{L}} = \hat{h}_0 + 2g|\phi_0|^2 - \mu$. We can then write our expression for $\hat{K}_2 = \hat{K}_2^1 + \hat{K}_2^2$ as

$$\begin{aligned} \hat{K}_2 = \int d\mathbf{r} \sum_{ij} \left\{ & \left[u_i^* \hat{\mathcal{L}} u_j + \frac{g}{2} ((\phi_0^*)^2 v_i^* u_j + \phi_0^2 u_i^* v_j) \right] \hat{\beta}_i^\dagger \hat{\beta}_j \\ & + \left[v_i^* \hat{\mathcal{L}} v_j^* + \frac{g}{2} ((\phi_0^*)^2 u_i v_j^* + \phi_0^2 v_i u_j^*) \right] \hat{\beta}_i \hat{\beta}_j^\dagger \\ & + \left[u_i^* \hat{\mathcal{L}} v_j^* + \frac{g}{2} ((\phi_0^*)^2 v_i^* v_j^* + \phi_0^2 u_i^* u_j^*) \right] \hat{\beta}_i^\dagger \hat{\beta}_j^\dagger \\ & + \left[v_i^* \hat{\mathcal{L}} u_j + \frac{g}{2} ((\phi_0^*)^2 u_i u_j + \phi_0^2 v_i v_j) \right] \hat{\beta}_i \hat{\beta}_j. \right\}. \end{aligned} \quad (1.101)$$

Denoting the Hermitian Conjugate as (H.C.), this can be simplified further down to

$$\begin{aligned} \hat{K}_2 = \frac{1}{2} \int d\mathbf{r} \sum_{ij} \left\{ & \left[u_i^* \hat{\mathcal{L}} u_j + v_i^* \hat{\mathcal{L}} v_j^* + g(\phi_0)^2 u_i^* v_j + g\phi_0^2 v_i u_j^* \right] \hat{\beta}_i^\dagger \hat{\beta}_j + [\text{H.C.}] \\ & + \left[v_i^* \hat{\mathcal{L}} u_j + v_i \hat{\mathcal{L}} u_j + g(\phi_0^*)^2 u_i u_j + g\phi_0^2 v_i v_j \right] \hat{\beta}_i \hat{\beta}_j + \text{H.C.} \right\}. \end{aligned} \quad (1.102)$$

Now, if u_j & v_j satisfy the coupled Bogoliubov equations and $\phi, \epsilon \in \mathbb{R}$ we have

$$\begin{aligned} \hat{\mathcal{L}} u_j + g\phi_0^2 v_j &= \epsilon_j u_j \\ \hat{\mathcal{L}} v_j + g\phi_0^2 u_j &= -\epsilon_j v_j. \end{aligned} \quad (1.103)$$

Utilising conjugation techniques of variables we can obtain the following expressions

$$\begin{aligned} u_i^* \hat{\mathcal{L}} u_j + g\phi_0^2 u_i^* v_j &= u_i^* \epsilon_j u_j \\ v_i^* \hat{\mathcal{L}} v_j^* + g(\phi_0^*)^2 v_i u_j^* &= -v_i \epsilon_j v_j^* \\ v_i \hat{\mathcal{L}} u_j + g\phi_0^2 v_i v_j &= v_i \epsilon_j u_j \\ v_j \hat{\mathcal{L}} u_i + g\phi_0^2 u_j u_i &= -v_j \epsilon_j^* u_i. \end{aligned} \quad (1.104)$$

These allow us to simplify our expression of \hat{K}_2 into

$$\begin{aligned} \hat{K}_2 = \frac{1}{2} \int d\mathbf{r} \sum_{ij} \left\{ & \left[\epsilon_j (u_i^* u_j - v_i v_j^*) \right] \hat{\beta}_i^\dagger \hat{\beta}_j + [\text{H.C.}] \hat{\beta}_i \hat{\beta}_j^\dagger \right. \\ & \left. + \left[\epsilon_j (v_i u_j - v_j u_i) \right] \hat{\beta}_i \hat{\beta}_j + \text{H.C.} \right\}. \end{aligned} \quad (1.105)$$

Using the orthonormality relations of Eq. (1.94), the third term and its hermitian conjugate vanish. So now we can write

$$\hat{K}_2 = \frac{1}{2} \int d\mathbf{r} \sum_{ij} \left\{ (\epsilon_j + \epsilon_i) (u_i^* u_j \hat{\beta}_i^\dagger \hat{\beta}_j - v_i v_j^* \hat{\beta}_i \hat{\beta}_j^\dagger) \right\}. \quad (1.106)$$

Using the bosonic commutation relations, we get $\hat{\beta}_i \hat{\beta}_j^\dagger = \hat{\beta}_j^\dagger \hat{\beta}_i + \delta_{ij}$ and so we can write

$$\hat{K}_2 = \frac{1}{2} \int d\mathbf{r} \sum_{ij} \left\{ (\epsilon_j + \epsilon_i) (u_i^* u_j \hat{\beta}_i^\dagger \hat{\beta}_j - v_i v_j^* (\hat{\beta}_j^\dagger \hat{\beta}_i + \delta_{ij})) \right\}. \quad (1.107)$$

This simplifies to

$$\hat{K}_2 = \frac{1}{2} \int d\mathbf{r} \sum_{ij} \left\{ (\epsilon_j + \epsilon_i) (u_i^* u_j - v_j v_i^*) \hat{\beta}_i^\dagger \hat{\beta}_j - (\epsilon_j + \epsilon_i) v_i v_j^* \delta_{ij} \right\}. \quad (1.108)$$

Once again utilising the orthonormality relations of Eq. (1.94), this becomes

$$\hat{K}_2 = \frac{1}{2} \sum_{ij} \left\{ (\epsilon_j + \epsilon_i) \delta_{ij} \hat{\beta}_i^\dagger \hat{\beta}_j \right\} - \frac{1}{2} \int d\mathbf{r} \sum_{ij} \left\{ (\epsilon_j + \epsilon_i) \delta_{ij} v_i v_j^* \delta_{ij} \right\}, \quad (1.109)$$

which is simply

$$\hat{K}_2 = \frac{1}{2} \sum_i \left\{ 2\epsilon_i \hat{\beta}_i^\dagger \hat{\beta}_i \right\} - \frac{1}{2} \int d\mathbf{r} \sum_i \left\{ 2\epsilon_i v_i v_i^* \right\}. \quad (1.110)$$

So finally we arrive at

$$\hat{K}_2 = \sum_i \epsilon_i \hat{\beta}_i^\dagger \hat{\beta}_i - \sum_i \epsilon_i \int d\mathbf{r} |v_i|^2. \quad (1.111)$$

Typically the second contribution is negligible (assuming quantum depletion) and so we are simply left with a system of non-interacting quasiparticles with an energy spectrum obtained from Eq. (1.88).

1.6 Sound speed of the weakly interacting Bose gas

At zero temperature, we can safely assume the system state is completely described by the order parameter ϕ_0 . In a uniform system, we can omit the trapping potential by setting $V_{\text{pot}} = 0$ and make the substitution $n_0 = |\phi_0|^2$, as well as $\mu = gn_0$. This allows us to express Eq. (1.88) as

$$\begin{bmatrix} \left(-\frac{\hbar^2 \mathbf{k}^2}{2m} + gn_0 - \epsilon_i \right) & gn_0^2 \\ gn_0^2 & \left(-\frac{\hbar^2 \mathbf{k}^2}{2m} + gn_0 + \epsilon_i \right) \end{bmatrix} \begin{bmatrix} u_i \\ v_i \end{bmatrix} = 0. \quad (1.112)$$

By imposing that determinant is zero-valued, this equation can be easily solved to give the excitation spectrum

$$\epsilon_i = \sqrt{\frac{\hbar^2 \mathbf{k}^2}{2m} \left(\frac{\hbar^2 \mathbf{k}^2}{2m} + 2gn \right)}. \quad (1.113)$$

We highlight that although this treatment seems futile in 2D since thermal fluctuations destroy the order parameter, the long-wavelength fluctuations only extinguish coherence at long distance. As such, the system still exhibits off-diagonal long range order. In fact the applicability of this treatment for quasi-condensates is discussed at length and justified in [48, 51, 52]. The long wavelength excitations are phonon modes

$$\lim_{\mathbf{k} \rightarrow 0} \epsilon_i = \sqrt{\frac{gn}{m}} \mathbf{k} = c_B \mathbf{k}, \quad (1.114)$$

where we have introduced the Bogoliubov phonon mode velocity

$$c_B = \sqrt{\frac{gn}{m}}, \quad (1.115)$$

corresponding to the Goldstone mode of the weakly interacting Bose gas. This arises from the spontaneous breaking of $U(1)$ symmetry. In contrast, for small-wavelength modes, the excitation spectrum is described by a single-particle kinetic energy term such that

$$\lim_{\mathbf{k} \rightarrow \infty} \epsilon_i = \frac{\hbar^2 \mathbf{k}^2}{2m}. \quad (1.116)$$

1.7 Chapter summary

In this chapter we introduced some of the theoretical tools and concepts relevant throughout this thesis. We considered the effects of dimensionality on the ideal Bose gas, bearing interesting insights into the effects of system dimensionality on the prospect of BEC. We then considered the effects of inter-atomic interaction, motivating the fundamental concepts behind the Gross-Pitaevskii equation. Following this, we discussed the quantised nature of vortices within superfluid systems, which will be of paramount importance in the following chapter. We then introduced a trapping potential capable of facilitating the study of a dimensional crossover from 2D to 3D and explored arguments concerning the energy scales of such a system. This motivated the definition of quasi-condensation, which will become important in the later parts of this thesis where quasi-condensation is thought to manifest the continuity of sound across the 2D phase transition. Finally we investigated Bogoliubov theory, revealing the phonon-like behaviour of first-order long-wavelength perturbations. This will become important in the final chapter of this thesis, where we probe the response in sound speed across temperature and through a dimensionality crossover.

Chapter 2

Spin-up of a superfluid vortex lattice driven by rough boundaries

The contents that follow in this chapter were published in Keepfer *et al* [53]. This chapter focuses on the proliferation of quantised vortex filaments generated from a rotating rough potential barrier, starting from an initially quiescent fluid. Here, we see the importance of vortex interactions and reconnections as we recover the simple vortex lattice solution for a superfluid under rotation.

2.1 Introduction to superfluidity

Superfluids are extraordinary fluids characterised by the absence of viscosity. They are irrotational everywhere except at vortex lines whose circulation is quantised in units of $\kappa = h/m$, where h is Planck's constant and m is the mass of the boson which composes the fluid [40, 54]. First discovered and studied in liquid helium-4 and, decades later, in helium-3, superfluidity has since been observed in ultracold gases and photonic systems. The constraint of quantised vorticity is a consequence of quantum mechanics - vorticity can only arise as 2π topological defects of the macroscopic single-particle wavefunction of the quantum many-body system. The characteristic density and phase profiles of a system containing a central vortex may be viewed in Fig. 2.1, where we see a density dip at the vortex core and a corresponding discontinuity in the phase profile. In addition, we observe the velocity profile in the presence of this topological defect.

These defects manifest as vortex lines, or filaments, in the three-dimensional cases. As well as possessing a circulating flow, the vortex lines have a core of depleted density about their axis, out to a core radius a_0 which is of the order of the superfluid healing length. In helium-4 and helium-3 the vortex core size a_0 is around 10^{-10}m and 10^{-8}m , respectively. In addition, vortices have been successfully visualised in ultracold atomic systems, wherein

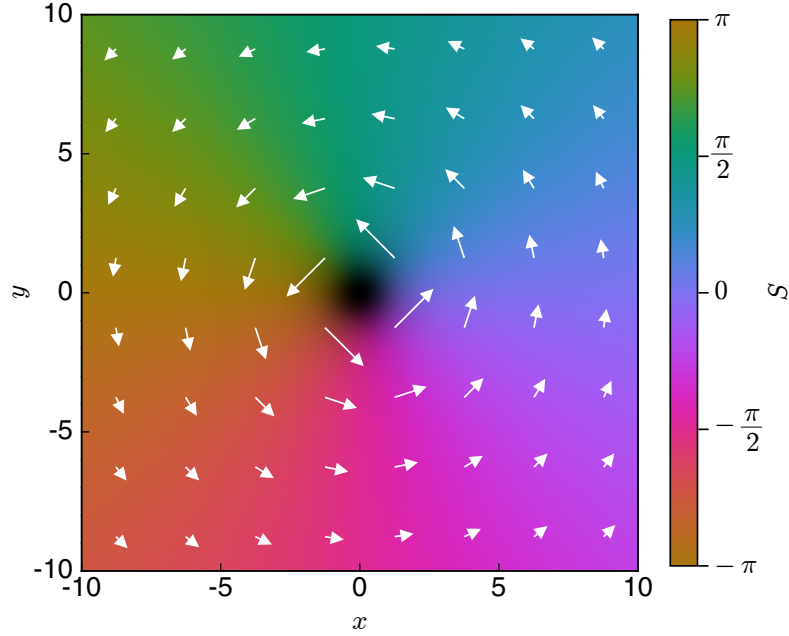


Figure 2.1: Density and phase information for a central singularly-charged vortex in a uniform 2D system. White arrows are superimposed whose size and orientation depict the amplitude and direction of the velocity profile of the fluid, as given by Eq. (1.62). We visualise the phase and density concurrently using a technique outlined by Stagg [55].

the healing length can vary in a wide range of the micron scale [56–60].

Superfluidity may be defined by the characteristic behaviour exhibited by a quantum fluid. For example, a superfluid state possesses phase stiffness, in that if we were to rotate a superfluid at given angular frequency Ω , then in the Galilean laboratory frame rotating at the same frequency the fluid would be at rest. Additionally, once in motion, the superfluid remains undamped by viscous boundary forces like in a typical fluid. The textbook paradigm of superfluidity is a cylindrical bucket of superfluid helium rotating at constant angular frequency Ω . Classical solid-body rotation is forbidden by the irrotational nature of the superfluid. At sufficiently small values of Ω , the fluid remains quiescent. However, if Ω is increased past a critical value Ω_c , the presence of a vortex line is energetically favourable. Using hydrodynamic arguments and up to a logarithmic correction, it is estimated [40] that this critical angular frequency is

$$\Omega_c = \frac{\hbar}{mR^2} \ln \left(\frac{R}{a_0} \right), \quad (2.1)$$

where m is the mass of a helium atom, and R is the radius of the bucket. At larger values of Ω , two vortices become favourable, and so on. For $\Omega \gg \Omega_c$ the stationary state of the fluid is the famed vortex lattice, an array of vortex lines aligned along the axis of rotation

with areal density

$$n_v = \frac{2\Omega}{\kappa}, \quad (2.2)$$

known as Feynman's rule. The vortex lattice was first imaged in superfluid helium by Packard *et al* [61] and more recently by Bewley *et al* [62]. The lattice has also been observed in ultracold gaseous superfluids trapped by smooth confining potentials [58, 63], with some containing more than 300 vortices [64].

The process in which the vortices enter the superfluid in the first place is called vortex nucleation. Being associated with a 2π phase singularity of the macroscopic wavefunction, a vortex line is topologically protected. Thus, starting from some initially vortex-free state, vortices must enter the superfluid as a result of some mechanism. In a trapped BEC, vortices may either be nucleated by rotating the trapping potential or alternatively by introducing a dynamical obstacle or impurity [65, 66]. In the former case, the vortex enters spontaneously via a dynamical instability from topological deformations on the condensate. In the latter case, vortex lines may be generated *extrinsically* by stretching some pre-existing vortex lines called "remanent vortices" which, under suitable conditions, can spool additional vortices [67]. Remanent vortices are thought to arise when cooling the helium sample through the superfluid transition, and can be avoided by using careful experimental protocols [68]. We note here that other protocols are available for vortex generation in ultracold atomic systems, including the Kibble-Zurek mechanism [69], spin-orbit coupling [70, 71], and others. The Kibble-Zurek mechanism predicts the formation and approximate density of topological defects (vortices) through a phase transition at a rate governed by quench duration [72, 73]. Spin-orbit coupling techniques utilise rotating Raman lasers which, through spin-orbit interaction, generate vortex structures.

Individual vortex nucleation in a rotating bucket, either intrinsic or extrinsic, has never been visualised in detail. Experimentally, it remains challenging to image the flow in the vicinity of a boundary, despite progress in flow visualisation in the bulk [62, 74, 75], more so because the microscopic scale of the vortices themselves. Theoretically, the nucleation problem has been addressed using energy arguments [76, 77] with no insight in the dynamics. With few exceptions [78], the effect of microscopic boundary roughness on the vortex nucleation has not been studied. A related and better understood nucleation process takes place when an ion bubble is driven in liquid helium by an applied electric field. Compared to the bucket, the nucleation is more controlled in terms of geometry (the shape of the bubble can be determined theoretically) and velocity (experimentally determined by time of flight measurements). Vortex nucleation by the ion bubble has received much more detailed experimental and theoretical attention [79–83] than nucleation by the walls of the bucket which contains the helium sample.

For what follows, we are not concerned with the vortex nucleation as such, but rather with the intermediate state between the nucleation and the final vortex lattice. This

intermediate stage is still unexplored, but, given that the length scales and the time scales involved depend on the vortex separation rather than the vortex core size (i.e. they are mesoscopic rather than microscopic), there is prospect of experimental visualisation in the near future. The focus of attention is therefore not individual vortex dynamics at nucleation but the collective dynamics of many vortex lines in the presence of a boundary which is not smooth. For simplicity we limit the scope of our problem to a low-temperature regime, in which the normal fluid does not play an important role.

The traditional method to model the dynamics of superfluid vortices is the Vortex Filament Method (VFM) [84], which models vortex lines as infinitesimally thin filaments interacting with themselves, their neighbours and the boundary (via suitable images). However, this approach is not applicable to our problem. Firstly, if the boundary varies on atomic length scales comparable to the vortex core (which is likely to be the case for any metal or glass bucket containing liquid helium), then the core lengthscale can no longer be ignored compared to other relevant lengthscale, invalidating the assumptions behind the VFM. Secondly, the implementation of the boundary condition is cumbersome to set up and not simple to change from one boundary shape to another; indeed, the VFM has been implemented for plane [85], semi-spherical [85, 86], spherical [87, 88] and cylindrical [89, 90] boundaries, but never for irregular boundaries relevant to our problem. Thirdly, the VFM does not describe vortex nucleation, but requires one to initialise the calculation with arbitrary seeding vortex lines. An alternative approach is through the Gross-Pitaevskii equation Eq. (1.56) [2, 40]. This formal description of a dilute weakly interacting gas of bosons, is equivalent to a continuity equation

$$\frac{\partial n}{\partial t} + \nabla \cdot (n\mathbf{v}) = 0 \quad (2.3)$$

and an Euler-like equation

$$n \left(\frac{\partial \mathbf{v}}{\partial t} + (\mathbf{v} \cdot \nabla) \mathbf{v} \right) = -\nabla p - \nabla \mathbf{P} - n \nabla \left(\frac{V}{m} \right) \quad (2.4)$$

for an inviscid fluid (the modification being the presence of a quantum pressure term) under the hydrodynamic decomposition

$$\Psi(\mathbf{r}, t) = \sqrt{n(\mathbf{r}, t)} \exp[iS(\mathbf{r}, t)]. \quad (2.5)$$

While the GPE is an excellent quantitative description of Bose gas superfluids, it is limited to being a qualitative description of superfluid helium due to the stronger interactions taking place in a liquid rather than in a gas. Nevertheless, its capability to describe the microscopic detail of superfluid dynamics - the finite-sized core, vortex interactions and reconnections, even the intrinsic nucleation - makes it a useful model to study superfluid

flows at a boundary. An important feature is that the GPE can easily implement irregular boundaries. Indeed, recent GPE simulations have predicted the occurrence of a turbulent boundary layer when the superfluid flows past a locally rough surface [78]: above a critical imposed flow speed, vortices are nucleated from the surface features, interact and become entwined in a layer adjacent to the surface.

Returning to the rotating bucket of superfluid helium, it is natural to ask if some kind of boundary layer may similarly form at the boundary of the rotating bucket in the transient evolution to the vortex lattice. Whether disordered or laminar, this layer will certainly involve vortex interactions. It is in fact unlikely that the vortex lines which nucleate extend from the top to the bottom of the bucket, as if the process were essentially two-dimensional (2D). More likely, the first vortex lines which nucleate are small, and become long only after a sequence of interactions and reconnections. To qualitatively explore and quantify these interactions, here we perform a series of numerical experiments, based on the GPE, of a superfluid being spun-up in a bucket whose walls are microscopically rough. These numerical experiments allow us to build a physical picture of how vorticity enters the superfluid and forms a vortex lattice, and of the role of remanent vortices, sharp intrusions, rotation rate, and dimensionality.

2.2 Numerical recipe

We make two physically-motivated modifications to the basic GPE in Eq. (1.56). Firstly, since the GPE conserves energy, we follow other works [91–93] in introducing a phenomenological dissipation term into the GPE to model, at least in a qualitative way, the damping of excitations of the superfluid (for example, by their interaction with the normal fluid). This is achieved by replacing the left-side of Eq. (1.56) with $(i - \gamma)\hbar \partial\Psi/\partial t$, where γ specifies the strength of the dissipation. Although not as accurate as the friction included within the VFM, this phenomenological dissipation will help damp out the oscillations of the vortex lines (Kelvin waves) [94, 95], which is the main effect of the friction which concerns us here. Secondly, given our rotating scenario, we work in the reference frame rotating at constant angular frequency Ω about the z axis; this is achieved by introducing the angular momentum operator defined as

$$\hat{\mathbf{L}} = \hat{\mathbf{R}} \times \hat{\mathbf{P}} \quad (2.6)$$

with $\hat{\mathbf{R}} = \mathbf{r}$ and $\hat{\mathbf{P}} = -i\hbar\nabla$. We can alternatively write the components of Eq. (2.6) as differential operators and introduce

$$\hat{L}_x = -i\hbar \left(y \frac{\partial}{\partial z} - z \frac{\partial}{\partial y} \right) \quad (2.7a)$$

$$\hat{L}_y = -i\hbar \left(z \frac{\partial}{\partial x} - x \frac{\partial}{\partial z} \right) \quad (2.7b)$$

$$\hat{L}_z = -i\hbar \left(x \frac{\partial}{\partial y} - y \frac{\partial}{\partial x} \right), \quad (2.7c)$$

where $\hat{L}_x, \hat{L}_y, \hat{L}_z$ correspond to rotation around the x, y , and z axis respectively. Thus we use Eq. (2.7c) to modify the GPE as necessary and write

$$i\hbar \frac{\partial \Psi(\mathbf{r}, t)}{\partial t} = \left(-\frac{\hbar^2}{2m} \nabla^2 + V(\mathbf{r}, t) + g|\Psi(\mathbf{r}, t)|^2 - \mu - i\hbar\Omega \left[x \frac{\partial}{\partial y} - y \frac{\partial}{\partial x} \right] \right) \Psi(\mathbf{r}, t). \quad (2.8)$$

The initial condition for Ψ in all of our simulations is the non-rotating ground state solution, found by the method of imaginary time propagation of the GPE, supplemented with low-amplitude white noise to Ψ (amplitude 0.001) to break any symmetries artificially presented in the initial condition. We then impose a constant rotation on the system for $t > 0$, with fixed rotation frequency Ω . Note that Ω far exceeds the critical rotation frequency to support vortices Ω_c , such that the lowest energy state of the fluid is a vortex lattice.

The non-dimensionalisation of the GPE is based on the natural units of the homogeneous fluid [40]: the unit of length is the healing length ξ , the unit of speed is c , the unit of time is $\tau = \xi/c = \hbar/\mu_0$, the unit of energy is μ_0 , and the unit of density is n_0 . Both our 3D and 2D numerical simulations of the GPE are performed using XMDS2 [96], an open-source partial and ordinary differential equation solver. The time evolution of the dimensionless GPE is computed via a fourth order Runge-Kutta integration scheme (see Appendix B.4) with typical time step $dt = 0.01\tau$ and grid spacing $dx = 0.4\xi$; these discretisation numbers are sufficiently small to resolve the smallest spatial features (vortices and the fluid boundary layer, which are of the order of a few healing lengths) and the shortest timescales in the fluid. We typically conduct our 3D simulations on a cubic grid of size 256^3 . Threaded parallel processing is employed using the OpenMP standard across typically 44 threads to improve processing speeds on computationally intensive simulations.

2.2.1 Bucket set-up

We consider the fluid to be confined within a cylindrical bucket of radius R and height H . The axis of the cylinder is the z -axis of rotation. The bucket is modelled through

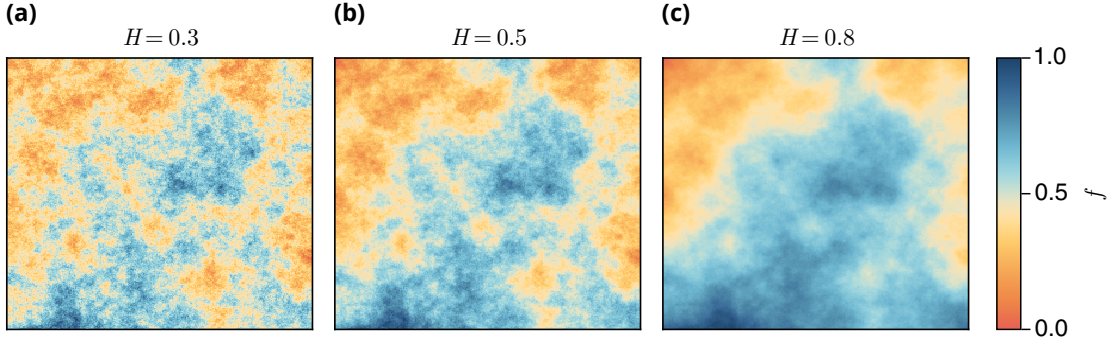


Figure 2.2: Example 2D fractional Brownian motion surfaces with the same numerical seed value with Hurst index (a) $H=0.3$, (b) $H=0.5$, (c) $H=0.8$ respectively. We stress that that the surface used to generate the rough bucket potential in our simulations is made periodic through a mirroring process, as discussed in the main text.

the potential $V(\mathbf{r})$: in the interior of the bucket we set $V = 0$ while at the boundary and beyond we set $V \gg \mu_0$. In the ground state, the fluid density has the bulk value n_0 in the centre of the bucket, while close to the bucket wall it heals to zero density over a length scale characterised by the healing length $\xi = \hbar/\sqrt{mn_0g}$. The healing length also characterises the size of the cores of vortices in the fluid. Note that the chemical potential in the bulk is $\mu_0 = n_0g$. The speed of sound in the uniform systems is $c = \sqrt{n_0g/m}$.

It is clearly computationally impossible to simulate the range of length scales which are realistic for a typical experiment with liquid helium in the context of the GPE model. The dimensions (radius and height) of typical buckets used in the experiments are of the order of the centimetre, which is around eight orders of magnitude larger than the vortex core size in helium-4, $a_0 = 10^{-10}\text{m}$ (in helium-3 the vortex core is about 100 times larger). Instead, in our numerical experiments we employ buckets whose scale is around 2 orders of magnitude larger than the vortex core size. While this is clearly a vast scale reduction compared to real systems, the separation of scales between the vortices and the bucket size is sufficient to give us a qualitative insight into the dynamics of the vortex lines.

2.2.2 Surface roughness

To mimic the experimentally unavoidable surface roughness, we modify the azimuthal face of the bucket away from a perfect cylindrical shape using a noisy continuous two-dimensional (2D) function f . This function is numerically generated through a two-dimensional fractal Brownian motion process [97–99] with Hurst index of $H = 0.3$, a parameter which describes the fractal dimension of the surface [100]. In Fig. 2.2 we demonstrate three realisations of fractional brownian motion with different Hurst indexes. Here we can observe a higher-frequency noise associated to a low Hurst index [Fig. 2.2(a)], and a lower frequency noise with increasing Hurst index [Fig. 2.2(b-c)]. The choice to

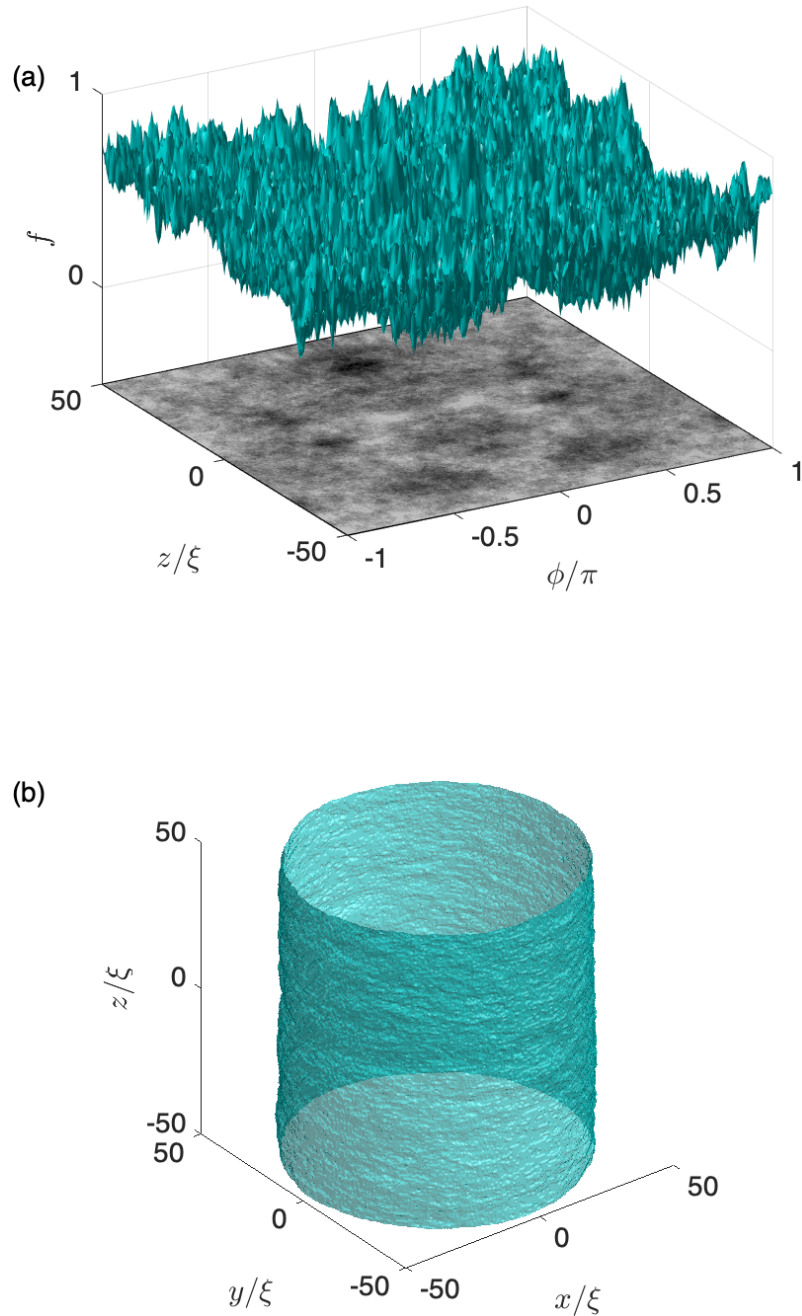


Figure 2.3: (a) An example of the 2D fractional Brownian motion function f , normalised to the range $[0,1]$ and mirrored about $\phi = 0$, shown as a surface plot and a heatmap. (b) The rough cylindrical boundary of our bucket is formed by using the surface in (a) to modulate the radius of the bucket boundary with an amplitude a , according to Eq. (2.9). Here $a = 0.1$, $R = 50\xi$.

model the roughness in this way is motivated by the well established fractal properties of real surfaces, including machined surfaces (of relevance to helium experiments), and the success of fractal brownian motion in modelling a wide variety of real rough surfaces [101]. The function is normalised between 0 and 1, and is mirrored about its edge and recombined with itself in order to create periodicity across one dimension; a single realisation of the function is depicted in Fig. 2.3(a). The function is mapped onto the space of axial coordinate z and azimuthal angle ϕ , and used to modify the radius of the bucket according to the form,

$$r(z, \phi) = R(1 - af(z, \phi)), \quad (2.9)$$

where R is the smooth bucket radius and a is the (dimensionless) roughness parameter. One could have chosen to implement the roughness via a summation of Fourier modes which would impose a natural periodicity. However this would require a spectral analysis of the surface of a typical confining potential, and goes beyond the scope of what we wish to investigate in what is already an analogue system of reduced complexity. The numerical procedure utilising Eq. (2.9) generates all of our rough 3D bucket shapes. By computing the local curvature of the surface roughness, we find that the values of the average radius of curvature corresponding to values $a = 0.05, 0.1, 0.2$ and 0.3 of the roughness parameter are $10.4\xi, 5.2\xi, 2.6\xi$ and 1.7ξ respectively (small values of a correspond to large radius of curvature, i.e. smoother surface). For simplicity, the top and bottom surfaces of the bucket are left smooth. The reason is that, by providing the vortex lines with pinning sites, any roughness on these surfaces will act essentially as an extra friction (an effect which is already qualitatively accounted for via the dissipation parameter γ) slowing down the final stage of crystallisation of the vortex lattice and prohibiting direct comparison to the 2D reduction of this system.

2.2.3 Typical spin-up dynamics

We now demonstrate the typical spin up of an initially quiescent fluid. Unless otherwise indicated, we present results for the following choice of parameters: bucket radius $R = 50\xi$, bucket height $H = 100\xi$, rotation frequency $\Omega = 0.02 \tau^{-1}$, dissipation parameter $\gamma = 0.05$, and roughness parameter $a = 0.1$ (meaning that the irregular surface of the bucket extends radially from 45ξ to 50ξ , corresponding to irregular ‘surface bumps’ of height up to 5 healing lengths).

The evolution of the fluid is illustrated by the snapshots shown in Fig. 2.4 in which the vortex lines are tracked in 3D space using a precise method introduced by Villois *et al* [102]; movies of the evolution are available in the supplementary material of [103]. From the initial quiescent and vortex-free fluid, first we see the nucleation of vortex lines at the cylindrical boundary of the fluid [Fig. 2.4(a)]. The nucleation takes place at the

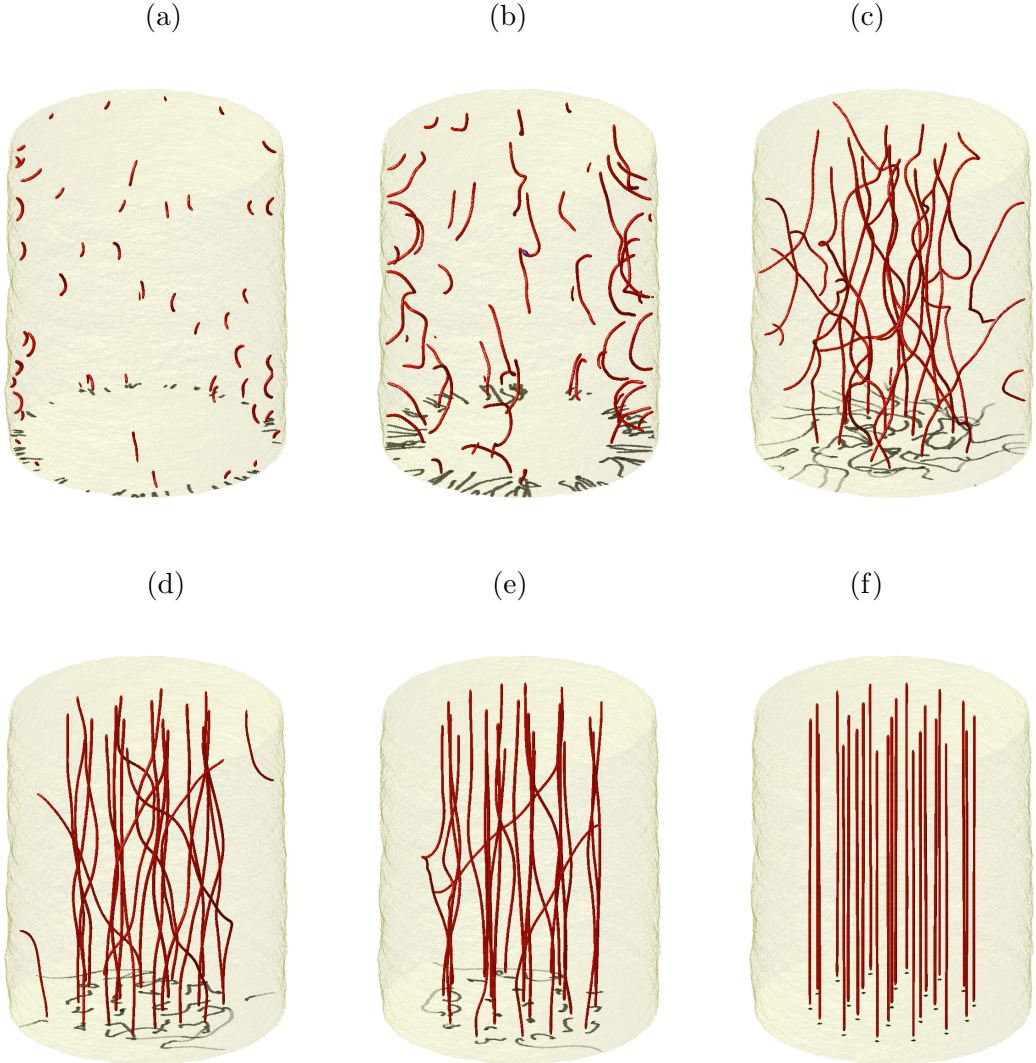


Figure 2.4: Three-dimensional snapshots at times $t/\tau = 100$ (a), 200 (b), 500 (c), 1000 (d), 1500 (e) and 3000 (f) during the spin-up of the initially quiescent fluid. The vortex cores are identified by density isosurfaces; vortices with positive and negative circulation (as determined by their pseudo-vorticity [102] in the z direction) are visualised in red and blue respectively. The faint yellow isosurface represents the confining bucket. A false-color shadow is projected onto the bottom surface to enhance the visualisation of the 3D vortex lines.

sharpest features on the surface, as seen in a previous calculation over a flat rough surface [78]: at these features the local (potential) flow velocity is raised by the curvature of the boundary, and exceeds the critical velocity of vortex nucleation, which, according to Landau's criterion, in a Bose gas is $v_c \approx c$. Since the local flow speed around a moving obstacle always exceeds the translational speed of the obstacle, Landau's criterion can be satisfied by a translational speed less than c . For example, a cylindrical obstacle moving at speed approximately equal to $0.4c$ will nucleate vortices [104, 105]. In our case

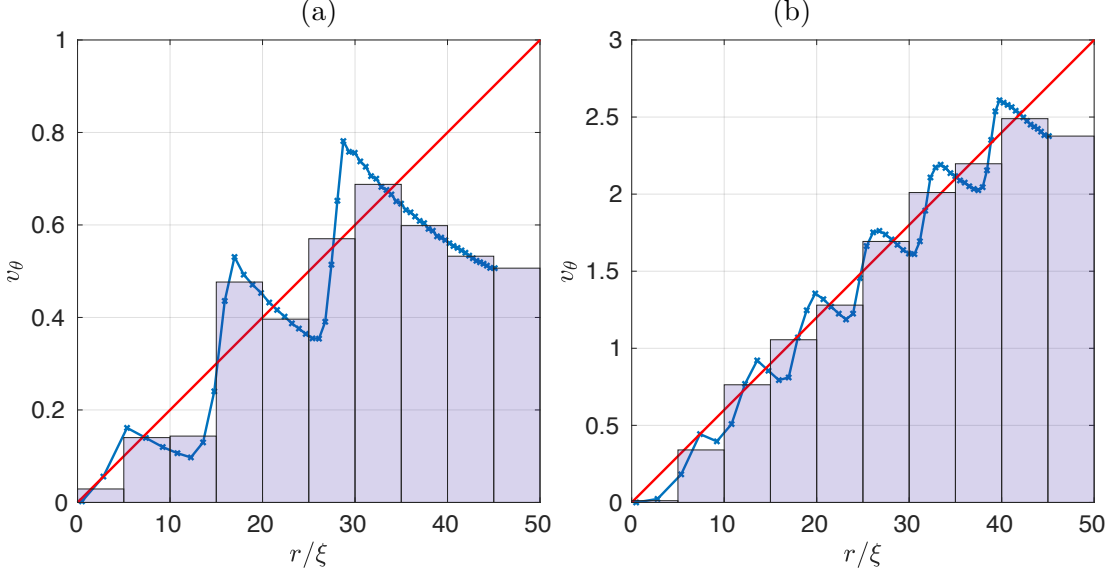


Figure 2.5: Azimuthal velocity v_θ of the fluid as a function of radius r , for rotation frequencies of $\Omega = 0.02 \tau^{-1}$ (a) and $\Omega = 0.06 \tau^{-1}$ (b). We use roughness parameter $a = 0.1$. The solid red lines represent solid body rotation $v_\theta = \Omega r$; the blue lines are values of $v_\theta(r)$ averaged in the θ direction; the pale blue rectangles are histograms with bin size $\Delta r = 5\xi$ (therefore the outer bins contain more data points). It is apparent that the more rapid rotation (b) creates a vortex lattice in better agreement with the solid body rotation, and that there is a vortex-free region near the boundary.

($\Omega = 0.02/\tau$ and $R = 50\xi$), the translational speed of the prominences on the rough boundary is approximately $\Omega R \approx c$, which is sufficient to exceed Landau's criterion and nucleate vortices. Figure 2.4 (a) and (b) show that the vortex lines which nucleate at the rough boundary have the shape of small half-loops or handles; similar vortex shapes have been reported in trapped Bose-Einstein condensates [106] and turbulent superfluid helium-4 near a heated cylinder [107], and have been called respectively “U-vortices” and “handles”.

The collection of U-vortices nucleated at the boundary is the superfluid’s analog of a boundary layer, the region separating the rotating boundary from the still quiescent bulk of the fluid. The U-vortices tend to be aligned along the z -direction, creating a superflow in the same direction of the rotating boundary. The vortex nucleation is therefore short-lived, since the nucleated U-vortices reduce the relative motion between the fluid and the boundary, suppressing further nucleations. In time, the U-vortices grow in size and extend further into the fluid [Fig. 2.4(b,c)], ultimately filling the bulk [Fig. 2.4(d)]. During this stage of the evolution, the U-vortices also grow in vertical extent in the z -direction, occasionally connecting and merging with each other, thus increasing their vertical extent. When the length in the z -direction becomes of the order of the bucket’s height H , one or both vortex endpoints start sliding along the smooth top and/or bottom of the bucket.

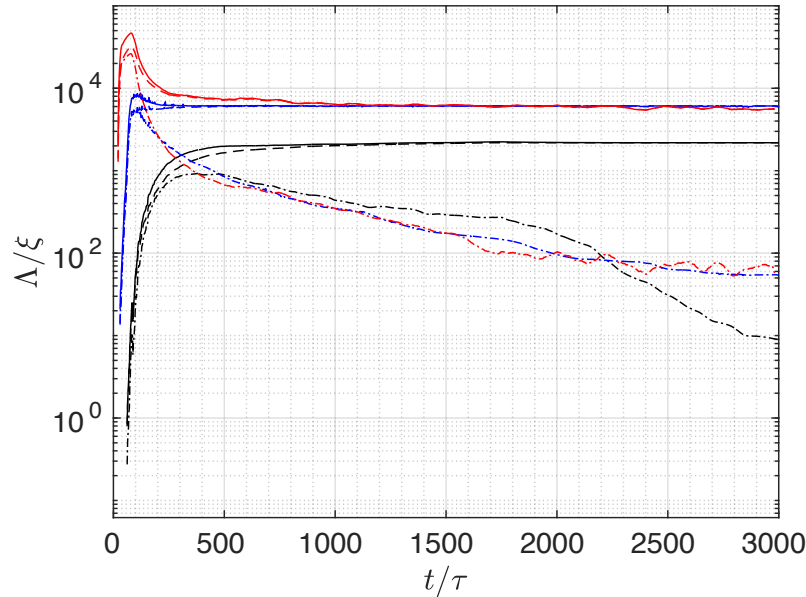


Figure 2.6: Evolution of the total vortex length, Λ (solid lines), as well as the vortex length in the z -direction, Λ_z (dashed lines) and the vortex length in the xy -plane, Λ_{xy} (dot-dashed lines), plotted versus time t for different angular velocity of rotation $\Omega = 0.02 \tau^{-1}$ (black), $0.04 \tau^{-1}$ (blue) and $0.06 \tau^{-1}$ (red) achieving final values of the vortex length $\Lambda_\infty = 2184\xi$, 6007ξ and 5568ξ respectively. All curves refer to roughness parameter $a = 0.1$.

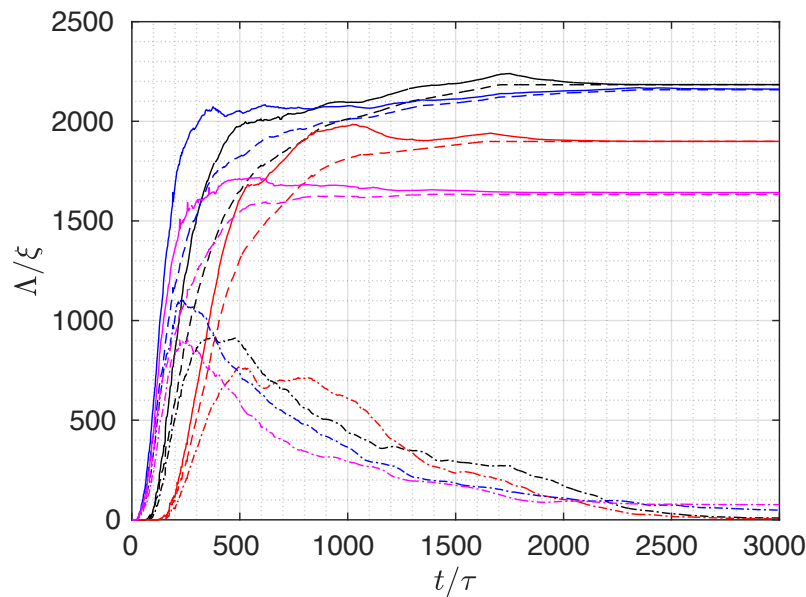


Figure 2.7: Evolution of the total vortex length, Λ (solid lines), as well as the vortex length in the z -direction, Λ_z (dashed lines) and the vortex length in the xy -plane, Λ_{xy} (dot-dashed lines), plotted versus time t for different boundary roughness $a = 0.05$ (red), 0.1 (black), 0.2 (blue), and 0.3ξ (magenta), achieving final values $\Lambda_\infty = 1899 \xi$, 2184ξ , 2161ξ and 1643ξ . All curves refer to the same angular velocity $\Omega = 0.02 \tau^{-1}$.

Once most of the vortex lines are fully extended from the top to the bottom of the bucket, they quickly drift into the bulk of the fluid. Although the vortex lines are aligned along the direction of rotation, they remain highly excited and undergo reconnection events when they collide with each other. Over time they relax towards a regular configuration of straight vortices. A small proportion of U-vortices remain attached to the side of the bucket for a longer period of time [Fig. 2.4(d)]; over a longer time they detach, and relax to the final lattice configuration. Some of the vortex lines end up diagonally across the rest of the vortex lattice [Fig. 2.4(e)]; eventually they also relax to the final lattice configuration [Fig. 2.4(f)]. The vortex lattice is stationary in the rotating frame, representing the lowest energy state of the rotating superfluid. In this final state, the coarse-grained fluid velocity approximates the solid-body result $\mathbf{v} = v_\theta \mathbf{e}_\theta = \Omega r \mathbf{e}_\theta$, where \mathbf{e}_ϕ is the azimuthal unit vector, as shown in Fig. 2.5. As expected, the agreement improves with increasing Ω , and there is a vortex-free region near the boundary.

2.2.4 Role of angular velocity and roughness

To analyse the vortex dynamics further it is useful to distinguish the total vortex length Λ , from the vortex length projected in the z -direction, Λ_z , and the vortex length projected in the xy -plane, Λ_{xy} . In the final vortex lattice all vortex lines are aligned along z , hence we expect that, after a sufficiently long time, $\Lambda_{xy} \approx 0$ and $\Lambda_z \approx \Lambda$, with $\Lambda \rightarrow N_v H$, where N_v is the final number of straight vortex lines. Figure 2.6 displays Λ (solid lines), Λ_z (dashed lines) and Λ_{xy} (dot-dashed lines) as a function of time for different angular velocities of rotation, $\Omega = 0.02, 0.04$ and 0.06 at the same roughness parameter $a = 0.1$. It is apparent that in the initial stage, a great amount of vorticity is in the xy -plane, before realignment of the vortex lines along the z -axis of rotation takes place. The effect is particularly noticeable at the largest angular velocities, for which, during the initial transient, the vortex length is considerably larger than the value Λ_∞ achieved in the final vortex lattice configuration. Moreover, we see that the final vortex line length increases with Ω due to the increasing number of vortices in the final state.

Figure 2.7 shows Λ , Λ_z and Λ_{xy} plotted versus time at the same angular velocity $\Omega = 0.02\tau^{-1}$ for different values of roughness parameter a . The largest values of the final vortex length Λ_∞ are achieved with $a = 0.1\xi$ and $a = 0.2\xi$. Smoother ($a = 0.05\xi$) and rougher ($a = 0.3\xi$) boundaries generate less vortex length. These variations in the final line length arise to the final number of vortex lines varying by a few vortices across these cases. It is not surprising that the final vortex lattice depends on the roughness which has nucleated the initial vorticity. We highlight that Feynman's rule, as introduced by Eq. (2.2) only refers to an idealised homogeneous system. Boundaries are known to have effects (e.g. missing vortex lines near the boundary) and it has been observed that the formation of the vortex lattice may be history-dependent and involve metastability

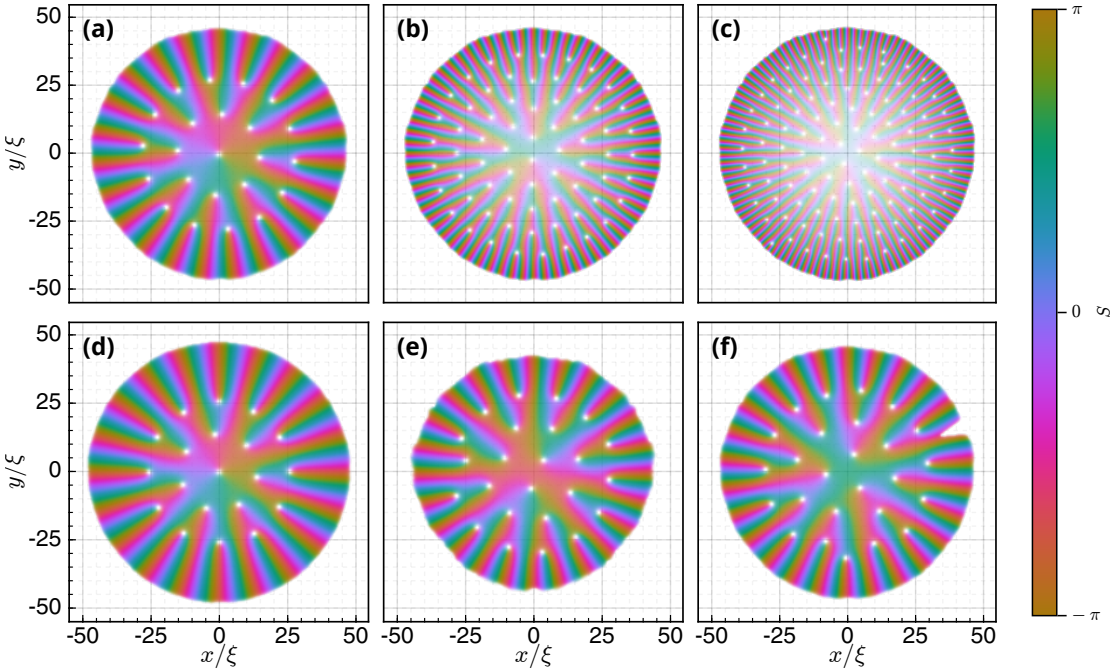


Figure 2.8: Normalised density n/n_0 and phase profile S in the xy -plane at the half-height of the bucket visualised by transparency and colour respectively, showing the final vortex configurations for the following cases: (a): $\Omega = 0.02 \tau^{-1}$ and $a = 0.1$ (default choice); (b): $\Omega = 0.04 \tau^{-1}$ and $a = 0.1$ (double rotation); (c): $\Omega = 0.06 \tau^{-1}$ and $a = 0.1$ (triple rotation); (d): $\Omega = 0.02 \tau^{-1}$ and $a = 0.05$ (half roughness); (e): $\Omega = 0.02 \tau^{-1}$ and $a = 0.2$ (double roughness); (f): $\Omega = 0.02 \tau^{-1}$ and $a = 0.1$ (single strong protuberance added, see Section 2.3.1).

[108, 109] and hysteresis [110].

Figure 2.8 illustrates some of the final vortex patterns which we have computed by concurrently plotting the superfluid density $|\psi(x, y)|^2$ and phase $S(x, y)$ in the xy -plane at half-height of the bucket. In these pictures the vortices appear as small holes; to clarify the lengthscales, we recall that on the vortex axis the density is zero and that at distance $r = 2\xi$ from the axis, the density recovers about 80% of the bulk value at infinity. It must be stressed that the figure shows slices of 3D vortex configurations, not vortex patterns. Note that at half-height the vortex lines are as far as possible from the top and bottom boundaries, therefore more likely to be bent away from the ideal 2D vortex pattern. It is interesting to compare the different final vortex configurations for halved/doubled rotation velocity and the roughness parameter with respect to our default choice ($\Omega = 0.02 \tau^{-1}$ and $a = 0.1$). While the ideal 2D vortex lattice has a vortex at the centre, surrounded by a first row of 6 vortices, a second row of 12 vortices, etc, the vortex configurations shown in Fig. 2.8 contain slightly different vortex numbers, in particular some configurations contain vortex lines which seem misplaced [Fig. 2.8(c)] or lack the vortex at the centre [Fig. 2.8(e)]. These configurations are metastable states corresponding

to local minima of the free energy in the rotating frame [108]. Moreover, at slow rotations [Fig. 2.8(a,d)] the predicted vortex-free region near the boundary [77, 111, 112] is clearly visible; this phenomenon affects the coarse-grained azimuthal velocity near the boundary shown previously in Fig. 2.5(a). The depletion of the background fluid density in the centre of the bucket - particularly evident in Fig. 2.8(b) and (c) - is due to coarse-grained centrifugal effects, analogous to the classical rotating case [40].

2.3 Other effects

In this section we repeat the simulation of Section 2.2.3 with several significantly modifications: the presence of a single strong protuberance, the presence of remanent vortex lines, and the 2D case. The aim is to determine whether these effects change qualitatively the dynamics described in Section 2.2.3.

2.3.1 Effect of a strong protuberance

First we consider the effect of a single strong imperfection in the form of a protuberance on the cylindrical wall. The question is whether, by enhancing vortex nucleation, the protuberance can induce a turbulent boundary layer. The protuberance is numerically created by adding a Gaussian-shaped potential to the existing (small-scale) roughness potential. Equation (2.9) is replaced by

$$r(z, \phi) = R[1 - a(f(z, \theta) + Gf_G(z, \theta))], \quad (2.10)$$

where $G = 2$ and $f_G(z, \theta)$ is a Gaussian-shape function taking values from 0 to 1 and rms width 4ξ . The approximate height of the strong protuberance in the simulation which we present is 10ξ , as also visible in Fig. 2.8(f).

Snapshots taken during the time evolution for $\Omega = 0.02 \tau^{-1}$ and $a = 0.1$ are shown in Fig. 2.9 and a movie can be viewed in the supplementary material of [103]. The protuberance catalyses the local nucleation of vortices at early times: large vortex loops (of the same size order as the protuberance) are rapidly generated [Fig. 2.9(a)], leading to a downstream trail of loops [Fig. 2.9(b, c)], in addition to the slower nucleation of U-vortices from the rough bucket wall. The vortex configuration becomes clearly anisotropic near the bucket edge [Fig. 2.9(d)]. However, once the vortices fill the bulk [Fig. 2.9(e)], memory of this effect is lost, and the subsequent evolution is very similar to the evolution without the strong protuberance. In fact, the final vortex lattice is not significantly different from the lattices considered in Section 2.2.3, as shown in Fig. 2.8(f). Figure 2.10 shows the time evolution of Λ , Λ_z and Λ_{xy} in the presence of the protuberance (magenta lines) and its absence (black lines). This confirms that the protuberance accelerates the generation of

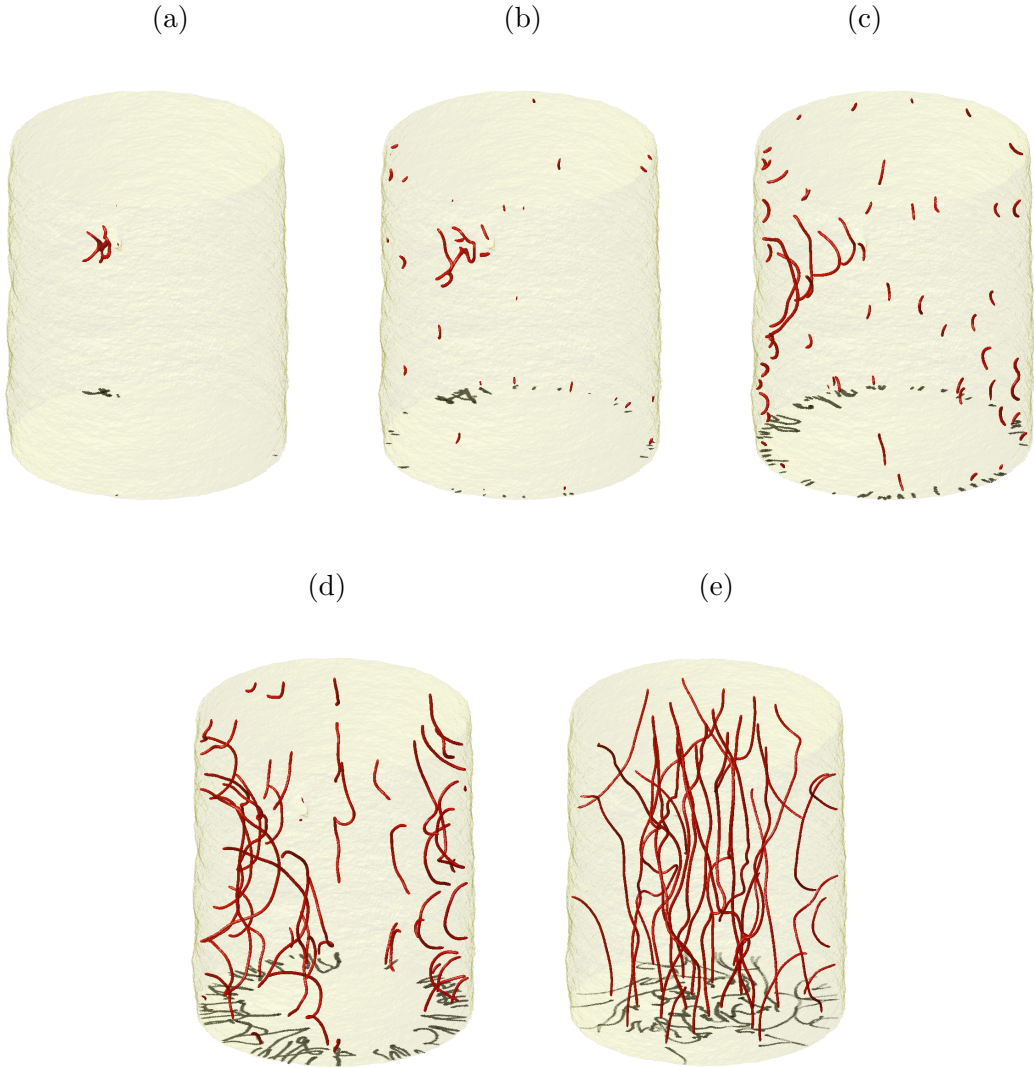


Figure 2.9: Early-time dynamics during the spin-up of the fluid in the presence of a single strong protuberance added to the rough cylindrical boundary. The snapshots, taken at $t/\tau = 26, 50, 100, 200$ and 500 , are presented in the same way as Fig. 2.4.

vortex line length at early times by inducing a region of increased superfluid velocity, but that its effect becomes washed out at later times.

2.3.2 Effect of remanent vortices

Secondly, we consider the effect of remanent vortex lines. In experiments with liquid helium, it is believed that so-called ‘remanent vortices’ may be present in the fluid, created via the Kibble-Zurek mechanism when cooling the helium sample through the superfluid transition to the final experimental temperature. The presence of remanent vortices may

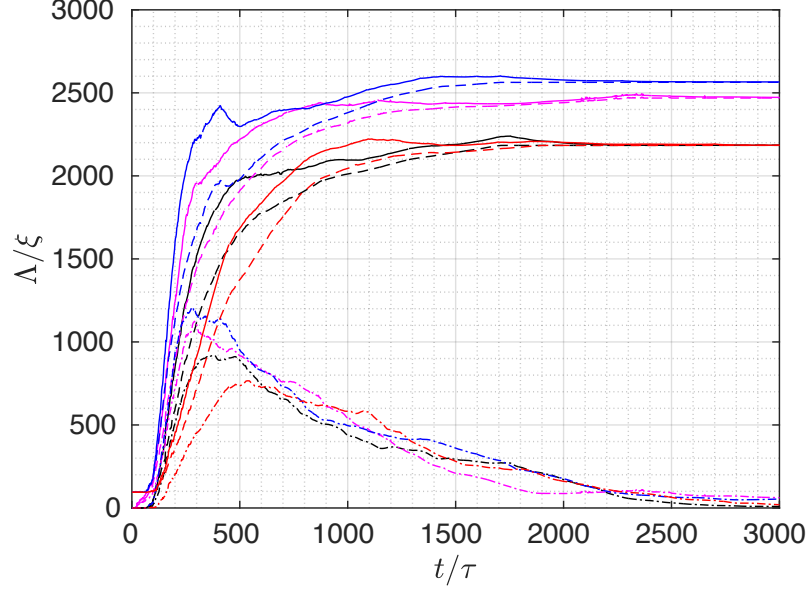


Figure 2.10: Time evolution of Λ (solid line), Λ_z (dashed line), Λ_{xy} (dot-dashed line). The colours correspond to the simulations with default parameters $\Omega = 0.02\tau^{-1}$, $a = 0.1\xi$ (black), the added surface protuberance (magenta), the added remanent negative vortex (blue), and the added remanent positive vortex (red), respectively.

modify the vortex nucleation and the formation of the vortex lattice when the sample is rotated. To explore this idea, we have repeated the simulations imposing a suitable phase profile to imprint a vortex to the initial state during the imaginary-time propagation that is given by

$$S_v(\mathbf{r}) = \Gamma \arctan \left(\frac{y - y_v}{x - x_v} \right) \quad (2.11)$$

which corresponds to a vortex of circulation Γ at position (x_v, y_v) . For simplicity we position the remanent vortex along the z -axis of rotation, such that $x_v = y_v = 0$ and restrict our analysis to the singularly charged vortex such that $|\Gamma| = 1$. The evolution of the superfluid with the standard rough cylindrical wall and a “positive” remanent vortex, that is, one whose circulation ($\Gamma = 1$) is oriented in the same direction of the bucket’s rotation is shown through Fig. 2.11 and the movie in the Supplementary Material of Keepfer *et al* [103]. Compared to Section 2.2.3, the only significant modification is a dampening of the initial injection of U-vortices; the effect is visible by eye when comparing like-time snapshots [Fig. 2.4(b) and Fig. 2.11(a)]. The remanent vortex acts in the same direction as the rotating container: it reduces the relative speed between the bucket’s wall and the superfluid, remaining largely undisturbed at early times [Fig. 2.11(a)] until the U-vortices that are nucleated fill the bulk and interact with it [Fig. 2.11(b)]. At this point the remanent vortex becomes subsumed within the other like-signed vortices [Fig. 2.11(c)], and

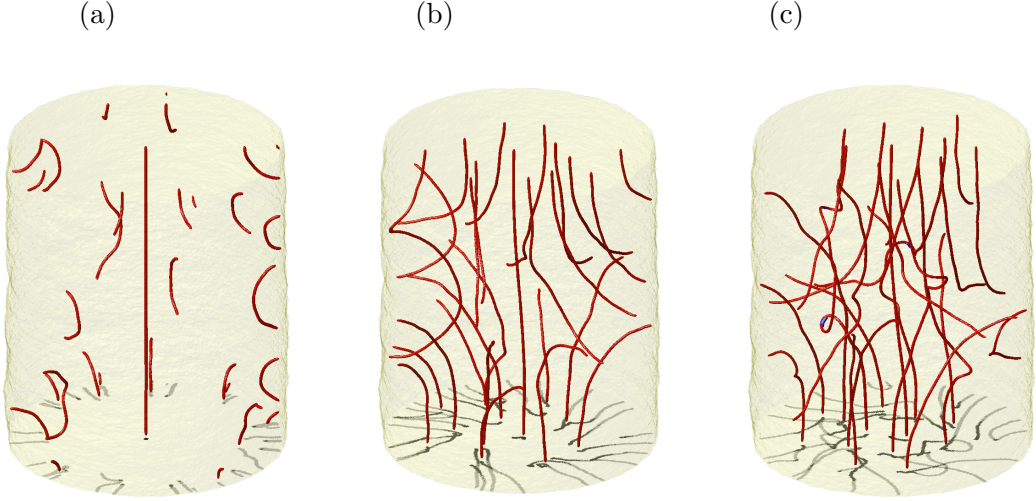


Figure 2.11: Spin-up of the superfluid in the presence of a positively-charged remanent vortex. Snapshots are taken at $t/\tau = 200, 400$ and 500 , and are presented in the same way as Fig. 2.4.

the subsequent relaxation of the vortex configuration into a vortex lattice largely proceeds as if there was not any remanent vortex initially. Confirming this, we see from Figure 2.10 that the presence of the positive vortex (red lines) depletes the generation of vortex line length at early times, but this recovers at later times such that the system reaches the same line length as in the absence of any remanent vortices (black lines).

If the remanent vortex is oriented in the direction opposite to the rotation of the bucket, i.e. a negative vortex ($\Gamma = -1$), the evolution proceeds differently, as seen in Fig. 2.12 and the movie in Supplementary Material [103]. The remanent vortex enhances the nucleation of U-vortices from the boundary, as evident from comparing Fig. 2.4(b) and Fig. 2.12(a). This effect is caused by the counter-flow induced by the remanent vortex, which increases the relative speed of the fluid over the rough boundary. Once the other vortices drift close to the remanent vortex, the remanent vortex becomes excited by their interaction [Fig. 2.12(b)]. A series of vortex reconnections break up the remanent vortex, forming progressively smaller vortex loops [Fig. 2.12(c,d)]. This leads to the rapid removal of vorticity of the ‘wrong’ sign from the fluid [Fig. 2.12(e)]. Hereafter the fluid evolves in a similar manner to when the remanent vortex is absent as in Section 2.2.3, albeit with a slightly higher final vortex line length as evidenced by Fig. 2.10.

2.3.3 2D case

Finally, we have also performed simulations of the spin-up of a 2D superfluid within a rough circular boundary; the boundary is taken from the central slice of the 3D rough bucket. A movie showing the typical dynamics is available in the supplementary material

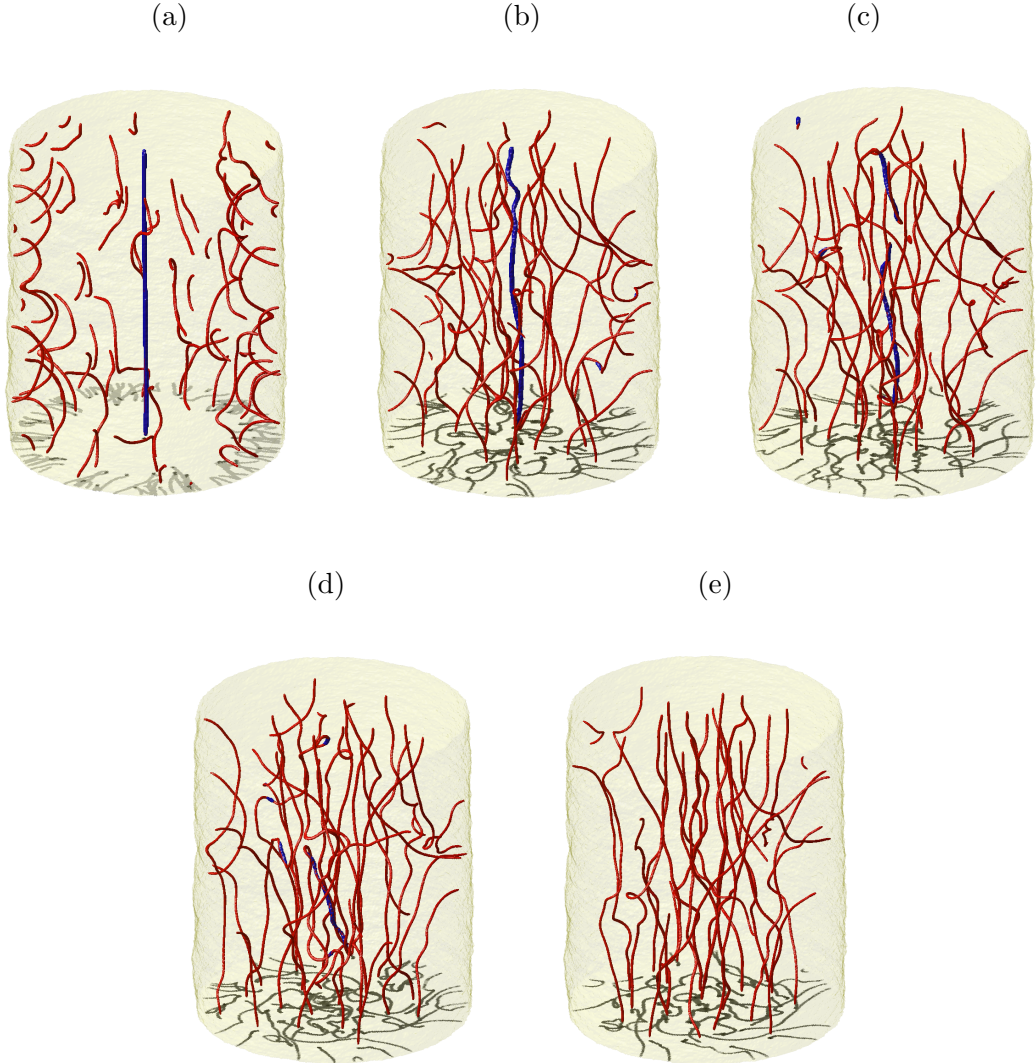


Figure 2.12: Spin-up of the superfluid in the presence of a negatively-charged remanent vortex. Snapshots are taken at $t/\tau = 200$ (a), 360 (b), 386 (c), 420 (d) and 500 (e). The images are presented in the same way as Fig. 2.4. Vortices with negative circulation are coloured blue.

of Keepfer *et al* [103]. The 2D geometry allows calculations of much larger buckets, up to $R = 200\xi$ with a 1024^2 numerical grid. We observe the same qualitative behaviour as in 3D in smaller buckets, albeit with many more vortices and without 3D effects such as vortex reconnections. Collisions of vortices of the opposite circulation result in the annihilation of the vortices and the emission of sound pulses [113–115]. In general we find that, in 2D, the timescales of injection, diffusion and lattice crystallisation are faster than in 3D. A particular feature that we see in the early-time dynamics of the 2D simulations is the nucleation of vortices with both positive and negative circulation (i.e. with circulation which is inconsistent with the imposed rotation). We notice that some negative

vortices originate from localised rarefaction pulses generated from the rough boundary when the bucket is set into rotation. We associate these pulses with Jones-Roberts (JR) solitons [116, 117], which are low energy/momentum solutions of the 2D GPE. At higher energy/momentum, these solutions become pairs of vortices of opposite sign (also called vortex dipoles in the literature). The conversion of JR solitons into vortex dipoles occurs if the pulse gains energy from the large positive vortex cluster which starts forming close to the sharp boundary. Occasionally, the vortices which are parts of a dipole separate and mix with the rest of the vortices. Over time, the vortices of negative circulation are lost from the system, either colliding (hence annihilating) with positive vortices within the bulk, or by exiting the fluid at the bucket's boundary (effectively annihilating with their images). The conversion from a JR soliton into a dipole pair is depicted in Fig. 2.13(a)-(c) in the 2D larger grid geometry. To fully capture the behaviour of this event, we decompose the hydrodynamic kinetic energy into its constituent compressible and incompressible parts [118] and visualise the energy density for each. In the hydrodynamic description of Eq. (2.5), the Hamiltonian becomes

$$H = \int d^3\mathbf{r} \left(\frac{m}{2}n|\mathbf{v}|^2 + \frac{\hbar^2}{2m}|\nabla\sqrt{n}|^2 + Vn + \frac{gn^2}{2} \right). \quad (2.12)$$

The first two terms are forms of kinetic energy and we can write

$$E_{\text{kin}} = \int d^3\mathbf{r} \left(\frac{m}{2}n|\mathbf{v}|^2 + \frac{\hbar^2}{2m}|\nabla\sqrt{n}|^2 \right). \quad (2.13)$$

The first term of this expression is a hydrodynamic one, whereas the second is known as the quantum pressure. Omitting the latter, we can write the hydrodynamic kinetic energy as

$$E_{\text{kin}}^h = \frac{m}{2} \int d^3\mathbf{r} n|\mathbf{v}|^2. \quad (2.14)$$

where \mathbf{v} is the superfluid velocity as given by Eq. (1.62). We can then introduce

$$\mathbf{u} = \sqrt{n}\mathbf{v}. \quad (2.15)$$

to remove the divergence in the velocity field around vortex cores where $n \rightarrow 0$ and permit the application of Parseval's theorem to calculate power spectra. This expression may be separated into a compressible and incompressible part via a Helmholtz decomposition

$$\mathbf{u}(\mathbf{r}) = \mathbf{u}_i(\mathbf{r}) + \mathbf{u}_c(\mathbf{r}) \quad (2.16)$$

such that the divergence of the incompressible part \mathbf{u}_i is zero and the curl of the compressible part \mathbf{u}_c is the zero vector. We can then write

$$E_{\text{kin}}^h = \frac{m}{2} \int d^3\mathbf{r} |\mathbf{u}_i|^2 + \frac{m}{2} \int d^3\mathbf{r} |\mathbf{u}_c|^2 = E_{\text{kin}}^i + E_{\text{kin}}^c. \quad (2.17)$$

The compressible part corresponds to acoustic energy (phonons) and the incompressible part corresponds to vortex structures. Using the spectral methods of Bradley *et al* [119], we perform this decomposition and plot the compressible kinetic energy density e_{kin}^c and incompressible kinetic energy density e_{kin}^i in the second and third rows of Fig. 2.13 respectively. Here we see an exchange in the energy associated to the transformation of a JR soliton into a vortex dipole pair. Before the transformation, the energy associated to the density depletion is phonon-like [Fig. 2.13(d)]. As it propagates, it transfers to be a combination of both compressible and incompressible energy [Fig. 2.13(e)-Fig. 2.13(h)], before separating into a dipole pair where the energy is transferred into the incompressible part [Fig. 2.13(i)].

2.4 Chapter conclusions

In this chapter, we have employed simulations of the Gross-Pitaevskii equation to study the spin-up of superfluid helium in a rotating bucket featuring microscopically rough walls. Within this model, we see several key stages of the dynamics. Firstly, vortices are nucleated at the boundary by the flow over the rough features, typically in the form of small U-shaped vortex lines. Secondly, these U-shaped vortices interact strongly and reconnect, creating a transient turbulent state. This becomes increasingly polarised by the imposed rotation until the vortex configuration consists of vortices of the correct orientation, extending from the top to the bottom of the bucket. Finally, the vortex lines slowly straighten and arrange themselves in the expected final vortex lattice configuration. Our results highlight the importance of vortex reconnections [120]: it is generally assumed that vortex reconnections are important in turbulence, but here we have seen that reconnections are essential to create, starting from potential flow, something as simple as solid body rotation (the vortex lattice). The addition of a single large protuberance or one additional remanent vortex line does not change the dynamics significantly, only speeding up or slowing down the injection of vorticity. Moreover, analogous dynamics arise in the 2D limit.

We reiterate that the GPE is not a quantitatively accurate model of superfluid helium and these results should be interpreted qualitatively only. More sophisticated energy functionals have indeed been developed previously for a quantitative description of superfluid helium [121] and are usually largely applied in the context of helium nanodroplets, but here these would require computationally-intensive simulations for large systems such

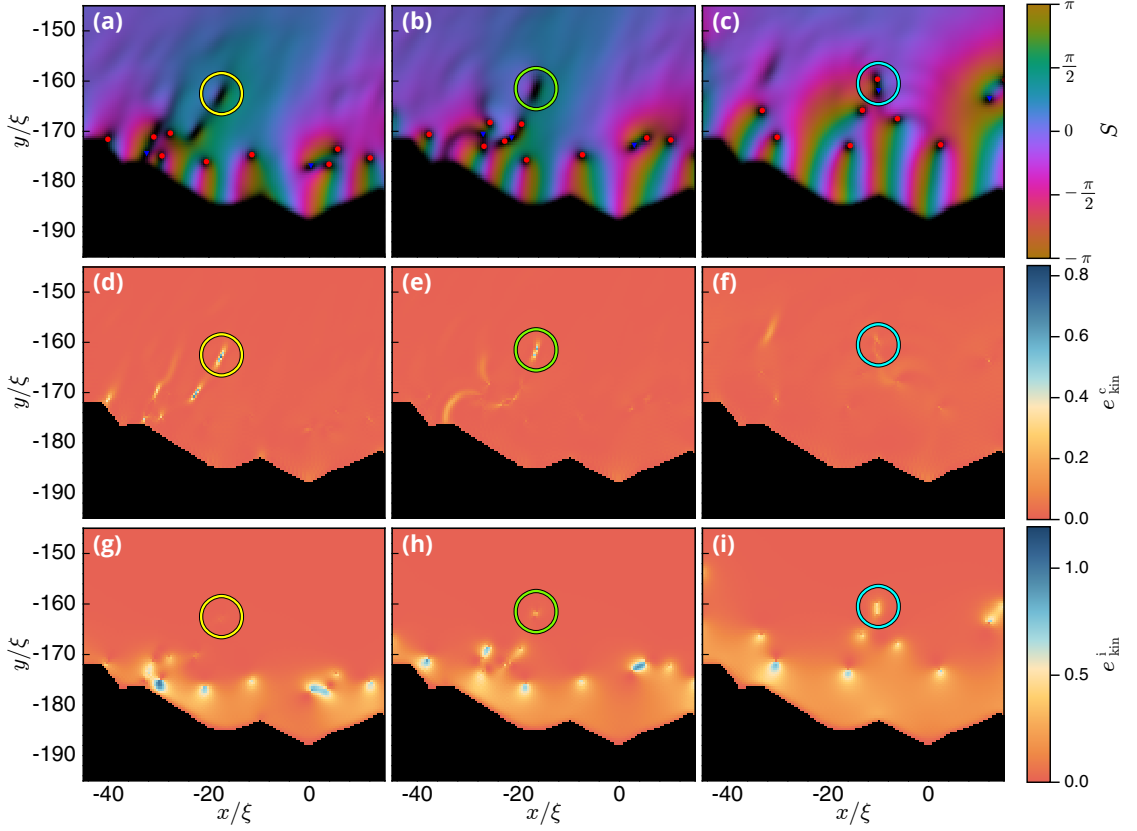


Figure 2.13: (a)-(c) Normalised density n/n_0 and phase profile S visualised concurrently at times (a) $t = 60\tau$, (b) $t = 70\tau$, (c) $t = 90\tau$. These times correspond to before, during and after a JR soliton transforms into a vortex dipole pair respectively. Circles of colour yellow, green and blue have been superimposed to mark the position of the event before, during and after respectively. The positions of positive (negative) vortices are indicated with red (blue) circles (triangles). Panels (d)-(f) show the compressible kinetic energy density $e_{\text{kin}}^c(\mathbf{r})$ whilst panels (g)-(i) show the incompressible kinetic energy density $e_{\text{kin}}^i(\mathbf{r})$ profile at the times indicated previously.

as the rotating bucket. Nevertheless, these functionals have successfully been applied to study the nature of vortices in liquid helium systems [122]. Another potential consideration is to accurately account for the role of friction. For example, the role of friction is introduced into the GPE through a widely-used phenomenological dissipation term. However, a more accurate physical model of this stage of the dynamics would be provided by the VFM. Also, a distinctive physical property of superfluid helium is its strong non-local interactions. This, for instance, supports a roton minimum in its excitation spectrum. A roton minimum arises from the interplay between short-range and long-range interactions and corresponds to a local minimum in the dispersion relation of the energy. While this is absent from the GPE model we have employed, it can be introduced through an additional non-local term [123, 124]. It would be interesting to see if this causes any significant departures from the dynamics we have reported here.

We now depart from the theory of trapped zero temperature Bose gases and in the next chapter begin to explore the effects of temperature on a trapped system. Whereas this chapter focused on the microscopic details of trapping topology on the dynamics of a superfluid, the later chapters will explore the broader effects of a dimensionality-altering trapping potential at finite temperature.

Part II

Finite Temperature

Chapter 3

Finite temperature stochastic Gross-Pitaevskii methods

In this chapter, we take the opportunity to describe the primary theoretical tools used within the second part of this thesis. Whilst there exists a plethora of novel classical field finite temperature theories for the Bose gas [34, 125–128], and modifications thereof [129–133], we focus on one in particular: the stochastic (projected) Gross-Pitaevskii equation. Derived independently and concurrently by the approaches of Duine and Stoof [134–136] and Gardiner and colleagues [137–139], each derivation gives rise to the same effective theory. We focus primarily on the latter framework of the stochastic projected Gross-Pitaevskii equation (SPGPE) and so use this chapter to introduce and motivate this theory for our work.

3.1 The stochastic projected Gross-Pitaevskii equation

In its complete form, the SPGPE [127, 137–141] is a grand-canonical truncated Wigner theory [127, 142] of Bose gases which explicitly separates atoms into a \mathcal{C} -field region and \mathcal{T} -field region, taking account of interactions and exchanges between them. Arising from developments in quantum kinetic theory [143–149] paired with finite temperature formalism for the GPE [137, 138, 150], the framework of SPGPE separates the fields into a classical coherent field and a quantum thermal reservoir. In essence, it encapsulates the dynamics of a finite temperature coherent field coupled to a thermal cloud where the two are assumed to be at equilibrium. Another pertinent assumption of this model is that the frequencies of the \mathcal{C} -field modes are much smaller than the thermal energy $k_B T$. Therefore the theory is better suited to describing systems at higher temperatures, close to and above the transition. The SPGPE allows direct and immediate control of the temperature of the thermal reservoir, which then equilibrates with the coherent modes.

As such, a number of studies investigating quench dynamics of a Bose gas have utilised this theory [28, 69, 151–153]. In general, the \mathcal{C} and \mathcal{I} fields may be out of equilibrium, where parameter control of the system thermal bath leads the evolution of the coupled condensate. The full derivation may be found in [138], although here we simply outline the key steps taken in this framework.

3.1.1 Formulating the SPGPE

We take as our starting point the second quantised Hamiltonian in the s -wave scattering limit as given by Eq. (1.47). Previously we used Eq. (1.49) to explicitly separate the condensate from non-condensate modes. On this occasion, we instead decompose the full quantum bosonic field as a sum

$$\hat{\Psi} = \hat{\mathcal{P}}\hat{\Psi} + \hat{\mathcal{R}}\hat{\Psi} = \hat{\Psi}_{\mathcal{C}} + \hat{\Psi}_{\mathcal{I}}, \quad (3.1)$$

where $\hat{\Psi}_{\mathcal{C}}$ and $\hat{\Psi}_{\mathcal{I}}$ are quantum field operators for a low energy band \mathcal{C} which contains macroscopically-occupied modes, and a high-energy band \mathcal{I} containing sparsely-occupied modes, respectively. The separation of these fields is performed through the introduction of orthogonal projection operators

$$\hat{\mathcal{P}} \equiv \sum_{\epsilon_n \leq \epsilon_{\text{cut}}} |n\rangle\langle n|, \quad (3.2)$$

and

$$\hat{\mathcal{R}} \equiv 1 - \hat{\mathcal{P}}. \quad (3.3)$$

Here ϵ_n corresponds to the energy of mode ψ_n which satisfies the eigen-equation

$$\hat{h}_0\psi_n(\mathbf{r}) = \epsilon_n\psi_n(\mathbf{r}), \quad (3.4)$$

and we have introduced the energy cutoff ϵ_{cut} and single-particle Hamiltonian specified by Eq. (1.42). The energy cutoff requires a careful choice in order to ensure the assumption of macroscopic occupation for modes within \mathcal{C} is met, and is discussed at length in Section 3.1.3. Our projection operators are defined such that $\hat{\mathcal{P}}\hat{\mathcal{P}} = \hat{\mathcal{P}}$, $\hat{\mathcal{R}}\hat{\mathcal{R}} = \hat{\mathcal{R}}$ and importantly $\hat{\mathcal{P}}\hat{\mathcal{R}} = \hat{\mathcal{R}}\hat{\mathcal{P}} = 0$. This partitions the full bosonic field into one of a classical field in contact with a thermal reservoir such that

$$\hat{\Psi} = \sum_{\epsilon_n \leq \epsilon_{\text{cut}}} \hat{a}_n\psi_n(\mathbf{r}) + \hat{\Psi}_{\mathcal{I}} \quad (3.5)$$

where \hat{a}_n are the single-mode creation operators satisfying $[\hat{a}_n, \hat{a}_m^\dagger] = \delta_{nm}$, with \hat{a}_m^\dagger corresponding to the single-mode annihilation operator. The formal derivation of the equation

of motion of the classical field proceeds by mapping the master equation for the \mathcal{C} -field to an equation for the Wigner distribution of the system [138]. A key assumption here is that energies of the coherent modes are small compared to the thermal energy $k_B T$, which limits the validity of this formalism to the range $0.5 \lesssim T \lesssim T_c$, where T_c is the critical temperature of the phase transition. The resultant equation for the evolution of the Wigner distribution effectively describes a diffusion process for the classical field Ψ_C in contact with the \mathcal{I} -field through rate functions which determine the strength of reservoir interaction processes [141, 154]. We note that a secondary assumption of the Wigner distribution approach is exactly the truncated Wigner approximation. Consider a system with a corresponding Wigner function $\mathcal{W}(\Psi_C(\mathbf{r}), \Psi_C^*(\mathbf{r}), t)$, whose full evolution contains third-order derivative terms of the form

$$\frac{\partial \mathcal{W}}{\partial t} \propto \left[\frac{\partial^3}{\partial^2 \Psi_C \partial \Psi_C^*} \right] (\Psi_C \mathcal{W}) - \left[\frac{\partial^3}{\partial \Psi_C \partial^2 \Psi_C^*} \right] (\Psi_C^* \mathcal{W}). \quad (3.6)$$

Such terms preclude the mapping to a full Langevin-type equation. However, one may omit them provided that all coherent modes are macroscopically occupied, something that is ensured with a careful choice of cutoff energy ϵ_{cut} . We may then truncate the equation of motion, allowing us to write the full SPGPE as

$$(S)d\Psi_C = d\Psi_C|_H + d\Psi_C|_\gamma + (S)d\Psi_C|_S. \quad (3.7)$$

In this expression, (S) denotes a Stratonovich integral [155] and

$$d\Psi_C(\mathbf{r}, t)|_H = \hat{\mathcal{P}}_C \left\{ -\frac{i}{\hbar} \left(-\frac{\hbar^2}{2m} \nabla^2 + V_{\text{tr}}(\mathbf{r}) + g |\Psi_C(\mathbf{r})|^2 \right) \Psi_C(\mathbf{r}, t) dt \right\}, \quad (3.8a)$$

$$d\Psi_C(\mathbf{r}, t)|_\gamma = \hat{\mathcal{P}}_C \left\{ \beta\gamma \left[\mu - \left(-\frac{\hbar^2}{2m} \nabla^2 + V_{\text{tr}}(\mathbf{r}) + g |\Psi_C(\mathbf{r})|^2 \right) \right] \Psi_C(\mathbf{r}, t) dt + d\xi_\gamma(\mathbf{r}, t) \right\}, \quad (3.8b)$$

$$(S)d\Psi_C(\mathbf{r}, t)|_S = \hat{\mathcal{P}}_C \left\{ -\frac{i}{\hbar} V_M(\mathbf{r}, t) \Psi_C(\mathbf{r}, t) dt + i\Psi_C(\mathbf{r}, t) d\xi_M(\mathbf{r}, t) \right\}, \quad (3.8c)$$

are the contributions due to the mixing of \mathcal{C} -field modes, growth and scattering processes respectively. Here, we have introduced the dimensionless dissipation strength [154]

$$\gamma = \frac{8a_s^2}{\lambda_{dB}^2} \sum_{j=1}^{\infty} \frac{e^{\beta\mu(j+1)}}{e^{2\beta\epsilon_{\text{cut}}j}} \Phi \left[\frac{e^{\beta\mu}}{e^{2\beta\epsilon_{\text{cut}}}}, 1, j \right]^2, \quad (3.9)$$

where Φ is the Lerch transcendent. We have also introduced the effective potential

$$V_M(\mathbf{r}) = -\frac{\hbar^2}{k_B T} \int d^3 \mathbf{r}' M(\mathbf{r} - \mathbf{r}') \nabla' \cdot \mathbf{j}(\mathbf{r}'), \quad (3.10)$$

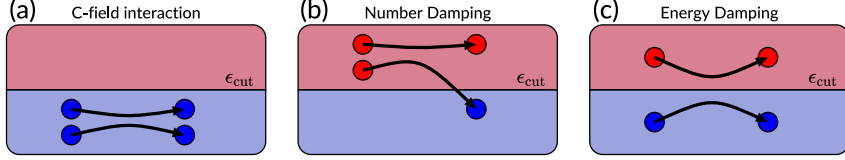


Figure 3.1: Schematic of SPGPE processes. (a) Mixing of modes within the \mathcal{C} -field (b) Number damping process, dictated by the rate set by γ for atoms to transfer from the thermal reservoir into the coherent modes of the \mathcal{C} -field (c) Scattering process whereby modes in the \mathcal{C} and \mathcal{I} fields may transfer energy at a rate set by $M(\mathbf{r})$, without a transfer of atoms.

which couples the divergence of the \mathcal{C} -field density current

$$\mathbf{j}(\mathbf{r}) = \frac{i\hbar}{2m} [\Psi_{\mathcal{C}} \nabla \Psi_{\mathcal{C}}^* - \Psi_{\mathcal{C}}^* \nabla \Psi_{\mathcal{C}}], \quad (3.11)$$

to the \mathcal{I} -field at a scattering rate governed by

$$M(\mathbf{r}) = \frac{2a_s^2 k_B T}{\pi^2 \hbar} \frac{1}{e^{\beta(\epsilon_{\text{cut}} - \mu)} - 1} \int d^3 \mathbf{k} \frac{e^{i\mathbf{k} \cdot \mathbf{r}}}{|\mathbf{k}|}. \quad (3.12)$$

The complex Gaussian noise $d\xi_\gamma$ and real Gaussian noise $d\xi_M$ have correlations of the form

$$\begin{aligned} \langle d\xi_\gamma^*(\mathbf{r}, t) d\xi_\gamma(\mathbf{r}', t') \rangle &= 2\gamma \delta(\mathbf{r} - \mathbf{r}') \delta(t - t') \\ \langle d\xi_M^*(\mathbf{r}, t) d\xi_M(\mathbf{r}', t') \rangle &= 2M(\mathbf{r} - \mathbf{r}') \delta(t - t') \end{aligned} \quad (3.13)$$

The former governs the rate of growth processes arising from high-energy collisions in \mathcal{I} , leading to growth in the particle number of \mathcal{C} , known as number-damping. The latter of these noise processes represents a stochastic real-valued effective potential that causes a phase-diffusion process for the \mathcal{C} -field that permits the exchange of energy and momentum with the \mathcal{I} -field with no change in particle number, known as energy-damping.

Keeping just the first term on the right hand side of Eq. (3.7) as given by Eq. (3.8a) yields exactly the projected Gross-Pitaevskii equation (PGPE). This corresponds to simulating the interaction of highly-occupied coherent modes, as portrayed by Fig. 3.1(a). The PGPE is formally an energy and number conserving theory sampling the micro-canonical ensemble in equilibrium. It can be used as a non-perturbative approach to describe the dynamics of the \mathcal{C} field, yielding a quantitatively accurate description of finite temperature systems near to equilibrium where the reservoir interaction can be neglected. Numerical implementations of the PGPE are mainly limited to the study of equilibrium solutions of finite temperature systems but there have been numerous forays into dynamical procedures such as the excitation of collective modes and vortex decay [156, 157].

The second term, Eq. (3.8b), describes growth processes arising from the collisions between the coherent and incoherent regions, as shown in Fig. 3.1(b). The interactions from

this term correspond to an exchange in both particle number and energy. We highlight here, that whilst formally the dissipation of Eq. (3.9) should be spatially dependent, a reservoir close to equilibrium maintains a spatially-constant growth rate [141] across the majority of the \mathcal{C} -field [154] and so we take a constant value.

Lastly, the third term Eq. (3.8c) introduces scattering processes, as schematically displayed in Fig. 3.1(c). These interactions are number-conserving and correspond to an exchange in energy exclusively. We have introduced $M(\mathbf{r} - \mathbf{r}')$ as the amplitude of collisions involved in the scattering processes. It is apparent from the final term in Eq. (3.8c) that the noise term is multiplicative in ψ_C and nonlocal. As such, the numerical implementation of the full SPGPE, or the energy damped SPGPE, is highly non-trivial. Here we refer to the energy-damped SPGPE [141] as one including contributions Eq. (3.8a) and Eq. (3.8c), such that $(S)d\Psi_C = d\Psi_C(\mathbf{r})|_H + (S)d\Psi_C(\mathbf{r})|_S$, which has been previously used for the study of bright solitons [132]. The effects of the inclusion of the scattering processes are negligible at equilibrium and small-amplitude in general [158], so one may omit them or instead disable interaction with the thermal reservoir before numerically studying dynamical processes by setting $\gamma = 0$ prior to dynamical evolution.

3.1.2 Simple growth stochastic projected Gross-Pitaevskii equation

Whilst there has been success in a full numerical implementation of the SPGPE [127, 137, 154, 159], the majority of numerical endeavours omit the scattering term, assuming it to be negligible. Fortunately, typical values of $M(\mathbf{r} - \mathbf{r}')$ are indeed small at equilibrium. Neglecting the scattering term allows us to define the *simple growth* SPGPE which is easier to numerically implement. With this in mind, and ignoring the scattering processes associated with Eq. (3.8c), we are able to formulate the Langevin field equation

$$\begin{aligned} d\Psi_C(\mathbf{r}) = \hat{\mathcal{P}}_C & \left\{ -\frac{i}{\hbar} \left(-\frac{\hbar^2}{2m} \nabla^2 + V_{\text{tr}}(\mathbf{r}) + g|\Psi_C(\mathbf{r})|^2 \right) \Psi_C(\mathbf{r}) dt \right. \\ & \left. + \frac{\gamma}{\hbar} \left[\mu - \left(-\frac{\hbar^2}{2m} \nabla^2 + V_{\text{tr}}(\mathbf{r}) + g|\Psi_C(\mathbf{r})|^2 \right) \right] \Psi_C(\mathbf{r}) dt + d\xi_\gamma(\mathbf{r}, t) \right\}. \end{aligned} \quad (3.14)$$

This modified SPGPE describes a finite temperature condensate coupled to a non-condensed thermal cloud and is of the form of a PGPE with additional dissipation and noise terms. Now, with the additional presence of a projector we have an equation which is in functional equivalence to the SGPE of Duine and Stoof [134–136, 160], as is formally documented by Proukakis and Jackson [34]. In fact, Proukakis *et al* [150] concluded that the densities and correlation functions of the two approaches, when numerically applied to a 1D Bose gas in a harmonic trap, recovered near-identical results up to a small difference in the thermal wings. With Eq. (3.14) we have now defined a useful stochastic numerical tool: individual runs of this equation correspond with a single experimental realisation and contain

information about the fluctuations [153, 161]. Physical observables are obtained through averaging over numerous simulations to remove noise inherent to the stochasticity of the equation. The first numerical implementation of this equation was performed by Stoof and Bijlsma [135] in an attempt to model the phenomenon of reversible condensation formation experimentally performed at MIT by Stamper-Kurn *et al* [162]. Subsequent implementations have diversified into a number of avenues such as numerical studies of coherence [163, 164], atom lasers [165], atom chip dynamics [166] and potential atomtronic devices [167].

3.1.3 Addressing the ultraviolet catastrophe

A major drawback of \mathcal{C} -field methods in general is that they assume a high occupation in the low-energy modes, effectively treating the quantum Bose operator as a classical object. As such, the intrinsic quantised nature of the quantum theory described above is replaced by a continuum of modes, such that the system can be described as a classical wave. In high-energy regimes, this approximation fails spectacularly, and is regarded in the literature as the ultraviolet catastrophe [168, §7]. Whilst modified theories [129] have been proposed to address the ultraviolet divergence through a dynamical constraint of high-energy modes to the Bose-Einstein distribution, we instead adopt a method which will remove high-energy modes and thus propose an alternate theory unaffected by short range interaction details. This is implemented through the splitting of the Bose field operator into a classically treated low-energy coherent part \mathcal{C} and a quantum mechanically treated high energy incoherent part \mathcal{I} via Eq. (3.1). This recasting of the complete field is achieved by projecting out the incoherent modes with the operation

$$\hat{\mathcal{P}}\{f(\mathbf{r})\} = \sum_{n \in \mathcal{C}} \varphi_n(\mathbf{r}) \int d\mathbf{r}' \varphi_n^*(\mathbf{r}') f(\mathbf{r}'), \quad (3.15)$$

such that

$$\hat{\Psi}_{\mathcal{C}}(\mathbf{r}) = \hat{\mathcal{P}}\{\hat{\Psi}(\mathbf{r})\} = \sum_{n \in \mathcal{C}} \hat{a}_n \varphi_n(\mathbf{r}), \quad (3.16)$$

where φ_n are the eigenvectors of the single-particle Hamiltonian for modes within the \mathcal{C} -field with eigenvalues $\epsilon_{\mathcal{C}}$. This separation occurs at a carefully selected cutoff value such that all modes in the coherent region are treated as classical objects and those above are treated as quantum objects forming a static thermal reservoir. Therefore we can treat $\hat{\Psi}_{\mathcal{C}}$ as a classical field and neglect the discrete nature of the atoms within the \mathcal{C} -field. The dynamics of the \mathcal{C} -field can hence be determined via a phase-space correspondence that maps the equations of motion for $\hat{\Psi}_{\mathcal{C}}$ to equations of motion for Ψ [127]. In this formalism, we can view Ψ as a stochastic sample of the \mathcal{C} -field's approximate phase-space distribution. In practice, we can treat Ψ as the outcome of a single experimental run

and recover expectations of physical observables through ensemble averaging over many independently realised trajectories. By setting the Bose-Einstein distribution to unity and solving for the energy, we find the appropriate cutoff such that the highest energy mode in the classical field correspondingly has occupation of order unity. In this choice, the cutoff is given by

$$\epsilon_{\text{cut}} = \mu + k_B T \log(2). \quad (3.17)$$

Schemes for choosing a cutoff vary across the literature, however each choice requires that physical observables calculated in the system are minimally sensitive to the value chosen [169]. Whilst the SPGPE reduces to the PGPE theory at low temperatures, care should be taken for simulations at low temperature when deciding a cutoff value. Using the protocol of Eq. (3.17), the cutoff reduces to a value of μ at low temperature and the projector may remove enough modes such that the healing length can no longer be accurately resolved. As such, we adopt the cutoff

$$\epsilon_{\text{cut}} = \max\{\mu + k_B T \log(2), 2\mu\} \quad (3.18)$$

which combines the well defined method of setting the occupation to unity at the cutoff, with an approach designed to minimise sporadic values when calculating observables at low temperature. Besides the approach of a grid-spacing enforced cutoff, a value of $\approx 2\mu$ is widely adopted in other theoretical works using the SPGPE [69, 151, 156, 157].

3.1.4 Hybrid trapping geometry

In Part II of this thesis, we focus on the specific trapping geometry of an in-plane box trap under transverse confinement. Before proceeding further, we take this opportunity to formally introduce the specific trapping we employ whilst considering the effects of dimensionality on our equilibrated system. We choose, as a reference, the experimentally viable trapping geometry employed by the group of Dalibard. To achieve a quasi-2D geometry, this group has devised an apparatus coined as an ‘‘optical accordion’’ which enforces strong transverse harmonic trapping along the z -direction whilst providing a homogeneous box trap along the xy -plane. A schematic of this apparatus is shown in Figure 3.2. This apparatus includes a pairing of Digital Micro-mirror Devices (DMDs), which may be dynamically configured, allowing time-dependent alteration of the confining potential and thus an easy implementation of an excitation protocol, as will become important later in this thesis. To emulate this apparatus, we begin with a gas of ^{87}Rb atoms trapped in a box-harmonic hybrid potential (see Section 2.3 of [171]) given by

$$V(\mathbf{r}) = V_{\text{box}}(x, y) + \frac{1}{2}m \left(\frac{\omega_{\text{ref}}}{A}\right)^2 z^2, \quad (3.19)$$

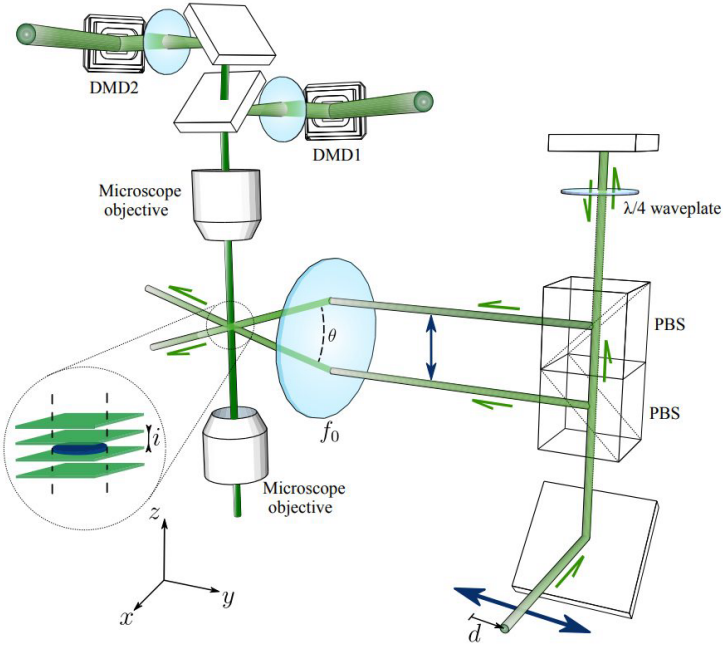


Figure 3.2: [Reprinted figure with permission from [170] Copyright (2022) by the American Physical Society]. Sketch of the optical accordion configuration. By moving the initial beam by a distance d , the angle between the two final beams θ can be adjusted, thus resulting in a configurable trapping frequency ω_z along the transverse direction. In-plane trapping can then be configured using DMD's. In this case, two are shown for an optional perturbation to be added in tandem with the confining box, as we will perform in Chapter 5.

where $\omega_{\text{ref}} = 2\pi \times 4.594 \text{ kHz}$ as in the experiment of Ville *et al* [26] and serves as the reference trapping frequency for the 2D case. Here, $V_{\text{box}}(x, y)$ is zero within a hard-walled rectangular planar box of size $L_x = 38\mu\text{m}$, $L_y = 30\mu\text{m}$, and very large outside. To systematically control the tightness of the harmonic confinement, we have introduced a dimensionless parameter Λ , such that the transverse trapping frequency is

$$\omega_z = \omega_{\text{ref}}/\Lambda \quad (3.20)$$

and one can define a typical transverse length $\ell_z = \sqrt{\hbar/m\omega_z} = \sqrt{\Lambda}l_{\text{ref}}$, where in our case $l_{\text{ref}} = \sqrt{\hbar/m\omega_{\text{ref}}} = 0.1592 \mu\text{m}$. Finally, the scattering length we employ is $a_s = 5.09 \text{ nm}$, which implies $g = (0.064 \mu\text{m})\hbar^2/m$. This interaction strength is chosen such that in the 2D limit ($\Lambda = 1$) it reduces to the dimensionless value $\tilde{g}_{2D} = (m/\hbar^2) g_{2D} = \sqrt{8\pi}a_s/l_{\text{ref}} = 0.16$ equivalent to the one used in the aforementioned study. The box of size L_x, L_y is embedded within a computational domain of size $\mathcal{L}_x = 43\mu\text{m}$, $\mathcal{L}_y = 35\mu\text{m}$. Due to our use of plane-wave modes in the computational basis we employ (discussed at length in Appendix B.2), this embedding removes unwanted periodicity within the system. We reserve discussion of the physics of the Bose gas within the hybrid trap until Section 4.2. Later, in Chapter 5

we will also explore the addition of a perturbation to this trapping potential, in order to subsequently probe the sound speed.

3.1.5 Numerical implementation of the simple growth SPGPE

Having established the analytical formulation behind the stochastic (projected) Gross-Pitaevskii equation, we now proceed to demonstrate the numerical implementation of this theory. Implementations of the SPGPE have been used extensively to study dilute ultracold Bose gases both dynamically [153, 172–175] and at equilibrium [28, 69, 71, 154, 157, 158, 176–186]. In addition, it has been used with remarkable success to match and quantitatively describe experimental data [27, 151, 187, 188]. With simplified notation, the equation we consider is

$$i\hbar \frac{\partial \Psi(\mathbf{r}, t)}{\partial t} = \mathcal{P} \left\{ (1 - i\gamma) \left[-\frac{\hbar^2 \nabla^2}{2m} + V(\mathbf{r}) + g_{3D} |\Psi(\mathbf{r}, t)|^2 - \mu \right] \Psi(\mathbf{r}, t) + \eta(\mathbf{r}, t) \right\}, \quad (3.21)$$

where $\Psi(\mathbf{r}, t)$ represents the order parameter for the lowest, coherent system modes in the C -field. The complex gaussian white noise $\eta(\mathbf{r}, t)$ has correlations of the form

$$\langle \eta^*(\mathbf{r}, t) \eta(\mathbf{r}', t') \rangle = 2\hbar\gamma k_B T \delta(\mathbf{r} - \mathbf{r}') \delta(t - t'), \quad (3.22)$$

where $\langle \dots \rangle$ indicates we are averaging over different realisations of noise. We can then consider this equation as a dissipative Gross-Pitaevskii equation with damping (from a static thermal cloud) determined at a rate governed by γ . Whilst the value of γ should theoretically depend on both position and time, given the uniform nature of potentials we consider, we may ignore the temporal dependence. In fact, neglecting spatial dependence is found to offer no significant alteration to the dynamics, as previously reported in the literature [189]. Since our use of the SPGPE is reserved to the case of calculating equilibrium configurations, we use a dissipation value of $\gamma = 0.05$, which is somewhat higher but indeed of the same order of magnitude than those typically used for SPGPE simulations [27, 28, 151, 190, 191]. Moreover, since we are not interested in the trajectory to equilibrium and instead the equilibrium solution itself, this provides a simple way to accelerate our numerical procedure. We introduce the characteristic time

$$\tau_\gamma = \hbar/\mu\gamma, \quad (3.23)$$

which acts as a reference timescale to systematically pick an equivalent length of time across dimensionality for the simulations we perform to equilibrate. (A detailed description of the preparation of a given equilibrium state is provided in Appendix B.1.) To be clear, as we vary the dimensionality parameter Λ , the system size is altered. If the chemical potential were to remain constant, then we would be comparing systems with

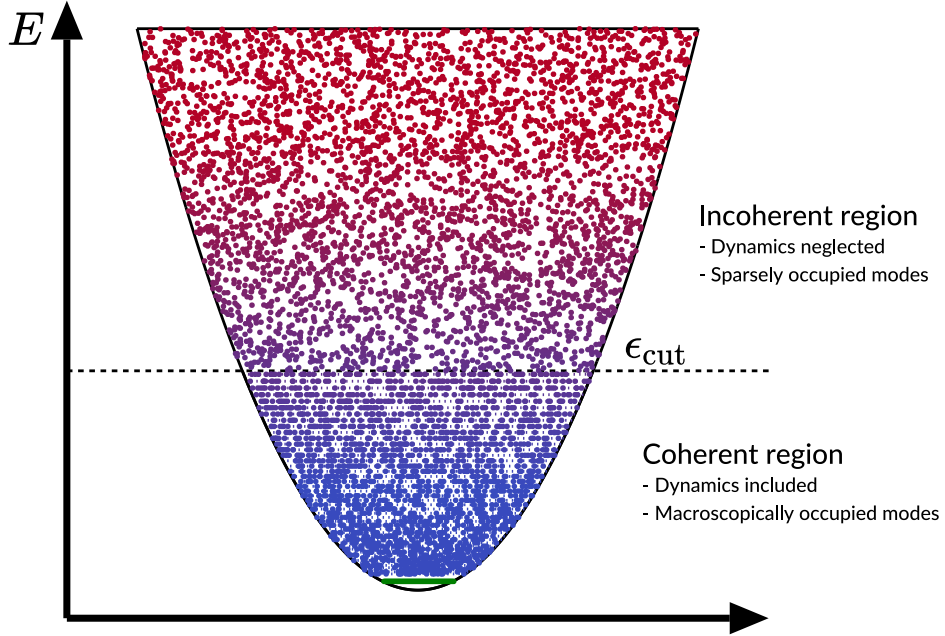


Figure 3.3: Schematic of the \mathcal{C} -field coherent region and \mathcal{I} -field incoherent region for a harmonically trapped Bose gas. Modes below cutoff are within the \mathcal{C} -field and are included in the dynamics of the SPGPE theory. This is in contrast to the sparsely occupied higher energy modes contained within the \mathcal{I} -field whose contribution to the dynamics are ignored. We display the lowest energy accessible mode, known as the condensate mode, in green.

vastly different atomic densities. Instead, we systematically adjust the chemical potential with dimensionality in order to maintain either the central atomic density or the Bogoliubov sound speed, as discussed in Section 4.3. In this way, our characteristic timescale τ_γ remains appropriate across dimensionality.

3.1.6 Numerical implementation of the projector

At every timestep during our simulation, we project the complete field using the projection operator defined by Eq. (3.16). The use of a projector allows the implementation of the high-energy cutoff discussed previously. Formally, this allows a dynamical description of only the low-energy system of interest, where we remove thermal atoms and consider them part of the thermal reservoir. A schematic of this process is displayed in Fig. 3.3. The cutoff ϵ_{cut} may be numerically implemented by zeroing all modes outside a sphere in momentum space of radius $k_{\text{cut}} = \sqrt{2m\epsilon_{\text{cut}}}$. When simulating the SPGPE using spectral methods, we need to be sure that the domains of our wavevectors are large enough such that we do not introduce artificial numerical aliasing. To negate this, following [127], for a 3D numerical box of size L one might employ a condition twice as strict as the Nyquist

sampling requirement such that the grid resolution

$$d\mathbf{r} = \frac{L}{N_{x,y,z}} \leq \frac{\pi}{2k_{\text{cut}}}. \quad (3.24)$$

In this way, we can be certain the relevant modes for the system are accessible, prior to the projection operator. In our numerical scheme, we will enforce this domain size requirement along the plane which is solved in the plane wave basis. However, as is discussed in Appendix B, along the transverse direction we will utilise a Hermite-Gauss basis. Instead, along the transverse direction, we take care to include enough modes to accurately capture the occupied modes of the transverse direction in the modified basis and enforce the grid resolution $n_z \geq (2\epsilon_{\text{cut}} - 1)/(2\hbar\omega_z)$ for harmonic trapping of strength ω_z . Since we will be investigating the effects of dimensionality in later sections, we must consider the effects of strong anisotropic harmonic trapping. To produce a quasi-2D condensate, we enforce strong anisotropic harmonic trapping solely along the z -direction in tandem with a hard-wall box trap along the plane. This causes a separation of energy scales, such that $\hbar\omega_z \gg (\pi^2\hbar^2/2m)(n_x^2/L_x^2 + n_y^2/L_y^2)$ where ω_z is the harmonic trapping frequency in the transverse direction and L_x, L_y are the box sizes along the planar directions. As such, it may be the case in strongly dimensionally suppressed systems that the projector is only enforced along the planar direction where modes are denser as opposed to the sparse harmonic energy levels. This can be understood when we consider the energy landscape of two model systems. In Fig. 3.4(a) we visualise the distribution of modes for the first 10 quantum numbers in x and y for a system with the same parameters as previously defined in our 2D system ($\Lambda = 1$). Whereas in Fig. 3.4(b) we consider the energy landscape for modes up to $\mathbf{n} = (30, 30, 10)$ for each dimensionality. Here we observe a staircase function at low dimensionalities with strong harmonic trapping due to the separation of energy scales between the normal and transverse directions. As dimensionality increases, these scales become comparable and a smooth energy landscape is recovered towards our 3D limit of $\Lambda = 50$.

3.2 Incoherent atomic density in the SPGPE

Despite the neglect of dynamics within the \mathcal{I} -field, as is standard within the SPGPE formalism [34, 127, 141], we should still account for atoms projected out when calculating numerical properties of the system. We want to calculate the number of incoherent atoms above an energy cutoff ϵ_{cut} in the same hybrid trap as prescribed in Section 3.1.4. In the SPGPE the chemical potential is fixed and the total number of atoms is determined as the sum of the coherent contribution N_C coming from the \mathcal{C} -field, solution of the SPGPE, and the incoherent contribution $N_{\mathcal{I}}$. The latter is estimated assuming that

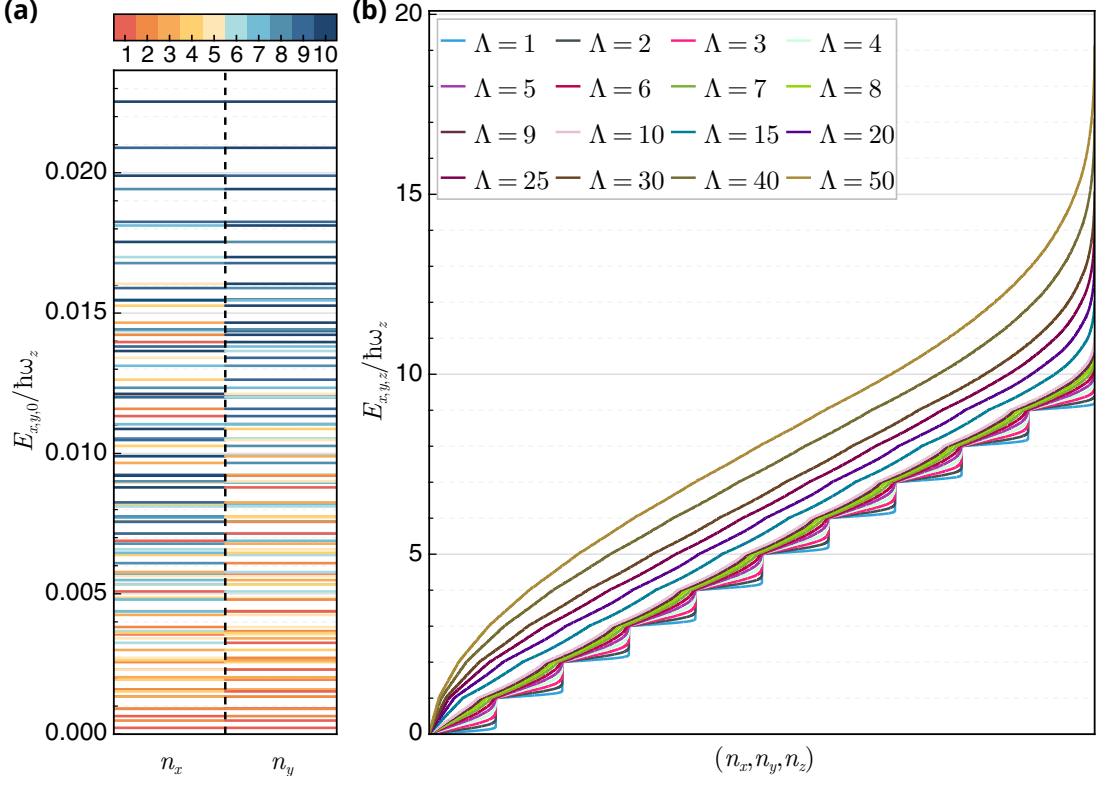


Figure 3.4: For the system with $L_x = 38\mu\text{m}$, $L_y = 30\mu\text{m}$ and $\omega_{\text{ref}}/(2\pi) = 4594\text{Hz}$ and ignoring the zero-point energy we plot: (a) Energy for each accessible modes up to $\mathbf{n} = (10, 10, 0)$, colour coded by the quantum numbers in x and y , normalised to the transverse energy scale $\hbar\omega_z$ for $\Lambda = 1$. (b) Energies for the accessible modes up to $\mathbf{n} = (30, 30, 10)$ sorted in ascending order for each of the considered dimensionalities, normalised by $\hbar\omega_z$.

the incoherent atoms occupy the single-particle states of an ideal gas in the same trap with mean occupation number at equilibrium given by the Bose-Einstein distribution: $N_{\mathcal{I}} = \sum_{E > \epsilon_{\text{cut}}} 1 / \{\exp[(E - \mu)/k_B T] - 1\}$. First, let us shift the scale of energy in order to remove the zero-point energy $\hbar\omega_z/2$. This must be done consistently also for the chemical potential and the cutoff energy. Then

$$N_{\mathcal{I}} = \sum_{\tilde{E}_{\mathbf{n}} > \tilde{\epsilon}_{\text{cut}}} \frac{1}{\exp[(\tilde{E}_{\mathbf{n}} - \tilde{\mu})/k_B T] - 1} , \quad (3.25)$$

with

$$\tilde{E}_{\mathbf{n}} = \frac{\pi^2 \hbar^2}{2m} \left(\frac{n_x^2}{L_x^2} + \frac{n_y^2}{L_y^2} \right) + n_z \hbar\omega_z = E_{xy} + n_z \hbar\omega_z , \quad (3.26)$$

$\tilde{\mu} = \mu - (1/2)\hbar\omega_z$ and $\tilde{\epsilon}_{\text{cut}} = \epsilon_{\text{cut}} - \hbar\omega_z/2$. In the following, we restrict our notation and choose the cutoff determined by Eq. (3.17), but pause here to specify that there is nothing special about this value and we are free to choose another. With the shifted chemical

potential $\tilde{\mu}$, this becomes

$$\tilde{\epsilon}_{\text{cut}} = \tilde{\mu} + k_B T \ln 2 . \quad (3.27)$$

The sum has to be performed over the values of n_x, n_y and n_z such that $\tilde{E}_{\mathbf{n}} > \tilde{\epsilon}_{\text{cut}}$. We assume that, for each n_z , the spectrum of states with different n_x and n_y is dense enough to replace the sums with an integral over the energy. For each n_z the states with different E_{xy} form a band, which starts from $n_z \hbar \omega_z$ and has constant density of states $m L_x L_y / (2\pi \hbar^2)$, as for a 2D gas. Hence one can write

$$N_{\mathcal{I}} = \frac{m L_x L_y}{2\pi \hbar^2} \sum_{n_z=0}^{\infty} \int_{E_{\min}}^{\infty} dE_{xy} \frac{1}{\exp[(E_{xy} + n_z \hbar \omega_z - \tilde{\mu})/k_B T] - 1} , \quad (3.28)$$

where

$$E_{\min} = \begin{cases} \tilde{\epsilon}_{\text{cut}} - n_z \hbar \omega_z & \text{for } \tilde{\epsilon}_{\text{cut}} > n_z \hbar \omega_z \\ 0 & \text{for } \tilde{\epsilon}_{\text{cut}} \leq n_z \hbar \omega_z . \end{cases} \quad (3.29)$$

Let us introduce the quantities $t = E_{xy}/k_B T$ and $z(n_z) = \exp[(\tilde{\mu} - n_z \hbar \omega_z)/k_B T]$. The incoherent atom number becomes

$$N_{\mathcal{I}} = \frac{L_x L_y}{\lambda_{\text{dB}}^2} \sum_{n_z=0}^{\infty} \int_{\bar{t}}^{\infty} dt \frac{1}{\frac{e^t}{z(n_z)} - 1} \quad (3.30)$$

where $\bar{t} = E_{\min}/k_B T$. It is convenient to separate the sum into two contributions,

$$N_{\mathcal{I}} = \frac{L_x L_y}{\lambda_{\text{dB}}^2} \left(\sum_{n_z=0}^{\bar{n}_z-1} \int_{\bar{t}}^{\infty} dt \frac{1}{\frac{e^t}{z(n_z)} - 1} + \sum_{n_z=\bar{n}_z}^{\infty} \int_0^{\infty} dt \frac{1}{\frac{e^t}{z(n_z)} - 1} \right) , \quad (3.31)$$

where \bar{n}_z is the lowest value of n_z for which $n_z \hbar \omega_z > \tilde{\epsilon}_{\text{cut}}$, that is

$$\bar{n}_z = \lceil \tilde{\epsilon}_{\text{cut}} / \hbar \omega_z \rceil . \quad (3.32)$$

Here, the lower integration limit in the second sum becomes zero in accordance with Eq. (3.29). The integrals in the second sum are thus Bose-Einstein integrals of order $s = 1$, so that

$$N_{\mathcal{I}} = \frac{L_x L_y}{\lambda_{\text{dB}}^2} \left(\sum_{n_z=0}^{\bar{n}_z-1} \int_{\bar{t}}^{\infty} dt \frac{1}{\frac{e^t}{z(n_z)} - 1} - \sum_{n_z=\bar{n}_z}^{\infty} \ln(1 - z(n_z)) \right) . \quad (3.33)$$

while those in the first sum can be calculated numerically (or even analytically as we will see below).

As will be discussed in the following chapter, we fix the chemical potential in the 2D

limit to the value

$$\mu = g_{2D} n_{2D} + \frac{\hbar\omega_z}{2} \quad (3.34)$$

with $n_{2D} = 29 \mu\text{m}^{-2}$ and $g_{2D} = 0.16 \hbar^2/m$. This ensures that the density and the chemical potential in the 2D limit reduce to the experimental values of Ref. [26], which implies that

$$\tilde{\mu} = g_{2D} n_{2D} = (4.64 \mu\text{m}^{-2}) \hbar^2/m. \quad (3.35)$$

As discussed in Section 3.1.4, we recall that the harmonic frequency ω_z is expressed in terms of a reference frequency $\omega_{\text{ref}} = 2\pi \times 4.59 \text{ kHz}$ and a dimensionless parameter Λ determining the tightness of the transverse confinement given by Eq. (3.20). We can define the function

$$\phi_{n_z}(T, \Lambda) = \frac{\tilde{\mu}}{k_B T} - n_z \frac{\hbar\omega_{\text{ref}}}{k_B T \Lambda}, \quad (3.36)$$

such that the fugacity is given by

$$z(n_z) = e^{\phi_{n_z}(T, \Lambda)}. \quad (3.37)$$

In addition, since the shifted cutoff energy is $\tilde{\epsilon}_{\text{cut}} = \tilde{\mu} + k_B T \ln 2$, the lower limit of integration \bar{t} in Eq. (3.33) is expressed as

$$\bar{t}(n_z, T, \Lambda) = \frac{\tilde{\mu} + k_B T \ln 2 - n_z \hbar\omega_z}{k_B T} = \ln 2 + \phi_{n_z}(T, \Lambda) \quad (3.38)$$

and the threshold value of n_z is

$$\bar{n}_z = \lceil (\tilde{\mu} + k_B T \ln 2) \Lambda / \hbar\omega_{\text{ref}} \rceil. \quad (3.39)$$

With these definitions, the incoherent atom number becomes

$$N_{\mathcal{I}} = \frac{mk_B T L_x L_y}{2\pi\hbar^2} \left(\sum_{n_z=0}^{\bar{n}_z-1} \int_{\ln 2 + \phi_{n_z}}^{\infty} dt \frac{1}{e^{t-\phi_{n_z}} - 1} - \sum_{n_z=\bar{n}_z}^{\infty} \ln \left(1 - e^{\phi_{n_z}} \right) \right). \quad (3.40)$$

We note that each integral in the first sum has to be calculated for fixed values of Λ, T and n_z . This means that the function ϕ_{n_z} in the integral behaves as a constant. Thus one can change the variable in $t' = t - \phi_{n_z}$ and write

$$N_{\mathcal{I}} = \frac{mk_B T L_x L_y}{2\pi\hbar^2} \left(\sum_{n_z=0}^{\bar{n}_z-1} \int_{\ln 2}^{\infty} dt' \frac{1}{e^{t'} - 1} - \sum_{n_z=\bar{n}_z}^{\infty} \ln \left(1 - e^{\phi_{n_z}} \right) \right). \quad (3.41)$$

But now the integral does not depend on n_z , and it can be calculated by substitution of

variable, $x = e^{t'}$:

$$\int_{\ln 2}^{\infty} dt' \frac{1}{e^{t'} - 1} = \int_2^{\infty} dx \frac{1}{x(x-1)} = \left[\ln \frac{x-1}{x} \right]_2^{\infty} = \ln 2. \quad (3.42)$$

Hence, the first sum in $N_{\mathcal{I}}$ is just \bar{n}_z times the above integral, and

$$N_{\mathcal{I}} = \frac{mk_B T L_x L_y}{2\pi\hbar^2} \left(\bar{n}_z \ln 2 - \sum_{n_z=\bar{n}_z}^{\infty} \ln \left(1 - e^{\phi_{n_z}} \right) \right), \quad (3.43)$$

or

$$N_{\mathcal{I}} = \frac{L_x L_y}{\lambda_{\text{dB}}^2} \left(\bar{n}_z \ln 2 - \sum_{n_z=\bar{n}_z}^{\infty} \ln \left(1 - e^{\phi_{n_z}} \right) \right). \quad (3.44)$$

A different way to write the prefactor is

$$N_{\mathcal{I}} = \frac{k_B T L_x L_y}{2\pi l_{\text{ref}}^2 \hbar \omega_{\text{ref}}} \left(\bar{n}_z \ln 2 - \sum_{n_z=\bar{n}_z}^{\infty} \ln \left(1 - e^{\phi_{n_z}} \right) \right). \quad (3.45)$$

One can also define the 2D phase-space density of incoherent atoms as $\mathcal{D}_{\mathcal{I}} = \lambda_{\text{dB}}^2 N_{\mathcal{I}} / L_x L_y$ so that

$$\mathcal{D}_{\mathcal{I}} = \bar{n}_z \ln 2 - \sum_{n_z=\bar{n}_z}^{\infty} \ln \left(1 - e^{\phi_{n_z}} \right). \quad (3.46)$$

These quantities can be calculated for each T and Λ . Note also that ϕ_{n_z} and \bar{n}_z can be expressed as follows:

$$\begin{aligned} \phi_{n_z}(T, \Lambda) &= \left(\frac{\tilde{\mu}}{\hbar\omega_{\text{ref}}} - \frac{n_z}{\Lambda} \right) \frac{\hbar\omega_{\text{ref}}}{k_B T} \\ &= \left(\frac{(4.64\mu\text{m}^{-2})\hbar}{m\omega_{\text{ref}}} - \frac{n_z}{\Lambda} \right) \frac{\hbar\omega_{\text{ref}}}{k_B T} \\ &= \left((4.64\mu\text{m}^{-2})\ell_{\text{ref}}^2 - \frac{n_z}{\Lambda} \right) \frac{\hbar\omega_{\text{ref}}}{k_B T}, \end{aligned} \quad (3.47)$$

with $\ell_{\text{ref}} = \sqrt{\hbar/m\omega_{\text{ref}}}$, and

$$\begin{aligned} \bar{n}_z(T, \Lambda) &= \lceil \left(\frac{\tilde{\mu}}{\hbar\omega_{\text{ref}}} + \frac{k_B T}{\hbar\omega_{\text{ref}}} \ln 2 \right) \Lambda \rceil \\ &= \lceil \left(\frac{(4.64\mu\text{m}^{-2})\hbar^2}{m\hbar\omega_{\text{ref}}} + \frac{k_B T}{\hbar\omega_{\text{ref}}} \ln 2 \right) \Lambda \rceil \\ &= \lceil \left((4.64\mu\text{m}^{-2})\ell_{\text{ref}}^2 + \frac{k_B T}{\hbar\omega_{\text{ref}}} \ln 2 \right) \Lambda \rceil. \end{aligned} \quad (3.48)$$

With the reference frequency ω_{ref} we can define a reference temperature $T_{\text{ref}} = \hbar\omega_{\text{ref}}/k_B$ and introduce a relative temperature $T' = T/T_{\text{ref}}$. Also, let us call a and b the dimension-

less constants $(4.64\mu\text{m}^{-2})\ell_{\text{ref}}^2$ and $L_xL_y/(2\pi l_{\text{ref}}^2)$, respectively. Thus

$$\phi_{n_z}(T', \Lambda) = \left(a - \frac{n_z}{\Lambda}\right) \frac{1}{T'} \quad (3.49)$$

$$\bar{n}_z(T', \Lambda) = \lceil (a + T' \ln 2) / \Lambda \rceil \quad (3.50)$$

and so finally

$$N_{\mathcal{I}}(T', \Lambda) = bT' \left(\bar{n}_z \ln 2 - \sum_{n_z=\bar{n}_z}^{\infty} \ln \left(1 - e^{\phi_{n_z}} \right) \right). \quad (3.51)$$

For the trapping configuration prescribed within Section 3.1.4, we can calculate the relevant quantities, yielding

$$\ell_{\text{ref}} = \sqrt{\frac{\hbar}{m\omega_{\text{ref}}}} = 0.1592 \times 10^{-6} \text{ m} = 0.1592 \text{ } \mu\text{m}, \quad (3.52a)$$

$$T_{\text{ref}} = \frac{\hbar\omega_{\text{ref}}}{k_B} = 22.03 \times 10^{-8} \text{ K} = 220.3 \text{ nK}, \quad (3.52b)$$

$$a = \frac{g_{2\text{D}}n_{2\text{D}}}{\hbar\omega_{\text{ref}}} = (4.64\mu\text{m}^{-2})\ell_{\text{ref}}^2 = 0.1176, \quad (3.52c)$$

$$b = \frac{L_xL_y}{2\pi l_{\text{ref}}^2} = 7159. \quad (3.52d)$$

It is also useful to introduce the following constants:

$$c_x = \frac{\pi\ell_{\text{ref}}}{L_x} = 1.316 \times 10^{-2} \quad \text{and} \quad c_y = \frac{\pi\ell_{\text{ref}}}{L_y} = 1.667 \times 10^{-2}. \quad (3.53)$$

The analytic result Eq. (3.51) could be compared with the *brute force* numerical summation Eq. (3.25). If we use the cutoff energy as in Eq. (3.17) and the constants of Eq. (3.52) and Eq. (3.53), we can express the latter as

$$N_{\mathcal{I}} = \sum_{n_z=0}^{\infty} \sum'_{n_x, n_y} \left\{ \exp \left[\frac{c_x^2 n_x^2 + c_y^2 n_y^2 + n_z/\Lambda - a}{T'} \right] - 1 \right\}^{-1}, \quad (3.54)$$

where the second sum includes all values of n_x and n_y such that

$$c_x^2 n_x^2 + c_y^2 n_y^2 + n_z/\Lambda - a > T' \ln 2, \quad (3.55)$$

and the normalised temperature $T' = T/T_{\text{ref}}$ has been introduced for simplified notation. Note that, by replacing the inequality with an equality, the mean occupation number becomes 1, which is consistent with the choice of the cutoff energy.

The analytic result of Eq. (3.51) can also be compared with the results that one obtains when the whole spectrum is dense on the scale of $k_B T$. In this limit the sum over n_z ,

together with the ones over n_x and n_y , can be converted into an integral on the energy, as done in Eq. (4.18). The condition that must be satisfied is $k_B T \gg \hbar\omega_z$ or $\Lambda T' \gg 1$. In this case one can write

$$\begin{aligned} N_{\mathcal{I}} &= \frac{mL_x L_y}{2\pi\hbar^3\omega_z} \int_{\tilde{E}_{\text{cut}}}^{\infty} d\tilde{E} \frac{\tilde{E}}{\exp[(\tilde{E} - \tilde{\mu})/k_B T] - 1} \\ &= \frac{mL_x L_y \Lambda k_B^2 T^2}{2\pi\hbar^3\omega_{\text{ref}}} \int_{\bar{t}}^{\infty} dt \frac{t}{\frac{e^t}{z} - 1} \\ &= b\Lambda T'^2 \int_{\bar{t}}^{\infty} dt \frac{t}{\frac{e^t}{z} - 1} \end{aligned} \quad (3.56)$$

with

$$\bar{t} = \frac{\tilde{E}_{\text{cut}}}{k_B T} = \frac{\tilde{\mu}}{k_B T} + \ln 2 = \frac{a}{T'} + \ln 2 \quad (3.57)$$

and the fugacity

$$z = \exp\left(\frac{\tilde{\mu}}{k_B T}\right) = \exp\left(\frac{a}{T'}\right). \quad (3.58)$$

One can then write the same expression in this way:

$$N_{\mathcal{I}} = b\Lambda T'^2 \int_{\frac{a}{T'} + \ln 2}^{\infty} dt \frac{t}{e^{t-a/T'} - 1} \quad (3.59)$$

or

$$N_{\mathcal{I}} = b\Lambda T'^2 \int_{\ln 2}^{\infty} dt \frac{t + a/T'}{e^t - 1}. \quad (3.60)$$

This must coincide with the limit $\Lambda T' \gg 1$ of expression Eq. (3.51), which means that

$$\lim_{\Lambda T' \rightarrow \infty} \left[\bar{n}_z \ln 2 - \sum_{n_z=\bar{n}_z}^{\infty} \ln(1 - e^{\phi_{n_z}}) \right] = \Lambda T' \int_{\ln 2}^{\infty} dt \frac{t + a/T'}{e^t - 1}. \quad (3.61)$$

In either case, the two results must approach each other. An alternative way to write Eq. (3.60) is the following

$$\frac{N_{\mathcal{I}}}{b\Lambda T'} = T' \left(\int_{\ln 2}^{\infty} dt \frac{t}{e^t - 1} + \frac{a}{T'} \int_{\ln 2}^{\infty} dt \frac{1}{e^t - 1} \right) = a \ln 2 + T' \int_{\ln 2}^{\infty} dt \frac{t}{e^t - 1}. \quad (3.62)$$

The last integral is just a number,

$$\Upsilon = \int_{\ln 2}^{\infty} dt \frac{t}{e^t - 1} = 1.0592 \quad (3.63)$$

so that

$$N_{\mathcal{I}} = b\Lambda T'(a \ln 2 + \Upsilon T') \quad (3.64)$$

and the limit Eq. (3.61) can be expressed as

$$\lim_{\Lambda T' \rightarrow \infty} \left[\bar{n}_z \ln 2 - \sum_{n_z=\bar{n}_z}^{\infty} \ln \left(1 - e^{\phi_{n_z}} \right) \right] = \Lambda(a \ln 2 + \gamma T') . \quad (3.65)$$

The difference between the two obtained results for $N_{\mathcal{I}}$ can be appreciated by plotting the function

$$N_f(T') = N_{\mathcal{I}}/(b\Lambda T') \quad (3.66)$$

as in Fig. 3.5. Here, the limit of a dense spectrum is represented by a black dashed straight line: $a \ln 2 + \gamma T'$, and all curves obtained with the discrete spectrum collapse onto this line for large Λ . The figure shows the results for each considered dimensionality in this chapter as given by $\Lambda = \{1, 2, 3, 4, 5, 6, 7, 8, 9, 10, 15, 20, 25, 30, 40, 50\}$, from top to bottom. With the same method one can also calculate the incoherent atom density in the SPGPE.

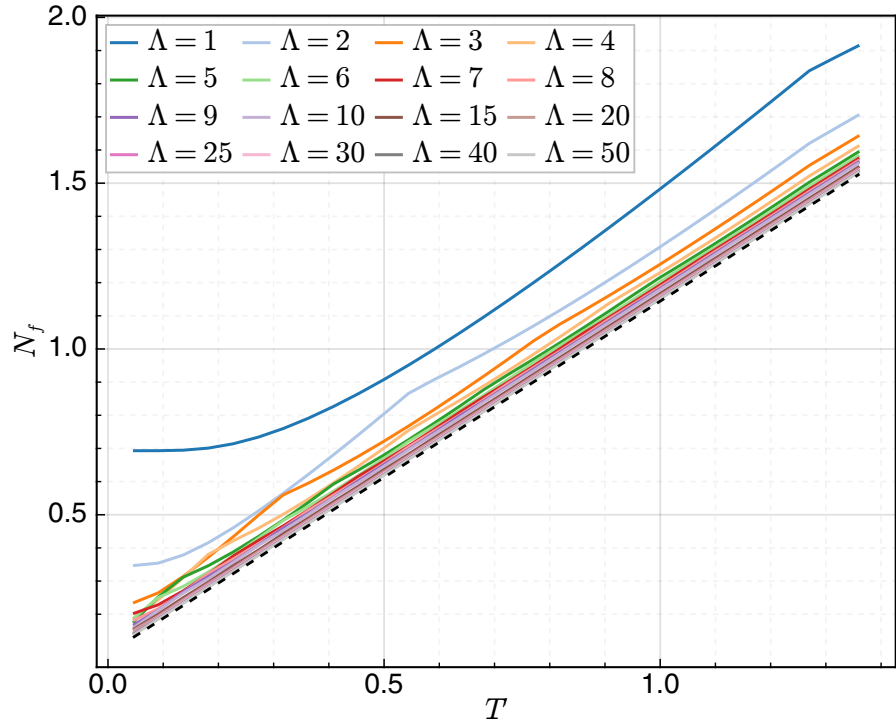


Figure 3.5: The function N_f given by Eq. (3.66) is plotted for each considered value of dimensionality to show the difference in value for the number of atoms between the discrete spectrum and dense spectrum formulations. The dense spectrum result ($\Lambda T' \rightarrow \infty$) is plotted as a dashed black line.

The starting point is the basis of eigenfunctions for a particle in the same hybrid trap, which can be written as

$$\Psi_{\mathbf{n}}(x, y, z) = c \sin \left(\frac{n_x \pi x}{L_x} \right) \sin \left(\frac{n_y \pi y}{L_y} \right) H_{n_z}(z/\ell_z) \exp(-z^2/2\ell_z^2) , \quad (3.67)$$

where c is a normalisation constant, fixing the norm of each state to 1, and H_{n_z} denotes a Hermite polynomial. The harmonic oscillator length is $\ell_z = \sqrt{\hbar/m\omega_z} = \sqrt{\Lambda} \ell_{\text{ref}}$. The meaning of the quantum numbers $\mathbf{n} = (n_x, n_y, n_z)$ is the same as in Eq. (A.27). Each state is populated according to the Bose-Einstein distribution Eq. (A.28). Hence the density associated to the incoherent atoms above the cutoff energy, treated as an ideal gas, can be estimated as

$$n_{\mathcal{I}}(x, y, z) = \sum_{\tilde{E}_{\mathbf{n}} > \tilde{\epsilon}_{\text{cut}}} \frac{|\Psi_{\mathbf{n}}(x, y, z)|^2}{\exp[(\tilde{E}_{\mathbf{n}} - \tilde{\mu})/k_B T] - 1}, \quad (3.68)$$

where all quantities entering this expression are the same as in Eq. (3.25). Ignoring interference effects in the sum of wavefunctions is consistent with the assumption that the states above the cutoff energy are incoherent and the effects of the relative phase vanish after configuration averages. The spatial integral of this density gives the incoherent atom number $N_{\mathcal{I}}$. We can also assume that the spectrum is dense in n_x and n_y , such that all \sin^2 functions sum up to a constant areal density along x and y , except for negligible boundary effects. The sum over n_x and n_y can be replaced with an integral over the energy, introducing the 2D density of state as in Eq. (3.28):

$$n_{\mathcal{I}}(z) = \frac{m}{2\pi\hbar^2} \sum_{n_z=0}^{\infty} |\psi_{n_z}(z)|^2 \int_{E_{\min}}^{\infty} dE_{xy} \frac{1}{\exp[(E_{xy} + n_z \hbar \omega_z - \tilde{\mu})/k_B T] - 1}, \quad (3.69)$$

where the wavefunction

$$\psi_{n_z}(z) = c_{n_z} H_{n_z}(z/\ell_z) \exp(-z^2/2\ell_z^2) \quad (3.70)$$

depends on z only and has norm 1 if

$$c_{n_z} = [\sqrt{\pi} 2^{n_z} n_z! \ell_z]^{-1/2}. \quad (3.71)$$

Following the same procedure used after Eq. (3.28), one can derive the expression

$$n_{\mathcal{I}}(z) = \frac{mk_B T}{2\pi\hbar^2} \left(\sum_{n_z=0}^{\bar{n}_z-1} |\psi_{n_z}(z)|^2 \int_{\bar{t}}^{\infty} dt \frac{1}{\frac{e^t}{z(n_z)} - 1} - \sum_{n_z=\bar{n}_z}^{\infty} |\psi_{n_z}(z)|^2 \ln(1 - z(n_z)) \right). \quad (3.72)$$

As before, we can also use the expressions of the chemical potential and the cutoff energy of our SPGPE equation and write

$$n_{\mathcal{I}}(z) = \frac{mk_B T}{2\pi\hbar^2} \left(\sum_{n_z=0}^{\bar{n}_z-1} |\psi_{n_z}(z)|^2 \ln 2 - \sum_{n_z=\bar{n}_z}^{\infty} |\psi_{n_z}(z)|^2 \ln(1 - e^{\phi_{n_z}}) \right), \quad (3.73)$$

or

$$n_{\mathcal{I}}(z) = \frac{bT'}{L_x L_y} \left(\sum_{n_z=0}^{\bar{n}_z-1} |\psi_{n_z}(z)|^2 \ln 2 - \sum_{n_z=\bar{n}_z}^{\infty} |\psi_{n_z}(z)|^2 \ln (1 - e^{\phi_{n_z}}) \right), \quad (3.74)$$

with

$$\phi_{n_z} = \left(a - \frac{n_z}{\Lambda} \right) \frac{1}{T'} \quad \text{and} \quad \bar{n}_z = \lceil (a + T' \ln 2) \Lambda \rceil. \quad (3.75)$$

Note that the Hermite polynomial vanishes in $z = 0$ if n_z is an odd integer. This implies that the incoherent density in the $z = 0$ plane is

$$n_{\mathcal{I}}(0) = \frac{bT'}{L_x L_y} \left(\sum_{n_z=0}^{\bar{n}_z-1} c_{n_z}^2 (H_{n_z}(0))^2 \ln 2 - \sum_{n_z=\bar{n}_z}^{\infty} c_{n_z}^2 (H_{n_z}(0))^2 \ln (1 - e^{\phi_{n_z}}) \right) \quad (3.76)$$

where the sums give non-zero contributions only for even values of n_z . Hence

$$n_{\mathcal{I}}(0) = \frac{bT'}{\sqrt{\pi} L_x L_y \ell_z} \left(\sum_{n_z=0}^{\bar{n}_z-1} \frac{(H_{n_z}(0))^2 \ln 2}{2^{n_z} n_z!} - \sum_{n_z=\bar{n}_z}^{\infty} \frac{(H_{n_z}(0))^2}{2^{n_z} n_z!} \ln (1 - e^{\phi_{n_z}}) \right) \quad (3.77)$$

or

$$n_{\mathcal{I}}(0) = \frac{bT'}{\sqrt{\pi \Lambda} L_x L_y \ell_{\text{ref}}} \left(\sum_{n_z=0}^{\bar{n}_z-1} \frac{(H_{n_z}(0))^2 \ln 2}{2^{n_z} n_z!} - \sum_{n_z=\bar{n}_z}^{\infty} \frac{(H_{n_z}(0))^2}{2^{n_z} n_z!} \ln (1 - e^{\phi_{n_z}}) \right). \quad (3.78)$$

This quantity is plotted as a function of normalised temperature for a number of different dimensionalities, as indicated in Fig. 3.6. It is worth noticing here, that the dependence on Λ is very weak with the largest deviation exhibited for the lowest dimensionality we consider $\Lambda = 1$ corresponding to the 2D limit. Now, considering the full transverse profile for the thermal atoms, we can see a clearer deviation in the density profiles of the above-cutoff atoms. Fig. 3.8 shows the incoherent density $n_{\mathcal{I}}(z)$ as a function of z/ℓ_z for $T' = 0.45$ and each value of $\Lambda \in [1, 50]$ that we consider, from the narrower to the broader. The values at $z = 0$ are the same as given in the previous plot. We also highlight that the incoherent atom number $N_{\mathcal{I}}$ can be roughly estimated by replacing each curve with a rectangle of height $n_{\mathcal{I}}(0)$ and width of the order of $z_{1/2}/\ell_z$ where $z_{1/2}$ is where the density is half its central value. The area of such a rectangle, multiplied by two (the density extends symmetrically on the left of $z = 0$) and by the volume $L_x L_y \ell_z$, reasonably approximates the exact result Eq. (3.51).

It is worth highlighting that the above-cutoff density $n_{\mathcal{I}}$ must not be confused with the “thermal” (or non-condensate) gas density as usually defined in 3D Bose gases when a condensate is present. The non-condensate density along the transverse direction $n_{nc}(z)$ can be estimated as the total density $n(z)$ minus the density $n_0(z)$ of the atoms in the condensate i.e., the eigenstate with the largest eigenvalue in the Penrose-Onsager diag-

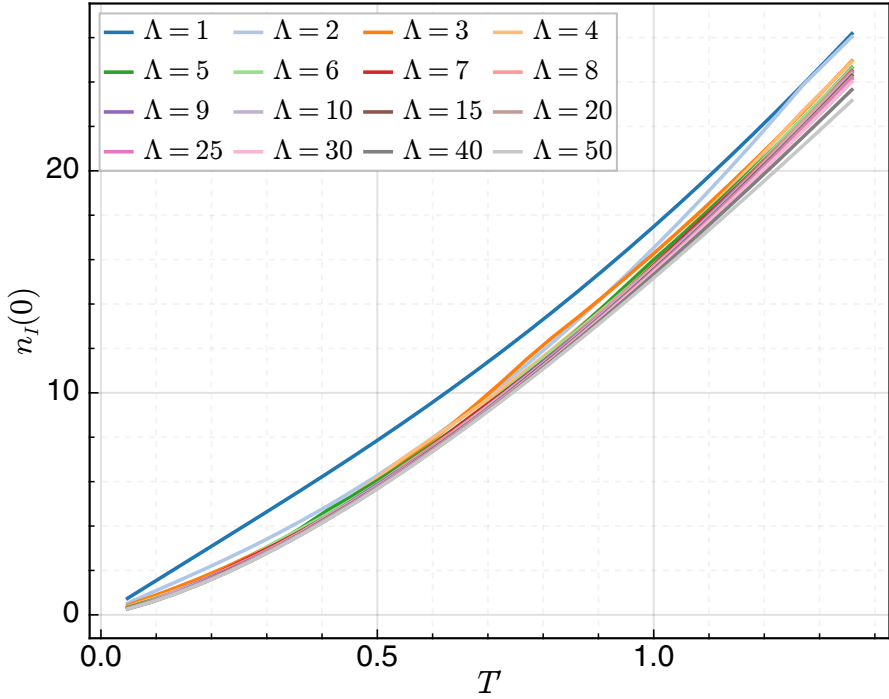


Figure 3.6: Central transverse density of the thermal above-cutoff atoms in the \mathcal{I} -field for various values of the dimensionality parameter Λ (as indicated by the legend) plotted as a function of normalised temperature T' .

nalisation of the one-body density matrix, as later discussed in Section 4.5.1. We stress that the non-condensate density contains contributions from above-cutoff atoms such that

$$n_{\text{nc}}(z) = n_C(z) + n_{\mathcal{I}}(z) - n_0(z). \quad (3.79)$$

Such a thermal density takes contributions from both the \mathcal{C} -field below and the incoherent states above the cutoff. Two examples are shown in Fig. 3.7 at temperatures close to the phase transition for two different values of Λ .

3.2.1 Density normalisation across dimensionality through tuning of the chemical Potential

Through the SPGPE, control of the system is facilitated by a careful choice of two parameters, namely the chemical potential μ and the temperature T . In defining values for these quantities, we can design specific conditions for the thermal cloud. This incoherent cloud then exchanges particles and energy with the condensed field, corresponding to a specific equilibration configuration for those conditions. Whilst equilibration is stochastic in nature, a careful choice in the chemical potential can be used to ensure an approximate atom number in our equilibrated system.

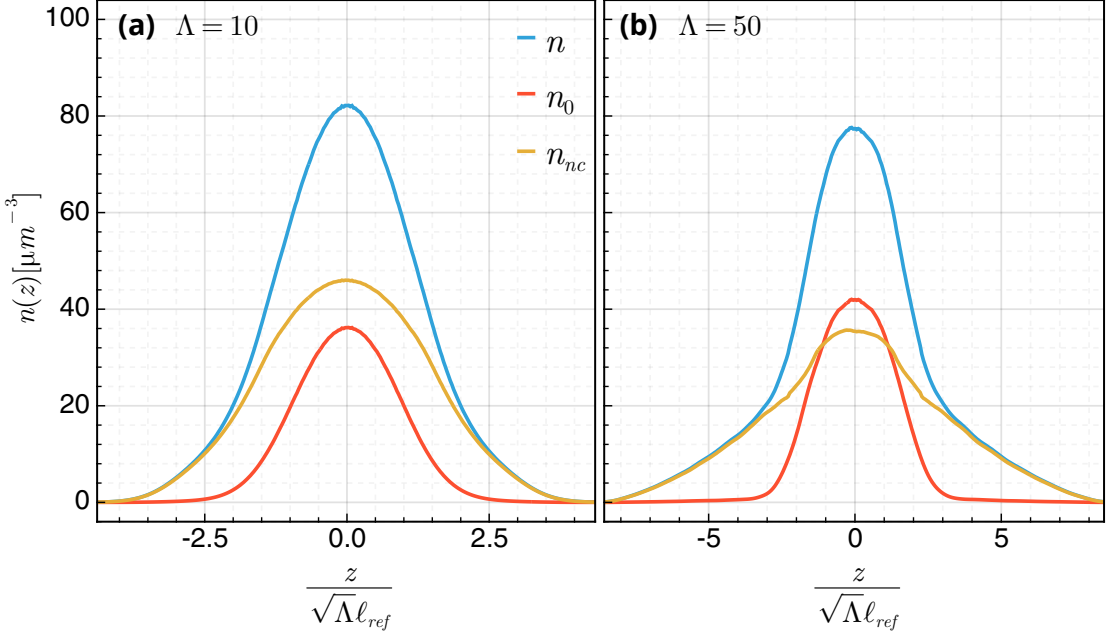


Figure 3.7: Total (n), condensate (n_0) and non-condensate ($n_{nc} = n - n_0$) density profiles along the transverse direction plotted in blue, red and yellow respectively for a quasi-2D (a) ($\Lambda = 10$) and 3D (b) ($\Lambda = 50$) trapping geometry at temperature $T=200nK$, for which $T/T_c = 0.83$ and $T/T_c = 0.75$ respectively.

Our simulations evolve from the initial condition $\psi(\mathbf{r}) = 0$, with a random realisation of the initial noisy field $\eta(\mathbf{r})$. This is akin to an input condition where all atoms possess initial energy larger than the cutoff energy ϵ_{cut} . These atoms then enter the coherent region at a rate governed by γ , which describes the collisional rate between atoms, until the gas saturates at thermal equilibrium. Our desire is to ensure an approximately equivalent total atomic density across various dimensionalities. To estimate the value of μ to generate N atoms in our equilibrated coherent system at a dimensionality Λ , we apply the Thomas Fermi approximation. Assuming we are at equilibrium and the number of atoms has saturated, we can neglect the dissipation and noise terms and write Eq. (3.21) as

$$i\hbar \frac{\partial \Psi}{\partial t} = \mathcal{P} \left\{ \left[-\frac{\hbar^2 \nabla^2}{2m} + V + g_{3D} |\Psi|^2 - \mu \right] \Psi \right\}. \quad (3.80)$$

Since we shall be emulating the experimental configuration of Ville *et al* [171] for our reference case of $\Lambda = 1$, we begin by considering this 2D limit and make the ansatz that

$$\Psi(\mathbf{r}, t) = \psi(x, y, t)\phi(z) \quad (3.81)$$

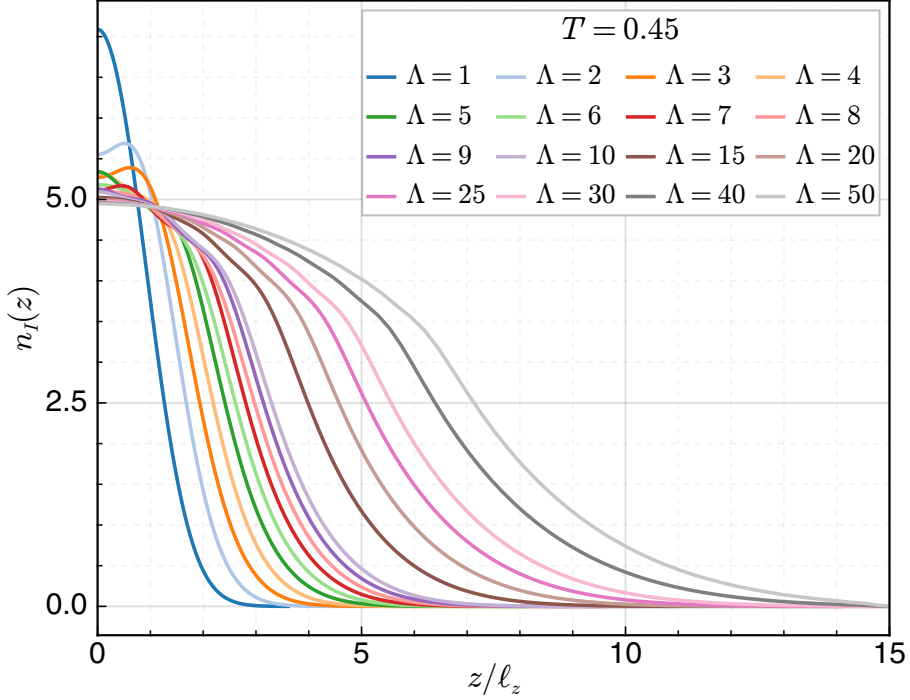


Figure 3.8: Transverse density profiles of above-cutoff atoms for various values of dimensionality taken at the normalised temperature $T' = 0.45$. Density profiles are symmetric about $z = 0$, with the symmetric half omitted for visual clarity.

where $\phi(z)$ is the ground state solution which is known to be of the form [40]

$$\phi(z) = \frac{e^{-\frac{z^2}{2\ell_z^2}}}{(\pi\ell_z^2)^{1/4}}. \quad (3.82)$$

where, as used previously, the characteristic trapping length ℓ_z corresponds to the transverse trapping frequency ω_z . Substituting Eq. (3.82) into Eq. (3.80), multiplying on the left by the conjugate $\phi^*(z)$ and integrating over all z gives

$$i\hbar \int_{-\infty}^{\infty} dz |\phi|^2 \frac{\partial \psi}{\partial t} = \mathcal{P} \left\{ \int_{-\infty}^{\infty} dz \phi^* \left[-\frac{\hbar^2 \nabla^2}{2m} + V + g_{3D} |\psi|^2 - \mu \right] \psi \phi \right\}. \quad (3.83)$$

Noting that the only constituent of our external potential which acts over the transverse direction is that of our harmonic trap, and since $\int_{-\infty}^{\infty} dz |\phi|^2 = 1$, $\int_{-\infty}^{\infty} dz |\phi|^4 = 1/\sqrt{2\pi}\ell_z$, this can be simplified down to

$$i\hbar \frac{\partial \psi}{\partial t} = \mathcal{P} \left\{ \left[-\frac{\hbar^2 \nabla^2}{2m} + \frac{\hbar\omega_z}{2} + \frac{g_{3D}}{\sqrt{2\pi}\ell_z} |\psi|^2 - \mu \right] \psi \right\}. \quad (3.84)$$

The projector is only important when considering numerics and thus we ignore it here for

simplicity. The stationary solution of the coherent modes in the Thomas-Fermi limit is then

$$\mu\psi = \left[\frac{\hbar\omega_z}{2} + \frac{g_{3D}}{\sqrt{2\pi}\ell_z} |\psi|^2 \right] \psi. \quad (3.85)$$

Substituting $|\psi|^2 = \frac{N}{L_x L_y}$ as the 2-dimensional density, we can estimate μ to be

$$\mu = \frac{\hbar\omega_z}{2} + \frac{g_{3D}N}{\sqrt{2\pi}\ell_z L_x L_y} \quad (3.86)$$

where we recall that L_x, L_y are the respective box side lengths in x and y . Now since we know the density value of the reference 2D system we wish to emulate, as well as the interaction strength we can substitute $\mu_{2D} = g_{2D}n_{2D} = g_{3D}N/(\sqrt{2\pi}\ell_z L_x L_y)$ and therefore have a simplistic method to normalise atomic density across different values of ω_z and thus dimensionality.

3.3 Chapter conclusions

In this chapter we introduced the finite temperature dynamical theory offered by the SPGPE. We outlined its derivation and discussed the approximations made that give rise to the simple growth SPGPE. We then discussed the implications and implementation details of a numerical projection operator to cast out incoherent modes. We went on to introduce the hybrid trapping geometry employed for the remainder of this thesis and derived expressions for the density contributions from above-cutoff modes in this given configuration. Lastly, we motivated a simple choice for a chemical potential to emulate the 2D experimental conditions of Ville *et al* [26] in such a way that we can maintain an equivalent central density across dimensionality by varying the parameter Λ .

With this foundation, we can now utilise the SPGPE formalism to explore the physics present in the dimensionality crossover from two to three dimensions. By varying the transverse harmonic trapping strength, the following chapter will explore the effects of dimensionality on the phase transition of the trapped Bose gas at equilibrium.

Chapter 4

Equilibrium analysis of the dimensionally reduced Bose gas from two to three dimensions

In this chapter we introduce and investigate the dimensionality crossover of the planar trapped Bose gas which is harmonically confined along a singular direction. This work documents in greater detail the study described in Keepfer *et al.*, “*Phase transition dimensionality crossover from two to three dimensions in a trapped ultracold atomic Bose gas*” (2022), accepted for publication in Phys. Rev. Research [192].

4.1 The role of dimensionality in the characterisation of the critical transition point

It is well documented that in lower-dimensional finite temperature systems with short-range interactions, the spontaneous breaking of a continuous symmetry is precluded. This is commonly referred to as the Mermin-Hohenberg-Wagner theorem [24, 25]. More plainly, in such lower-dimensional systems, long-range coherence remains elusive due to the strong thermal fluctuations inherent to the system which acts to destroy any long-range order. However, for the case of the dilute Bose gas with repulsive interactions, a topological ordering may be induced through the binding of vortex pairs [193, 194] below a critical transition temperature. We also know that in 3D the macroscopic occupation of the lowest energy allows the formation of a Bose-Einstein condensate [1, 2, 195], which in turn, occurs at another distinct critical temperature. This dichotomy between phase transition mechanisms at the dimensional extremes presents an open question on the phase transition mechanism in quasi-2D systems. That is, as we apply harmonic trapping with increasing strength along the transverse direction, there must be a crossover region

in which we shift from the superfluidity as a consequence of BEC, to the superfluidity as a consequence of BKT topological ordering. Whilst dimensionality crossovers have been previously considered both theoretically [41, 164, 196–203] and experimentally [5, 42, 46, 204–207], relevant questions on the effects of dimensionality between the BKT and BEC phase transitions of a dilute Bose gas within experimentally viable geometries remain open. We highlight that this specific crossover has previously been investigated as a function of interactions [207], but in our work these remain fixed.

4.2 Equilibration physics inside the hybrid trapping Geometry

Before discussing the equilibrium properties, we first visualise in Fig. 4.1 a few snapshots of single SPGPE trajectories for three different values of Λ during the preparatory stage of the dynamical equilibration process we employ. Projected density slices along the axial planes reveal a homogeneous profile along the xy plane. Along the other planes we have a fusion of homogenous and harmonic density profiles. In addition to the density slices, the integrated density along each individual axis is shown, revealing a clear homogeneous profile along the planar directions and a Thomas-Fermi like solution along the harmonically trapped transverse direction. Lastly, the isosurface renderings reveal the global change in system topology through the dimensionality crossover as we modify Λ . In each case, the system evolves starting from a zero-field condition and a snapshot is taken at some instant during the equilibration dynamics. In such a dynamical process, one may easily observe quantum vortex structures forming spontaneously during the growth [151, 187, 208–210] as a consequence of symmetry breaking in the region of critical fluctuations. Whilst we employ an instantaneous quench, a careful control of quench rate can be used to effectively control vortex number through the Kibble-Zurek mechanism [69, 211, 212]. The figure shows that, by increasing Λ , vortices change from point-like to filament-like defects, clearly signposting a transition in dimensionality, which roughly occurs when the vortex core size (i.e., the healing length) is of the same order of the transverse size of the atomic cloud. This is further evidenced when we consider the full relationship between the healing length ξ and transverse width ℓ_z as plotted in Fig. 4.2. Here we see a rapid change in dimensionality between $1 \leq \Lambda \leq 10$, which slows with increasing Λ . As such, we expect the majority of the dimensional shift to occur within this range.

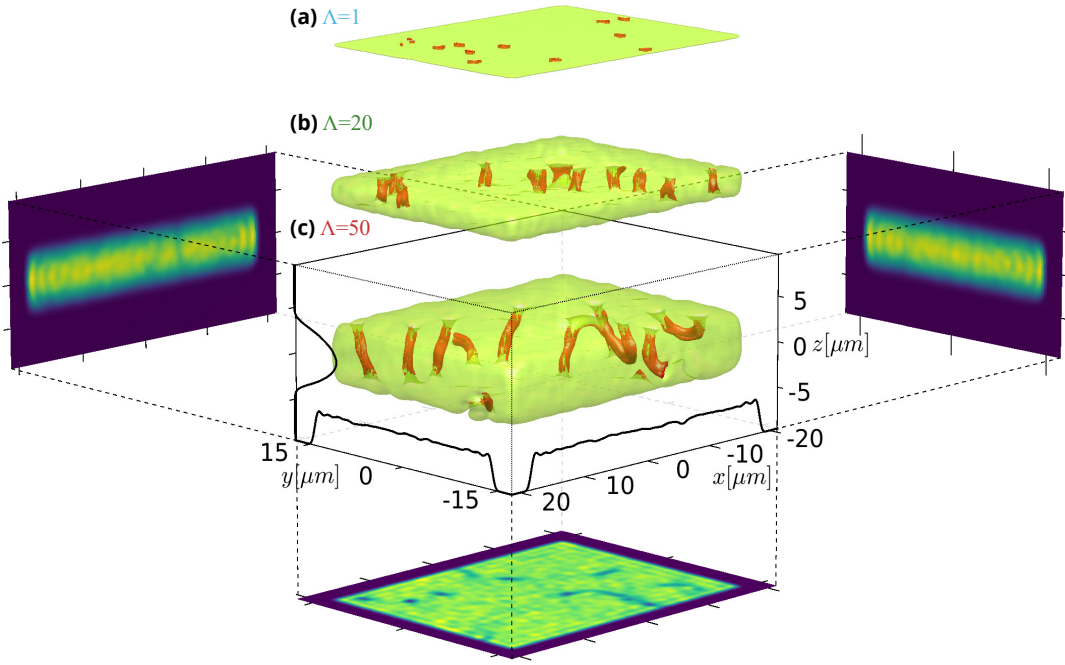


Figure 4.1: Examples of isosurface rendering (green) of \mathcal{C} -field density, $|\Psi_{\mathcal{C}}|^2$, during a quench from zero-field conditions to equilibrium for $\Lambda = 1, 20, 50$ as labelled by (a), (b) and (c) respectively. The temperature of the gas in all cases is 20nK, which is well below the transition temperature where the system is superfluid. In red, we plot an isosurface of high velocity regions, indicating vortex structures. In the $\Lambda = 50$ case, integrated line density profiles are overlayed for each axis. The image at the bottom is the column density, i.e., the density integrated along z , for the case of $\Lambda = 50$. The images on the left and right are the column densities in the planar directions.

4.3 Normalising atomic density and Bogoliubov sound speed across dimensionality and temperature

As previously outlined in Section 3.1.4, our aim is to compare equilibrium configurations with similar average density but different dimensionality, as this facilitates the most direct way to compare different regimes across the dimensionality crossover. However, the SPGPE does not allow one to directly fix the total atom number $N = N_{\mathcal{C}} + N_{\mathcal{I}}$ as an input without the postulation of an additional term as has been previously investigated [131] in 1D. One instead has to impose upon the thermal reservoir, and consequently the Bose gas, an input chemical potential which is carefully chosen to ensure consistent atomic densities. A simple choice, as motivated in Section 3.2.1, corresponds to use μ according to

$$\mu = \mu_{2D} + \frac{\hbar\omega_z}{2} = \mu_{2D} + \frac{\hbar\omega_{\text{ref}}}{2\Lambda}, \quad (4.1)$$

where μ_{2D} is a constant, independent of Λ . When Λ increases, this choice of μ implies an increase of the number of atoms in the trap: typical \mathcal{C} -field atom numbers for a given

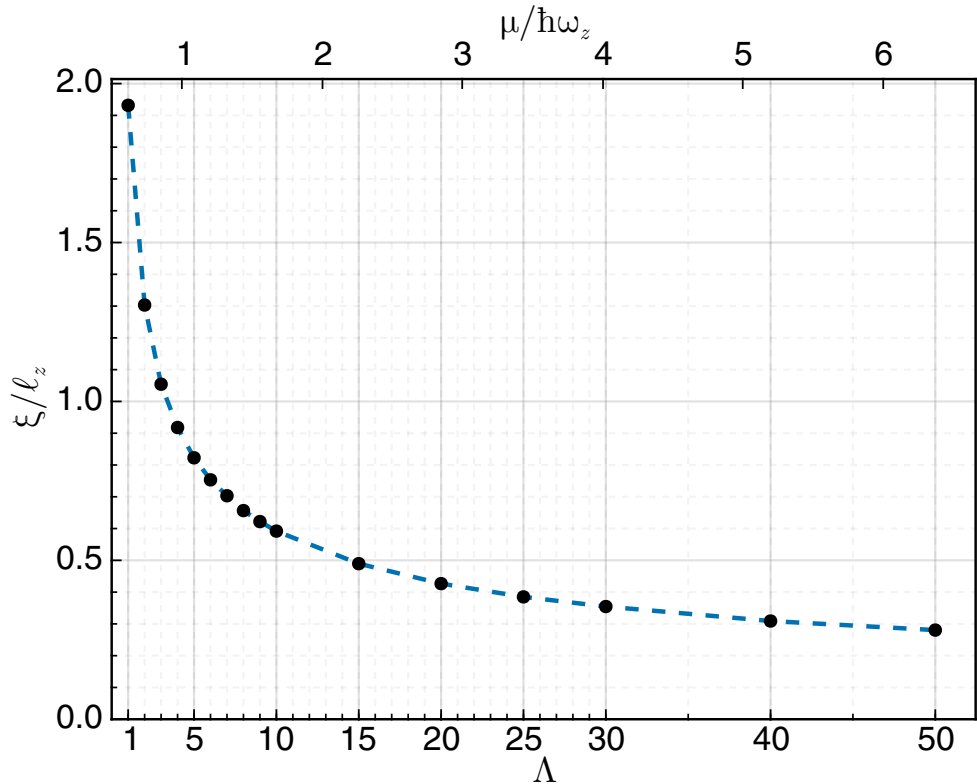


Figure 4.2: Relationship between the ratio of the healing length $\xi = \hbar/\sqrt{2mgn(0)}$ and the transverse width of the gas as a function of dimensionality. We use the top x -axis to additionally show the relationship between the chemical potential, from the protocol as defined by Eq. (4.1). Black points correspond to the specific values of Λ we consider across this chapter with a blue dotted line to guide the eye.

ensemble range between $N_C \sim 10^3$ for $\Lambda = 1$ to $N_C \sim 10^6$ for $\Lambda = 50$. However, as we will see later, the central density remains of the same order in the whole range of Λ , decreasing by about 30% only and approaching the constant value μ/g for $T = 0$ and large Λ . The results presented in the next sections are obtained by using the chemical potential of Eq. (4.1) with $\mu_{2D} = (4.64\mu\text{m}^{-2})\hbar^2/m$, which ensures that the density and the chemical potential for $\Lambda = 1$ reduce to the experimental values of Ville *et al* [26]. We will also discuss some results obtained with a chemical potential having a different dependence on Λ , in order to show that main qualitative features of the dimensional crossover remain unchanged. One such way to normalise results across dimensionalities would be to consider normalising the zero temperature second sound speed across the dimensional extremes. Thus, the goal is to find a proper way to realise the 2D-3D dimensional crossover in the hybrid trap by keeping this key property of the gas almost constant. For this purpose, let us start from the Gross-Pitaevskii equation, ignoring boundary effects in the horizontal

xy-plane. Then the order parameter only depends on the vertical coordinate z and we can write

$$\Psi(z) = \sqrt{\frac{n_{2D}}{\ell_z}} f(z') \quad (4.2)$$

where f is a real function and

$$\begin{aligned} z' &= z/\ell_z, \\ \int dz' f^2(z') &= 1, \\ n_{2D} &= \int dz n(z) = \frac{N}{L_x L_y}. \end{aligned} \quad (4.3)$$

Then the 3D GP equation reduces to the one-dimensional equation

$$\left(-\frac{1}{2} \frac{d^2}{dz'^2} + \frac{1}{2} z'^2 + 4\pi a_s \ell_z n_{2D} f^2(z') \right) f(z') = \frac{\mu}{\hbar \omega_z} f(z') \quad (4.4)$$

Now, in the 2D mean-field limit, when $a_s \ell_z n_{2D} \ll 1$, the solution of the GP equation approaches a Gaussian

$$f(z') = \frac{1}{\pi^{1/4}} e^{-z'^2/2} \quad (4.5)$$

and we note that the central density of the gas, $n(0)$ is related to the effective 2D density by

$$n(0) = \frac{n_{2D}}{\ell_z} f^2(0) = \frac{n_{2D}}{\sqrt{\pi} \ell_z} = \frac{N}{\sqrt{\pi} L_x L_y \ell_z}. \quad (4.6)$$

The sound speed can be obtained from the definition $mc^2 = n_{2D} \partial \mu / \partial n_{2D}$ which gives

$$mc^2 = g_{2D} n_{2D} = \sqrt{\frac{1}{2}} g_{3D} n(0) \quad (4.7)$$

Conversely, in the Thomas-Fermi limit, when $a_s \ell_z n_{2D} \gg 1$, the solution of the GP equation approaches the Thomas-Fermi solution, where the density is given by

$$n(z) = n(0) \left(1 - \frac{z^2}{R_z^2} \right) \quad (4.8)$$

where R_z is the Thomas-Fermi radius which obeys the condition $n(z) = n(0) \left(1 - \frac{z^2}{R_z^2} \right)$ with

$$\mu = g_{3D} n(0) = \left(\frac{3\pi \hbar^2 \omega_z a_s n_{2D}}{\sqrt{2m}} \right)^{2/3} = \left(\frac{3\pi \hbar^2 \omega_z a_s N}{\sqrt{2m} L_x L_y} \right)^{2/3} \quad (4.9)$$

The sound speed can again be obtained from the definition $mc^2 = n_{2D} \partial \mu / \partial n_{2D}$ which in this instance gives

$$mc^2 = \frac{2}{3} \mu = \frac{2}{3} g_{3D} n(0). \quad (4.10)$$

In our SPGPE simulations, the quantity $\tilde{\mu} = g_{2D}n_{2D} = (4.64\mu\text{m}^{-2}) \hbar^2/m$ is a constant. This implies that, in the 2D limit, we have

$$c = \sqrt{\frac{\tilde{\mu}}{m}} = (2.154\mu\text{m}^{-1}) \hbar/m \quad (4.11)$$

whilst in the 3D limit we have

$$c = \sqrt{\frac{2\mu}{3m}}. \quad (4.12)$$

However, for large Λ , the zero-point energy becomes negligible and one can replace μ with $\tilde{\mu}$, thus obtaining

$$c = \sqrt{\frac{2}{3}} \sqrt{\frac{\tilde{\mu}}{m}} = \sqrt{\frac{2}{3}} (2.154\mu\text{m}^{-1}) \hbar/m \quad (4.13)$$

which is about 20% smaller than in the 2D limit. Now, the central density in the 2D limit is

$$n(0) = \frac{n_{2D}}{\sqrt{\pi}\ell_z} = \frac{\tilde{\mu}}{g_{2D}\sqrt{\pi}\ell_z} = \sqrt{2} \frac{\tilde{\mu}}{g_{3D}}, \quad (4.14)$$

whereas in the 3D limit we have

$$n(0) = \frac{\tilde{\mu}}{g_{3D}}, \quad (4.15)$$

which is a factor of $\sqrt{2}$ smaller. Thus in order to obtain almost the same speed of sound at zero temperature for any Λ the input chemical potential $\tilde{\mu}$ should vary with Λ , instead of being a constant; in particular, it should grow from the reference value at $\Lambda = 1$ to a value a factor of 3/2 larger for $\Lambda = 50$. For simplicity we use a linear interpolation between these two extremes such that

$$\mu = \left(1 + \frac{\Lambda - 1}{2(50 - 1)}\right) \mu_{2D} + \frac{\hbar\omega_{\text{ref}}}{2\Lambda} \quad (4.16)$$

For most of the work in this section focusing on equilibrium properties, we adopt the former definition of the chemical potential specified by Eq. (4.1) for simplicity and will specify any instances of the latter protocol in this chapter. However, in Chapter 5 which discusses sound speed, we utilise the secondary protocol and adopt Eq. (4.16) globally across that chapter.

4.4 Limiting regimes

To understand the crossover behaviour, we first focus on the limiting regimes. That is, the characterisation of the thermal transition point in the well-documented 2D and 3D limits. In the limit of 2D, thermal fluctuations at any temperature are strong enough to preclude long-range coherence in the phase of the system. As such, spontaneous symmetry breaking cannot occur and the formation of a true condensate is not feasible, in accordance with the

Mermin-Hohenberg-Wagner theorem [24, 25]. Specifically, this theorem precludes the existence of a condensate for a system with short range interactions at non-zero temperature for dimensions 2 or fewer. Nevertheless, the phenomenon of quasi-long-range order in low-dimensional atomic gases with repulsive interactions leads to a decrease in the first-order correlation function. As such, a topological phase transition can be induced below some critical temperature, T_{BKT} . Formally, this is known as the Berezinskii-Kosterlitz-Thouless (BKT) superfluid phase transition, first introduced in the seminal works of Kosterlitz and Thouless [194]. This mechanism permits the onset of superfluidity in 2D Bose gases despite the preclusion of condensation in this limit. The BKT superfluid transition [193, 194] arises from the binding of vortex pairs and occurs at a critical temperature dependent on the superfluid density of the system. Conversely, in 3D, a phase transition occurs via the macroscopic occupation of the lowest energy level, or as we recognise it, the Bose-Einstein condensation [1, 2, 195]. The following subsections will explore these two limiting regimes for our trapping geometry in greater detail.

4.4.1 The BEC transition

In order to probe the transition, we must first elucidate the temperature at which a transition will occur for our given system. We begin by writing the number of atoms in the system as

$$N = N_0 + \int_0^\infty d\epsilon g(\epsilon) f_{BE}(\epsilon) \quad (4.17)$$

Then, as done for the derivation of the density of states in Eq. (A.36), we assume here that $k_B T$ is much larger than the level spacing, including the harmonic oscillator energy $\hbar\omega_z$. Then Eq. (A.32) becomes

$$N = N_0 + \frac{m L_x L_y}{2\pi\hbar^3\omega_z} \int_0^\infty d\tilde{E} \frac{\tilde{E}}{\exp[(\tilde{E} - \tilde{\mu})/k_B T] - 1}. \quad (4.18)$$

Let us define

$$t = \frac{\tilde{E}}{k_B T}, \quad z = e^{\tilde{\mu}/k_B T} \quad (4.19)$$

so that

$$N - N_0 = \frac{2\pi L_x L_y \ell_z^2}{\lambda_{\text{dB}}^4} \int_0^\infty dt \frac{t}{\frac{e^t}{z} - 1}. \quad (4.20)$$

The integral is a standard Bose-Einstein integral of order 2. Using Eq. (1.31) we can then write

$$N - N_0 = \frac{2\pi L_x L_y \ell_z^2}{\lambda_{\text{dB}}^4} \text{Li}_2(z), \quad (4.21)$$

where

$$\text{Li}_2(z) = - \int_0^z dt \frac{\ln(1-t)}{t}. \quad (4.22)$$

The occupation of the lowest state, N_0 , becomes macroscopic (i.e, of order N) only when $\tilde{\mu}$ approaches 0 from below, which corresponds to $z = \exp(\tilde{\mu}/k_B T) \rightarrow 1$ under the assumption that the total number of particles can be accommodated in excited states. The value of $\text{Li}_2(z)$ for $z = 1$ is

$$\text{Li}_2(1) = \pi^2/6 \quad (4.23)$$

and the relation between the total particle number and temperature at this critical point, where N_0 vanishes, becomes

$$N = \frac{\pi^3 L_x L_y \ell_z^2}{3\zeta \lambda_{\text{dB}}^4}, \quad (4.24)$$

or

$$N = \frac{\pi L_x L_y m k_B^2 T^2}{12\omega_z \hbar^3}. \quad (4.25)$$

This can be used to define a critical temperature

$$T_{\text{BEC}} = \sqrt{\frac{12\hbar^3 \omega_z N}{\pi k_B^2 m L_x L_y}} \quad (4.26)$$

for Bose-Einstein condensation for a given total number of atoms N . It is worth reiterating here that in a true 2D system corresponding to the limit $\omega_z \rightarrow \infty$, the formation of a condensate is prohibited, corresponding to an infinite temperature transition. However, due to the phenomenon of transverse condensation as discussed in Section 1.1.3, it is possible to achieve a macroscopic occupation of the lowest modes and hence condensation even in a strongly confined quasi-2D system.

4.4.2 The BKT transition

The theory of Berezinskii, Kosterlitz and Thouless [194, 213] stipulates that a topologically-induced phase transition may occur in the 2D Bose gas, below some critical temperature. At high temperatures, above the transition, there is a proliferation of free vortices. This proliferation of free vortices prevents any phase rigidity from appearing in the system leading to a fluctuating phase and vanishingly small correlation lengths. As the temperature is lowered, these vortices instead become bound to vortex/antivortex pairs, bearing little influence on the coherence properties of the gas and allowing the phase to stabilise and become coherent over a larger correlation length. Let us first consider the energy associated with a vortex/antivortex pair; it can be shown [161, 214] that the kinetic energy of

a pair separated by a distance l is given by the result

$$E_{\text{kin}}^{2V} \approx 2\pi \frac{\hbar^2 n}{m} \log\left(\frac{l}{\xi}\right). \quad (4.27)$$

It is also fairly simple, upon the assumption of a step-like density profile at the vortex core, to derive the kinetic energy associated with a single vortex. This is given by the result

$$E_{\text{kin}}^V = \pi \frac{\hbar^2 n}{m} \log\left(\frac{R}{\xi}\right), \quad (4.28)$$

for a circular system of size R . The difference here is startling, as although appearing similar in form, the kinetic energy for an isolated vortex diverges with the system size. In addition, an isolated central vortex causes the bulk density to change due to the change in area from πR^2 to $\pi(R^2 - \xi^2)$ for the same number of particles. This causes a shift in the interaction energy from the quiescent state given by $\Delta E_{\text{int}}^V = \pi \hbar^2 n / 4m$. In the same vein, it simply follows that this shift in the interaction strength of the dipole pair is just twice the shift for the isolated vortex. Now, it becomes possible to define the probability of a pair separated by distance l from the relation

$$P_{2V}(l) = e^{-\frac{2\Delta E_{\text{int}}^V + E_{\text{kin}}^{2V}(l)}{k_B T}} \approx z_v^2 (\xi/l)^{\mathcal{D}_s} \quad (4.29)$$

where we have introduced the vortex fugacity $z_v = \exp(-\Delta E_{\text{int}}^V/k_B T)$ with the superfluid phase space density \mathcal{D}_s . The vortex fugacity can be approximated as $z_v \approx \exp(-\mathcal{D}_s/4)$ for a step-like density profile within the vortex core. One can now define the average distance between a vortex pair as the quantity $\langle l^2 \rangle$, which is reported by Kosterlitz and Thouless [194] to be the expression

$$\langle l^2 \rangle = \xi^2 \frac{\mathcal{D}_s - 2}{\mathcal{D}_s - 4}. \quad (4.30)$$

We now see the famous prediction of the universal superfluid jump and corresponding BKT phase transition. The relation is universal as it is, perhaps surprisingly, independent of the interaction strength. In fact, from Eq. (4.30), we can see that for $\mathcal{D}_s = 4$ the mean separation diverges. Additionally, we can see that for $\mathcal{D}_s < 4$, we are in the non-degenerate case and above the topologically induced phase transition. In this region, free vortices proliferate and preclude the emergence of a stiff phase and hence superfluidity is not possible. Whereas, for $\mathcal{D}_s > 4$, we have a degenerate system where vortices are bound to pairs whose average separation decreases with increasing phase space density. This stabilisation in the phase from the topological ordering of dipole pairs enables superfluid behaviour below the transition. In order to further understand the nature of the transition, it becomes useful to find an expression in terms of the critical temperature at which it occurs.

Previous works [47, 215] have developed a thermodynamic theory by determining the equation of state for an interacting planar 2D Bose gas, leading to the critical expression in the thermodynamic limit described by

$$\left. \frac{\mu_{2D}}{k_B T} \right|_{BKT} \approx \frac{mg_{2D}}{\pi \hbar^2} \ln \left(\frac{C_\mu}{\tilde{g}_{2D}} \right), \quad (4.31)$$

where μ_{2D} is the effective chemical potential for the 2D system, as in Eq. (4.1). The quantity $\tilde{g}_{2D} = (m/\hbar^2) g_{2D} = \sqrt{8\pi} a_s/l_{ref} = 0.16$ is a dimensionless interaction strength in the 2D limit chosen to once again match the value used by Ville *et al* [26]. Numerical quantum Monte Carlo simulations [216, 217] have recovered the value $C_\mu = 13.2$ for the case of a weakly interacting Bose gas.

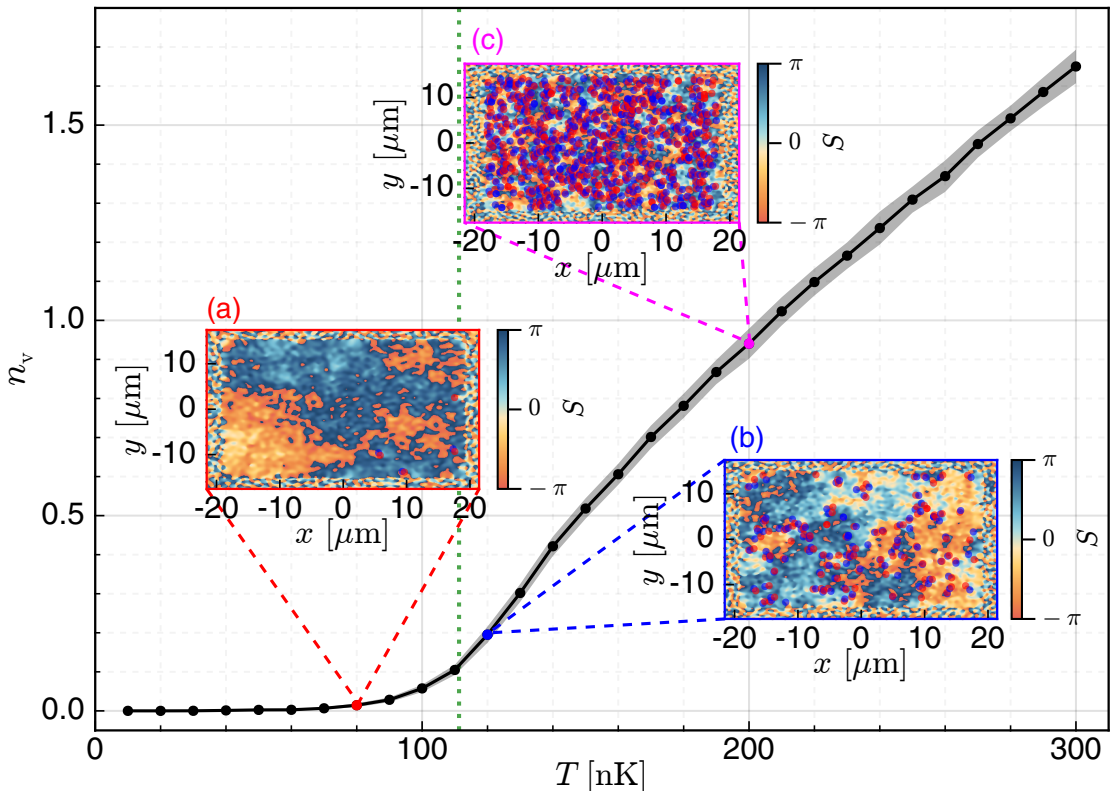


Figure 4.3: Vortex density as a function of temperature for the 2D case $\Lambda = 1$. Black line corresponds to average value with errorbars signifying one standard deviation. Additional red, blue and magenta points correspond to subplots (a), (b) and (c) at temperatures $T = 80\text{nK}, 120\text{nK}, 200\text{nK}$ respectively. In each subplot we show a phase profile of a single stochastic trajectory along the central $z = 0$ plane, superimposing the position of positive and negative vortices as red and blue circles respectively. A dotted green vertical line has been added to demarcate the analytic BKT temperature for $\Lambda = 1$, as given by Eq. (4.31).

A measure of the degeneracy one may consider is the vortex density which can be

defined for our planar system in the $\Lambda = 1$ case to be

$$n_v = \frac{N_v}{L_x L_y}, \quad (4.32)$$

where N_v is the number of vortices identified in the central $z = 0$ plane. Across the BKT transition, we expect this value to saturate [161]. In fact, this is exactly the behaviour observed in Fig. 4.3. Although vortices may exist at temperatures below the BKT transition, they will eventually annihilate. Thus, we observe that there is a steep increase in the number of vortices close to the BKT transition temperature, in close agreement with previous work [28]. This can be seen by the phase profiles in which Fig. 4.3(a) contains few vortices, Fig. 4.3(b) contains a significant number of vortices and Fig. 4.3(c) displays a near-full saturation of vortices within the system. Vortex positions in these plots are detected with sub-resolution precision using an interpolating plaquette method which calculates the phase integral around each 4-point plaquette on a cartesian grid. We only apply this method on the central $z = 0$ plane for the 2D case $\Lambda = 1$ where vortices are point-like.

4.5 Dimensional crossover

Having investigated the dimensional extremes, we now focus our attention towards the dimensional crossover. We first perform a survey, as shown in Table 4.1, of modern experimental trapping protocols that have defined themselves as investigating either the 2D or quasi-2D regime. Some of these experimental realisations use a trapping similar to the hybridised planar-harmonic trap we employ and others explore avenues such as full harmonic traps or even lattices. The large range of trapping strengths exhibited here indicate a clear need for a systematic analysis of the effects of dimensionality and temperature on the trapped dilute Bose gas. For the scope of our work, which considers $\Lambda \in [1, 50]$, we expect a clear transition from 2D behaviour at $\Lambda = 1$ where one would expect dynamics to be frozen along the transverse direction and a Thomas-Fermi transverse profile towards 3D behaviour with a Gaussian transverse profile at the 3D limit approximated here by $\Lambda = 50$. This is precisely what we see in Fig. 4.4(a), where for $\Lambda \leq 5$, Gaussian profiles are indistinguishable from one another, as the gas is subject to very strong trapping and unable to occupy high transverse modes. At $\Lambda = 10$ we see a minor deviation from this Gaussian profile as atoms are promoted into the transverse modes of the system and at $\Lambda = 50$ we see a full Thomas-Fermi solution, as evidenced by the inset plot which agrees excellently with the Thomas-Fermi prediction.

Laboratory	$\omega_z/(2\pi)$	Λ	Refs.	Year
Cambridge ¹ (UK)	5500-4100	0.84-1.12	[207, 218]	2015-2021
Paris ² (France)	4594-350	1-13.13	[5, 26, 46, 219]	2010-2018
Chicago ³ (USA)	1900	2.42	[220]	2011
Maryland ⁴ (USA)	1000	4.59	[45]	2009
Seoul ⁵ (Korea)	350	13.13	[221]	2017
Massachusetts ⁶ (USA)	250	18.38	[222]	2021
Innsbruck ⁷ (Austria)	133	34.54	[133]	2021
Queensland ⁸ (Australia)	108	42.54	[223]	2019
Monash ⁹ (Australia)	100	45.94	[224, 225]	2017-2019
Arizona ¹⁰ (USA) *	90	51.04	[226]	2010

Table 4.1: Harmonic trapping frequencies ω_z and their associated dimensionality Λ across experimental publications from different worldwide laboratories which claim to investigate 2D or quasi-2D behaviour sorted from most confined (2D) to least confined (3D). Here we see values as large as $\Lambda = 45$ and as low as $\Lambda = 0.84$ showcasing a wide interpretation of 2D or quasi-2D in published works. (* Authors specify a highly-oblate system as opposed to quasi-2D)

4.5.1 Equilibrium statistics

Since we do not have access to an analytic critical temperature of the transition point for a gas in the hybridised trap we employ, we need to instead implement a set of suitable observables to indicate the transition numerically. To locate the critical region of the phase transition, we use a set of different relevant equilibrium quantities, in close analogy to earlier works [28, 69, 227–230]. The combination of such indicators is then used to determine the critical temperature across the crossover, without any bias on any particular quantity, as discussed in Section 4.5.2.

¹ Cavendish Laboratory, University of Cambridge, J. J. Thomson Avenue, Cambridge CB3 0HE, United Kingdom.

²Laboratoire Kastler Brossel, Collège de France, CNRS, ENS-PSL Research University, Sorbonne Université, Paris, France.

³The James Franck Institute and Department of Physics, University of Chicago, Chicago, Illinois 60637, USA.

⁴Atomic Physics Division, National Institute of Standards and Technology, Gaithersburg, Maryland 20899-8424, USA.

⁵Department of Physics and Astronomy, and Institute of Applied Physics, Seoul National University, Seoul, 08826, Korea.

⁶MIT-Harvard Center for Ultracold Atoms, Research Laboratory of Electronics, and Department of Physics, Massachusetts Institute of Technology, Cambridge, Massachusetts 02139, USA.

⁷Institut für Quantenoptik und Quanteninformation, Österreichische Akademie der Wissenschaften, Innsbruck 6020, Austria.

⁸Australian Research Council Centre of Excellence for Engineered Quantum Systems, School of Mathematics and Physics, University of Queensland, St. Lucia, QLD 4072, Australia.

⁹School of Physics and Astronomy, Monash University, Victoria 3800, Australia.

¹⁰College of Optical Sciences, University of Arizona, Tucson, Arizona 85721, USA.

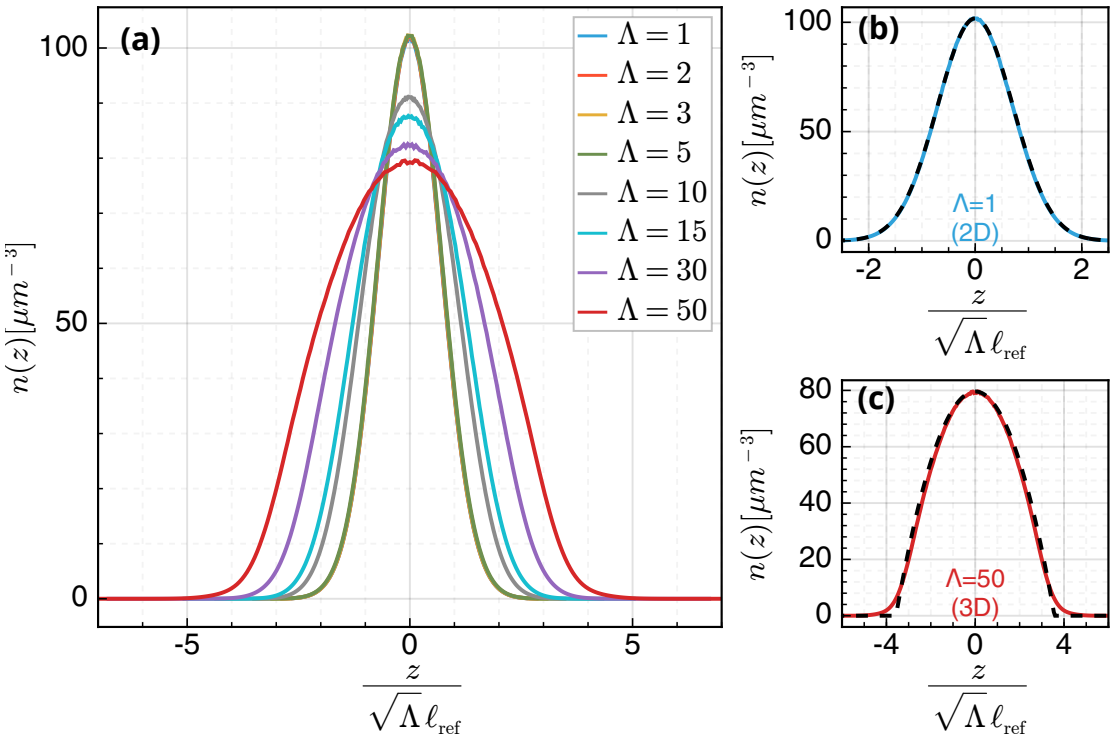


Figure 4.4: (a) Transverse profile of the total density of the gas for varying dimensionality Λ at a fixed temperature $T = 50$ nK and a chemical potential prescribed by Eq. (4.1). The coordinate z is normalised to the harmonic oscillator length ℓ_{ref} . Note that the curves for $\Lambda = 1, 2, 3$ are not visible, as they coincide with the one for $\Lambda = 5$. (b) Zoomed-in profile for extreme case of $\Lambda = 1$ where the expected Gaussian ground-state is plotted as a dashed black line. (c) Zoomed-in profile for extreme case of $\Lambda = 50$ (right) where the expected Thomas-Fermi ground-state profile is plotted as a dashed black line.

At this juncture, it is worth remarking that the SPGPE is inherently a high-temperature theoretical framework, in the sense that the equilibration processes described by the SPGPE become inefficient when T/T_c is significantly less than 1. At such low temperatures, the criterion that the thermal reservoir contains many weakly populated thermal modes is not met [127] and large fluctuations in equilibrium statistics are expected. The order parameter introduced in Section 4.5.1 is particularly susceptible to such fluctuations (see Fig. 4.9) at low temperatures where the assumption of many macroscopically occupied coherent modes below the cutoff fails. We stress that the region of highest significance from a numerical standpoint is close to the critical region. Therefore the spurious values in equilibrium statistics at low-temperature are deemed negligible to our main results in this chapter.

Penrose-Onsager diagonalisation

Firstly, to identify the existence of a condensate in the system, we use a standard procedure [127] based on extracting atom numbers, N_i , corresponding to the i -th mode through Penrose-Onsager diagonalisation [51] of the one-body density matrix $\rho(\mathbf{r}, \mathbf{r}') = \langle \Psi^*(\mathbf{r}) \otimes \Psi(\mathbf{r}') \rangle_{\mathcal{N}}$, where $\langle \dots \rangle_{\mathcal{N}}$ denotes an averaging over \mathcal{N} stochastic realisations. Eigenvalues extracted in this manner allow, for $i = 0$, the reconstruction of the corresponding mode, $\psi_0(\mathbf{r})$, with the largest eigenvalue, which we henceforth identify as the condensate mode. In Fig. 4.5, we see clearly that for the $A = 50$ system along the central plane, the condensate mode ψ_0 [Fig. 4.5(a)] corresponds to the minimally excited ground state solution, whilst the subsequent modes ψ_1 [Fig. 4.5(b)], ψ_2 [Fig. 4.5(c)] and ψ_3 [Fig. 4.5(d)] correspond to the first excited modes along the planar directions. Beyond identifying dis-

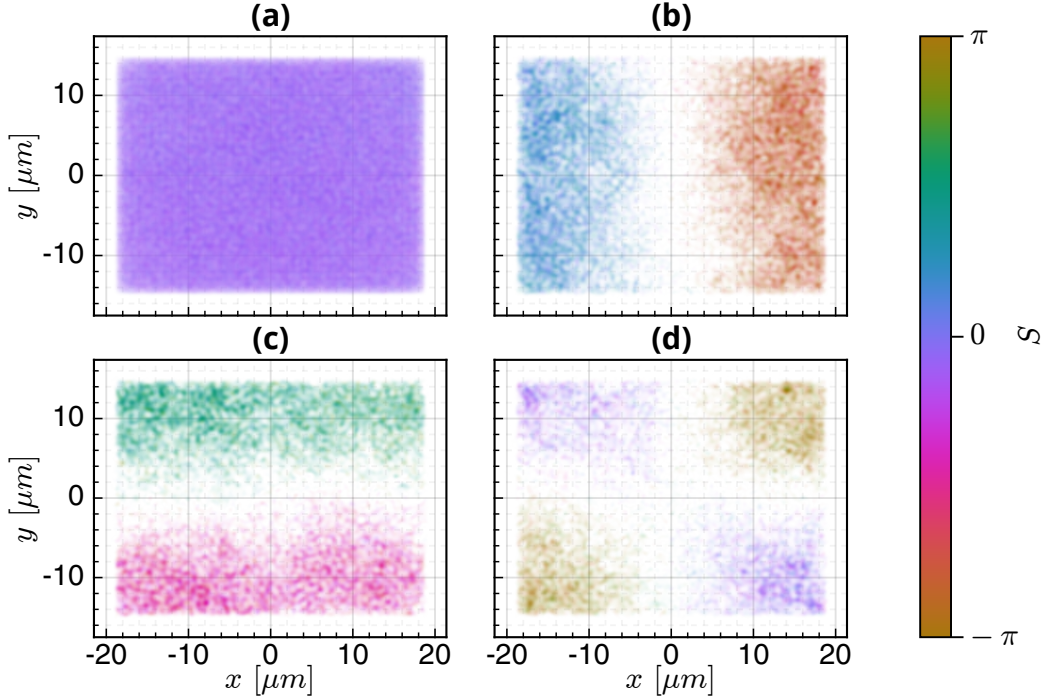


Figure 4.5: Normalised density and phase of the lowest four system modes (a) ψ_0 , (b) ψ_1 , (c) ψ_2 and (d) ψ_3 along the $z = 0$ plane for the $A = 50$ system at $T = 200\text{nK}$ visualised concurrently by transparency and colour respectively. We highlight that each mode is normalised to its own individual maximum amplitude and that each mode has a distinct atom number that decreases with the mode index.

tinct modes and the condensate fraction N_0/N , we can also extract the ratio, N_1/N_0 . This gives the ratio of atoms in the second lowest in respect to the lowest (condensate) mode. Here, one would expect an imminent crossing of the phase transition typically when there are half as many atoms in the second-lying mode as in the first.

Quasi-condensation

The second indicator we utilise to locate a crossing is the quasi-condensate. Condensation refers to a state with stable coherent phase and a single macroscopically occupied mode, arising when both density and phase fluctuations are suppressed. While this is highly-relevant in 3D systems (below the regime of critical fluctuations), lower dimensional systems feature pronounced phase fluctuations even when density fluctuations are suppressed [164, 198, 200], leading to a state of quasi-condensation, which spans multiple microscopically occupied modes [231, 232]. A quasi-condensate can be considered as a condensate with a fluctuating phase [229, 233]. One may numerically determine the number of atoms in the quasi-condensate via [47, 217]

$$N_{\text{QC}} = \sqrt{2 \langle |A_0|^2 \rangle_{\mathcal{N}}^2 - \langle |A_0|^4 \rangle_{\mathcal{N}}} , \quad (4.33)$$

where $A_0 = \int d\mathbf{r} \psi_0^*(\mathbf{r})\Psi(\mathbf{r})$. These two independent equilibrium measures reveal a deeper understanding on the character of condensation within the system. In addition, one may introduce a further measure of the difference between quasi-condensation and Bose-Einstein condensation through the parameter

$$\zeta = \frac{N_{\text{QC}} - N_0}{N_{\text{QC}}} \quad (4.34)$$

which should reveal a noticeable difference in behaviour in the 2D, where BEC is precluded, and 3D cases. This is exactly demonstrated in Fig. 4.6. Here we see a noticeable shift in behaviour across dimensionality. As dimensionality increases, we see a more gradual increase in ζ before a saturation at the crossing of the phase transition. For the analysis of the critical temperature, we omit the behaviour of the quantity ζ , due to the relatively smooth behaviour of the quasi-condensate across the phase transition.

Binder cumulant

An additional important quantity which is commonly used to characterise the critical region is the Binder cumulant [28, 69, 229, 230, 234–236], which is known to display critical behaviour across the phase transition, yielding – in the limit of infinitely large 3D boxes – a step-like behaviour from 1 (fully coherent system) to 2 (pure thermal state), with such transition being smoothed in finite systems, or due to the presence of harmonic confinement [28, 69, 229]. For the analysis and determination of the phase transition temperature we choose to employ the cumulant defined by

$$C_B = \frac{\langle |A_0|^4 \rangle_{\mathcal{N}}}{\langle |A_0|^2 \rangle_{\mathcal{N}}^2} , \quad (4.35)$$

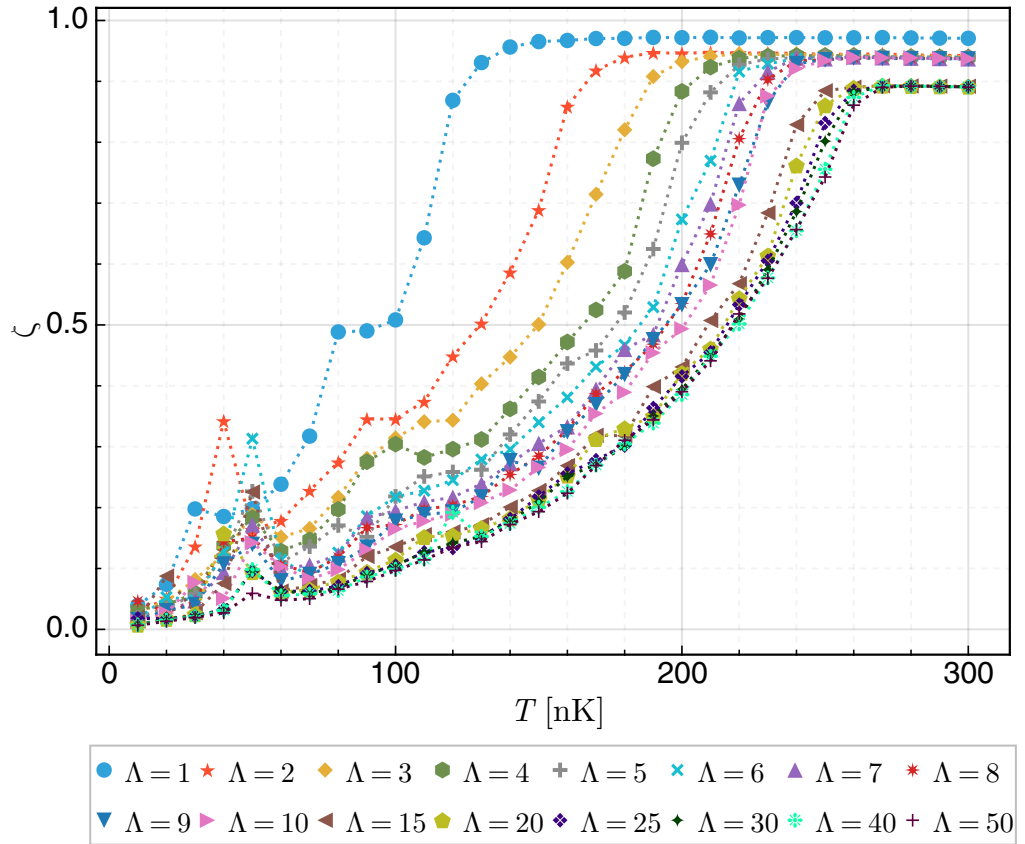


Figure 4.6: Difference between the quasi-condensate number and condensate number as defined by Eq. (4.34) for each dimensionality we consider as indicated by the legend. Dotted lines are added as guides to the eye.

which considers the lowest condensate mode as opposed to the entire \mathcal{C} -field sometimes employed in the literature.

Order parameter

Finally, we also use the order parameter defined by [28, 69, 230]

$$m = \frac{\langle \left| \int d\mathbf{r} \Psi(\mathbf{r}) \right| \rangle_{\mathcal{N}}}{\sqrt{\langle \int d\mathbf{r} |\Psi(\mathbf{r})|^2 \rangle_{\mathcal{N}}}} \quad (4.36)$$

which acts as a further measure of the degree of the degeneracy of the system associated to the breaking of a $U(1)$ symmetry. The order parameter should stabilise given enough time for the system to settle into its equilibrium configuration. The order parameter offers a computationally simpler calculation than the condensate fraction, however lacks

robustness against fluctuations, especially at lower temperatures.

4.5.2 Determination of the phase transition via equilibrium statistic thresholding

We now proceed to extract the critical phase transition temperatures across dimensionality by tracking our equilibrium statistics as introduced in Section 4.5.1 across temperature. Localisation of the phase transition and the respective critical region is performed by numerical thresholding for each considered equilibrium parameter. We find both the minimum and maximum temperature at which any of our equilibrium statistics indicate a crossing from coherent to incoherent behaviour for a given dimensionality, we then average across the identified extrema to identify the critical phase transition point T_c . Then, accounting for the thermal resolution of our simulations, we combine the half-width of the numerically-extracted band (where present) with an additional independent uncertainty of $\pm 5\text{nK}$ to define the overall width of our critical region. We emulate previous works [69] and stipulate the crossing of a phase transition occurs once the condensate fraction falls below 5% and introduce the cutoff $(N_0/N)^{\text{cut}} = 0.05$ to signpost a crossing of the critical region. At the phase transition point, occupation levels in the lowest and second-lowest mode should become comparable. Considering the ratio of the two lowest system modes N_1/N_0 [184], one would expect a transition when there are approximately half as many atoms in the second-lying mode as in the first. At this point, the thermal energy is large enough such that the occupation of the condensate mode is of the same order of other coherent modes, signalling an imminent phase transition. As such, we introduce a cutoff value $r^{\text{cut}} = 0.5$ to indicate a crossing. The Binder cumulant, as previously defined in Eq. (4.35), is a well established parameter to signal the crossing of a phase transition [28, 230]. In the thermodynamic limit for a homogeneous system, the critical value is known to be $C_B^\infty = 1.2430$ [237], whereas for trapped systems, where finite-size effects can manifest, this value is lower [228]. In this vein, we select a critical value of $C_B^{\text{cut}} = 1.2$ to indicate a crossing of the critical region. Lastly, we consider the order parameter m as defined in Eq. (4.36) normalised to its value at zero temperature m_0 . For a zero temperature system $m/m_0 = 1$, falling to $m/m_0 \sim 0$ across the transition [161, 230]. To capture the transition, we introduce a threshold value of $m^{\text{cut}} = 0.25$. Using each of the aforementioned threshold values in combination, a systematic simultaneous crossing of the critical region is revealed for each of the equilibrium statistics chosen.

4.6 Phase transition temperature as a function of dimensionality

In this section we explore, in a systematic way, the effects of dimensionality on the trapped Bose gas in a planar potential under transverse harmonic confinement. We begin with the 2D ($\Lambda = 1$) and 3D ($\Lambda = 50$) dimensional extremes, before considering the dimensionality crossover region between them.

4.6.1 Localising the BKT transition

To characterise the 2D phase transition in our numerics, we plot in Fig. 4.7 the relevant quantities discussed previously (namely N_0/N , N_1/N_0 , C_B and ζ) for $\Lambda = 1$ as a function of scaled temperature, T/T_{BKT} . Here T corresponds to the temperature of the thermal reservoir in contact with which the Bose gas has reached equilibrium, and T_{BKT} is defined in Eq. (4.31). Since the transition is not sharp in a finite size system [28, 229, 238] the determination of the actual transition temperature depends on the criterion and the indicator that is chosen to define it. The sharpest indicator is the Binder cumulant [Fig. 4.7(c)], which suggests that the critical temperature in the trapped gas is indeed very close to T_{BKT} , i.e., the expected value in the thermodynamic limit. The occupation of the lowest states is smooth across the BKT transition [Fig. 4.7(a)-(b)], with the quasi-condensate density remaining significantly larger than the condensate fraction N_0/N : the latter is evident by the fact that ζ remains finite and significantly nonzero for all $T < T_{\text{BKT}}$. Overall, the results that we obtain here with a 3D SPGPE in a tight transverse confinement ($\Lambda = 1$) are fully consistent with the purely 2D SPGPE simulations of Comaron *et al* [28], where the relevant features of the transition were discussed in detail. This validates our 3D formulation of what is essentially 2D physics within the hybrid-basis approach we enact. Previous works have also used the average number of vortices at equilibrium as a signature of the BKT transition in the 2D gas (see, e.g. [28, 229]). From Fig. 4.3, we see that by employing a plaquette method to identify vortex cores across the central plane of our $\Lambda = 1$ simulations, we indeed achieved, as expected, results which are in agreement with the purely 2D simulations of Comaron *et al* [28]. Specifically, in our 2D limit of $\Lambda = 1$ we find qualitative agreement with these results, across all of our considered quantities. We thus use this study as a premise of our work as we extend across dimensionalities.

4.6.2 Localising the BEC transition

The corresponding 3D limit can be well probed by our largest choice of $\Lambda = 50$, as can be seen by comparing such results with the predictions for BEC in 3D. In particular, using

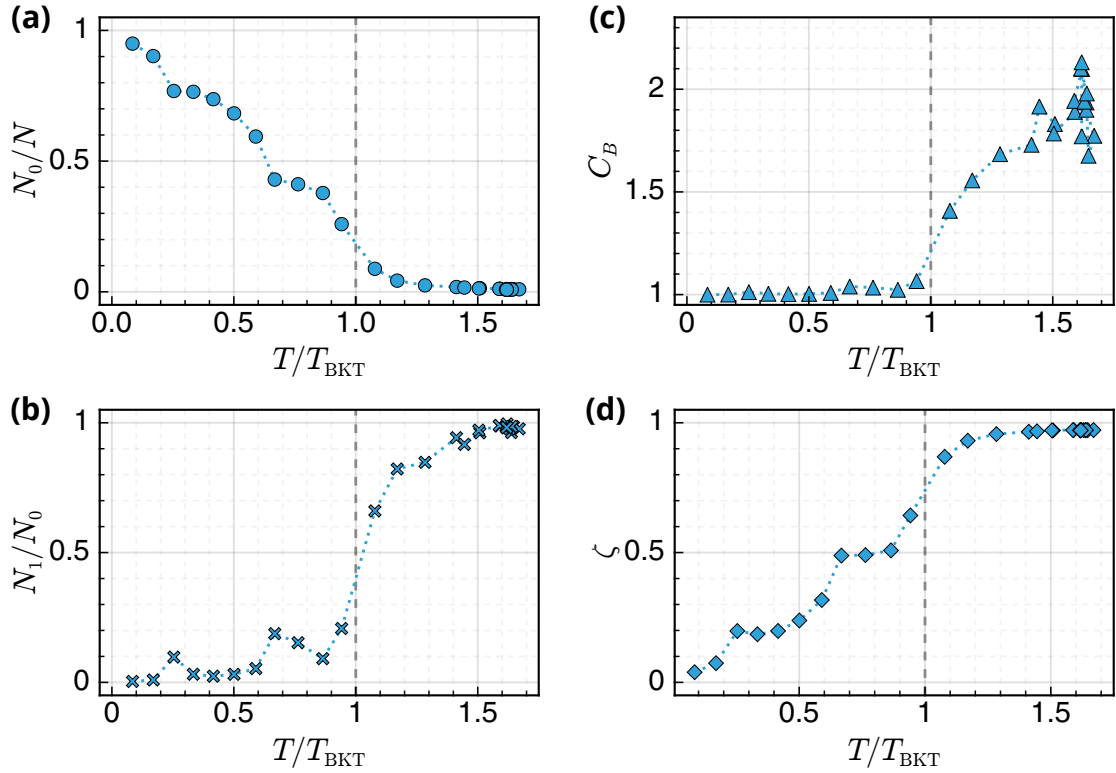


Figure 4.7: Results for $\Lambda = 1$ (2D limit). (a) Equilibrium condensate fraction N_0/N as a function of rescaled temperature. (b) Equilibrium ratio of lowest modes N_1 and N_0 as a function of rescaled temperature. (c) Equilibrium Binder cumulant C_B as calculated from the Penrose-Onsager condensate as a function of rescaled temperature. (d) Difference between quasi-condensate and condensate as identified by ζ as a function of rescaled temperature. In each plot, temperature has been rescaled to the BKT critical temperature as given by Eq. (4.31) for an infinite 2D system and marked as a vertical dashed line.

the density of states

$$g(\epsilon) = \frac{m L_x L_y \epsilon}{2\pi \hbar^3 \omega_z} \quad (4.37)$$

with $\omega_z = \omega_{\text{ref}}/\Lambda$, one can calculate the temperature at which the condensate forms in an ideal gas in the same hybrid trap:

$$T_{\text{BEC}} = \sqrt{\frac{12\hbar^3 \omega_{\text{ref}} N}{\pi k_B^2 m \Lambda L_x L_y}}. \quad (4.38)$$

Due to interaction and finite-size effects, the actual transition temperature of a confined weakly interacting Bose gas is expected to be downwardly shifted [1, 2, 69, 169, 239], the shift depending on the type of confinement.

As in the 2D case, we calculate the Binder cumulant, the fractions N_0/N and N_1/N_0 , and the quasi-condensate density. For each equilibrium configuration at a temperature T

we calculate the total number of atoms, N , and we use it to estimate the ideal gas critical temperature T_{BEC} from Eq. (4.38); then, all quantities are plotted as a function of the rescaled temperature T/T_{BEC} . The results are shown in Fig. 4.8. Compared to the 2D case, the equilibrium statistics exhibit a narrower critical region, with sharp transitions present in the ratio of dominant modes N_1/N_0 and the Binder cumulant. The condensate fraction N_0/N vanishes at the transition and its temperature dependence is similar to the one predicted for an ideal gas in the same trap except for a downward shift [240]. The observed transition temperature is at about $0.9T_{\text{BEC}}$.

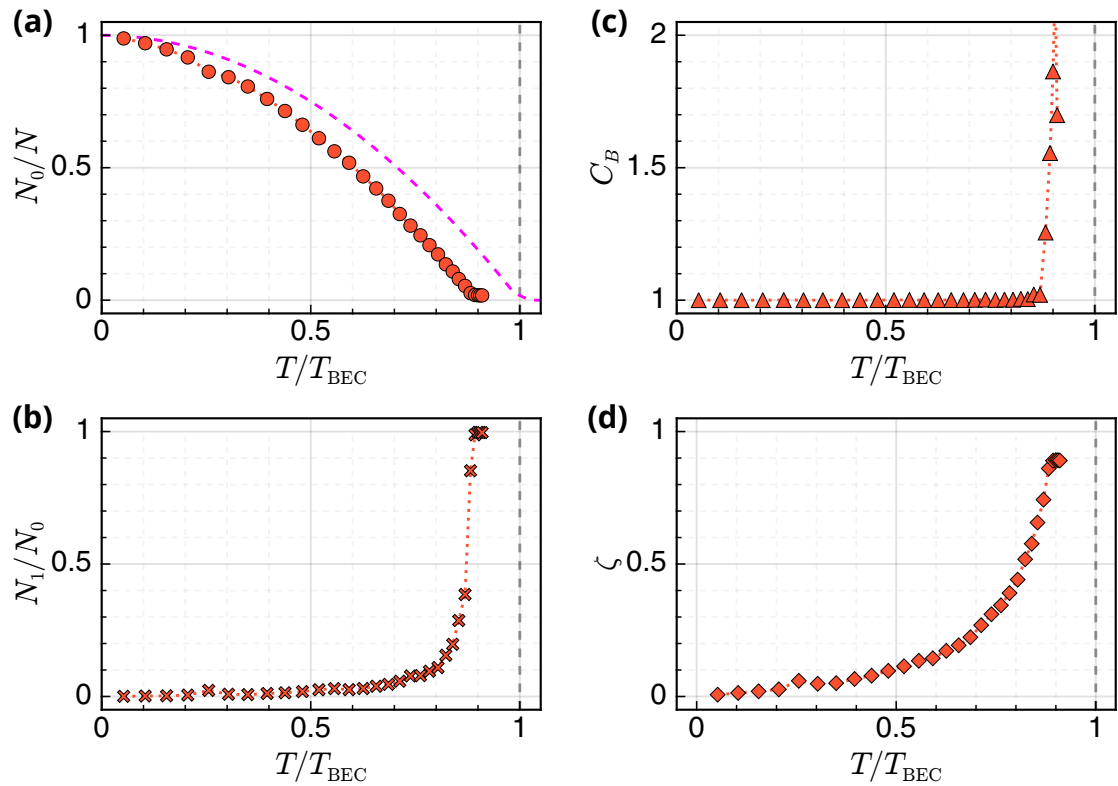


Figure 4.8: Results for $\Lambda = 50$ (3D limit). (a) Condensate fraction N_0/N , alongside the ideal gas law result (dashed magenta line). (b) Ratio of lowest modes N_1 and N_0 . (c) Binder cumulant C_B . (d) Difference between quasi-condensate and condensate as identified by ζ as a function of rescaled temperature. In each plot, temperature has been rescaled to the ideal gas BEC transition temperature defined in Eq. (4.38) and marked as a vertical dashed line.

4.6.3 From 2D to 3D

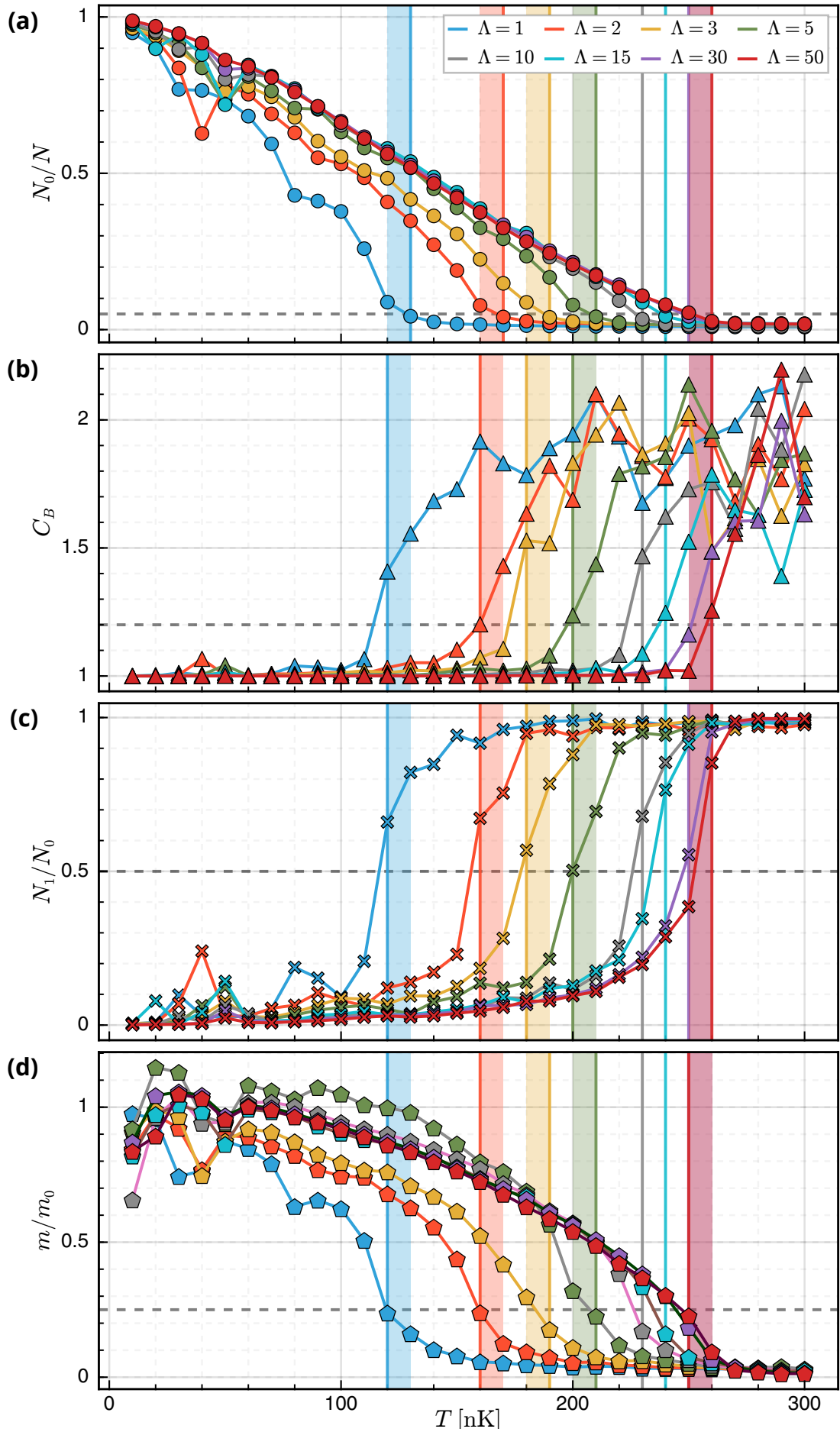
By systematically evaluating the equilibrium statistics across dimensionality and temperature we can recover a global picture of the character of the phase transition as we vary dimensionality. This is exactly what we show in Fig. 4.9, where for visual clarity we present a subset of dimensionalities that capture the characteristic change across the

range of dimensionalities we consider.

To estimate the transition temperature T_c we use, for each probed quantity, the relevant cutoff value marking the transition from coherent to incoherent regime as discussed in Section 4.5.2, with each cutoff value indicated by the horizontal dashed line in each panel of Fig. 4.9. Using these as our critical values, we identify a specific temperature at which the transition likely occurs, as the first value within the incoherent region which crosses the indicated threshold. Although in some cases such numerical temperature identification perfectly overlaps (within our temperature and numerical resolution) across all panels (see $\Lambda = 15, 30$ cases), in most cases the different probed quantities yield slightly different numerical values for the critical temperature. Such an effect is accommodated by adding to each plot a coloured vertical band indicating the uncertainty, as discussed in Section 4.5.2, across all probed markers for a given value of Λ . In Fig. 4.9, we plot only a subset of the dimensionalities we consider for visual clarity in distinguishing the critical temperature bands. However, to establish a global picture of the systematic crossing of the phase transition across dimensionality we perform this analysis across each considered dimensionality.

Having located systematic crossings of the equilibrium statistics for each dimensionality considered, the identification of the critical temperature is then accessible as a function of the dimensionality parameter Λ as displayed in Fig. 4.10, with panels (a) and (b) based on two different numerically-generated datasets, differing in the way μ is changed when transitioning from 2D to 3D. Fig. 4.10(a) corresponds to results extracted from the data shown in Fig. 4.9, for which the chemical potential μ is defined according to Eq. (4.1) with μ_{2D} independent of Λ . Fig. 4.10(b) is based on a different protocol for our chemical potential choice, where we substitute the first term on the right-hand-side of Eq. (4.1) with a function of Λ that linearly interpolates from its quoted 2D value, μ_{2D} for $\Lambda = 1$, towards its 3D value $(3/2)\mu_{2D}$, assumed here to arise when $\Lambda = 50$ as discussed in Section 4.3.

Figure 4.9 (following page): Dependence of equilibrium parameters characterising the degree of phase coherence of the system as a function of absolute temperature, plotted for different values of the dimensionality parameter Λ . (a) Equilibrium condensate fraction N_0/N . (b) Ratio of lowest modes N_1 and N_0 . (c) Binder cumulant C_B . (d) Order parameter m normalised to the zero temperature result m_0 . The dashed horizontal line in each subplot corresponds to a cutoff value used to identify the transition for the respective equilibrium observable (with details of such choice discussed in Section 4.5.2). Each colour corresponds to a different value of dimensionality Λ as indicated in legend. Solid vertical coloured lines in each subplot correspond to the first numerical point deemed to have crossed the phase transition for the respective quantity towards the incoherent regime, thus marking the identification of the critical temperature for each value of Λ based on that physical quantity. Vertical coloured bands (where present) are identical throughout (a)-(d) and indicate the full range of numerically-identified critical temperature values across the different quantities plotted in (a)-(d). The midpoint of such band is subsequently chosen as our numerically identified critical temperature for each value of Λ .



This choice is designed to match the $T = 0$ Bogoliubov sound speed across the dimensional extremes (see Section 23.1 in [2]). The corresponding ratios of $\mu/\hbar\omega_z$ differ across the two panels, as shown by the upper labels.

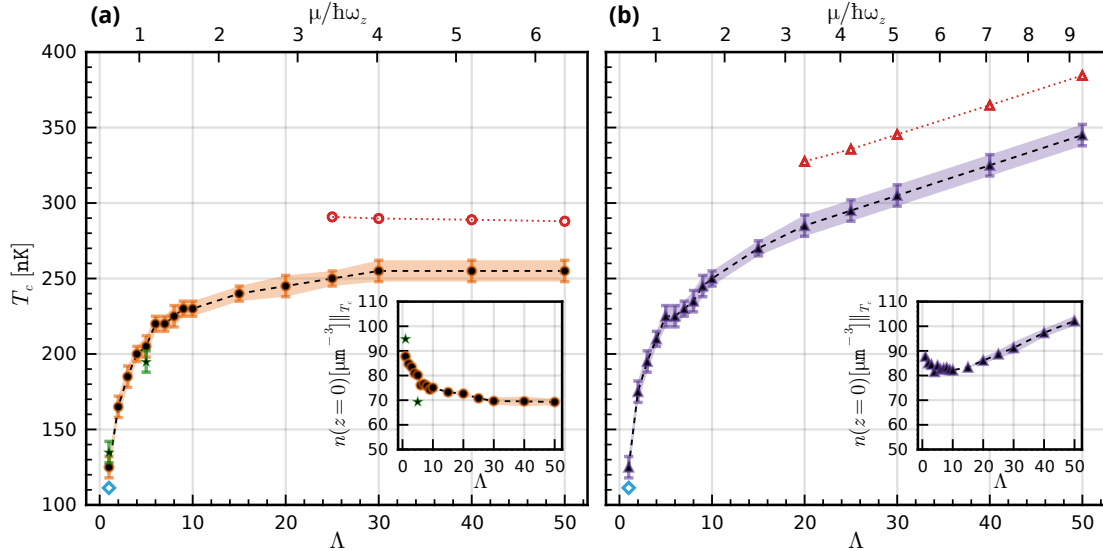


Figure 4.10: Numerically-extracted phase transition temperature T_c (main plots), and central densities (insets) as a function of dimensionality parameter Λ , for two different protocols for our choice of chemical potential μ based on Eq. (4.1). Specifically, they correspond to (see text): (a) a constant $\mu_{2D} = (4.64\mu m^{-2})\hbar^2/m$ value, and (b) a value linearly interpolated between such μ_{2D} value, for $\Lambda = 1$, and $(3/2)\mu_{2D}$, for our most 3D case with $\Lambda = 50$. In both cases, black filled points correspond to the mean extracted transition temperature as determined by the equilibrium statistics (Fig. 4.9), with dashed black lines as a guide to the eye. Error bars and shaded regions highlight the associated uncertainty, arising from a combination of the width of the bands in Fig. 4.9 and a systematic uncertainty of ± 5 nK due to our limited resolution in probing distinct temperatures. The Hollow blue diamond marks the analytical T_{BKT} transition temperature at $\Lambda = 1$, from Eq. (4.31). Red hollow points for $\mu/\hbar\omega_z > 3$, with dotted red lines as a guide to the eye, indicate the analytical 3D ideal gas temperature, T_{BEC} , in our chosen geometry, using the same total atom number N in Eq. (4.38) as in the corresponding SPGPE simulation for the same Λ . We highlight that the characteristic shift in our results compared to the ideal gas critical temperature is expected due to interaction and finite-size effects [240]. Green points in (a) correspond to further simulations with two different values of μ at small Λ aimed at demonstrating the limited sensitivity of the rapid initial growth of T_c with Λ on density. Insets: Total density at the centre of the trap; for each Λ , the point represent an average of the central density in a few SPGPE simulations for $T \sim T_c$, and the coloured bands indicate the corresponding numerical uncertainty.

In both cases the numerically identified critical temperature exhibits a very rapid increase with increasing value of Λ between the expected limits. For small Λ we recover the analytically-expected BKT transition temperature, given by Eq. (4.31) and marked by the leftmost hollow blue diamond. It is worth stressing that Eq. (4.31) is strictly applicable to the pure 2D gas; in our case, it can be safely used for a comparison with our $\Lambda = 1$ results, but it should not be used as a relevant scale when extrapolating across

dimensionality. We observe a monotonic increase of T_c with Λ as the system transitions to 3D, with the dominant increase in the critical temperature occurring for $\mu/\hbar\omega_z \lesssim 2$. As $\mu/\hbar\omega_z$ increases beyond that, the critical temperature dependence on Λ rapidly mimics the one expected analytically for an ideal Bose gas in the 3D limit as given by Eq. (4.38) for the given atom number (strictly valid in the $\Lambda \rightarrow \infty$ limit): these are marked, for $\mu/\hbar\omega_z > 3$, by the hollow red symbols in each subplot; note that the increase seen in panel (b) for large Λ is a direct consequence of our chemical potential protocol, associated with a linearly increasing density/atom number with Λ . As expected, our numerically-extracted values are consistently lower than the analytical ideal gas ones, due to finite-size and interactions effects.

The insets plot the dependence of the central condensate density, averaged along the planar directions and evaluated at the phase transition T_c for each given geometry, as a function of Λ , with the different observed behaviour arising from the different chemical potential protocols adopted. Although the densities exhibit up to 20% variation, it is important to highlight that the dominant dependence of T_c on Λ for small values of Λ is not a consequence of the changing density. To this aim, we have added two further *ad hoc* simulation points, spanning the density extrema in (a) and observe no noticeable change (within our uncertainties) to the numerically-extracted value for T_c . We thus directly conclude that the observed changes to the location of the phase transition are a consequence of dimensionality.

In the SPGPE formalism, care must be taken to ensure macroscopic occupation of modes below the cutoff. Nevertheless, the precise value of the cutoff may be somewhat arbitrary, and one should indeed ensure slight variations in cutoff do not overshadow the determination of quantities being probed. To ensure this is the case, we have varied the cutoff by $\pm 10\%$ for the specific case of $\Lambda = 5$ (firmly within the dimensionality crossover region) and, repeating our same scheme for locating the phase transition, find an indiscernible shift in identified critical temperature, which falls within numerical uncertainties for the critical temperature determination, as laid out in Section 4.5.2. This specific value of $\Lambda = 5$ lies within the region of largest variation in T_c as later evidenced by Fig. 4.10 and hence this relationship should hold across all dimensionalities we consider.

4.7 Chapter conclusions

In this chapter, we have revealed that a marginally stronger harmonic trapping strength can lead to large differences in phase transition temperature when exploring BKT physics. This is an important consideration in view of the current experiments with quasi-2D configurations. It is also worth noticing that the range $\mu/\hbar\omega_z$ where T_c ramps up toward the asymptotic 3D behaviour is the same where the healing length, ξ , becomes comparable to

the transverse size of the gas, ℓ_z ; in particular, for $\mu/\hbar\omega_z = 2$ the healing length at $T = 0$ is $\xi = \hbar/\sqrt{2mgn(0)} \sim (1/2)\ell_z$. In terms of vortices, as mentioned earlier when commenting about Fig. 4.1, this implies a transition from point-like defects in a 2D background to vortical filaments in a 3D superfluid. This is not surprising, but our simulations provide a quantitative and systematic description of the dimensional crossover in terms of equilibrium properties, going beyond the known qualitative picture. In addition, Fig. 4.10 also suggests an interpretation of the behaviour of T_c in terms of BEC vs. BKT physics. In the large Λ limit, if one cools down the Bose gas close to T_c , the quantum degeneracy manifests itself almost at the same temperature at which the lowest state becomes macroscopically occupied and the BEC soon forms together with the superfluid phase. Conversely, for small Λ , due to stronger effects of fluctuations, quantum degeneracy is associated to a quasi-condensation, where many modes have large occupation; one then needs to cool the gas further in order to allow the system to develop coherence and superfluidity as a result of vortex-pair binding. For gases with similar densities, as in our simulations, this implies a critical temperature lower in 2D than in 3D. This is also consistent with the results obtained by Delfino *et al* [203] for a weakly interacting Bose gas confined within a slab geometry (an anisotropic $L^2 \times Z$ lattices with $Z \ll L$ governed by a Bose-Hubbard Hamiltonian), where T_{BKT} was also found to depend on the slab thickness, approaching T_{BEC} from below in the 3D limit.

The final topic in this thesis will build upon the results of this chapter. With the phase transition across dimensionality successfully extracted, we are now able to build a systematic picture of how the sound speed might change in response to a dimensional crossover. In the 2D limit, it was thought that the second sound, associated to collective excitations on top of the coherent modes of the system, would vanish at the phase transition [241]. However, recent articles have suggested a continuity of the second sound across the phase transition [26, 27] facilitated through a quasi-condensate. The following chapter will reformulate this problem in terms of a numerically extracted phase transition temperature, instead of the analytic predictions of BKT. In addition, through a variation of Λ , we will probe the effects of dimensionality on the character of the sound across temperature.

Chapter 5

Characterisation of sound speed in the weakly interacting Bose gas through the 2D-3D dimensionality crossover

In this chapter we again investigate the dimensional crossover of the trapped ultracold Bose gas; this time focusing on the dynamical response of the system to a small-amplitude perturbation. Such a perturbation will generate a phonon-like density wave propagating at the sound speed. We systematically probe the effects of a dimensional crossover on the propagation of sound within the same system as Chapter 4. Here we use our numerically extracted phase transition temperature to explore the nature of sound close to the phase transition. The findings of this chapter are preliminary and our results are currently being written up to form a paper on the nature of sound through the phase transition dimensionality crossover from 2D-3D.

5.1 Propagation of sound in quantum fluids

One of the hallmarks of superfluidity in quantum systems is the second sound, as predicted by the two-fluid hydrodynamic theory of Landau [32, 242]. The second sound has been observed in both liquid helium experiments and atomic gases [32, 243–246]. Hydrodynamic two-fluid theory stipulates that a fluid below T_c is comprised of both a normal part and a superfluid part, where the two are in thermodynamic equilibrium. The two sound speeds derived through this theory pertain to different variations of the total density and entropy per particle. That is, in homogeneous gases [247], the first sound is a pure density wave and the second sound is a pure entropy wave. Specific to the case of a weakly interacting

Bose gas, the first and second sounds are essentially uncoupled oscillations of the thermal cloud and condensate respectively [248]. In fact, the second sound is the low-frequency continuation of the low-temperature Bogoliubov symmetry-breaking mode as discussed in Section 1.6. Above T_c , the normal fluid supports just the regular density wave oscillations, and hence the second sound is exactly a phenomenological manifestation of superfluidity.

5.2 Collisional regimes

Here we take the opportunity to briefly introduce the differences between a hydrodynamic and collisionless regime. Typically, one may consider a fluid to be in the collisional hydrodynamic regime if the mean rate between interactions of fluid particles Γ_{coll} is much larger than the typical timescales of the fluid dynamics ω^{-1} . Here ω is the frequency of the sound $c = k/\omega$, with wavevector k . Conversely, a fluid is said to be in the collisionless regime if instead the collisions between particles are much slower than the typical dynamical timescales of the fluid. It is worth clarifying that the term collisionless does not correspond to a lack of interactions, but rather simply that collisions are rare. Formally we can consider these individual regimes as

$$\begin{aligned} \Gamma_{\text{coll}} \gg \omega & \quad \text{Hydrodynamic collisional} \\ \Gamma_{\text{coll}} \ll \omega & \quad \text{Collisionless.} \end{aligned} \tag{5.1}$$

In the 2D study conducted by Ville *et al* [26] at $\Lambda = 1$ which serves as our baseline for the exploration of dimensionality, the authors report a collisional rate $\Gamma_{\text{coll}} \sim 1.6\text{--}3.4\omega$, placing them in a crossover region between the hydrodynamic and collisionless regimes. This is important, as in the hydrodynamic picture, one expects Landau damping [249]. This form of damping is associated with the decay of low-lying collective excitations via scattering events upon thermal excitations at the same frequency. As temperature increases, the number of thermal excitations increases in tandem, leading to a decrease in measured quality factor for a perturbation at higher temperature. Therefore, agreement with the predictions of damping rate for an excitation across temperature provides strong evidence for the hydrodynamic regime in which an experiment is thought to reside.

5.3 Experimental works on the second sound as a function of temperature

In this section we review previous studies which specifically aim to measure the speed of sound in a trapped ultracold atomic Bose gas. We pay particular attention to the collisional regime reported in each, since the hydrodynamic picture of each experimental configuration largely determines the nature of sound speed across temperature.

5.3.1 Experiments in quasi-1D geometry

The experimental measurement of sound speed was an alluring topic shortly after the first experimental realisation of a BEC. It offers a fundamental viewpoint to study the effects of collective dynamics within a system and acts as a reliable tool to probe superfluid properties. In the field of weakly interacting Bose gases, the first measurement of sound was achieved by the group of Ketterle at MIT [250] and later explored by the group of van der Straten [251] at Utrecht University¹ at finite temperature. In each experiment, they observe how, in a highly elongated 1D anharmonic trap, a density defect propagates spatiotemporally. Both measurements were in close agreement with the prediction of Bogoliubov theory for the phonon-speed. However, due to the anisotropic nature of the trapping potential, a large amount of effort was expended to account for the inhomogeneity of the generated sound wave. The experimental protocol of Meppelink *et al* [251] involved preparing the condensate in the presence of an optical repulsive dipole potential, positioned centrally within a strongly anisotropic 1D harmonic trap. Upon releasing this potential, an outwards travelling density wave is produced. The shape of this initial gaussian perturbation deforms during the propagation due to the dependence of the sound speed on density. This causes the centre of the dip to move slower than the outer edges, leading to an eventual shockwave when the density gradient between the centre and the edges is of the order ξ^{-1} . The authors argue that, taking this effect into account, they accurately measure the second sound to be systematically within 7% of the Bogoliubov sound speed for the given condensate density. In this experiment, the authors report a hydrodynamicity $\tilde{\Gamma} \leq 10$ in the axial direction and the authors find that the experimental data is best described by hydrodynamic Landau theory. However, due to large uncertainty in the measurement in the modest temperature range, it is difficult to conclude that they are truly in the collisional regime. This can be seen from the overlapping diamonds and squares within the experimental data in Fig. 5.1 corresponding to the predictions from Landau and collisionless ZNG theory respectively.

The ZNG theory is encapsulated in the broader literature of finite temperature non-equilibrium theory developed by the group of Zaremba, Nikuni and Griffin. Popularly referred to as the ZNG model [252–256], this theory stemmed from the work of Kirkpatrick and Dorfman [257] who extended two-fluid hydrodynamic theory to the dilute Bose gas. We highlight that studying the propagation of sound in this framework is beyond the scope of this thesis. This is predominantly due to the fact that the ZNG approach relies on the existence of a well-defined condensate, which is unsuitable in the framework of a quasi-2D theory due to the preclusion of condensation in the 2D limit at finite temperatures.

¹Atom Optics and Ultrafast Dynamics, Utrecht University, The Netherlands.

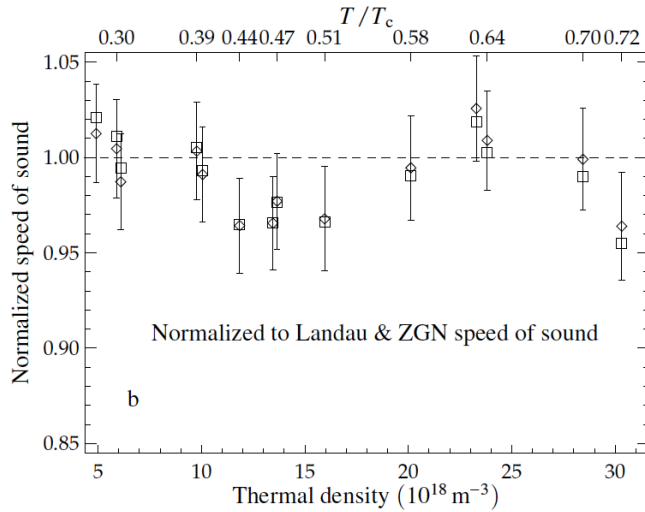


Figure 5.1: [Reprinted figure with permission from [251] Copyright (2022) by the American Physical Society.] Measured phonon velocity as a function of the thermal density. Sound speed is normalised for each data point to both the second sound speed calculated from hydrodynamic Landau and Zaremba-Nikuni-Griffin theory, showing agreement with both.

5.3.2 Experiments in quasi-2D geometry

With the recent developments of box potentials for Bose gases [3, 4, 171], a new playground of experiments probing sound speed has opened up. The homogeneous background density in these configurations leads to a more careful extraction of the sound speeds and has been a topic of great interest. We now pay particular attention to a number of works in the 2D limit. The first, conducted by the Paris experimental group of Dalibard [26], entails the probing of sound speed in a two dimensional Bose gas. In this work, they report a second sound mode in both the superfluid and normal phases. Deep within the superfluid regime, the sound speed agrees well with the Bogoliubov prediction. With increasing temperature, they measure a decrease in the sound speed consistent with the predictions of two-fluid hydrodynamic theory where the damping of the sound mode increases with temperature, equivalent to Landau damping. Most interestingly, on crossing the BKT critical point, they measure a non-vanishing strongly damped density wave, suggesting a departure from hydrodynamic theory. As previously remarked in Section 5.2, the authors quote an estimated collision rate $\Gamma_{coll} \approx (1.6 - 3.4)\omega$, likely placing the experiment within the collisionless regime. The experiment consists of a rectangular box trap with an additional step-like potential spanning 1/4 of the box length engineered to reduce density in this perturbed region to 1/3 of the background density. The study of the propagation and subsequent damping of this perturbation reveals information about the second sound for the system. In Figure 5.2 we see a clear decrease in measured sound with increasing temperature, matching the prediction of hydrodynamic theory closely up until the critical

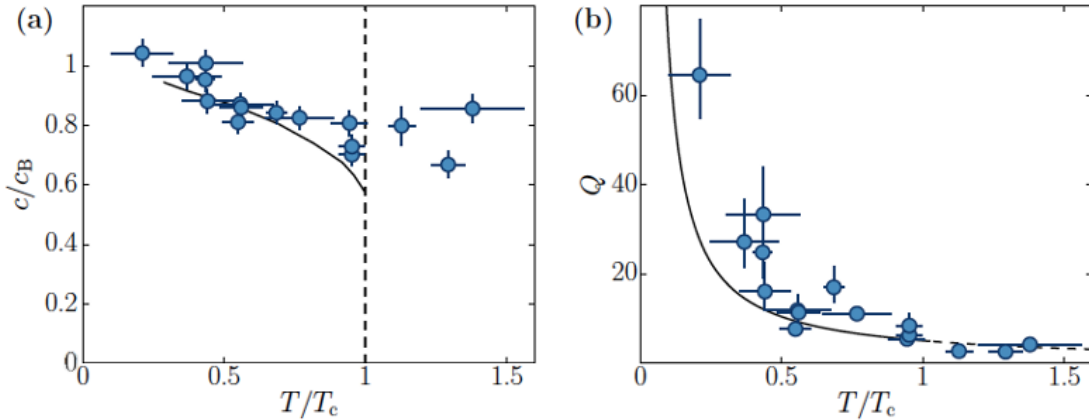


Figure 5.2: [Reprinted figure with permission from [26] Copyright (2022) by the American Physical Society.] (a) Measured speed of sound c normalised to Bogoliubov phonon speed. Vertical dashed line highlights the position of the BKT critical point. The solid line shows the result from Landau two-fluid hydrodynamic theory applied to the 2D Bose gas. Blue data points are experimental data with corresponding error bars showing statistical uncertainty of fitting procedures to extract the measured quantities. (b) Extracted quality factor Q from experimental data shown through blue data points with errorbars indicating statistical uncertainty. Result for Landau damping is depicted as a solid line below the transition and a dashed line above the transition.

point. At this point, we deviate from the hydrodynamic theory and a non-vanishing sound speed is measured across the transition. The decreasing quality factor of sound mode is consistent with Landau damping. It appears then, that this experiment falls within the collisionless regime. Another experiment aiming to investigate the propagation of sound in quasi-2D boxes comes from the group of Hadzibabic in Cambridge [218]. Here, they measure both the first and second sound as a function of temperature and in addition observe the superfluid density jump inherent to the BKT transition. Interestingly, in this experimental study they report the expected discontinuity in second sound across the transition. In this paper, the reported dimensionless interaction strength is $\tilde{g} = 0.64$ and measured density $n \approx 3\mu\text{m}^{-2}$. As such they report an elastic collision rate which is sufficient for collisional hydrodynamic behaviour, with a reported collisional rate of $\Gamma_{\text{coll}} \approx 4\omega$. In this experiment, the longest-wavelength sound mode $k = \pi/L_y$ is induced through sinusoidal oscillation of the trap. Through measuring the absorptive response on either side of the transition as shown in Fig. 5.3a, it is clear that there is a vanishing peak associated to the second sound. This is exemplified further on the comparison with the dynamical structure factor in Fig. 5.3b. In this Figure, we see the strong peak at $\omega = 0$ correspondent with the diffusive mode above T_c . The included inset, which considers the fitted contributions to the dynamical structure factor with the first sound contributions omitted reveals the clear and distinct peaks corresponding to the vanishing second sound across the phase transition. In the same work, the authors provide the first measurement of a superfluid density within an atomic 2D Bose gas. As such, they were able to measure the superfluid density

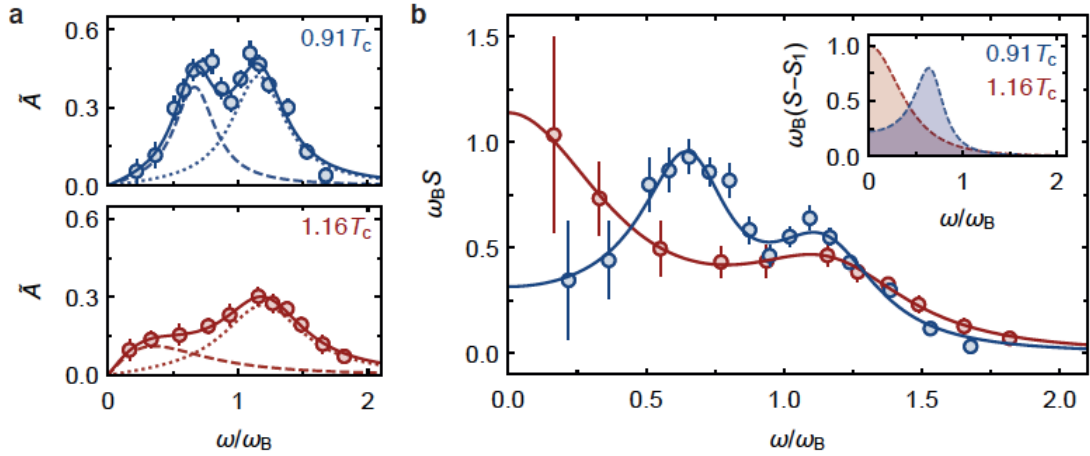


Figure 5.3: [Reprinted by permission from Nature: [218], Copyright (2022)] (a) Normalised response spectra both below (top) and above (bottom) the phase transition plotted against frequency normalised by the Bogoliubov frequency ω_B . Depicts two resonances corresponding to the first (dotted) and second (dashed) sound for each case. (b) Dynamical structure factors. Here, we see a clear peak for the diffusive mode at $\omega = 0$ which is distinct from the second sound mode below the transition. Inset displays fitted contributions to the dynamical structure factor with the first-sound contributions removed for clarity.

as a function of temperature to reveal the superfluid density jump as predicted by Landau two-fluid hydrodynamics. This measurement strengthens the finding that this experiment is truly within the collisionless hydrodynamic regime and thus meets the predictions of the corresponding hydrodynamic theory as we have seen.

5.4 Excitation protocol

To emulate the previous experimental forays into the analysis of the second sound of a Bose gas, we choose to excite our system with a low amplitude perturbation to selectively excite the lowest accessible mode. We reformulate our previous potential given by Eq. (3.19) with the addition of a sinusoidal perturbation and a modified in-plane confinement. As such we write

$$V(\mathbf{r}, t) = V_{\text{box}}(x, y) + \frac{1}{2}m \left(\frac{\omega_{\text{ref}}}{\Lambda} \right)^2 z^2 + V_{\text{pert}}(x), \quad (5.2)$$

where the perturbation we add to the system is designed to excite the lowest-frequency standing wave we can fit within our system and takes the form

$$V_{\text{pert}}(x, t) = 0.05\mu \sin \left(\frac{2\pi x}{L_x} \right). \quad (5.3)$$

Our value of excitation amplitude is half as strong as that employed in a previous analysis of the 2D reference system [161] in which it was found that the amplitude is sufficiently

weak enough to minimise coupling to other modes of the system. Whereas the previous study performed calculations in a periodic box, where Fourier transforms can plague dynamics with spurious behaviour, we work in the embedded box in order to minimise coupling outside of the system domain. Moreover, in experimental trapping geometries, in-planar trapping is provided by a DMD which does not have infinitely sharp walls. To emulate this behaviour, we make a modification to the in-plane confinement by introducing a \tanh^2 -ramp at the edges of the planar box to replace the previous hard-wall confinement. In this case, the confinement of the planar box more accurately portrays the DMD confinement typically used in 2D experiments and minimises numerical anomalies in the reflection of sound waves at the boundaries. The modified boundary can be evaluated by

$$\Xi = 30\mu \left(\min \left\{ 1, 4 - \tanh^2 \left(\frac{x \pm (L_x + \frac{w}{2})}{w} \right) - \tanh^2 \left(\frac{y \pm (L_y + \frac{w}{2})}{w} \right) \right\} \right) \quad (5.4)$$

such that

$$V_{\text{box}}(x, y) = \begin{cases} \Xi, & -\frac{L_x}{2} \leq x \leq \frac{L_x}{2}, -\frac{L_y}{2} \leq y \leq \frac{L_y}{2} \\ 30\mu, & \text{otherwise,} \end{cases} \quad (5.5)$$

where w is a width parameter and is chosen to be $0.2\mu\text{m}$ to minimally affect atom number but provide a significant ramping of the density at the boundary. The full potential of Eq. (5.2) at the $z = 0$ plane is depicted in Fig. 5.4. Notice that the amplitude of the excitation is barely visible in comparison to the hard-wall potential boundary and the excitation excites a standing sine wave in the range of the embedded box (L_x, L_y) as opposed to the auxiliary box in which it is embedded of size $(\mathcal{L}_x, \mathcal{L}_y)$.

In order to prepare equilibrated realisations in the presence of the perturbation, we take each of the \mathcal{C} -field wavefunctions of the previous chapter and evolve for another $25\tau_\gamma$ to rethermalise in the presence of the sinusoidal perturbation. This procedure is explained in greater detail in Appendix A. It is clear, that for systems with lower dimensionality and thus a lower chemical potential, the effect of the excitation is amplified, due to the nature of the chemical potential across dimensionality as provided by Eq. (4.16).

5.5 Dynamical evolution

Once equilibrium has been reached in the presence of the modified potential, we are now free to explore the dynamical properties of the given system. Whilst equilibration takes place under SPGPE theory we, akin to other works [27, 166, 186, 191, 258], evolve the \mathcal{C} -field in the absence of dissipation and noise by setting $\gamma = 0$. This decoupling to the \mathcal{I} -field allows a conservation in atomic density, which might otherwise exhibit large fluctuations. Therefore we propagate the state forward with just a projected Gross-Pitaevskii equation

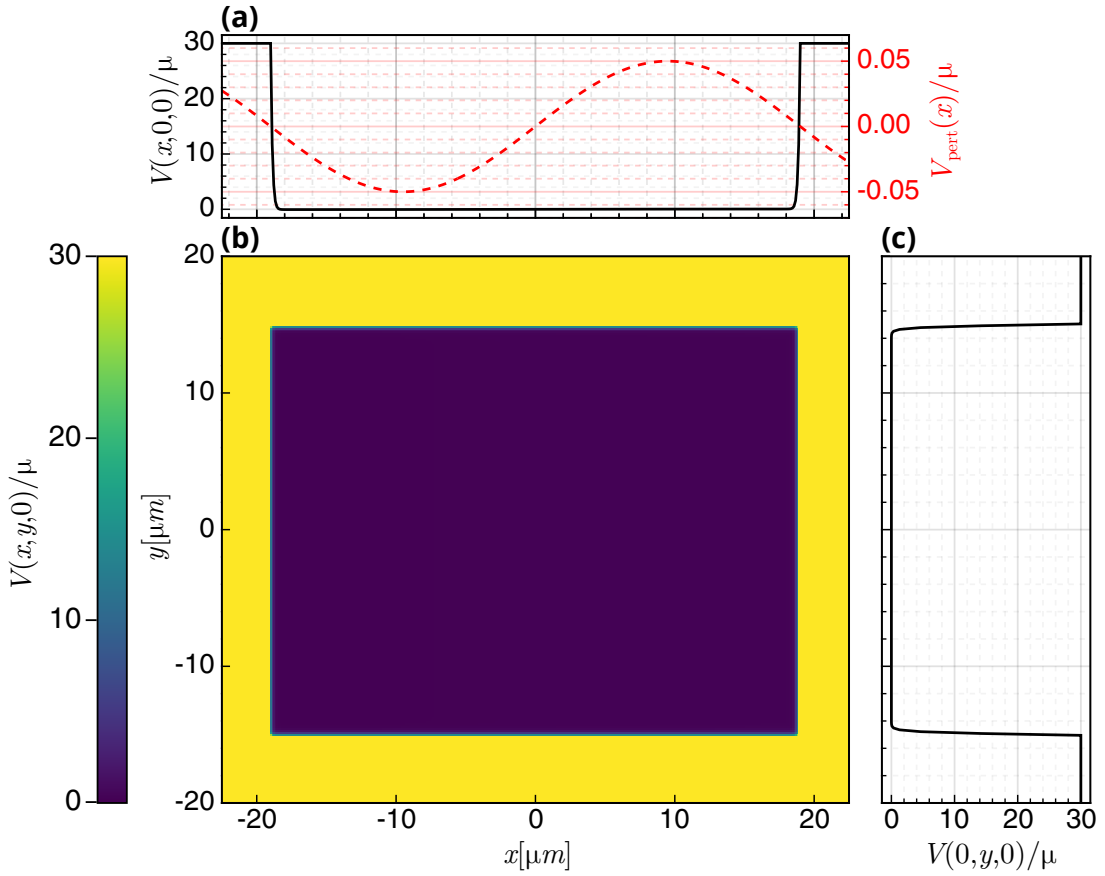


Figure 5.4: For the trapping specified by Eq. (5.2) we plot (a) the central points along the x -axis in black. In red we also plot the sinusoidal perturbation V_{pert} . In (b) we plot the shape of the trapping potential along along the $z = 0$ plane. In (c) we display the trapping profile along the y direction. Each subplot is normalised to the chemical potential μ .

when considering dynamics. By an instantaneous removal of the sinusoidal perturbation we produce a standing wave along the x -direction. Monitoring the speed and damping of the resultant density wave across both dimensionality and temperature, we may elucidate the character of the second sound through the phase transition dimensionality crossover. The density profile of the system oscillates in time, due to the singular mode excited. This can be seen clearly for each value of dimensionality, for which a subset is shown as a carpet plot for choice values of Λ in Fig. 5.5. We also note here, that since we only consider the evolution of the \mathcal{C} -field, it is not possible to extract the first sound speed due to the projection operator casting out the dynamics of the thermal modes. From the evolution of the density along the excited x direction, we extract the amplitude of the first mode using a Fourier analysis and normalise by the maximum ($t = 0$) value A_0 to generate $\hat{A} = A/A_0$. Typical dynamical evolutions of this quantity are demonstrated for a range of dimensionalities at various temperatures in Fig. 5.6. From the shape of the curves

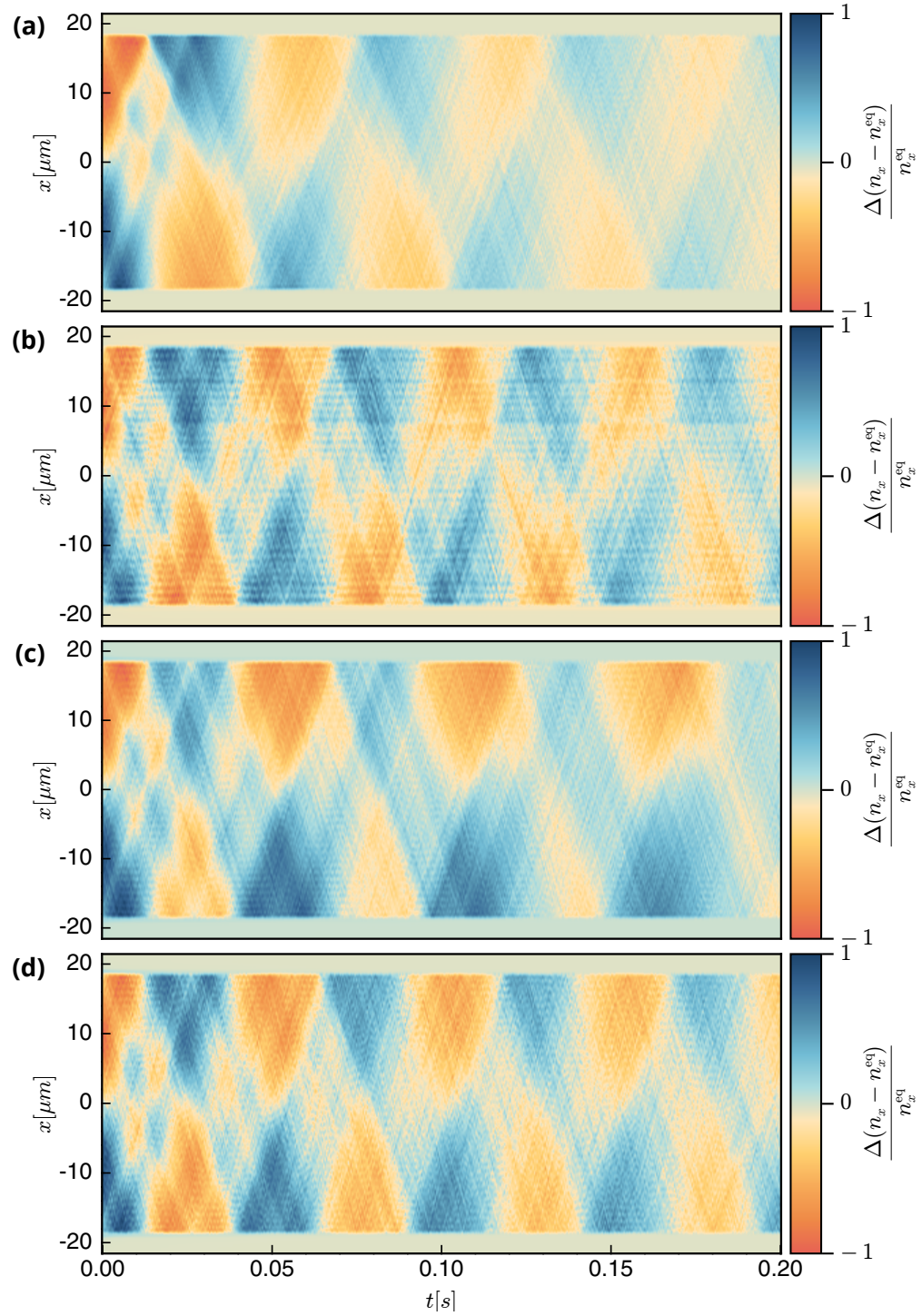


Figure 5.5: Density profiles along the x -direction as a function of time. The density is differenced with and normalised to the ensemble-averaged equilibrium solution n_x^{eq} for the cases of (a) $\Lambda = 1$, (b) $\Lambda = 10$, (c) $\Lambda = 25$, (d) $\Lambda = 50$ at temperatures corresponding to $T/T_c = 0.4$, $T/T_c = 0.4$, $T/T_c = 0.41$, $T/T_c = 0.41$ of their numerically identified transition temperature respectively.

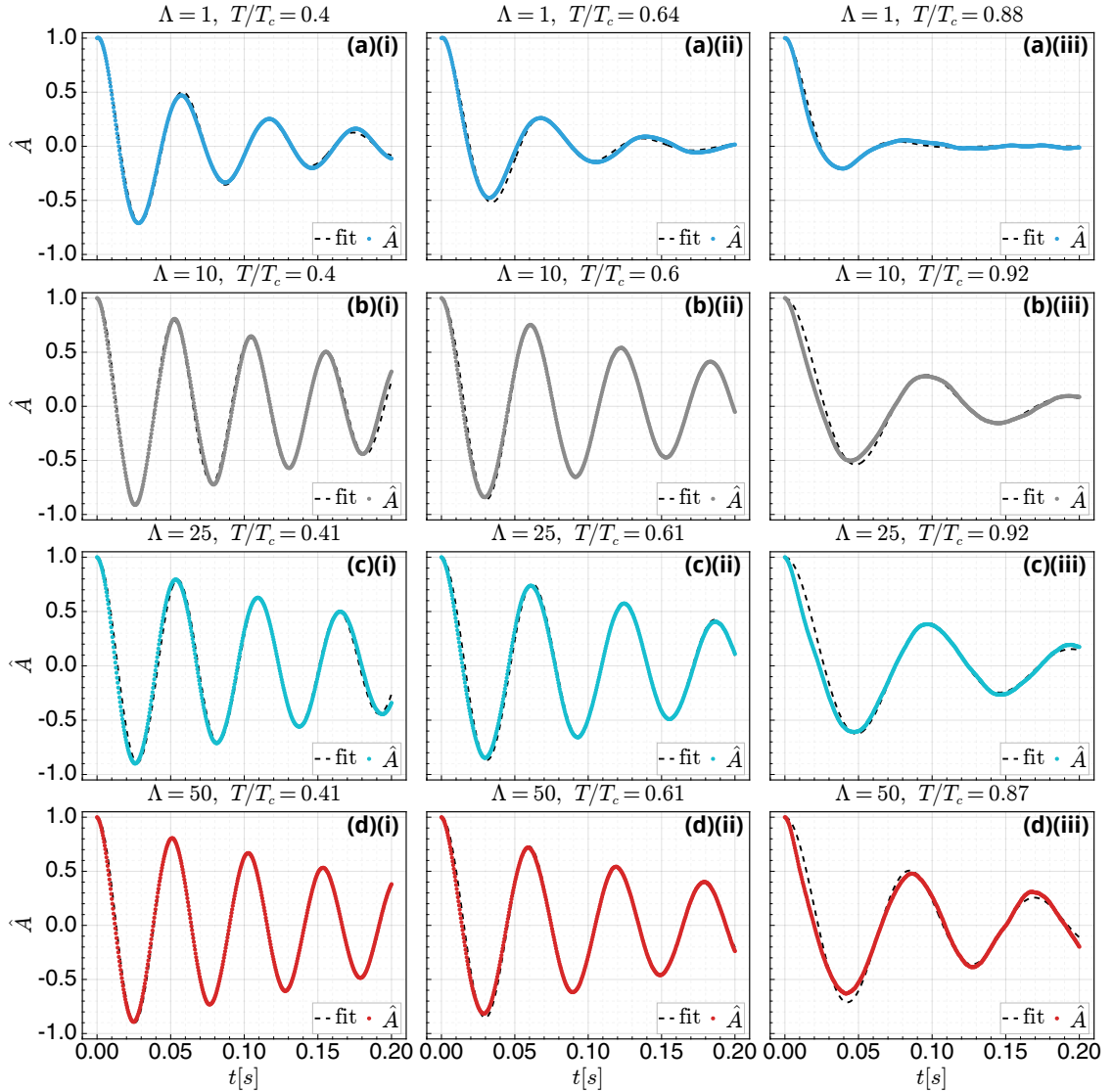


Figure 5.6: For the same values of Λ as in Fig. 5.5, we plot the dynamical evolution of the amplitude of the normalised first Fourier mode \hat{A} for three selected equivalent temperatures. In row (a) we plot, for $\Lambda = 1$, the response at temperatures (i) $T/T_c = 0.4$, (ii) $T/T_c = 0.64$, (iii) $T/T_c = 0.88$. In row (b) we plot, for $\Lambda = 10$, the response at temperatures (i) $T/T_c = 0.4$, (ii) $T/T_c = 0.6$, (iii) $T/T_c = 0.92$. In row (c) we plot, for $\Lambda = 25$, the response at temperatures (i) $T/T_c = 0.41$, (ii) $T/T_c = 0.61$, (iii) $T/T_c = 0.92$. In row (d) we plot, for $\Lambda = 50$, the response at temperatures (i) $T/T_c = 0.41$, (ii) $T/T_c = 0.61$, (iii) $T/T_c = 0.87$. In each plot, the temperature is normalised by the critical temperatures for the given Λ as extracted and presented in Fig. 4.10(b).

produced, it becomes convenient to introduce the fitting function of a damped harmonic oscillator via

$$\mathcal{F}_{\text{DHO}} = e^{-t/\tau} \left(\cos(\omega t) + \frac{1}{\omega\tau} \sin(\omega t) \right) \quad (5.6)$$

to track the lifetime of the excitation on the density profile. This fitting function was also used in the previous analysis of standing wave oscillations in the trapping-configuration of Ville *et al* [26, 27] and so our analysis is consistent with their methodology. In this expression, we have the decay and oscillation frequency of the standing wave, symbolised by τ and $\omega/2\pi$ respectively. The damping rate can thus simply be defined as $1/\tau$ and the quality factor follows as

$$Q = \omega\tau. \quad (5.7)$$

This quantity expresses the energy loss in a single cycle of the harmonic oscillator, relative to the total energy within the system. From the frequency, it becomes possible to extract the second sound speed via

$$c = \frac{L_x\omega}{\pi}, \quad (5.8)$$

which we will subsequently normalise by the Bogoliubov sound speed c_B extracted from zero-temperature PGPE simulations.

These zero temperature PGPE simulations are performed with the same parameters as previously specified in Chapter 4 for each considered Λ . The relationship between dimensionality and Bogoliubov sound speed for these simulations is presented by Fig. 5.7 in blue. In addition, we plot the result corresponding to the analytic formula of Eq. (1.115) in red. Here we see a reasonably stable Bogoliubov sound through the dimensionality crossover for both definitions. Improvement could be gained in future work through a more careful interpolation than the linear one we implemented with Eq. (4.16).

At low temperatures, where the macroscopic occupation of all modes below the cutoff fails in the SPGPE theory, we omit ensembles where an undesirable coupling to transverse modes is detected. In our analysis, we restrict the extraction of fitting parameters to cases where $Q > 1$. In cases where $Q < 1$, we consider the sound to be overdamped and thus the calculation of a sound speed is no longer feasible. The falloff in excitation amplitude for the case of $\Lambda = 1$ is visible in Fig. 5.8 where we plot the evolution of $\hat{\Lambda}$ for each temperature where a valid quality factor is measured. Here we see a pronounced increase in the damping as the phase transition is approached from below, leading to an immeasurable sound speed very close to the critical point.

5.6 Effects of dimensionality on the second sound speed

Our systematic analysis of the effects of dimensionality on the second sound begins by checking our method against one in the pure 2D formalism. We remark here, that since we achieve comparable atomic densities and the same interaction strength across dimensionality, we expect to remain within the same hydrodynamic regime. In our quasi-2D

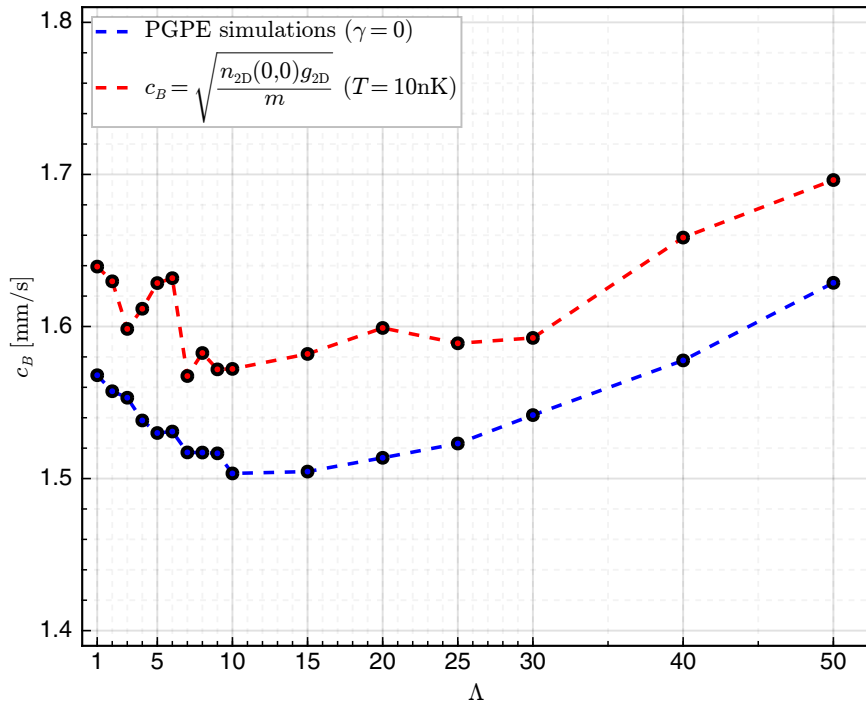


Figure 5.7: Bogoliubov sound speed c_B as a function of dimensionality, calculated for two different methodologies. In blue we plot the values used in our work, corresponding to zero-temperature PGPE simulations with the same parameters. In red we plot the analytical result of Eq. (1.115) from total central densities of our simulations at $T = 10\text{nK}$.

system, we can estimate the hydrodynamic parameter [259] with

$$\Gamma_{\text{coll}} \simeq \sqrt{\frac{1}{n_{2\text{D}} \tilde{g}_{2\text{D}}^3} \frac{2\pi}{L_x}} \approx 0.48. \quad (5.9)$$

With this value, it is most probable that our work takes place within the collisionless regime. In Fig. 5.9, we compare our measurement of second sound in the 2D limit ($\Lambda = 1$) with previous works [27, 161] and see a close agreement. Our data, shown in blue, reports a sound speed approximately 10% smaller across temperature than that reported by Ota *et al* [27], shown in red. Here the simulations used to extract the sound speed vary somewhat, in that a single standing wave is excited within a fully periodic box. In green, we plot the data from Larcher [161]. Here a step-like potential barrier as previously described in Section 5.3.2 is used to excite the lowest system modes within a computationally embedded box, like ours. In this case we report a much closer agreement with the measured sound. This qualitative agreement with both sets of results is promising and suggests that our full 3D formalism correctly reduces to the 2D theory in low dimensionality. Additionally, we also report a close agreement with the result of Landau theory for the hydrodynamic second sound [241, 260] below the phase transition as plotted in black. Most importantly

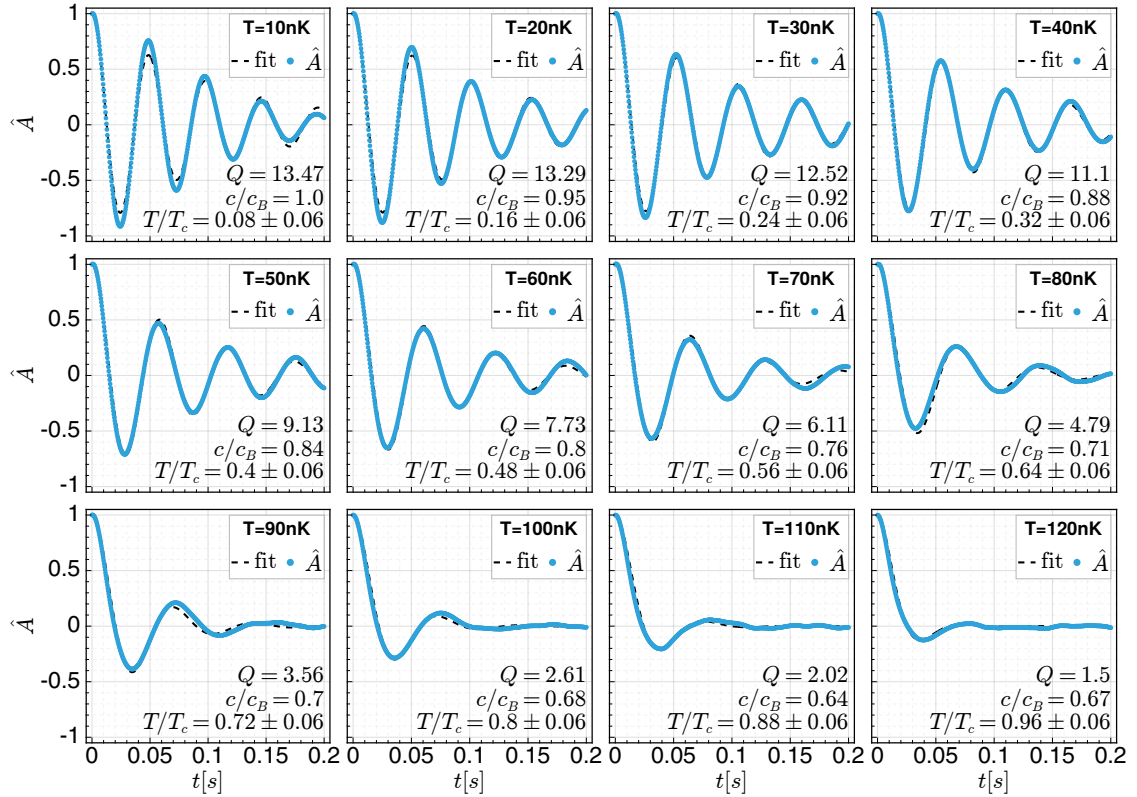


Figure 5.8: Oscillation of the normalised amplitude \hat{A} as defined in the text of Section 5.5 for $\Lambda = 1$. Extracted points are plotted in blue for each value of temperature where the quality factor $Q > 1$. The dashed black line for each subplot indicates the fit provided by Eq. (5.6). The measured sound speed, quality factor and normalised temperature are overlayed with text for each individual subplot.

however, we report a continuity in the second sound across the analytically defined BKT phase transition, as was previously unexpected in the hydrodynamic regime [241, 261]. This continuation was previously attributed to the presence of a quasi-condensate across the phase transition [26].

In the 3D limit ($\Lambda = 50$), we expect for the sound speed to disappear across the transition. Therefore, one might expect an interesting behaviour in the nature of sound at the phase transition in the dimensionality crossover. To verify this hypothesis, we perform our dynamical procedure as in Section 5.5 for each value of dimensionality and temperature employed. In doing so, we are able to recover a global parameter-space relationship between the sound speed across the phase transition and the system dimensionality. Differently from Fig. 5.9, we henceforth normalise temperature to the numerically extracted phase transition temperature as reported in Fig. 4.10(b). In Fig. 5.10 we plot the behaviour of the sound across temperature for each considered dimensionality. Here we observe, for values of dimensionality $\Lambda > 1$, a universality in the measured second sound speed as

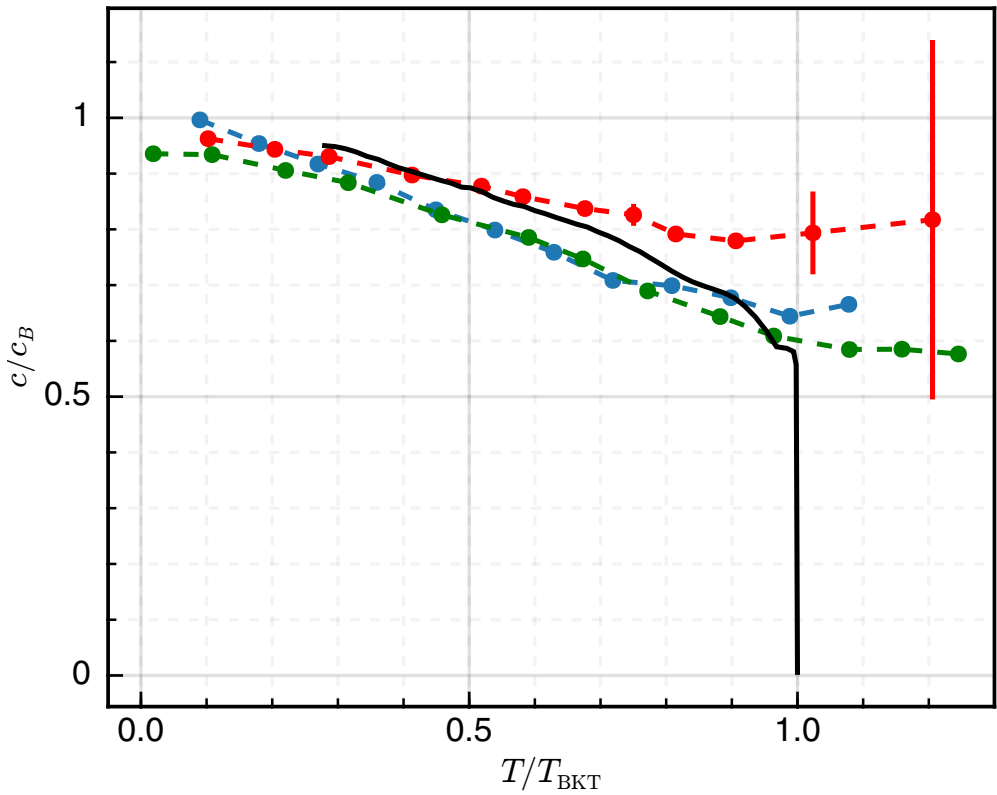


Figure 5.9: Sound speed normalised to the Bogoliubov sound speed is plotted in red, blue and green as a function of Temperature. In each case, temperature is normalised to the analytical BKT phase transition temperature T_{BKT} as identified by Eq. (4.30). In green we plot the 2D results reported in [161] which closely emulates the experiment of Ville *et al* [26]. In red we plot the results published in [27], which use a more careful excitation protocol exciting the lowest modes through a sinusoidal perturbation with errorbars to represent statistical uncertainty. In black we plot the expected hydrodynamic result from [241]. In blue we plot our results as extracted from the fitting function specified by Eq. (5.6) with vertical errorbars to reflect the 95% confidence interval; they are globally of the same order as the marker size.

a function of temperature between the ranges $0.4T_c \lesssim T \lesssim 0.9T_c$. Below this temperature, there are spurious results as one would expect when applying the high-temperature SPGPE theory to low temperatures. We reiterate that specific low-temperature ensembles have been removed where a coupling to transverse modes was manually detected. For low values of Λ , larger sound speeds are reported close to the phase transition before a loss of measurable sound due to overdamping across the phase transition. Most strikingly, whereas Ville *et al* [26] measured a continuity across the phase transition, we report no such behaviour. We surmise that this is due to the overdamped nature of the system beyond the phase transition temperature (T_c) which was identified by our systematic analysis in Chapter 4 as opposed to the analytic BKT result (T_{BKT}) of Eq. 4.30. As dimensionality increases, we see an overall decrease in the sound speed close to the transition and

again no evidence of continuity in the second sound at any Λ through the dimensionality crossover. Moreover, we also report a distinct characteristic uptick in the second sound, clearly visible in the inset plot of Fig. 5.10, just before the transition. To our knowledge, this uptick remains unreported in the literature and highlights an interesting avenue of inquiry for future work.

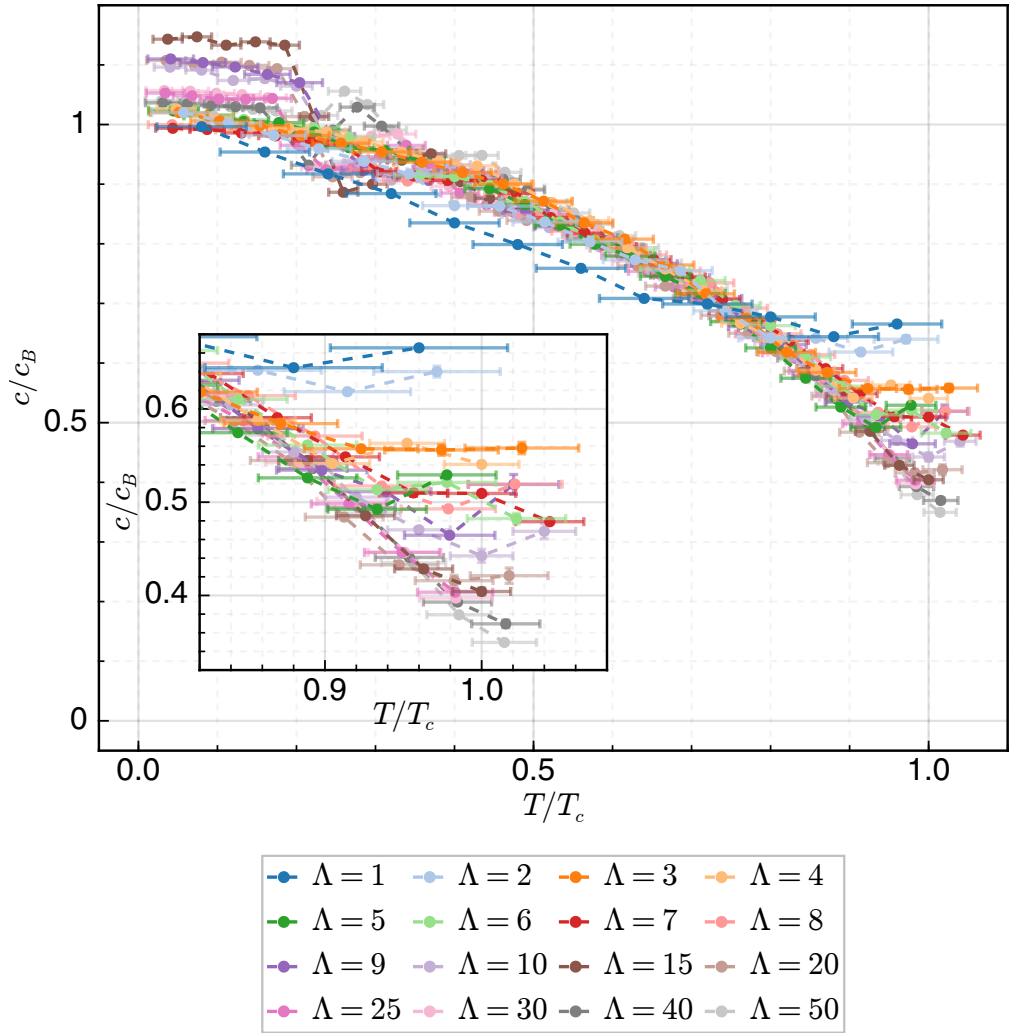


Figure 5.10: Sound speed normalised by the zero temperature Bogoliubov sound speed for each considered dimensionality as a function of temperature. In this case, temperature has been normalised to the numerically extracted phase transition temperature T_c . Vertical errorbars correspond to 95% confidence intervals in the fitting function specified by Eq. 5.6. Horizontal errorbars correspond to the uncertainty in numerically extracted value of transition temperature T_c as previously extracted and plotted in Fig. 4.10. Inset plots the same data zoomed-in at the phase transition in order to aid visibility.

As well as considering the second sound speed, we are able to track the level of damping in the system, as provided by the fitting parameter τ . The response of damping rate

to changes in dimensionality and temperature is reported in Fig. 5.11. For low dimensionalities, we see a continuous and monotonic increase in the damping rate as we cross the phase transition. As dimensionality increases, we see a sharper crossover into high damping across the phase transition.

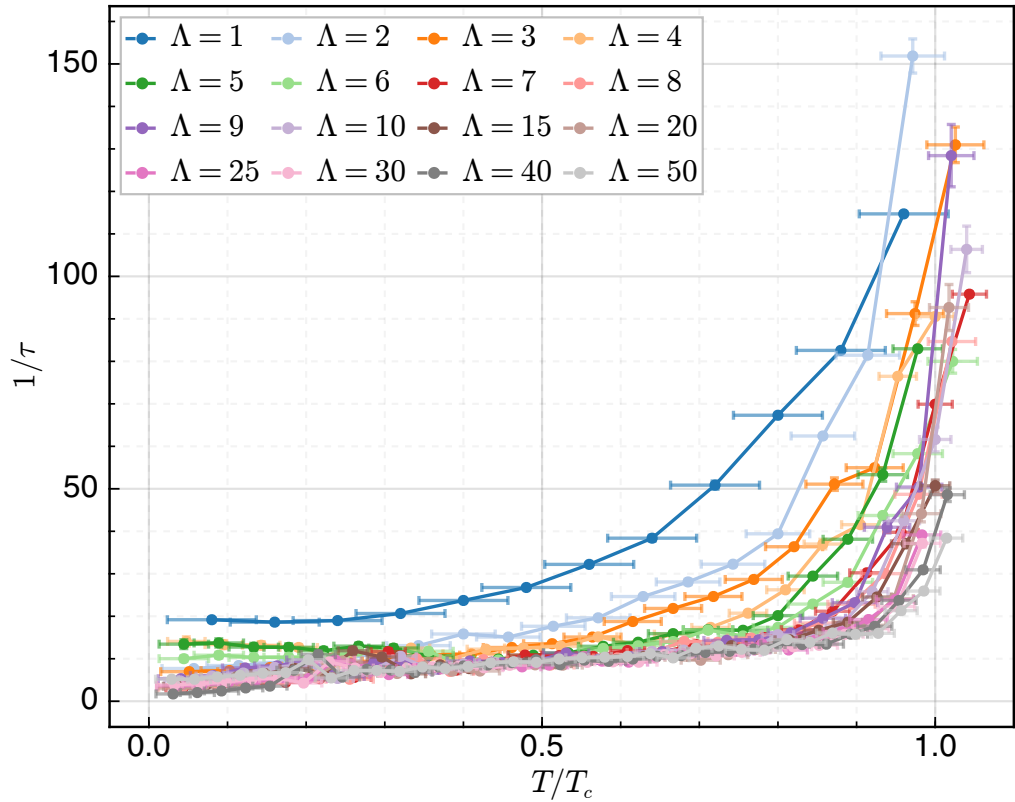


Figure 5.11: Damping rate $1/\tau$ for each considered dimensionality across temperature. Vertical errorbars correspond to 95% confidence intervals in the fitting function specified by Eq. 5.6. Horizontal errorbars correspond to the uncertainty in numerically extracted value of transition temperature T_c as previously extracted and plotted in Fig. 4.10.

Lastly, we consider the quality factor Q for each of the fits we have considered and plot this quantity in Fig. 5.12. The quality factor in each case of dimensionality decays as a function of temperature, with a simultaneous collapse to order unity as the phase transition is crossed. Lower values of dimensionality systematically have lower qualities, and larger values systematically have higher qualities. Our analysis reveals that a measurement of sound across the phase transition is infeasible due to the simultaneous sharp increase in damping rate and fall in sound speed giving rise to a quality factor below unity. This is in stark contrast to previous works, where a continuity in the sound across the BKT phase transition was reported [26, 27]. It is our tentative view, that in this case, the analytical BKT phase transition temperature used, as given by Eq. (4.30), is systematically lower than the true phase transition temperature T_c for the given systems,

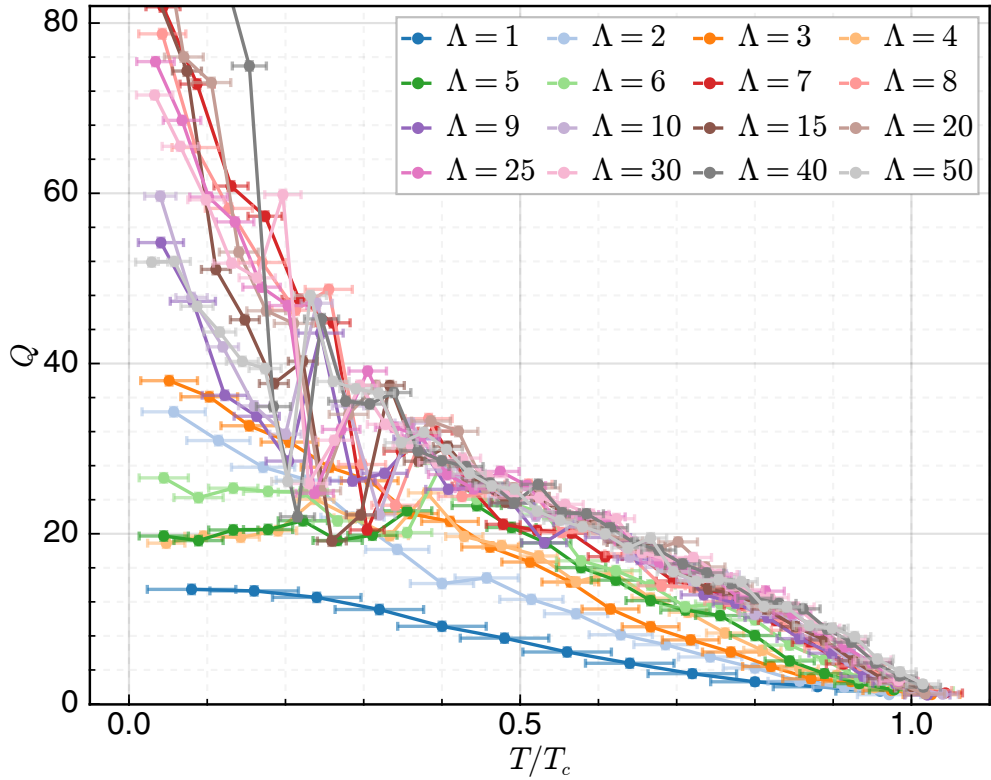


Figure 5.12: Quality factor for each considered dimensionality across temperature. Vertical errorbars correspond to 95% confidence intervals in the fitting function specified by Eq. 5.6. Horizontal errorbars correspond to the uncertainty in numerically extracted value of transition temperature T_c as previously extracted and plotted in Fig. 4.10.

leading to a misrepresentation of the crossing of the phase transition. This subtle shift in the transition temperature gives the impression of sound propagating across the phase transition, whereas in our analysis using T_c we observe a transition to overdamped behaviour exactly at the phase transition, leading to an immeasurable sound. This shows that, even in heavily dimensionally suppressed systems, the effects of dimensionality need to be carefully taken into account when interrogating systems across or close to the phase transition.

5.7 Chapter conclusions

In this chapter we have investigated the effects of dimensionality on the behaviour of the second sound through the phase transition. Our low-dimensional results are comparable with those in a purely 2D system [26, 27] when we normalise via the analytic BKT temperature. However, if instead we normalise to the numerically-extracted phase transition temperature identified in Chapter 4, we report no propagation of sound across the tran-

sition. In fact, we tentatively suggest that the analytic BKT formula used in previous works provides a systematic underestimate of the true phase transition temperature. This underestimate could lead to the mischaracterisation of sound close to the phase transition and perhaps an unfounded identification of a continuous sound across it. With increasing dimensionality we see a sound speed that is lower at the phase transition. In addition, we report a slight uptick in the normalised second sound just prior to the transition which is accentuated in, but not limited to, lower dimensionalities. This may indicate some interesting physics occurring close to the phase transition that have been previously unexplored. Moreover, the damping rate of the Bose gas in the hybridised trapping we employ displays a clear transition in behaviour as dimensionality increases, suggesting a fundamental change in the mechanism of energy dissipation as we move between the dimensional extremes. We also report a clear global increase in the measured quality factor across dimensionality, where for each measured dimensionality the quality falls to unity at the phase transition. Our work motivates further experimental forays into the nature of the second sound for quasi-2D systems, with the caveat of careful consideration on the effects of dimensionality.

Thesis conclusions and further work

General conclusions

We take this opportunity to compound the insights gathered from the work carried out within this thesis. At a glance, we investigated the zero temperature Bose gas in confined rough geometries. Here we found vortex reconnections were vital and inherently necessary in the formation of the vortex lattice in the spin-up from a quiescent state. We then studied the effects of dimensionality on the phase transition of a trapped Bose gas and found a monotonic increase in transition temperature with a decrease in trapping frequency. Lastly we investigated the effects of dimensionality on the sound propagation of a trapped Bose gas. We measured no discontinuity in second sound across the phase transition for any dimensionality we consider and instead a transition to overdamping occurring at the phase transition.

Conclusions

In Chapter 1 we visited the theory of the Bose gas in different geometries and the phenomenon of Bose-Einstein condensation. We explored the effects of dimensionality and the more specific case of a rectangular box with transverse confinement. We then considered the effect of atomic interactions which gave rise to the Gross-Pitaevskii equation before focusing our investigation onto the rectangular box under transverse confinement with the interactions considered. We went on to introduce the concept of quasi-condensation and the response of the system under a weak perturbation. We then briefly visited Bogoliubov theory and sound propagation as it relates to superfluid systems.

With the Gross-Pitaevskii theory introduced, Chapter 2 focuses this tool on the specific case of vortices inside a rough walled bucket potential. Here, we investigated the often overlooked effects of a rough-walled potential in the spin-up of a quiescent system. Despite the differences in scale between helium experiments and the system we consider,

the relative lengthscales between system and vortex core are comparable. As such, we investigated the effects of roughness on the bucket surface and found that this roughness acts as a catalyst to bring vorticity into the system, acting to increase superfluid velocity in localised pockets which give rise to the formation of vortex structures. These vortices then grow in size, reconnecting with one another in a turbulent boundary layer before diffusing into the bulk and ordering themselves into a vortex lattice structure. We considered the effects of a localised protuberance and found that such a protuberance acts to localise the generated vorticity in the initial spin-up, whilst ultimately bearing little effect on the final lattice configuration. We considered the effects of a centralised remnant vortex present in the initial state. For the case of a vortex possessing the polarity of the same circulation as those generated by the rotation direction, there is little-to-no effect. However for the case of a negative vortex, we measured an injection of extra vorticity in the system as the superfluid velocity imposed by the central vortex acts to generate a bigger difference in relative flow speed at the boundary. These extra vortices emerge into the bulk and subsequently reconnect subsume the central vortex, dissolving it into vortex rings which are then lost. The resultant vortex lattice state is one with a slightly larger number of final vortices, an important consideration that could potentially be experimentally observed or exploited. Lastly, we performed simulations on a larger grid in 2D where we observed a faster timescale for crystallisation of the vortex lattice structure as well as an interesting case of a Jones-Roberts soliton transforming into a vortex dipole pair. The findings of this chapter have been published to Physical Review B [53].

In Chapter 3, we switch focus to consider the effects of finite temperature on a confined Bose gas. We began by introducing the SPGPE theory, a \mathcal{C} -field theory that accounts for a thermal system in constant equilibrium with a surrounding thermal bath. We then discuss how in practice, the simple growth SPGPE provides a simpler numerical implementation and therefore motivate the reasons for choosing this theory. We go on to discuss the role of the projection operator and the care that must be taken in choosing a cutoff value within this theoretical framework. We then introduced the specific trapping geometry employed in later sections of the thesis. We chose a trapping geometry that reduces to the experimental configuration of Ville *et al* [26] in the 2D limit, but allows one to modify the dimensionality towards 3D through a variation in the transverse harmonic trapping strength. We later discuss subtleties of the SPGPE and the parameter choices we make for our numerical investigation. In SPGPE theory, care must be taken to include the contribution to the atomic density from atoms that have been cast out by the projection operator, we spent some time deriving expressions for the incoherent atomic density in the trapping employed.

In Chapter 4, we applied the theoretical tools introduced in the previous chapter to perform a systematic analysis of the effects of dimensionality for the trapped Bose gas.

We began this chapter by discussing the choice in chemical potential such that across dimensionalities we can normalise either the atomic density or the Bogoliubov sound speed. We then focused on the dimensional extremes of 2D and 3D, where one expects the BKT and BEC phase transitions respectively. Here we found close agreement in phase transition temperature with the analytic expressions, motivating further analysis in the dimensional crossover. In the crossover, we instead introduce select equilibrium statistics utilised to locate the phase transition in a systematic way across dimensionality. When applied to the crossover we detected that a small difference in the harmonic trapping strength leads to vast differences in the specific phase transition temperature, especially when close to the 2D limit. We also noticed a topological transition in the nature of vortices in our system where vortices transitioned from point-like to filament-like as we move from 2D towards 3D. Our analysis reveals that for gases with similar densities, we always recover a critical phase transition temperature that is lower in 2D than in 3D. The analysis performed within this chapter was submitted and accepted to the Physical Review Research journal and is due to be published shortly [192].

In Chapter 5, we modify our trapping geometry in order to investigate the propagation of sound across dimensionalities. Here we found close agreement with previous works [26, 27] in the framework of a BKT phase transition temperature in the 2D limit. However, when temperature is normalised to a numerically-extracted transition temperature, we found no continuity in the second sound speed across the phase transition. Instead a characteristic transition to overdamping occurs at the numerically-extracted phase transition temperature. Meanwhile, at the 3D limit of our work, approximated by $\Lambda = 50$, we find a similar behaviour in the sound, deviating towards a slightly lower speed at the transition. Moreover, we find that the damping rate is also modified by the dimensionality of the system. For tightly confined systems there is a globally higher damping rate and a smoother increase in the rate as we approach the phase transition from below. In the opposite dimensional limit, there is a very small change in damping across temperature up until the phase transition. At this point, we measure a sharp increase in the damping rate. This modification to the damping rate and sound speed across dimensionality corresponds to an increasing quality factor for higher dimensional systems. In all cases, the quality factor falls to an order of unity at the phase transition, corresponding to an overdamped system from which one can no longer effectively measure the sound speed. The findings of this chapter are preliminary and will form the basis of a paper exploring the sound speed as a function of temperature through the dimensionality crossover from 2D to 3D.

Further work

This thesis largely focused on the response of a weakly-interacting Bose gas to novel trapping geometries, exploring in particular microscopic roughness and dimensionality crossovers. A series of highly-efficient dedicated numerical tools have been developed and implemented. These may be applied to a multitude of various systems, allowing an exploration of a variety of trapping geometries. For example, the hybrid basis techniques we utilised could easily be adapted to study dimensionality crossovers from 3D to 1D. This would provide a greater understanding of the effects of dimensionality on the phase transition of the trapped Bose gas. Future work could take numerous directions and so we break potential avenues down into work naturally extending the two parts of this thesis on the zero temperature and finite temperature Bose gas respectively.

Zero temperature

Using the insights from Part I, we could explore the effects of a more accurate model for superfluid helium, where the strong nonlocal interactions, inducing a roton minimum, may cause a significant deviation from the results we observed here in Chapter 2. While this is absent from the GPE model we employed, it can be simply introduced through an additional non-local term [123, 124].

Another potential avenue for further work is through a dipolar interaction term. In dipolar Bose gases [262, 263], one could use the long-range anisotropic interaction to stir [264, 265] the superfluid in a direction perpendicular to the rotating frame we employed. This interplay between rotation mechanisms would generate competition on the alignment of the vortex lattice. This would certainly lead to interesting dynamics and could be a novel approach to study quantum turbulence [266, 267] in dipolar gases.

In a different vein, and in analogue to recent numerical experiments which emulate classical fluid instabilities such as that of Baggaley *et al* [268]; we could harness roughness to act as a semi-slipping boundary layer to study a superfluid analogue of Plane-Couette flow [269, 270]. By mapping the summation of Fourier modes to a top and bottom plate and translating the surface features on just a single plate, one could effectively realise the Plane-Couette channel flow. It would be interesting to observe whether the quantised vorticity inherent to superfluids causes a significant alteration to the classical result.

Finite temperature

The hybridised basis SPGPE we developed for use in Part II of this thesis forms an excellent foundation for the study of dimensionality. Whilst we investigated the dimensional crossover, one could also consider dimensional quenches. For instance, the dynamical properties of a system are likely to change with a sudden or gradual change in the system

dimensionality. One would expect fascinating behaviour of vortices and their topology through a dimensional quench as they would likely transition from point-like to filament-like, or vice versa. One could also explore temperature quenches [151, 271, 272] across the dimensional crossover. Here, the topology and dimensionality of the system trapping may significantly alter the number [273] and type of vortices generated through a Bose-Einstein condensation. Temperature quenches of the trapped Bose gas have already been numerically [69, 274] and experimentally [5, 275] investigated in harmonically-confined systems, so this work is well motivated.

We could also explore the effects of a dipolar interaction term within the finite temperature SPGPE formalism, as has been previously introduced by Bland *et al* [133]. The anisotropic dipolar interaction term is likely to affect the critical temperature of the phase transition, and so revisiting Chapter 4 with consideration for dipolar gases would provide fruitful insights. Not only this, but the excitation spectrum exhibiting a roton minimum is likely to significantly alter the propagation of sound, forming a natural extension of our work in Chapter 5.

Lastly, we highlight the possibility of extending our work to model the behaviour of mixtures or spin-orbit coupled Bose gases. With coherent coupling between species, the possibility to explore exotic phenomena such as quantum droplets [276], magnetic solitons [277] and even analogue gravity [278, 279] becomes feasible. An application of our numerical techniques to explore the role of dimensionality in each of these contexts would certainly reveal important and fascinating insights.

Appendices

Appendix A

Density of states across geometries

It is crucial within the SPGPE framework to consider the effects of particles above the cutoff energy E_{cut} when calculating observables. Here we outline how one might compute such effects for a number of common trapping configurations. Let us begin by considering a particle in a potential V , which represents a potential well with minimum $V = 0$. Choose V such that all the available states are bound states and the spectrum is discrete. Count the number of states up to an energy E and call it N_E . If E is much larger than the typical spacing between states, then one can define the number of states within an interval from E to $E + dE$ as the quantity

$$dN_E = \frac{dN_E}{dE} dE \quad (\text{A.1})$$

where the derivative has the meaning of number of state per unit energy, or *density of state*:

$$g(E) = \frac{dN_E}{dE} \quad (\text{A.2})$$

which is a continuous function in the limit of a dense spectrum. In the same limit one can write

$$N_E = \int_{E_{\min}}^E dE' g(E') , \quad (\text{A.3})$$

where E_{\min} is the lowest value of energy for which $g(E) \neq 0$. If a gas of noninteracting particles, in the same potential V , behaves in such a way that the population of the energy levels is determined by a function $f(E)$, then the number of particles which occupy states above a certain energy E_{cut} is given by

$$N = \int_{E_{\text{cut}}}^{\infty} dE g(E) f(E) . \quad (\text{A.4})$$

In the SPGPE framework, particles above the energy cutoff ϵ_{cut} are assumed to be ideal and distributed according to Maxwell-Boltzmann statistics, and so the distribution function is

just

$$f(E) = \frac{1}{(e^{(E-\mu)/k_B T} - 1)}. \quad (\text{A.5})$$

Note that sometimes the density of states is defined as $(1/\mathcal{V})dN_E/dE$, where \mathcal{V} is the volume of the system. This is useful if one wants to calculate the energy density (energy per unit volume), but this is not what we consider here.

A.1 Particle in a square box in two-dimensions

Consider a particle of mass m in an infinite two-dimensional square box of length L . The spectrum is

$$E_{n_x, n_y} = \frac{\hbar^2}{2m}(k_x^2 + k_y^2) = \frac{\pi^2 \hbar^2}{2mL^2}(n_x^2 + n_y^2), \quad (\text{A.6})$$

with n_x and n_y positive integers. Let us count the number of states with $E_{n_x, n_y} \leq E$, for a given E . In the space defined by the quantum numbers n_x and n_y , the condition $E_{n_x, n_y} = E$ corresponds to a quarter of a circumference of radius $r = \sqrt{2mL^2 E / \pi^2 \hbar^2}$ and the states satisfying the condition $E_{n_x, n_y} \leq E$ are those within the corresponding quarter of a circle. Since there is one state per unit area, the number of states is approximately given by a quarter of the area of the circle. This approximation becomes exact when the radius is large, that is, when E is much larger than the typical scale $\pi^2 \hbar^2 / 2mL^2$. This implies

$$N_E = \frac{1}{4}\pi r^2 = \frac{mL^2 E}{2\pi\hbar^2}, \quad (\text{A.7})$$

from which one obtains

$$g(E) = \frac{dN_E}{dE} = \frac{mL^2}{2\pi\hbar^2}. \quad (\text{A.8})$$

A.2 Particle in a rectangular box in two-dimensions

Proceeding as before, but with lengths L_x and L_y in the x and y directions respectively. The spectrum is

$$E_{n_x, n_y} = \frac{\hbar^2}{2m}(k_x^2 + k_y^2) = \frac{\pi^2 \hbar^2}{2m} \left(\frac{n_x^2}{L_x^2} + \frac{n_y^2}{L_y^2} \right), \quad (\text{A.9})$$

In the space defined by the quantum numbers n_x and n_y , the condition $E_{n_x, n_y} = E$ now corresponds to an ellipse:

$$\frac{n_x^2}{L_x^2} + \frac{n_y^2}{L_y^2} = \frac{2mE}{\pi^2 \hbar^2}. \quad (\text{A.10})$$

The states satisfying the condition $E_{n_x, n_y} \leq E$ are those within a quarter of an ellipse with semiaxes

$$a = \sqrt{\frac{2mL_x^2 E}{\pi^2 \hbar^2}} \quad \text{and} \quad b = \sqrt{\frac{2mL_y^2 E}{\pi^2 \hbar^2}}. \quad (\text{A.11})$$

Again there is a state per unit area, so that the number of states is

$$N_E = \frac{1}{4}\pi ab = \frac{mL_x L_y E}{2\pi \hbar^2}, \quad (\text{A.12})$$

from which one obtains

$$\boxed{g(E) = \frac{dN_E}{dE} = \frac{mL_x L_y}{2\pi \hbar^2}}. \quad (\text{A.13})$$

A.3 Particle in a square box in three dimensions

In a 3D box of size L , the spectrum is

$$E_{n_x, n_y, n_z} = \frac{\hbar^2}{2m}(k_x^2 + k_y^2 + k_z^2) = \frac{\pi^2 \hbar^2}{2mL^2}(n_x^2 + n_y^2 + n_z^2), \quad (\text{A.14})$$

with n_x, n_y and n_z positive integers. Let us count the number of states with $E_{n_x, n_y, n_z} \leq E$, for a given E . In the space defined by the quantum numbers n_x, n_y and n_z , the condition $E_{n_x, n_y, n_z} = E$ corresponds to an octant of radius $r = \sqrt{2mL^2 E / \pi^2 \hbar^2}$ and the states satisfying the condition $E_{n_x, n_y, n_z} \leq E$ are those within the corresponding octant. Since there is one state per unit volume, the number of states is approximately given by the volume of the octant:

$$N_E = \frac{1}{8} \frac{4\pi r^3}{3} = \frac{\pi}{6} \left(\frac{2mL^2 E}{\pi^2 \hbar^2} \right)^{3/2}, \quad (\text{A.15})$$

from which one obtains

$$g(E) = \frac{dN_E}{dE} = \frac{\pi}{4} \left(\frac{2mL^2}{\pi^2 \hbar^2} \right)^{3/2} E^{1/2}, \quad (\text{A.16})$$

or

$$\boxed{g(E) = \frac{mL^3}{2\pi^2 \hbar^3} \sqrt{2mE}}. \quad (\text{A.17})$$

A.4 Harmonic trap in three dimensions

A particle in a harmonic potential with frequencies ω_x , ω_y and ω_z has the spectrum

$$E_{n_x,n_y,n_z} = \left(n_x + \frac{1}{2}\right) \hbar\omega_x + \left(n_y + \frac{1}{2}\right) \hbar\omega_y + \left(n_z + \frac{1}{2}\right) \hbar\omega_z , \quad (\text{A.18})$$

where again n_x , n_y and n_z are positive integers. Since we are interested in the spectrum for large values of E , we can ignore the zero-point energies $\hbar\omega/2$, which become irrelevant if the quantum numbers are large. Hence we can write

$$E_{n_x,n_y,n_z} = n_x \hbar\omega_x + n_y \hbar\omega_y + n_z \hbar\omega_z . \quad (\text{A.19})$$

In the space defined by the quantum numbers n_x , n_y and n_z , the condition $E_{n_x,n_y,n_z} \leq E$ corresponds to the volume bounded from above by the planar surface having vertices on the axes in $\tilde{n}_x = E/\hbar\omega_x$, $\tilde{n}_y = E/\hbar\omega_y$, and $\tilde{n}_z = E/\hbar\omega_z$. The volume of such a region can be easily calculated, for instance, by integrating in dn_z (taking n_z as a continuous variable), from 0 to \tilde{n}_z , the area of the triangle formed by the boundaries at fixed n_z . The result is

$$N_E = \frac{1}{6} \tilde{n}_x \tilde{n}_y \tilde{n}_z = \frac{1}{6} \frac{E^3}{\hbar^3 \omega_x \omega_y \omega_z} , \quad (\text{A.20})$$

from which one obtains

$$\boxed{g(E) = \frac{E^2}{2(\hbar\omega_{\text{ho}})^3}} , \quad (\text{A.21})$$

where $\omega_{\text{ho}} = (\omega_x \omega_y \omega_z)^{1/3}$ is the geometric average of the trapping frequencies.

A.5 Square box with transverse harmonic potential

Consider a particle confined in a square box of size L along x and y and subject to a harmonic potential of frequency ω_z in the z direction. The spectrum is

$$E_{n_x,n_y,n_z} = \frac{\pi^2 \hbar^2}{2mL^2} (n_x^2 + n_y^2) + \left(n_z + \frac{1}{2}\right) \hbar\omega_z , \quad (\text{A.22})$$

where n_x , n_y and n_z are positive integers. Let us assume that all of them are much greater than 1. Thus we can neglect the zero-point energy in the last term and write

$$E_{n_x,n_y,n_z} = \frac{\pi^2 \hbar^2}{2mL^2} (n_x^2 + n_y^2) + n_z \hbar\omega_z . \quad (\text{A.23})$$

In the space defined by the quantum numbers n_x , n_y and n_z , the condition $E_{n_x,n_y,n_z} \leq E$ corresponds to the volume contained in the paraboloid of revolution which is obtained by

taking the parabola

$$n_z = \frac{E}{\hbar\omega_z} - \frac{\pi^2\hbar}{2m\omega_z L^2} n_x^2 , \quad (\text{A.24})$$

in the n_x - n_z plane and rotating it around the n_z axis in the region where n_x , n_y are n_z are positive. This corresponds to a quarter of the volume contained in a circular paraboloid of depth $D = \frac{E}{\hbar\omega_z}$ and radius of the rim $r = \sqrt{2mL^2E/\pi^2\hbar^2}$, so that

$$N_E = \frac{1}{4} \frac{\pi}{2} r^2 D = \frac{\pi}{8} \frac{2mL^2 E}{\pi^2\hbar^2} \frac{E}{\hbar\omega_z} = \frac{mL^2 E^2}{4\pi\hbar^3\omega_z} , \quad (\text{A.25})$$

from which one obtains

$$g(E) = \frac{mL^2 E}{2\pi\hbar^3\omega_z} .$$

(A.26)

A.6 Rectangular box with transverse harmonic potential

For the case of the rectangular box with transverse harmonic confinement, we make a more detailed approach. Consider a gas of noninteracting bosons confined in a rectangular box of size L_x along x and L_y along y and subject to a harmonic potential of frequency ω_z in the z direction. The energy spectrum is given by

$$E = \frac{\pi^2\hbar^2}{2m} \left(\frac{n_x^2}{L_x^2} + \frac{n_y^2}{L_y^2} \right) + \left(n_z + \frac{1}{2} \right) \hbar\omega_z , \quad (\text{A.27})$$

where the quantum numbers are integers, with n_x , $n_y > 1$ and $n_z \geq 0$. At a given temperature T the mean occupation number of the energy states is given by the Bose-Einstein distribution

$$\langle n_E \rangle = \frac{1}{\exp[(E - \mu)/k_B T] - 1} , \quad (\text{A.28})$$

where μ is the chemical potential of the gas, which cannot be larger than the lowest energy in the spectrum. When it approaches this value, the occupation of the state with $\mathbf{n} = (1, 1, 0)$ diverges. Let us call N_0 the occupation of this state and write the total particle number N as

$$N = N_0 + N_T = N_0 + \sum'_{\mathbf{n}} \frac{1}{\exp[(E - \mu)/k_B T] - 1} , \quad (\text{A.29})$$

where the sum is over all states except the lowest one.

The spacing between the energy levels is about $\hbar^2/(2mL_x^2)$ and $\hbar^2/(2mL_y^2)$ for states characterised by different planar wave vectors, and $\hbar\omega_z$ for different states of the transverse harmonic oscillator. If $k_B T$ is much larger than all these quantities, then the spectrum

can be considered as a continuum and the sums over the discrete index \mathbf{n} can be replaced with integrals over the energy E . Hence, the total number of atoms becomes

$$N = N_0 + \int_{E_{\min}}^{\infty} dE \frac{g(E)}{\exp[(E - \mu)/k_B T] - 1}, \quad (\text{A.30})$$

where E_{\min} is the lowest value of energy for which $g(E) \neq 0$. In our case, $E_{\min} = \hbar\omega_z/2$. Let us define the shifted energy

$$\tilde{E}_{\mathbf{n}} = E - \frac{1}{2}\hbar\omega_z = \frac{\pi^2\hbar^2}{2m} \left(\frac{n_x^2}{L_x^2} + \frac{n_y^2}{L_y^2} \right) + n_z\hbar\omega_z, \quad (\text{A.31})$$

and the shifted chemical potential $\tilde{\mu} = \mu - (1/2)\hbar\omega_z$, so that

$$N = N_0 + \int_0^{\infty} d\tilde{E} \frac{g(\tilde{E})}{\exp[(\tilde{E} - \tilde{\mu})/k_B T] - 1}. \quad (\text{A.32})$$

In order to calculate the density of states one can explicitly count the states up to a given energy \tilde{E} and then take the derivative of this number with respect to \tilde{E} . In the space defined by the quantum numbers n_x , n_y and n_z , where there is one state per unit volume, the condition $\tilde{E}_{\mathbf{n}} \leq \tilde{E}$ corresponds to the volume contained in the elliptic paraboloid which has a depth $D = \tilde{E}/\hbar\omega_z$ and whose rim is an ellipse defined by the equation

$$\frac{n_x^2}{L_x^2} + \frac{n_y^2}{L_y^2} = \frac{2m\tilde{E}}{\hbar^2} \quad (\text{A.33})$$

with semiaxes

$$a = \sqrt{\frac{2mL_x^2\tilde{E}}{\hbar^2}} \quad \text{and} \quad b = \sqrt{\frac{2mL_y^2\tilde{E}}{\hbar^2}}. \quad (\text{A.34})$$

The volume containing the states below \tilde{E} is a quarter of the volume of the paraboloid, so that

$$N_{\tilde{E}} = \frac{1}{4} \frac{\pi}{2} abD = \frac{\pi}{8} \frac{2mL_x L_y \tilde{E}}{\pi^2 \hbar^2} \frac{\tilde{E}}{\hbar\omega_z} = \frac{m L_x L_y \tilde{E}^2}{4\pi \hbar^3 \omega_z}. \quad (\text{A.35})$$

Then, by taking the derivative, one obtains

$$g(\tilde{E}) = \frac{m L_x L_y \tilde{E}}{2\pi \hbar^3 \omega_z}.$$

(A.36)

It is worth noticing that the density of states in our hybrid trap turns out to be equal to the density of states of a purely 2D rectangular box as given by Eq. (A.13) (which does not depend on the energy), multiplied by the number of transverse states below the energy \tilde{E} , which is $\tilde{E}/\hbar\omega_z$. Note that this hybrid box-harmonic potential has three typical

energy scales: the two scales associated to the box, $\hbar^2/(2mL_x^2)$ and $\hbar^2/(2mL_y^2)$ and the one associated to the transverse harmonic confinement, $\hbar\omega_z$. The result Eq. (A.26) is valid if E is much larger than all of them. In this case, the density of states turns out to be equal to the density of states of a 2D rectangular box, as in Eq. (A.13), times the number of transverse states within the energy E , which is $E/\hbar\omega_z$. This follows from the fact that, for each n_z , there exists a dense set of planar waves with different k_x and k_z , and all those sets (whose wave functions can be distinguished by the number of nodes in the z direction) equally contribute to the density of states.

Care must be taken in cases where the transverse confinement is tight and the relevant range of energy E is of the order of $\hbar\omega_z$ or even smaller. In this situation, only one or a few values of n_z have to be considered, the zero-point energy cannot be ignored, and the transverse spectrum cannot be approximated with a continuum. Let us rewrite the energy spectrum given by Eq. (A.27) in the form

$$E_{n_x, n_y, n_z} - \frac{\hbar\omega_z}{2} = \frac{\pi^2\hbar^2}{2m} \left(\frac{n_x^2}{L_x^2} + \frac{n_y^2}{L_y^2} \right) + n_z \hbar\omega_z , \quad (\text{A.37})$$

Now we remember (from the solution of the Schrödinger equation) that the lowest value of the integers n_x and n_y is 1, while the lowest value of the quantum number n_z of the harmonic potential is 0. This means that the lowest energy in the spectrum is $\hbar\omega_z/2$ plus either $\pi^2\hbar^2/2mL_x^2$ or $\pi^2\hbar^2/2mL_y^2$ depending on which length is larger between L_x and L_y . Let us suppose that both are much larger than the transverse harmonic length $\ell_z = \sqrt{\hbar/m\omega_z}$, which is equivalent to say that the spectrum of the planar states is dense on the energy scale $\hbar\omega_z$. This means that $g(E)$ is a staircase function, with a step every $\hbar\omega_z$ starting from the zero-point energy. In the extreme case where $\hbar\omega_z$ is much larger than any other energy scale, only planar waves with no transverse nodes are allowed and the density of state is the one of a purely 2D box Eq. (A.13). In the opposite limit, where $\hbar\omega_z$ is small, the steps themselves become dense, and $g(E)$ appears to increase linearly with E as in Eq. (A.26). Finally, note that, in the intermediate case where $g(E)$ has a staircase shape, a gas of noninteracting particles with distribution function $f(E)$ (either Bose-Einstein or Boltzmann) is expected to have an energy density $Eg(E)f(E)$ with sharp maxima whenever $E = (n_x + 1/2)\hbar\omega_z$. Correspondingly, the momentum distribution should also exhibits spikes.

Appendix B

Hybrid basis SPGPE

In this appendix chapter we discuss numerical details pertaining to the simulation of the SPGPE as presented in the latter part of this thesis. We begin by discussing the protocol for independent stochastic realisations for our parameters of choice and go on to discuss the hybrid-basis formulation of the SPGPE we utilise. We then present how this is implemented upon Graphical Processing Units (GPUs) to achieve vast numerical speedup in our calculations and the specific algorithm for propagation of the wavefunction. Numerics and visualisation of the SPGPE are performed using Julia [280–282], whereby we utilise CUDA to offload calculations to a graphical processing unit (GPU) through the use of a parallelised stencil.

B.1 System preparation

To prepare equilibrium configurations for each value of Λ and temperature, we evolve the system dynamically from a zero-field initial condition for a time $t \sim 500\tau_\gamma$, where $\tau_\gamma = \hbar/\mu\gamma$. Evolving from initial condition $\psi(\mathbf{r}) = 0$, with a random realisation of the initial noisy field $\eta(\mathbf{r})$ is akin to an initial condition where all atoms possess initial energy larger than the cutoff energy ϵ_{cut} . These will then enter the coherent region at a rate governed by γ , which describes the collisional rate between atoms, until the gas reaches thermal equilibrium. Throughout this work we employ a value $\gamma = 0.05$ as a reasonable estimate for our system, noting that similar values have been used in previous SPGPE simulations [27, 28, 161, 191]; nonetheless, we stress that the precise value of γ is not relevant for the present work, as it determines the rate at which the system relaxes to equilibrium, but has little effect on the properties of the system once equilibrium is reached. We consider our simulations to be in thermal equilibrium once the number of \mathcal{C} -field atoms $N_{\mathcal{C}}$ and the number of atoms in the condensate mode N_0 has stabilised with minimal phase fluctuations. As can be seen in Figure B.1, the \mathcal{C} -field, has been evolved for long enough

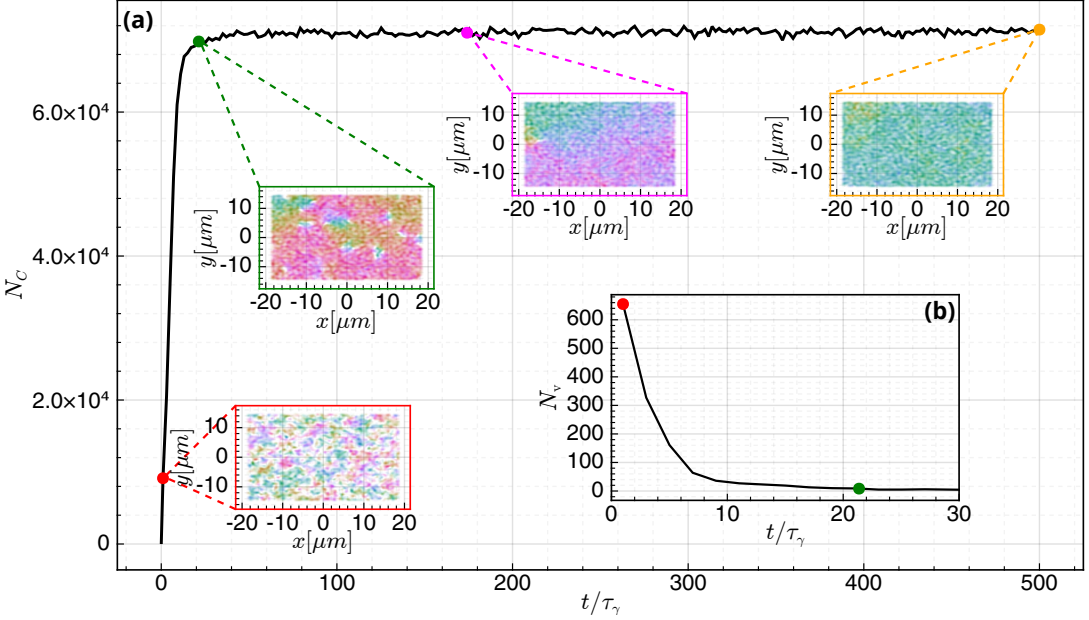


Figure B.1: (a) \mathcal{C} -field number of atoms N_C for a single realisation at $\Lambda = 5$ from zero-field to equilibrium. At select points $t \approx 5\tau_\gamma, 25\tau_\gamma, 180\tau_\gamma, 500\tau_\gamma$ highlighted with red, green, magenta and orange markers respectively we visualise the density and phase profile concurrently using transparency and colour on the $z = 0$ plane in a panel bordered by the same colour. In subplot (b) we track the number of vortices N_v in this plane at early times.

such that all vortices have been annihilated and the system has a global phase coherence. To obtain distinct/independent realisations at fixed Λ and T for our subsequent stochastic analysis, we then propagate such equilibrium solution further in time with Eq. (3.21), sampling an additional realisation every $\sim 10\tau_\gamma$. Such a procedure is justified under the ergodic principle, within which the time average over the evolution of a single system at equilibrium is indiscernible from the ensemble average over many different systems [283, 284]. This procedure is well adopted in the literature [127, 151, 229, 285, 286] and provides a significant speed-up in the generation of distinct equilibrium configurations for a given system. For a given Λ , we prepare between $\mathcal{N} = 50 - 100$ realisations for each probed temperature T in 10nK increments from 10nK up to 300nK. This procedure gives a thermal resolution of ± 5 nK in identifying critical behaviour of the phase transition across the range of Λ we consider. A schematic of the procedure is presented in Fig. B.2. This entire procedure is completed twice, once for the simple choice of chemical potential as given by Eq. (4.1), and then again for the interpolated value which is justified in Section 4.3, based on the zero temperature sound speed in the dimensional extremes.

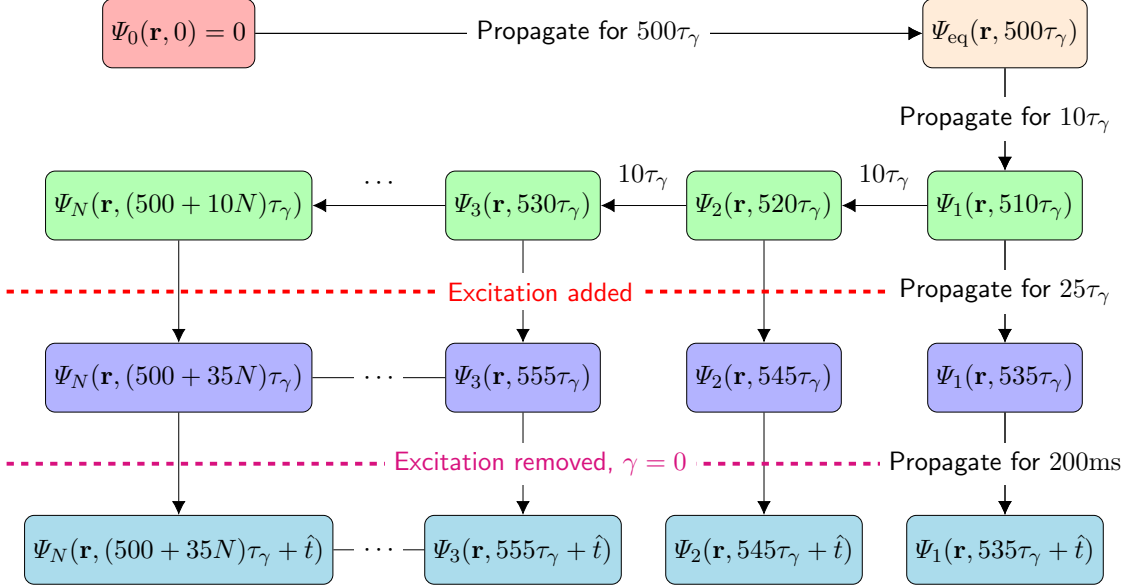


Figure B.2: Complete simulation procedure to generate \mathcal{N} stochastic realisations of the SPGPE at a given dimensionality A and temperature T . We begin with a zero-field condition $\Psi_0(\mathbf{r}, 0) = 0$ and equilibrate for multiple relaxation time centuries to ensure full equilibration has been reached and extract the equilibrium wavefunction Ψ_{eq} . Under the assumption of ergodicity, we can then continually propagate the wavefunction and take samples every $10\tau_\gamma$. This allows us to collect independent realisations to average over whilst not having to propagate every solution from the zero field. For the equilibrium portion of this work we need not continue further. However, for Chapter 5 on sound, we then take the diverged equilibrium configurations and propagate for a further $25\tau_\gamma$ in the presence of a small-amplitude sinusoidal excitation along x . We then remove dissipation and noise by setting $\gamma = 0$ and run for a final $\hat{t} = 200\text{ms}$, collecting 500 samples of the integrated profile along the x -direction for each realisation.

B.2 Hybrid basis

To solve the SPGPE for the considered box-harmonic hybrid potential, Eq. (3.19), we adopt a novel hybrid basis composed of plane waves along the x and y axes and the harmonic oscillator basis along the z axis. Since the SPGPE simulations are time consuming, we prefer to make the calculations faster by implementing efficient Fourier and inverse Fourier transformations in the xy -plane. This requires the use of periodic boundary conditions. We thus embed the physical $L_x \times L_y$ box into a slightly larger auxiliary $\mathcal{L}_x \times \mathcal{L}_y$ box. The potential outside the physical box is taken to be very large (decades larger than the chemical potential) so that the density is negligible in that region. Periodic boundary conditions are then safely applied to the auxiliary box, with no effect on the physical box due to its embedding within a region of negligible density. Typically numerical simulations are conducted entirely in a plane-wave or harmonic oscillator; to our knowledge this is the first implementation of a mixed basis SPGPE solver in the current literature. The SPGPE is numerically solved in its dimensionless form in which the physical quantities

and variables are scaled by reference length, energy and times scales, l_{ref} , $\hbar\omega_{\text{ref}}$ and ω_{ref}^{-1} , respectively, according to their dimensions, and in the following the dimensionless quantities and variables are denoted by prime notation. The \mathcal{C} -field is expanded in the hybrid basis

$$\Psi'(\mathbf{r}', t') = \sum_{\varepsilon_{pqn} \leq \epsilon'_{\text{cut}}} A'_{pqn}(t') \phi_p(x') \phi'_q(y') \varphi'_n(z') \quad (\text{B.1})$$

where the dimensionless single-particle energies are

$$\epsilon'_{pqn} = 2\pi^2 \left[\frac{p^2}{\mathcal{L}'_x^2} + \frac{q^2}{\mathcal{L}'_y^2} \right] + \frac{1}{\Lambda} \left(n + \frac{1}{2} \right) . \quad (\text{B.2})$$

The wavefunctions are

$$\phi'_p(x') = (1/\sqrt{\mathcal{L}'_x}) \exp(i2\pi p x'/\mathcal{L}'_x) \quad (\text{B.3})$$

$$\phi'_q(y') = (1/\sqrt{\mathcal{L}'_y}) \exp(i2\pi q y'/\mathcal{L}'_y) \quad (\text{B.4})$$

$$\varphi'_n(z') = \frac{\Lambda^{-1/4}}{\sqrt{2^n n! \pi^{1/4}}} H_n \left(\frac{z'}{\sqrt{\Lambda}} \right) e^{-z'^2/2\Lambda} \quad (\text{B.5})$$

where H_n are the Hermite polynomials and p, q, n are integer quantum numbers with $p, q \geq 1$ and $n \geq 0$. This hybrid basis satisfies the eigen-equation

$$\left[-\frac{\nabla'^2}{2} + \frac{1}{2\Lambda^2} z'^2 \right] \phi_p(x') \phi'_q(y') \varphi'_n(z') = \varepsilon'_{pqn} \phi_p(x') \phi'_q(y') \varphi'_n(z') \quad (\text{B.6})$$

and forms a complete set obeying the orthogonality condition

$$\int d\mathbf{r} \phi_{p'}^*(x) \phi_{q'}^*(y) \varphi_{n'}^*(z) \phi_p(x) \phi_q(y) \varphi_n(z) = \delta_{pp'} \delta_{qq'} \delta_{nn'} . \quad (\text{B.7})$$

The amplitude of each mode in the \mathcal{C} -field can be expressed in the form

$$A'_{pqn}(t') = \int d\mathbf{r}' \phi_p'^*(x) \phi_q'^*(y) \varphi_n'^*(z) \Psi'(\mathbf{r}', t') \equiv \mathcal{F}_{x,p} \left[\mathcal{F}_{y,q} \left[\mathcal{H}_{z,n} [\Psi'(\mathbf{r}', t')] \right] \right] \quad (\text{B.8})$$

where $\mathcal{F}_{x,p}$ and $\mathcal{F}_{y,q}$ denote the Fourier transform and $\mathcal{H}_{z,n}$ is the Hermite transformation. We remark here that these transforms are permutable due to the orthogonality of the utilised basis. The corresponding inverse transformation is

$$\Psi'(\mathbf{r}', t') = \sum_{p,q,n} \mathcal{F}_{x,p}^{-1} \left[\mathcal{F}_{y,q}^{-1} \left[\mathcal{H}_{z,n}^{-1} [A'_{pqn}(t')] \right] \right] . \quad (\text{B.9})$$

The Fourier and inverse Fourier transformation can be straightforwardly computed by fast Fourier transformation with homogeneous grids along x and y axes. The Hermite trans-

formation can be computed with the Hermite-Gaussian quadrature, a form of Gaussian quadrature for approximating the value of integrals by a summation with n points, given by

$$\int dz' e^{-z'^2} f(z') \approx \sum_{i=1}^{n_{\max}} w_{i,n} f(\alpha_i), \quad (\text{B.10})$$

where

$$w_{i,n} = \frac{2^{n-1} n! \sqrt{\pi}}{n^2 [H_{n_{\max}-1}(\alpha_i)]^2} \quad (\text{B.11})$$

are roots of the Hermite polynomial $H_{n_{\max}}(\alpha_i)$, for $i = 1, 2 \dots, n$ [127, 287]. In order to compute the Hermite transformation accurately, the grid is set by α_i and is not homogeneous along the z -axis. Then we can write

$$\mathcal{H}_{z,n} [\Psi'(\mathbf{r}', t')] = \sum_i w_{i,n} \frac{\Lambda^{1/4} H_n(\alpha_i)}{\sqrt{2^n n! \pi^{1/4}}} e^{\alpha_i^2} \Psi(x', y', \alpha_i, t'), \quad (\text{B.12})$$

and this can be numerically implemented through a matrix multiplication such that

$$\mathcal{H}_{z,n} [\Psi'(\mathbf{r}', t')] = \mathcal{Q} \Psi(x', y', \alpha'_i, t'), \quad (\text{B.13})$$

where \mathcal{Q} is a block-diagonal matrix specified by Eq. (B.18). The inverse Hermite transformation is the product of the basis weight and the n -th harmonic basis,

$$\mathcal{H}_{z,n}^{-1} [A'_{pqn}(t')] = A'_{pqn}(t') \varphi'_n(z'). \quad (\text{B.14})$$

During the SPGPE evolution addressed below, the z -position grid is set by the roots of the Hermite polynomial with $n_{\max} = 300$ in all our simulations. Besides, it is worth noting that unlike the Hermite transformation, one can reconstruct the wave function with arbitrary spatial resolution from the inverse transformation with the knowledge of A'_{pqn} , and thus it will allow us to visualise the data with finer grid spacing in z' .

The equation of motion of the basis amplitude A'_{pqn} for $\varepsilon'_{pqn} \leq \varepsilon'_{\text{cut}}$ can be obtained by the SPGPE

$$i \frac{\partial}{\partial t'} A'_{pqn}(t') = (1 - i\gamma) [\varepsilon'_{pqn} + \mathcal{P}[G'_{pqn}] - \mu'] A'_{pqn}(t) + \tilde{\eta}'_{pqn}(t')$$

where

$$G'_{pqn}(t') = \mathcal{F}_{x,p} \left[\mathcal{F}_{y,q} \left[\mathcal{H}_{z,n} [V'(x', y') + g' |\Psi'(\mathbf{r}', t')|^2 \Psi'(\mathbf{r}', t')] \right] \right]$$

is the combination of external box potential and the nonlinear term. Here, we introduced $g' = 4\pi a_s / l_{\text{ref}}$ as the dimensionless interaction strength. Meanwhile the complex white

noise follows the correlation relation

$$\langle \tilde{\eta}_{ijk}^*(t'') \tilde{\eta}'_{pqr}(t') \rangle = 2\gamma \frac{k_B T}{\hbar \omega_{\text{ref}}} \delta(t' - t'') \delta_{pi} \delta_{qj} \delta_{nk} \quad (\text{B.15})$$

only for modes below the cutoff. The projector limits the modes evolved in the dynamic for modes satisfying $\varepsilon'_{pqn} \leq \varepsilon'_{\text{cut}}$ while higher modes could be created during the *s*-wave collision.

B.3 Utilisation of GPUs

When running stochastic simulations of 3D partial differential equations, one needs to find a delicate balance between generating enough trajectories for strong convergence whilst simultaneously minimising the scope of the project in terms of memory and computational runtime. The nature and scope of this project requires the running and storing of hundreds of thousands of 3D wavefunctions, thus we are met with a problem of having our simulations finish within a reasonable timeframe and storing data in a limited system. To address the former of these issues, we turn to graphical processing units (GPUs). These were originally designed to perform low-cost computational operations across many pixels simultaneously for use in computer graphics. Fortunately, recent advances in software have allowed the use of GPUs for general-purpose programming. The mass-parallelisation of low-power compute provided by GPUs compared to the centralised high-power compute provided by CPUs can be summarised by the adage: *Would you rather plow a field with two oxen, or a thousand chickens?*. Of course, this prompts several responses, the most important of which is: *How big is the field?* In the context of compute, this corresponds to whether the time saved by developing code to speed-up calculations through GPU (coordinating chickens) is worth the time lost by simply using a CPU code (using oxen). For our case, we report a $\sim 10\times$ speedup when utilising GPUs, which is overwhelmingly worthwhile. This project utilised NVidia Tesla V100 GPUs to offload calculations for a vast speed-up in computational speed. As a summary, this involved casting all arrays onto the GPU memory and propagating the solution there, before casting it back over to the CPU for data analysis. Whilst GPUs are efficient at performing distributed low-cost operations within their memory, they are comparatively slow in the transfer of data between system and device. As such, it is highly advantageous to cast the equation over to the device and keep it there for the duration of the simulation, minimising data transfer. This remains feasible if matrices are small enough to reside in video memory, known as VRAM. For the GPUs which we had access to for the duration of this project, we may store matrices that reside within 16GB of memory. Unfortunately, for the highly dimensional ($A = 50$) high temperature simulations we overwhelm the VRAM and instead require a number of

different algorithms to perform the same task, dependent on the size of the problem. The basis amplitude matrix A'_{pqn} and its inverse are generated through block diagonal sparse matrices which act upon the column-vectorised \mathcal{C} -field wavefunction of the form

$$\mathcal{Q} = \left\{ \begin{array}{c} \overbrace{\hat{Q}_{n,i} \quad 0 \quad \cdots \quad 0}^{n_x n_y \text{ columns}} \\ 0 \quad \hat{Q}_{n,i} \quad \cdots \quad 0 \\ \vdots \quad \vdots \quad \ddots \quad \vdots \\ 0 \quad 0 \quad \cdots \quad \hat{Q}_{n,i} \end{array} \right\}_{\text{ROWS}}^{\text{COLS}} , \quad \mathcal{Q}^{-1} = \left\{ \begin{array}{c} \overbrace{\hat{Q}_{i,n}^{-1} \quad 0 \quad \cdots \quad 0}^{n_x n_y \text{ columns}} \\ 0 \quad \hat{Q}_{i,n}^{-1} \quad \cdots \quad 0 \\ \vdots \quad \vdots \quad \ddots \quad \vdots \\ 0 \quad 0 \quad \cdots \quad \hat{Q}_{i,n}^{-1} \end{array} \right\}_{\text{COLS}}^{\text{ROWS}} \quad (\text{B.16})$$

where $\hat{Q}_{n,i}$ and $\hat{Q}_{i,n}^{-1}$ are themselves matrices of size (n_z^h, n_z^h) , with n_z^h as the number of points in Hermite space along the transverse direction, selected via

$$n_z^h = \max \left(\frac{2\epsilon_{\text{cut}}\Lambda - \hbar\omega_{\text{ref}}}{2\hbar\omega_{\text{ref}}}, 11 \right). \quad (\text{B.17})$$

A minimum value of 11 grid points is used to prevent numerical issues from the nonlinear term of the SPGPE in the 2D limit where $n_z^h \sim 1$. Specifically, $\hat{Q}_{n,i}$ and $\hat{Q}_{i,n}^{-1}$ can be thought of as matrices which transform between the spatial-domain and quantum number domain forwards and backwards respectively. They can be defined as

$$\hat{Q}_{n,i} = \sqrt{\Lambda} \begin{bmatrix} w_{1,1}h_1(\alpha_1)e^{\alpha_1^2/2} & w_{1,2}h_1(\alpha_2)e^{\alpha_2^2/2} & \cdots & w_{1,n_{\max}}h_1(\alpha_{n_{\max}})e^{\alpha_{n_{\max}}^2/2} \\ w_{2,1}h_2(\alpha_1)e^{\alpha_1^2/2} & w_{2,2}h_2(\alpha_2)e^{\alpha_2^2/2} & \cdots & w_{2,n_{\max}}h_2(\alpha_{n_{\max}})e^{\alpha_{n_{\max}}^2/2} \\ \vdots & \vdots & \ddots & \vdots \\ w_{n_{\max},1}h_{n_{\max}}(\alpha_1)e^{\alpha_1^2/2} & w_{n_{\max},2}h_{n_{\max}}(\alpha_2)e^{\alpha_2^2/2} & \cdots & w_{n_{\max},n_{\max}}h_{n_{\max}}(\alpha_{n_{\max}})e^{\alpha_{n_{\max}}^2/2} \end{bmatrix} \quad (\text{B.18})$$

where $h_n(z') = H_n(z') / (\sqrt{2^n n!} \pi^{1/4})$ is the normalised Hermite polynomial and

$$\hat{Q}_{i,n}^{-1} = \begin{bmatrix} \varphi'_0(\alpha_1) & \varphi'_1(\alpha_1) & \cdots & \varphi'_{n_{\max}}(\alpha_1) \\ \varphi'_0(\alpha_2) & \varphi'_1(\alpha_2) & \cdots & \varphi'_{n_{\max}}(\alpha_2) \\ \vdots & \vdots & \ddots & \vdots \\ \varphi'_0(\alpha_{n_{\max}}) & \varphi'_1(\alpha_{n_{\max}}) & \cdots & \varphi'_{n_{\max}}(\alpha_{n_{\max}}) \end{bmatrix}, \quad (\text{B.19})$$

respectively. In fact, we can write

$$\hat{Q}_{n,i}\dot{\psi}^{(pqi)} = \dot{A}_{(pqn)} \quad (\text{B.20})$$

$$\hat{Q}_{i,n}^{-1}\dot{A}_{(pqn)} = \dot{\psi}^{(pqi)}. \quad (\text{B.21})$$

where $\hat{\psi}^{(pq)}_i$ and $\hat{A}_{(pqn)}$ are column-vectorised $\psi'(\alpha_i)$ in real space and A'_{pqn} in energy space respectively. By definition, the relation

$$\hat{Q}_{n,i}\hat{Q}_{i,n}^{-1} = \hat{Q}_{i,n}^{-1}\hat{Q}_{n,i} = \hat{I} \quad (\text{B.22})$$

should always hold. If the total Hermite grid size $n_x \times n_y \times n_z^h$ becomes too large, we are no longer able to fit the matrices of Eq. (B.18) and Eq. (B.19) inside the GPU memory. In this event, we can store either or both of these matrices in system memory instead and transfer the wavefunction from GPU to CPU when we need these matrices to act upon it. In the context of memory, the hybridised basis we employ greatly aids on the memory footprint of our project. Since, without loss of information, we can arbitrarily choose the number of transverse homogeneous grid points n_{\max} when transferring back and forth between real space and the hybrid basis. As such, we store all data in the hybrid basis with a total memory footprint of approximately 10 Terabytes.

B.4 Fourth order Runge-Kutta numerical integration

The numerical integration of both the GPE and SPGPE performed in this thesis employ the use of the Runge-Kutta fourth order algorithm (for a detailed derivation, see [55, §A.2]). Consider the partial differential equation described by

$$\frac{\partial \psi}{\partial t} = f(\psi, t). \quad (\text{B.23})$$

To propagate the equation forward by a step $dt > 0$, and generate $\psi(t_n) = \psi_n$ we calculate the quantities

$$k_1 = f(t_n, \psi_n), \quad (\text{B.24a})$$

$$k_2 = f\left(t_n + \frac{dt}{2}, \psi_n + \frac{k_1}{2}\right), \quad (\text{B.24b})$$

$$k_3 = f\left(t_n + \frac{dt}{2}, \psi_n + \frac{k_2}{2}\right), \quad (\text{B.24c})$$

$$k_4 = f(t_n + dt, \psi_n + k_3), \quad (\text{B.24d})$$

which are then used to propagate the solution forward one timestep such that

$$\psi_{n+1} = dt \left(\psi_n + \frac{k_1}{6} + \frac{k_2}{3} + \frac{k_3}{3} + \frac{k_4}{4} \right) + \mathcal{O}(dt^5). \quad (\text{B.25})$$

For simulations of the GPE in Chapter 2, we employ a fixed step size of $dt = 0.01$ in dimensionless time units, whereas for the SPGPE simulations of Chapter 4 and Chapter 5 we utilise a time step which varies across dimensionalities but is typically $dt \sim dx dy \Lambda / 2$.

Bibliography

- [1] F. Dalfovo, S. Giorgini, L. P. Pitaevskii, and S. Stringari, Rev. Mod. Phys. **71**, 463 (1999), URL <https://link.aps.org/doi/10.1103/RevModPhys.71.463>.
- [2] L. Pitaevskii and S. Stringari, *Bose-Einstein condensation and superfluidity*, vol. 164 (Oxford University Press, 2016).
- [3] A. L. Gaunt, T. F. Schmidutz, I. Gotlibovych, R. P. Smith, and Z. Hadzibabic, Phys. Rev. Lett. **110**, 200406 (2013), URL <https://link.aps.org/doi/10.1103/PhysRevLett.110.200406>.
- [4] G. Gauthier, I. Lenton, N. M. Parry, M. Baker, M. J. Davis, H. Rubinsztein-Dunlop, and T. W. Neely, Optica **3**, 1136 (2016), URL <http://opg.optica.org/optica/abstract.cfm?URI=optica-3-10-1136>.
- [5] L. Chomaz, L. Corman, T. Bienaime, R. Desbuquois, C. Weitenberg, S. Nascimbene, J. Beugnon, and D. J., Nat. Commun. **6**, 6162 (2015), URL <https://doi.org/10.1038/ncomms7162>.
- [6] Bose, Zeitschrift für Physik **26**, 178 (1924), ISSN 0044-3328, URL <https://doi.org/10.1007/BF01327326>.
- [7] A. Einstein, Sitzungsber. Preuss. Akad. Wiss **1**, 3 (1925).
- [8] C. Gruber and A. Pelster, The European Physical Journal D **68**, 341 (2014), URL <https://doi.org/10.1140/epjd/e2014-50380-3>.
- [9] M. H. Anderson, J. R. Ensher, M. R. Matthews, C. E. Wieman, and E. A. Cornell, Science **269**, 198 (1995), URL <https://www.science.org/doi/abs/10.1126/science.269.5221.198>.
- [10] K. B. Davis, M. O. Mewes, M. R. Andrews, N. J. van Druten, D. S. Durfee, D. M. Kurn, and W. Ketterle, Phys. Rev. Lett. **75**, 3969 (1995), URL <https://link.aps.org/doi/10.1103/PhysRevLett.75.3969>.

- [11] C. C. Bradley, C. A. Sackett, J. J. Tollett, and R. G. Hulet, Phys. Rev. Lett. **75**, 1687 (1995), URL <https://link.aps.org/doi/10.1103/PhysRevLett.75.1687>.
- [12] S. Chu, Rev. Mod. Phys. **70**, 685 (1998), URL <https://link.aps.org/doi/10.1103/RevModPhys.70.685>.
- [13] C. N. Cohen-Tannoudji, Rev. Mod. Phys. **70**, 707 (1998), URL <https://link.aps.org/doi/10.1103/RevModPhys.70.707>.
- [14] W. D. Phillips, Rev. Mod. Phys. **70**, 721 (1998), URL <https://link.aps.org/doi/10.1103/RevModPhys.70.721>.
- [15] H. Metcalf and P. van der Straten, Physics Reports **244**, 203 (1994), ISSN 0370-1573, URL <https://www.sciencedirect.com/science/article/pii/037015739400353>.
- [16] F. Schreck and K. v. Druten, Nature Physics **17**, 1296 (2021), URL <https://doi.org/10.1038/s41567-021-01379-w>.
- [17] H. F. Hess, Phys. Rev. B **34**, 3476 (1986), URL <https://link.aps.org/doi/10.1103/PhysRevB.34.3476>.
- [18] N. Masuhara, J. M. Doyle, J. C. Sandberg, D. Kleppner, T. J. Greytak, H. F. Hess, and G. P. Kochanski, Phys. Rev. Lett. **61**, 935 (1988), URL <https://link.aps.org/doi/10.1103/PhysRevLett.61.935>.
- [19] O. J. Luiten, M. W. Reynolds, and J. T. M. Walraven, Phys. Rev. A **53**, 381 (1996), URL <https://link.aps.org/doi/10.1103/PhysRevA.53.381>.
- [20] K. Henderson, C. Ryu, C. MacCormick, and M. G. Boshier, New Journal of Physics **11**, 043030 (2009), URL <https://doi.org/10.1088/1367-2630/11/4/043030>.
- [21] C. A. Sackett, J. M. Gerton, M. Welling, and R. G. Hulet, Phys. Rev. Lett. **82**, 876 (1999), URL <https://link.aps.org/doi/10.1103/PhysRevLett.82.876>.
- [22] T. Lahaye, J. Metz, B. Fröhlich, T. Koch, M. Meister, A. Griesmaier, T. Pfau, H. Saito, Y. Kawaguchi, and M. Ueda, Phys. Rev. Lett. **101**, 080401 (2008), URL <https://link.aps.org/doi/10.1103/PhysRevLett.101.080401>.
- [23] C. Chin, R. Grimm, P. Julienne, and E. Tiesinga, Rev. Mod. Phys. **82**, 1225 (2010), URL <https://link.aps.org/doi/10.1103/RevModPhys.82.1225>.
- [24] P. C. Hohenberg, Phys. Rev. **158**, 383 (1967), URL <https://link.aps.org/doi/10.1103/PhysRev.158.383>.

- [25] N. D. Mermin and H. Wagner, Phys. Rev. Lett. **17**, 1133 (1966), URL <https://link.aps.org/doi/10.1103/PhysRevLett.17.1133>.
- [26] J. L. Ville, R. Saint-Jalm, E. Le Cerf, M. Aidelsburger, S. Nascimbène, J. Dalibard, and J. Beugnon, Phys. Rev. Lett. **121**, 145301 (2018), URL <https://link.aps.org/doi/10.1103/PhysRevLett.121.145301>.
- [27] M. Ota, F. Larcher, F. Dalfovo, L. Pitaevskii, N. P. Proukakis, and S. Stringari, Phys. Rev. Lett. **121**, 145302 (2018), URL <https://link.aps.org/doi/10.1103/PhysRevLett.121.145302>.
- [28] P. Comaron, F. Larcher, F. Dalfovo, and N. P. Proukakis, Phys. Rev. A **100**, 033618 (2019), URL <https://link.aps.org/doi/10.1103/PhysRevA.100.033618>.
- [29] L. Corman, *The two-dimensional Bose Gas in box potentials*, Theses, PSL Research University (2016), URL <https://tel.archives-ouvertes.fr/tel-01449982>.
- [30] N. J. van Druten and W. Ketterle, Phys. Rev. Lett. **79**, 549 (1997), URL <https://link.aps.org/doi/10.1103/PhysRevLett.79.549>.
- [31] J. Armijo, T. Jacqmin, K. Kheruntsyan, and I. Bouchoule, Phys. Rev. A **83**, 021605 (2011), URL <https://link.aps.org/doi/10.1103/PhysRevA.83.021605>.
- [32] L. Landau, Phys. Rev. **60**, 356 (1941), URL <https://link.aps.org/doi/10.1103/PhysRev.60.356>.
- [33] A. L. Fetter and J. D. Walecka, *Quantum theory of many-particle systems* (Courier Corporation, 2012).
- [34] N. P. Proukakis and B. Jackson, Journal of Physics B: Atomic, Molecular and Optical Physics **41**, 203002 (2008), URL <https://doi.org/10.1088/0953-4075/41/20/203002>.
- [35] C. C. Tannoudji, Leçons du Collège de France, (13 10 1998) (1998).
- [36] H. Nishimori and G. Ortiz, *Elements of phase transitions and critical phenomena* (OUP Oxford, 2010).
- [37] V. I. Yukalov, Laser Physics Letters **4**, 632 (2007), URL <https://doi.org/10.1002/lapl.200710029>.
- [38] E. P. Gross, Il Nuovo Cimento **20**, 454 (1961), URL <https://doi.org/doi/10.1007/BF02731494>.

- [39] L. P. Pitaevskii, Soviet Physics JETP **13**, 451 (1961), URL <http://www.jetp.ac.ru/cgi-bin/e/index/e/13/2/p451?a=list>.
- [40] C. F. Barenghi and N. G. Parker, *A primer on quantum fluids* (Springer, 2016).
- [41] D. S. Petrov, M. Holzmann, and G. V. Shlyapnikov, Phys. Rev. Lett. **84**, 2551 (2000), URL <https://link.aps.org/doi/10.1103/PhysRevLett.84.2551>.
- [42] Z. Hadzibabic, P. Krüger, M. Cheneau, B. Battelier, and J. Dalibard, Nature **441**, 1118 (2006), URL <https://doi.org/10.1038/nature04851>.
- [43] S. Tung, G. Lamporesi, D. Lobser, L. Xia, and E. A. Cornell, Phys. Rev. Lett. **105**, 230408 (2010), URL <https://link.aps.org/doi/10.1103/PhysRevLett.105.230408>.
- [44] T. Yefsah, R. Desbuquois, L. Chomaz, K. J. Günter, and J. Dalibard, Phys. Rev. Lett. **107**, 130401 (2011), URL <https://link.aps.org/doi/10.1103/PhysRevLett.107.130401>.
- [45] P. Cladé, C. Ryu, A. Ramanathan, K. Helmerson, and W. D. Phillips, Phys. Rev. Lett. **102**, 170401 (2009), URL <https://link.aps.org/doi/10.1103/PhysRevLett.102.170401>.
- [46] Z. Hadzibabic and J. Dalibard, La Rivista del Nuovo Cimento **34**, 389 (2011), URL <https://doi.org/10.1393/ncr/i2011-10066-3>.
- [47] N. Prokof'ev, O. Ruebenacker, and B. Svistunov, Phys. Rev. Lett. **87**, 270402 (2001), URL <https://link.aps.org/doi/10.1103/PhysRevLett.87.270402>.
- [48] C. Mora and Y. Castin, Phys. Rev. A **67**, 053615 (2003), URL <https://link.aps.org/doi/10.1103/PhysRevA.67.053615>.
- [49] J. Dalibard, Lecture Notes at College de France **34**, 389 (2017).
- [50] V. Popov, *Å functional integrals and collective modes* (1987).
- [51] O. Penrose and L. Onsager, Phys. Rev. **104**, 576 (1956), URL <https://link.aps.org/doi/10.1103/PhysRev.104.576>.
- [52] Y. Castin, J. Phys. IV France **116**, 89 (2004), URL <https://doi.org/10.1051/jp4:2004116004>.
- [53] N. A. Keepfer, G. W. Stagg, L. Galantucci, C. F. Barenghi, and N. G. Parker, *Spin-up of a superfluid vortex lattice driven by rough boundaries* (2020), URL <https://link.aps.org/doi/10.1103/PhysRevB.102.144520>.

- [54] J. F. Annett et al., *Superconductivity, superfluids and condensates*, vol. 5 (Oxford University Press, 2004).
- [55] G. W. Stagg, *A numerical study of vortices and turbulence in quantum fluids*, Ph.D. thesis, Newcastle University (2016), URL <http://theses.ncl.ac.uk/jspui/handle/10443/3340>.
- [56] E. Hodby, G. Hechenblaikner, S. A. Hopkins, O. M. Maragò, and C. J. Foot, Phys. Rev. Lett. **88**, 010405 (2001), URL <https://link.aps.org/doi/10.1103/PhysRevLett.88.010405>.
- [57] F. Dalfovo, R. N. Bisset, C. Mordini, G. Lamporesi, and G. Ferrari, Journal of Experimental and Theoretical Physics **127**, 804 (2018), URL <https://doi.org/10.1134/S1063776118110018>.
- [58] J. R. Abo-Shaeer, C. Raman, J. M. Vogels, and W. Ketterle, Science **292**, 476 (2001), URL <https://www.science.org/doi/abs/10.1126/science.1060182>.
- [59] K. W. Madison, F. Chevy, W. Wohlleben, and J. Dalibard, Phys. Rev. Lett. **84**, 806 (2000), URL <https://link.aps.org/doi/10.1103/PhysRevLett.84.806>.
- [60] B. P. Anderson, P. C. Haljan, C. A. Regal, D. L. Feder, L. A. Collins, C. W. Clark, and E. A. Cornell, Phys. Rev. Lett. **86**, 2926 (2001), URL <https://link.aps.org/doi/10.1103/PhysRevLett.86.2926>.
- [61] E. J. Yarmchuk, M. J. V. Gordon, and R. E. Packard, Phys. Rev. Lett. **43**, 214 (1979), URL <https://link.aps.org/doi/10.1103/PhysRevLett.43.214>.
- [62] G. P. Bewley, D. P. Lathrop, and K. R. Sreenivasan, Nature **441**, 588 (2006), URL <https://doi.org/10.1038/441588a>.
- [63] K. W. Madison, F. Chevy, W. Wohlleben, and J. Dalibard, Journal of Modern Optics **47**, 2715 (2000), URL <https://www.tandfonline.com/doi/abs/10.1080/09500340008232191>.
- [64] P. Engels, I. Coddington, V. Schweikhard, and E. A. Cornell, Journal of Low Temperature Physics **134**, 683 (2004), URL <https://doi.org/10.1023/B:JOLT.0000012628.78400.ef>.
- [65] U. Giuriato, G. Krstulovic, and D. Proment, Journal of Physics A: Mathematical and Theoretical **52**, 305501 (2019), URL <https://doi.org/10.1088/1751-8121/ab2607>.

- [66] R. Doran, A. J. Groszek, and T. P. Billam, *Critical velocity and arrest of a superfluid in a point-like disordered potential* (2022), URL <https://arxiv.org/abs/2201.11887>.
- [67] K. W. Schwarz, Phys. Rev. Lett. **64**, 1130 (1990), URL <https://link.aps.org/doi/10.1103/PhysRevLett.64.1130>.
- [68] N. Hashimoto, R. Goto, H. Yano, K. Obara, O. Ishikawa, and T. Hata, Phys. Rev. B **76**, 020504 (2007), URL <https://link.aps.org/doi/10.1103/PhysRevB.76.020504>.
- [69] I.-K. Liu, J. Dziarmaga, S.-C. Gou, F. Dalfovo, and N. P. Proukakis, Phys. Rev. Research **2**, 033183 (2020), URL <https://link.aps.org/doi/10.1103/PhysRevResearch.2.033183>.
- [70] J. Radić, T. A. Sedrakyan, I. B. Spielman, and V. Galitski, Phys. Rev. A **84**, 063604 (2011), URL <https://link.aps.org/doi/10.1103/PhysRevA.84.063604>.
- [71] C.-F. Liu, Y.-M. Yu, S.-C. Gou, and W.-M. Liu, Phys. Rev. A **87**, 063630 (2013), URL <https://link.aps.org/doi/10.1103/PhysRevA.87.063630>.
- [72] T. Kibble, Physics Today **60**, 47 (2007).
- [73] W. Zurek, Physics Reports **276**, 177 (1996), ISSN 0370-1573, URL <https://www.sciencedirect.com/science/article/pii/S0370157396000099>.
- [74] D. E. Zmeev, F. Pakpour, P. M. Walmsley, A. I. Golov, W. Guo, D. N. McKinsey, G. G. Ihlas, P. V. E. McClintock, S. N. Fisher, and W. F. Vinen, Phys. Rev. Lett. **110**, 175303 (2013), URL <https://link.aps.org/doi/10.1103/PhysRevLett.110.175303>.
- [75] D. Duda, P. Švančara, M. La Mantia, M. Rotter, and L. Skrbek, Phys. Rev. B **92**, 064519 (2015), URL <https://link.aps.org/doi/10.1103/PhysRevB.92.064519>.
- [76] A. L. Fetter, Phys. Rev. **152**, 183 (1966), URL <https://link.aps.org/doi/10.1103/PhysRev.152.183>.
- [77] D. Stauffer and A. L. Fetter, Phys. Rev. **168**, 156 (1968), URL <https://link.aps.org/doi/10.1103/PhysRev.168.156>.
- [78] G. W. Stagg, N. G. Parker, and C. F. Barenghi, Phys. Rev. Lett. **118**, 135301 (2017), URL <https://link.aps.org/doi/10.1103/PhysRevLett.118.135301>.

- [79] C. Muirhead, W. F. Vinen, R. J. Donnelly, W. F. Vinen, and R. J. Donnelly, Philosophical Transactions of the Royal Society of London. Series A, Mathematical and Physical Sciences **311**, 433 (1984), URL <https://doi.org/10.1098/rspa.1985.0116>.
- [80] P. McClintonck and R. Bowley (Elsevier, 1995), vol. 14 of *Progress in Low Temperature Physics*, pp. 1–68, URL <https://www.sciencedirect.com/science/article/pii/S0079641706800156>.
- [81] N. G. Berloff and P. H. Roberts, Physics Letters A **274**, 69 (2000), ISSN 0375-9601, URL <https://www.sciencedirect.com/science/article/pii/S0375960100005168>.
- [82] T. Winiecki and C. S. Adams, Europhysics Letters (EPL) **52**, 257 (2000), URL <https://doi.org/10.1209/epl/i2000-00432-x>.
- [83] A. Villois and H. Salman, Phys. Rev. B **97**, 094507 (2018), URL <https://link.aps.org/doi/10.1103/PhysRevB.97.094507>.
- [84] K. W. Schwarz, Phys. Rev. B **38**, 2398 (1988), URL <https://link.aps.org/doi/10.1103/PhysRevB.38.2398>.
- [85] K. W. Schwarz, Phys. Rev. B **31**, 5782 (1985), URL <https://link.aps.org/doi/10.1103/PhysRevB.31.5782>.
- [86] M. Tsubota and S. Maekawa, Phys. Rev. B **47**, 12040 (1993), URL <https://link.aps.org/doi/10.1103/PhysRevB.47.12040>.
- [87] K. W. Schwarz, Phys. Rev. A **10**, 2306 (1974), URL <https://link.aps.org/doi/10.1103/PhysRevA.10.2306>.
- [88] D. Kivotides, C. F. Barenghi, and Y. A. Sergeev, Journal of Low Temperature Physics **144**, 121 (2006), URL <https://doi.org/10.1007/s10909-006-9253-1>.
- [89] R. Hänninen, A. Mitani, and M. Tsubota, Journal of Low Temperature Physics **138**, 589 (2005), URL <https://doi.org/10.1007/s10909-005-2266-3>.
- [90] R. Hänninen and A. W. Baggaley, Proceedings of the National Academy of Sciences **111**, 4667 (2014), ISSN 0027-8424, URL https://www.pnas.org/content/111/Supplement_1/4667.
- [91] S. Choi, S. A. Morgan, and K. Burnett, Phys. Rev. A **57**, 4057 (1998), URL <https://link.aps.org/doi/10.1103/PhysRevA.57.4057>.

- [92] M. Tsubota, K. Kasamatsu, and M. Ueda, Phys. Rev. A **65**, 023603 (2002), URL <https://link.aps.org/doi/10.1103/PhysRevA.65.023603>.
- [93] E. M. Madarassy and C. F. Barenghi, Journal of Low Temperature Physics **152**, 122 (2008), URL <https://doi.org/10.1007/s10909-008-9811-9>.
- [94] M. Leadbeater, T. Winiecki, D. C. Samuels, C. F. Barenghi, and C. S. Adams, Phys. Rev. Lett. **86**, 1410 (2001), URL <https://link.aps.org/doi/10.1103/PhysRevLett.86.1410>.
- [95] N. G. Berloff, Phys. Rev. A **69**, 053601 (2004), URL <https://link.aps.org/doi/10.1103/PhysRevA.69.053601>.
- [96] G. R. Dennis, J. J. Hope, and M. T. Johnsson, Computer Physics Communications **184**, 201 (2013), ISSN 0010-4655, URL <http://www.sciencedirect.com/science/article/pii/S0010465512002822>.
- [97] R. Brown, *A brief account of microscopical observations made... on the particles contained in the pollen of plants, and on the general existence of active molecules in organic and inorganic bodies* (1828).
- [98] B. B. Mandelbrot and J. W. Van Ness, SIAM Review **10**, 422 (1968), URL <https://doi.org/10.1137/1010093>.
- [99] A. Fournier, D. Fussell, and L. Carpenter, Commun. ACM **25**, 371384 (1982), ISSN 0001-0782, URL <https://doi.org/10.1145/358523.358553>.
- [100] B. B. Mandelbrot, Physica Scripta **32**, 257 (1985), URL <https://doi.org/10.1088/0031-8949/32/4/001>.
- [101] A. Majumdar and B. Bhushan, Journal of Tribology **112**, 205 (1990), ISSN 0742-4787, URL <https://doi.org/10.1115/1.2920243>.
- [102] A. Villois, G. Krstulovic, D. Proment, and H. Salman, Journal of Physics A: Mathematical and Theoretical **49**, 415502 (2016), URL <https://doi.org/10.1088/1751-8113/49/41/415502>.
- [103] N. A. Keepfer, G. W. Stagg, L. Galantucci, C. F. Barenghi, and N. G. Parker, *Supplementary material* (2020), URL <https://link.aps.org/doi/10.1103/PhysRevB.102.144520>.
- [104] T. Frisch, Y. Pomeau, and S. Rica, Phys. Rev. Lett. **69**, 1644 (1992), URL <https://link.aps.org/doi/10.1103/PhysRevLett.69.1644>.

- [105] G. W. Stagg, N. G. Parker, and C. F. Barenghi, Journal of Physics B: Atomic, Molecular and Optical Physics **47**, 095304 (2014), URL <https://doi.org/10.1088/0953-4075/47/9/095304>.
- [106] A. Aftalion and I. Danaila, Phys. Rev. A **68**, 023603 (2003), URL <https://link.aps.org/doi/10.1103/PhysRevA.68.023603>.
- [107] E. Rickinson, C. F. Barenghi, Y. A. Sergeev, and A. W. Baggaley, Phys. Rev. B **101**, 134519 (2020), URL <https://link.aps.org/doi/10.1103/PhysRevB.101.134519>.
- [108] L. J. Campbell and R. M. Ziff, Phys. Rev. B **20**, 1886 (1979), URL <https://link.aps.org/doi/10.1103/PhysRevB.20.1886>.
- [109] T. S. Wood, M. Mesgarnezhad, G. W. Stagg, and C. F. Barenghi, Phys. Rev. B **100**, 024505 (2019), URL <https://link.aps.org/doi/10.1103/PhysRevB.100.024505>.
- [110] P. Mathieu, J. C. Marechal, and Y. Simon, Phys. Rev. B **22**, 4293 (1980), URL <https://link.aps.org/doi/10.1103/PhysRevB.22.4293>.
- [111] J. A. Northby and R. J. Donnelly, Phys. Rev. Lett. **25**, 214 (1970), URL <https://link.aps.org/doi/10.1103/PhysRevLett.25.214>.
- [112] D. S. Shenk and J. B. Mehl, Phys. Rev. Lett. **27**, 1703 (1971), URL <https://link.aps.org/doi/10.1103/PhysRevLett.27.1703>.
- [113] W. J. Kwon, G. Moon, J.-y. Choi, S. W. Seo, and Y.-i. Shin, Phys. Rev. A **90**, 063627 (2014), URL <https://link.aps.org/doi/10.1103/PhysRevA.90.063627>.
- [114] G. W. Stagg, A. J. Allen, N. G. Parker, and C. F. Barenghi, Phys. Rev. A **91**, 013612 (2015), URL <https://link.aps.org/doi/10.1103/PhysRevA.91.013612>.
- [115] A. J. Groszek, T. P. Simula, D. M. Paganin, and K. Helmerson, Phys. Rev. A **93**, 043614 (2016), URL <https://link.aps.org/doi/10.1103/PhysRevA.93.043614>.
- [116] C. A. Jones and P. H. Roberts, Journal of Physics A: Mathematical and General **15**, 2599 (1982), URL <https://doi.org/10.1088/0305-4470/15/8/036>.
- [117] S. Tsuchiya, F. Dalfovo, and L. Pitaevskii, Phys. Rev. A **77**, 045601 (2008), URL <https://link.aps.org/doi/10.1103/PhysRevA.77.045601>.
- [118] M. T. Reeves, T. P. Billam, B. P. Anderson, and A. S. Bradley, Phys. Rev. A **89**, 053631 (2014), URL <https://link.aps.org/doi/10.1103/PhysRevA.89.053631>.

- [119] A. S. Bradley, R. K. Kumar, S. Pal, and X. Yu, *Spectral analysis for compressible quantum fluids* (2021), URL <https://arxiv.org/abs/2112.04012>.
- [120] L. Galantucci, A. W. Baggaley, N. G. Parker, and C. F. Barenghi, Proceedings of the National Academy of Sciences **116**, 12204 (2019), URL <https://www.pnas.org/doi/abs/10.1073/pnas.1818668116>.
- [121] M. Barranco, M. Pi, S. M. Gatica, E. S. Hernández, and J. Navarro, Phys. Rev. B **56**, 8997 (1997), URL <https://link.aps.org/doi/10.1103/PhysRevB.56.8997>.
- [122] F. Dalfovo, Phys. Rev. B **46**, 5482 (1992), URL <https://link.aps.org/doi/10.1103/PhysRevB.46.5482>.
- [123] N. G. Berloff, M. Brachet, and N. P. Proukakis, Proceedings of the National Academy of Sciences **111**, 4675 (2014), URL <https://www.pnas.org/doi/abs/10.1073/pnas.1312549111>.
- [124] J. Reneuve, J. Salort, and L. Chevillard, Phys. Rev. Fluids **3**, 114602 (2018), URL <https://link.aps.org/doi/10.1103/PhysRevFluids.3.114602>.
- [125] A. Sinatra, C. Lobo, and Y. Castin, Phys. Rev. Lett. **87**, 210404 (2001), URL <https://link.aps.org/doi/10.1103/PhysRevLett.87.210404>.
- [126] M. Brewczyk, M. Gajda, and K. Rzażewski, Journal of Physics B: Atomic, Molecular and Optical Physics **40**, R1 (2007), URL <https://doi.org/10.1088/0953-4075/40/2/r01>.
- [127] P. Blakie, A. Bradley, M. Davis, R. Ballagh, and C. Gardiner, Advances in Physics **57**, 363 (2008), URL <https://doi.org/10.1080/00018730802564254>.
- [128] S. P. Cockburn and N. P. Proukakis, Phys. Rev. A **86**, 033610 (2012), URL <https://link.aps.org/doi/10.1103/PhysRevA.86.033610>.
- [129] P. Deuar and J. Pietraszewicz, *A semiclassical field theory that is freed of the ultraviolet catastrophe* (2019), URL <https://arxiv.org/abs/1904.06266>.
- [130] A. S. Bradley and P. B. Blakie, Phys. Rev. A **90**, 023631 (2014), URL <https://link.aps.org/doi/10.1103/PhysRevA.90.023631>.
- [131] J. Pietraszewicz, E. Witkowska, and P. Deuar, Phys. Rev. A **96**, 033612 (2017), URL <https://link.aps.org/doi/10.1103/PhysRevA.96.033612>.
- [132] R. G. McDonald and A. S. Bradley, Phys. Rev. A **93**, 063604 (2016), URL <https://link.aps.org/doi/10.1103/PhysRevA.93.063604>.

- [133] T. Bland, E. Poli, C. Politi, L. Klaus, M. A. Norcia, F. Ferlaino, L. Santos, and R. N. Bisset, Phys. Rev. Lett. **128**, 195302 (2022), URL <https://link.aps.org/doi/10.1103/PhysRevLett.128.195302>.
- [134] H. T. Stoof, Journal of low temperature physics **114**, 11 (1999), URL <https://doi.org/10.1023/A:1021897703053>.
- [135] H. Stoof and M. Bijlsma, Journal of low temperature physics **124**, 431 (2001), URL <https://doi.org/10.1023/A:1017519118408>.
- [136] R. A. Duine and H. T. C. Stoof, Phys. Rev. A **65**, 013603 (2001), URL <https://link.aps.org/doi/10.1103/PhysRevA.65.013603>.
- [137] C. W. Gardiner, J. R. Anglin, and T. I. A. Fudge, Journal of Physics B: Atomic, Molecular and Optical Physics **35**, 1555 (2002), URL <https://doi.org/10.1088/0953-4075/35/6/310>.
- [138] C. W. Gardiner and M. J. Davis, Journal of Physics B: Atomic, Molecular and Optical Physics **36**, 4731 (2003), URL <https://doi.org/10.1088/0953-4075/36/23/010>.
- [139] D. Matthew et al., *Quantum Gases: Finite temperature and non-equilibrium dynamics*, vol. 1 (World Scientific, 2013).
- [140] A. S. Bradley and C. W. Gardiner, *The stochastic gross-pitaevskii equation: Iii* (2006), URL <https://arxiv.org/abs/cond-mat/0602162>.
- [141] S. J. Rooney, P. B. Blakie, and A. S. Bradley, Phys. Rev. A **86**, 053634 (2012), URL <https://link.aps.org/doi/10.1103/PhysRevA.86.053634>.
- [142] A. Sinatra, C. Lobo, and Y. Castin, Journal of Physics B: Atomic, Molecular and Optical Physics **35**, 3599 (2002), URL <https://doi.org/10.1088/0953-4075/35/17/301>.
- [143] C. W. Gardiner and P. Zoller, Phys. Rev. A **55**, 2902 (1997), URL <https://link.aps.org/doi/10.1103/PhysRevA.55.2902>.
- [144] D. Jaksch, C. W. Gardiner, and P. Zoller, Phys. Rev. A **56**, 575 (1997), URL <https://link.aps.org/doi/10.1103/PhysRevA.56.575>.
- [145] C. W. Gardiner and P. Zoller, Phys. Rev. A **58**, 536 (1998), URL <https://link.aps.org/doi/10.1103/PhysRevA.58.536>.
- [146] D. Jaksch, C. W. Gardiner, K. M. Gheri, and P. Zoller, Phys. Rev. A **58**, 1450 (1998), URL <https://link.aps.org/doi/10.1103/PhysRevA.58.1450>.

- [147] C. W. Gardiner and P. Zoller, Phys. Rev. A **61**, 033601 (2000), URL <https://link.aps.org/doi/10.1103/PhysRevA.61.033601>.
- [148] M. D. Lee and C. W. Gardiner, Phys. Rev. A **62**, 033606 (2000), URL <https://link.aps.org/doi/10.1103/PhysRevA.62.033606>.
- [149] M. J. Davis, C. W. Gardiner, and R. J. Ballagh, Phys. Rev. A **62**, 063608 (2000), URL <https://link.aps.org/doi/10.1103/PhysRevA.62.063608>.
- [150] N. Proukakis, S. Gardiner, M. Davis, and M. Szymaska, eds., *Quantum Gases: Finite Temperature and Non-Equilibrium Dynamics: 1 (Cold Atoms)* (ICP, 2013).
- [151] I. K. Liu, S. Donadello, G. Lamporesi, G. Ferrari, S. C. Gou, F. Dalfovo, and N. P. Proukakis, Communications Physics **1**, 24 (2018), URL <https://doi.org/10.1038/s42005-018-0023-6>.
- [152] A. J. Groszek, P. Comaron, N. P. Proukakis, and T. P. Billam, Phys. Rev. Research **3**, 013212 (2021), URL <https://link.aps.org/doi/10.1103/PhysRevResearch.3.013212>.
- [153] S. P. Cockburn, D. Gallucci, and N. P. Proukakis, Phys. Rev. A **84**, 023613 (2011), URL <https://link.aps.org/doi/10.1103/PhysRevA.84.023613>.
- [154] A. S. Bradley, C. W. Gardiner, and M. J. Davis, Phys. Rev. A **77**, 033616 (2008), URL <https://link.aps.org/doi/10.1103/PhysRevA.77.033616>.
- [155] C. Gardiner, P. Zoller, and P. Zoller, *Quantum noise: a handbook of Markovian and non-Markovian quantum stochastic methods with applications to quantum optics* (Springer Science & Business Media, 2004).
- [156] R. G. McDonald, P. S. Barnett, F. Atayee, and A. S. Bradley, SciPost Phys. **8**, 29 (2020), URL <https://scipost.org/10.21468/SciPostPhys.8.2.029>.
- [157] S. J. Rooney, A. S. Bradley, and P. B. Blakie, Phys. Rev. A **81**, 023630 (2010), URL <https://link.aps.org/doi/10.1103/PhysRevA.81.023630>.
- [158] Z. Mehdi, A. S. Bradley, J. J. Hope, and S. S. Szigeti, SciPost Phys. **11**, 80 (2021), URL <https://scipost.org/10.21468/SciPostPhys.11.4.080>.
- [159] A. S. Bradley, S. J. Rooney, and R. G. McDonald, Phys. Rev. A **92**, 033631 (2015), URL <https://link.aps.org/doi/10.1103/PhysRevA.92.033631>.
- [160] H. Stoof, in *Dynamics: Models and Kinetic Methods for Non-equilibrium Many Body Systems* (Springer, 2000), pp. 491–502.

- [161] F. Larcher, *Dynamical excitations in low-dimensional condensates: sound, vortices and quenched dynamics*, Ph.D. thesis, University of Trento (2018), URL <http://eprints-phd.biblio.unitn.it/2902>.
- [162] D. M. Stamper-Kurn, H.-J. Miesner, A. P. Chikkatur, S. Inouye, J. Stenger, and W. Ketterle, Phys. Rev. Lett. **81**, 2194 (1998), URL <https://link.aps.org/doi/10.1103/PhysRevLett.81.2194>.
- [163] N. P. Proukakis, Phys. Rev. A **74**, 053617 (2006), URL <https://link.aps.org/doi/10.1103/PhysRevA.74.053617>.
- [164] U. Al Khawaja, J. O. Andersen, N. P. Proukakis, and H. T. C. Stoof, Phys. Rev. A **66**, 013615 (2002), URL <https://link.aps.org/doi/10.1103/PhysRevA.66.013615>.
- [165] N. Proukakis, Laser Physics (2003), URL <https://arxiv.org/abs/cond-mat/0311003>.
- [166] N. P. Proukakis, J. Schmiedmayer, and H. T. C. Stoof, Phys. Rev. A **73**, 053603 (2006), URL <https://link.aps.org/doi/10.1103/PhysRevA.73.053603>.
- [167] T. Bland, Q. Marolleau, P. Comaron, B. A. Malomed, and N. P. Proukakis, Journal of Physics B: Atomic, Molecular and Optical Physics **53**, 115301 (2020), URL <https://doi.org/10.1088/1361-6455/ab81e9>.
- [168] R. K. Pathria, *Statistical mechanics*, vol. 45 (Pergamon, 1972).
- [169] M. J. Davis and P. B. Blakie, Phys. Rev. Lett. **96**, 060404 (2006), URL <https://link.aps.org/doi/10.1103/PhysRevLett.96.060404>.
- [170] J. L. Ville, T. Bienaimé, R. Saint-Jalm, L. Corman, M. Aidelsburger, L. Chomaz, K. Kleinlein, D. Perconte, S. Nascimbène, J. Dalibard, et al., Phys. Rev. A **95**, 013632 (2017), URL <https://link.aps.org/doi/10.1103/PhysRevA.95.013632>.
- [171] J.-L. Ville, *Quantum gases in box potentials: Sound and light in bosonic Flatland*, Ph.D. thesis, Université Paris sciences et lettres (2018), URL <https://tel.archives-ouvertes.fr/tel-01925194v2>.
- [172] M. J. Davis, P. B. Blakie, A. H. van Amerongen, N. J. van Druten, and K. V. Kheruntsyan, Phys. Rev. A **85**, 031604 (2012), URL <https://link.aps.org/doi/10.1103/PhysRevA.85.031604>.
- [173] M. C. Garrett, T. M. Wright, and M. J. Davis, Phys. Rev. A **87**, 063611 (2013), URL <https://link.aps.org/doi/10.1103/PhysRevA.87.063611>.

- [174] C. Henkel, T.-O. Sauer, and N. P. Proukakis, Journal of Physics B: Atomic, Molecular and Optical Physics **50**, 114002 (2017), URL <https://doi.org/10.1088/1361-6455/aa6888>.
- [175] S.-W. Su, S.-C. Gou, A. Bradley, O. Fialko, and J. Brand, Phys. Rev. Lett. **110**, 215302 (2013), URL <https://link.aps.org/doi/10.1103/PhysRevLett.110.215302>.
- [176] S. J. Rooney, P. B. Blakie, B. P. Anderson, and A. S. Bradley, Phys. Rev. A **84**, 023637 (2011), URL <https://link.aps.org/doi/10.1103/PhysRevA.84.023637>.
- [177] T. W. Neely, A. S. Bradley, E. C. Samson, S. J. Rooney, E. M. Wright, K. J. H. Law, R. Carretero-González, P. G. Kevrekidis, M. J. Davis, and B. P. Anderson, Phys. Rev. Lett. **111**, 235301 (2013), URL <https://link.aps.org/doi/10.1103/PhysRevLett.111.235301>.
- [178] M. T. Reeves, T. P. Billam, B. P. Anderson, and A. S. Bradley, Phys. Rev. Lett. **110**, 104501 (2013), URL <https://link.aps.org/doi/10.1103/PhysRevLett.110.104501>.
- [179] S. J. Rooney, P. B. Blakie, and A. S. Bradley, Phys. Rev. E **89**, 013302 (2014), URL <https://link.aps.org/doi/10.1103/PhysRevE.89.013302>.
- [180] E. B. Linscott and P. B. Blakie, Phys. Rev. A **90**, 053605 (2014), URL <https://link.aps.org/doi/10.1103/PhysRevA.90.053605>.
- [181] R. G. McDonald and A. S. Bradley, Phys. Rev. A **92**, 033616 (2015), URL <https://link.aps.org/doi/10.1103/PhysRevA.92.033616>.
- [182] S. J. Rooney, A. J. Allen, U. Zülicke, N. P. Proukakis, and A. S. Bradley, Phys. Rev. A **93**, 063603 (2016), URL <https://link.aps.org/doi/10.1103/PhysRevA.93.063603>.
- [183] I. Bouchoule, S. S. Szigeti, M. J. Davis, and K. V. Kheruntsyan, Phys. Rev. A **94**, 051602 (2016), URL <https://link.aps.org/doi/10.1103/PhysRevA.94.051602>.
- [184] I.-K. Liu, R. W. Pattinson, T. P. Billam, S. A. Gardiner, S. L. Cornish, T.-M. Huang, W.-W. Lin, S.-C. Gou, N. G. Parker, and N. P. Proukakis, Phys. Rev. A **93**, 023628 (2016), URL <https://link.aps.org/doi/10.1103/PhysRevA.93.023628>.
- [185] S. A. Simmons, F. A. Bayocboc, J. C. Pillay, D. Colas, I. P. McCulloch, and K. V. Kheruntsyan, Phys. Rev. Lett. **125**, 180401 (2020), URL <https://link.aps.org/doi/10.1103/PhysRevLett.125.180401>.

- [186] A. J. Groszek, M. J. Davis, and T. P. Simula, SciPost Phys. **8**, 39 (2020), URL <https://scipost.org/10.21468/SciPostPhys.8.3.039>.
- [187] C. N. Weiler, T. W. Neely, D. R. Scherer, A. S. Bradley, M. J. Davis, and B. P. Anderson, Nature **455**, 948 (2008), URL <https://doi.org/10.1038/nature07334>.
- [188] S. J. Rooney, T. W. Neely, B. P. Anderson, and A. S. Bradley, Phys. Rev. A **88**, 063620 (2013), URL <https://link.aps.org/doi/10.1103/PhysRevA.88.063620>.
- [189] S. P. Cockburn, A. Negretti, N. P. Proukakis, and C. Henkel, Phys. Rev. A **83**, 043619 (2011), URL <https://link.aps.org/doi/10.1103/PhysRevA.83.043619>.
- [190] K. Brown, T. Bland, P. Comaron, and N. P. Proukakis, Phys. Rev. Research **3**, 013097 (2021), URL <https://link.aps.org/doi/10.1103/PhysRevResearch.3.013097>.
- [191] A. Roy, M. Ota, A. Recati, and F. Dalfovo, Phys. Rev. Research **3**, 013161 (2021), URL <https://link.aps.org/doi/10.1103/PhysRevResearch.3.013161>.
- [192] N. Keepfer, I.-K. Liu, F. Dalfovo, and N. Proukakis, *Phase transition dimensionality crossover from two to three dimensions in a trapped ultracold atomic bose gas* (2022), URL <https://arxiv.org/abs/2204.10120>.
- [193] V. Berezinskii, Sov. Phys. JETP **34**, 610 (1972).
- [194] J. M. Kosterlitz and D. J. Thouless, Journal of Physics C: Solid State Physics **6**, 1181 (1973), URL <https://doi.org/10.1088/0022-3719/6/7/010>.
- [195] C. J. Pethick and H. Smith, *Bose-Einstein condensation in dilute gases* (Cambridge university press, 2008).
- [196] W. Mullin, J. Low Temp. Phys. **106**, 615 (1997), URL <https://doi.org/10.1007/BF02395928>.
- [197] J. O. Andersen, U. Al Khawaja, and H. T. C. Stoof, Phys. Rev. Lett. **88**, 070407 (2002), URL <https://link.aps.org/doi/10.1103/PhysRevLett.88.070407>.
- [198] U. Al Khawaja, J. O. Andersen, N. P. Proukakis, and H. T. C. Stoof, Phys. Rev. A **66**, 059902 (2002), URL <https://link.aps.org/doi/10.1103/PhysRevA.66.059902>.
- [199] U. Al Khawaja, N. P. Proukakis, J. O. Andersen, M. W. J. Romans, and H. T. C. Stoof, Phys. Rev. A **68**, 043603 (2003), URL <https://link.aps.org/doi/10.1103/PhysRevA.68.043603>.

- [200] D.S. Petrov, D.M. Gangardt, and G.V. Shlyapnikov, J. Phys. IV France **116**, 5 (2004), URL <https://doi.org/10.1051/jp4:2004116001>.
- [201] B. P. van Zyl, R. K. Bhaduri, and J. Sigitich, Journal of Physics B: Atomic, Molecular and Optical Physics **35**, 1251 (2002), URL <https://iopscience.iop.org/article/10.1088/0953-4075/35/5/311>.
- [202] R. N. Bisset and P. B. Blakie, Phys. Rev. A **80**, 035602 (2009), URL <https://link.aps.org/doi/10.1103/PhysRevA.80.035602>.
- [203] F. Delfino and E. Vicari, Phys. Rev. A **96**, 043623 (2017), URL <https://link.aps.org/doi/10.1103/PhysRevA.96.043623>.
- [204] A. Görlitz, J. M. Vogels, A. E. Leanhardt, C. Raman, T. L. Gustavson, J. R. Abo-Shaeer, A. P. Chikkatur, S. Gupta, S. Inouye, T. Rosenband, et al., Phys. Rev. Lett. **87**, 130402 (2001), URL <https://link.aps.org/doi/10.1103/PhysRevLett.87.130402>.
- [205] P. Krüger, Z. Hadzibabic, and J. Dalibard, Phys. Rev. Lett. **99**, 040402 (2007), URL <https://link.aps.org/doi/10.1103/PhysRevLett.99.040402>.
- [206] Z. Hadzibabic, P. Krger, M. Cheneau, S. P. Rath, and J. Dalibard, New Journal of Physics **10**, 045006 (2008), URL <https://doi.org/10.1088/1367-2630/10/4/045006>.
- [207] R. J. Fletcher, M. Robert-de Saint-Vincent, J. Man, N. Navon, R. P. Smith, K. G. H. Viebahn, and Z. Hadzibabic, Phys. Rev. Lett. **114**, 255302 (2015), URL <https://link.aps.org/doi/10.1103/PhysRevLett.114.255302>.
- [208] S. P. Cockburn and N. P. Proukakis, Laser Physics **19**, 558 (2009), URL <https://doi.org/10.1134/S1054660X09040057>.
- [209] B. Damski and W. H. Zurek, Phys. Rev. Lett. **104**, 160404 (2010), URL <https://link.aps.org/doi/10.1103/PhysRevLett.104.160404>.
- [210] A. del Campo and W. H. Zurek, *Universality of phase transition dynamics: Topological defects from symmetry breaking* (World Scientific, 2014), pp. 31–87, URL https://www.worldscientific.com/doi/abs/10.1142/9789814583060_0002.
- [211] T. W. B. Kibble, Journal of Physics A: Mathematical and General **9**, 1387 (1976), URL <https://doi.org/10.1088/0305-4470/9/8/029>.
- [212] W. H. Zurek, Nature **317**, 505 (1985), URL <https://doi.org/10.1038/317505a0>.
- [213] V. Berezinskii, Sov. Phys. JETP **32**, 493 (1971).

- [214] P. Nozières and D. Pines, *The Theory of Quantum Liquids (Advanced Book Classics)* (Perseus Books, LLC, 1999).
- [215] D. S. Fisher and P. C. Hohenberg, Phys. Rev. B **37**, 4936 (1988), URL <https://link.aps.org/doi/10.1103/PhysRevB.37.4936>.
- [216] S. Pilati, S. Giorgini, and N. Prokof'ev, Phys. Rev. Lett. **100**, 140405 (2008), URL <https://link.aps.org/doi/10.1103/PhysRevLett.100.140405>.
- [217] N. Prokof'ev and B. Svistunov, Phys. Rev. A **66**, 043608 (2002), URL <https://link.aps.org/doi/10.1103/PhysRevA.66.043608>.
- [218] P. Christodoulou, M. Galka, N. Dogra, R. Lopes, J. Schmitt, and Z. Hadzibabic, Nature **594**, 191 (2021), ISSN 1476-4687, URL <https://doi.org/10.1038/s41586-021-03537-9>.
- [219] S. P. Rath, T. Yefsah, K. J. Günter, M. Cheneau, R. Desbuquois, M. Holzmann, W. Krauth, and J. Dalibard, Phys. Rev. A **82**, 013609 (2010), URL <https://link.aps.org/doi/10.1103/PhysRevA.82.013609>.
- [220] C.-L. Hung, X. Zhang, N. Gemelke, and C. Chin, Nature **470**, 236 (2011), URL <https://doi.org/10.1038/nature09722>.
- [221] S. W. Seo, B. Ko, J. H. Kim, and Y. Shin, Scientific Reports **7**, 4587 (2017), ISSN 2045-2322, URL <https://doi.org/10.1038/s41598-017-04122-9>.
- [222] J. Hertkorn, J.-N. Schmidt, M. Guo, F. Böttcher, K. S. H. Ng, S. D. Graham, P. Uerlings, H. P. Büchler, T. Langen, M. Zwierlein, et al., Phys. Rev. Lett. **127**, 155301 (2021), URL <https://link.aps.org/doi/10.1103/PhysRevLett.127.155301>.
- [223] G. Gauthier, M. T. Reeves, X. Yu, A. S. Bradley, M. A. Baker, T. A. Bell, H. Rubinsztein-Dunlop, M. J. Davis, and T. W. Neely, Science **364**, 1264 (2019), URL <https://www.science.org/doi/abs/10.1126/science.aat5718>.
- [224] S. Tempone-Wiltshire, S. Johnstone, and K. Helmerson, Opt. Express **25**, 296 (2017), URL <http://opg.optica.org/oe/abstract.cfm?URI=oe-25-1-296>.
- [225] S. P. Johnstone, A. J. Groszek, P. T. Starkey, C. J. Billington, T. P. Simula, and K. Helmerson, Science **364**, 1267 (2019), URL <https://www.science.org/doi/abs/10.1126/science.aat5793>.
- [226] T. W. Neely, E. C. Samson, A. S. Bradley, M. J. Davis, and B. P. Anderson, Phys. Rev. Lett. **104**, 160401 (2010), URL <https://link.aps.org/doi/10.1103/PhysRevLett.104.160401>.

- [227] R. N. Bisset, M. J. Davis, T. P. Simula, and P. B. Blakie, Phys. Rev. A **79**, 033626 (2009), URL <https://link.aps.org/doi/10.1103/PhysRevA.79.033626>.
- [228] A. Bezett and P. B. Blakie, Phys. Rev. A **79**, 033611 (2009), URL <https://link.aps.org/doi/10.1103/PhysRevA.79.033611>.
- [229] C. J. Foster, P. B. Blakie, and M. J. Davis, Phys. Rev. A **81**, 023623 (2010), URL <https://link.aps.org/doi/10.1103/PhysRevA.81.023623>.
- [230] M. Kobayashi and L. F. Cugliandolo, Phys. Rev. E **94**, 062146 (2016), URL <https://link.aps.org/doi/10.1103/PhysRevE.94.062146>.
- [231] Y. M. Kagan, B. Svistunov, and G. Shlyapnikov, Sov. Phys. JETP **75**, 387 (1992).
- [232] D. S. Petrov, G. V. Shlyapnikov, and J. T. M. Walraven, Phys. Rev. Lett. **87**, 050404 (2001), URL <https://link.aps.org/doi/10.1103/PhysRevLett.87.050404>.
- [233] Y. Kagan and B. Svistunov, Zh. Eksp. Teor. Fiz. **105**, 353 (1994).
- [234] K. Binder, Zeitschrift für Physik B Condensed Matter **43**, 119 (1981), URL <https://doi.org/10.1007/BF01293604>.
- [235] M. J. Davis and S. A. Morgan, Phys. Rev. A **68**, 053615 (2003), URL <https://link.aps.org/doi/10.1103/PhysRevA.68.053615>.
- [236] M. Kobayashi and L. F. Cugliandolo, EPL (Europhysics Letters) **115**, 20007 (2016), URL <https://doi.org/10.1209/0295-5075/115/20007>.
- [237] M. Campostrini, M. Hasenbusch, A. Pelissetto, P. Rossi, and E. Vicari, Phys. Rev. B **63**, 214503 (2001), URL <https://link.aps.org/doi/10.1103/PhysRevB.63.214503>.
- [238] K. Gawryluk and M. Brewczyk, Phys. Rev. A **99**, 033615 (2019), URL <https://link.aps.org/doi/10.1103/PhysRevA.99.033615>.
- [239] S. Giorgini, L. P. Pitaevskii, and S. Stringari, Phys. Rev. A **54**, R4633 (1996), URL <https://link.aps.org/doi/10.1103/PhysRevA.54.R4633>.
- [240] S. Giorgini, L. P. Pitaevskii, and S. Stringari, Journal of Low Temperature Physics **109**, 309 (1997), URL <https://doi.org/10.1007/BF02396737>.
- [241] T. Ozawa and S. Stringari, Phys. Rev. Lett. **112**, 025302 (2014), URL <https://link.aps.org/doi/10.1103/PhysRevLett.112.025302>.
- [242] R. J. Donnelly, Physics Today **62**, 34 (2009), <https://doi.org/10.1063/1.3248499>, URL <https://doi.org/10.1063/1.3248499>.

- [243] L. Tisza, Nature **141**, 913 (1938), URL <https://doi.org/10.1038/141913a0>.
- [244] V. Peshkov, Sov. Phys. JETP **11**, 580 (1960).
- [245] D. M. Stamper-Kurn, H.-J. Miesner, S. Inouye, M. R. Andrews, and W. Ketterle, Phys. Rev. Lett. **81**, 500 (1998), URL <https://link.aps.org/doi/10.1103/PhysRevLett.81.500>.
- [246] L. A. Sidorenkov, M. K. Tey, R. Grimm, Y.-H. Hou, L. Pitaevskii, and S. Stringari, Nature **498**, 78 (2013), URL <https://doi.org/10.1038/nature12136>.
- [247] H. Hu, E. Taylor, X.-J. Liu, S. Stringari, and A. Griffin, New Journal of Physics **12**, 043040 (2010), URL <https://doi.org/10.1088/1367-2630/12/4/043040>.
- [248] A. Griffin and E. Zaremba, Phys. Rev. A **56**, 4839 (1997), URL <https://link.aps.org/doi/10.1103/PhysRevA.56.4839>.
- [249] L. Pitaevskii and S. Stringari, Physics Letters A **235**, 398 (1997), ISSN 0375-9601, URL <https://www.sciencedirect.com/science/article/pii/S037596019700666X>.
- [250] M. R. Andrews, D. M. Kurn, H.-J. Miesner, D. S. Durfee, C. G. Townsend, S. Inouye, and W. Ketterle, Phys. Rev. Lett. **79**, 553 (1997), URL <https://link.aps.org/doi/10.1103/PhysRevLett.79.553>.
- [251] R. Meppelink, S. B. Koller, and P. van der Straten, Phys. Rev. A **80**, 043605 (2009), URL <https://link.aps.org/doi/10.1103/PhysRevA.80.043605>.
- [252] T. Nikuni, E. Zaremba, and A. Griffin, Phys. Rev. Lett. **83**, 10 (1999), URL <https://link.aps.org/doi/10.1103/PhysRevLett.83.10>.
- [253] T. Nikuni and A. Griffin, Journal of Low Temperature Physics **111**, 793 (1998), URL <https://doi.org/10.1023/A:1022221123509>.
- [254] E. Zaremba, Phys. Rev. A **57**, 518 (1998), URL <https://link.aps.org/doi/10.1103/PhysRevA.57.518>.
- [255] E. Zaremba, T. Nikuni, and A. Griffin, Journal of Low Temperature Physics **116**, 277 (1999), URL <https://doi.org/10.1023/A:1021846002995>.
- [256] A. Griffin, T. Nikuni, and E. Zaremba, *Bose-condensed gases at finite temperatures* (Cambridge University Press, 2009).
- [257] T. R. Kirkpatrick and J. R. Dorfman, Phys. Rev. A **28**, 2576 (1983), URL <https://link.aps.org/doi/10.1103/PhysRevA.28.2576>.

- [258] S. Gautam, A. Roy, and S. Mukerjee, Phys. Rev. A **89**, 013612 (2014), URL <https://link.aps.org/doi/10.1103/PhysRevA.89.013612>.
- [259] M. Ota, *Sound propagation in dilute Bose gases*, Ph.D. thesis, University of Trento (2020).
- [260] M. Ota and S. Stringari, Phys. Rev. A **97**, 033604 (2018), URL <https://link.aps.org/doi/10.1103/PhysRevA.97.033604>.
- [261] S. Stringari, Nature Physics **17**, 770 (2021), URL <https://doi.org/10.1038/s41567-021-01276-2>.
- [262] M. A. Baranov, M. Dalmonte, G. Pupillo, and P. Zoller, Chemical Reviews **112**, 5012 (2012), pMID: 22877362, <https://doi.org/10.1021/cr2003568>, URL <https://doi.org/10.1021/cr2003568>.
- [263] T. Lahaye, C. Menotti, L. Santos, M. Lewenstein, and T. Pfau, Reports on Progress in Physics **72**, 126401 (2009), URL <https://doi.org/10.1088/0034-4885/72/12/126401>.
- [264] S. B. Prasad, T. Bland, B. C. Mulkerin, N. G. Parker, and A. M. Martin, Phys. Rev. A **100**, 023625 (2019), URL <https://link.aps.org/doi/10.1103/PhysRevA.100.023625>.
- [265] S. B. Prasad, T. Bland, B. C. Mulkerin, N. G. Parker, and A. M. Martin, Phys. Rev. Lett. **122**, 050401 (2019), URL <https://link.aps.org/doi/10.1103/PhysRevLett.122.050401>.
- [266] P. M. Walmsley and A. I. Golov, Phys. Rev. Lett. **100**, 245301 (2008), URL <https://link.aps.org/doi/10.1103/PhysRevLett.100.245301>.
- [267] C. F. Barenghi, Y. A. Sergeev, and A. W. Baggaley, Scientific Reports **6**, 35701 (2016), URL <https://doi.org/10.1038/srep35701>.
- [268] A. W. Baggaley and N. G. Parker, Phys. Rev. A **97**, 053608 (2018), URL <https://link.aps.org/doi/10.1103/PhysRevA.97.053608>.
- [269] S. A. Orszag and L. C. Kells, Journal of Fluid Mechanics **96**, 159205 (1980).
- [270] D. Jou, M. Sciacca, and M. S. Mongiovì, Phys. Rev. B **78**, 024524 (2008), URL <https://link.aps.org/doi/10.1103/PhysRevB.78.024524>.
- [271] L. E. Sadler, J. M. Higbie, S. R. Leslie, M. Vengalattore, and D. M. Stamper-Kurn, Nature **443**, 312 (2006), URL <https://doi.org/10.1038/nature05094>.

- [272] G. Lamporesi, S. Donadello, S. Serafini, F. Dalfovo, and G. Ferrari, Nature Physics **9**, 656 (2013), URL <https://doi.org/10.1038/nphys2734>.
- [273] J. Dziarmaga, P. Laguna, and W. H. Zurek, Phys. Rev. Lett. **82**, 4749 (1999), URL <https://link.aps.org/doi/10.1103/PhysRevLett.82.4749>.
- [274] M. Kim, T. Rabga, Y. Lee, J. Goo, D. Bae, and Y.-i. Shin, *Suppression of spontaneous defect formation in inhomogeneous bose gases* (2022), URL <https://arxiv.org/abs/2208.02395>.
- [275] S. Donadello, S. Serafini, M. Tylutki, L. P. Pitaevskii, F. Dalfovo, G. Lamporesi, and G. Ferrari, Phys. Rev. Lett. **113**, 065302 (2014), URL <https://link.aps.org/doi/10.1103/PhysRevLett.113.065302>.
- [276] C. R. Cabrera, L. Tanzi, J. Sanz, B. Naylor, P. Thomas, P. Cheiney, and L. Tarruell, Science **359**, 301 (2018), <https://www.science.org/doi/pdf/10.1126/science.aao5686>, URL <https://www.science.org/doi/abs/10.1126/science.aao5686>.
- [277] A. Farolfi, D. Trypogeorgos, C. Mordini, G. Lamporesi, and G. Ferrari, Phys. Rev. Lett. **125**, 030401 (2020), URL <https://link.aps.org/doi/10.1103/PhysRevLett.125.030401>.
- [278] T. P. Billam, K. Brown, and I. G. Moss, Phys. Rev. A **102**, 043324 (2020), URL <https://link.aps.org/doi/10.1103/PhysRevA.102.043324>.
- [279] T. P. Billam, K. Brown, A. J. Groszek, and I. G. Moss, *Simulating cosmological supercooling with a cold atom system ii* (2021), URL <https://arxiv.org/abs/2104.07428>.
- [280] J. Bezanson, A. Edelman, S. Karpinski, and V. B. Shah, SIAM review **59**, 65 (2017), URL <https://doi.org/10.1137/141000671>.
- [281] S. Omlin, L. Räss, G. Kwasniewski, B. Malvoisin, and Y. Podladchikov, *Solving nonlinear multi-physics on GPU supercomputers with Julia* (2020), URL https://www.youtube.com/watch?v=vPsfZUqI4_0.
- [282] S. Danisch and J. Krumbiegel, Journal of Open Source Software **6**, 3349 (2021), URL <https://doi.org/10.21105/joss.03349>.
- [283] M. J. Davis, S. A. Morgan, and K. Burnett, Phys. Rev. A **66**, 053618 (2002), URL <https://link.aps.org/doi/10.1103/PhysRevA.66.053618>.
- [284] L. E. Reichl, *A modern course in statistical physics* (American Association of Physics Teachers, 1999).

- [285] S.-W. Su, I.-K. Liu, S.-C. Gou, R. Liao, O. Fialko, and J. Brand, Phys. Rev. A **95**, 053629 (2017), URL <https://link.aps.org/doi/10.1103/PhysRevA.95.053629>.
- [286] M. J. Davis, S. A. Morgan, and K. Burnett, Phys. Rev. Lett. **87**, 160402 (2001), URL <https://link.aps.org/doi/10.1103/PhysRevLett.87.160402>.
- [287] P. B. Blakie, Phys. Rev. E **78**, 026704 (2008), URL <https://link.aps.org/doi/10.1103/PhysRevE.78.026704>.